Cardiff University
School of Engineering

A MODELLING AND EXPERIMENTAL STUDY TO REDUCE BOUNDARY LAYER FLASHBACK WITH MICROSTRUCTURE

By

Mohamed Abdulridha Hussien Al-fahham

SUPERVISORS:

Dr. Agustin Valera-Medina
Dr. Samuel Bigot

Thesis submitted in fulfilment of the requirement for the degree of

Doctor of Philosophy in Mechanical Engineering, 2017

DECLARATION

This work has not been submitted in substance for any other degree or award at this or any other university or place of learning, nor is being submitted concurrently in candidature for any degree or other award.

Signed …………………………..……… (candidate)   Date ……………..………

STATEMENT 1

This thesis is being submitted in partial fulfillment of the requirements for the degree of ………(insert MCh, MD, MPhil, PhD etc, as appropriate)

Signed …………………………..……… (candidate)   Date ……………..………

STATEMENT 2

This thesis is the result of my own independent work/investigation, except where otherwise stated, and the thesis has not been edited by a third party beyond what is permitted by Cardiff University's Policy on the Use of Third Party Editors by Research Degree Students. Other sources are acknowledged by explicit references. The views expressed are my own.

Signed …………………………..……… (candidate)   Date ……………..………

STATEMENT 3

I hereby give consent for my thesis, if accepted, to be available online in the University's Open Access repository and for inter-library loan, and for the title and summary to be made available to outside organisations.

Signed …………………………..……… (candidate)   Date ………..………

DEDICATION

Dedicated to memory of the man who believed in me until the last moment of his life

………….. my father

Dedicated to the holiest person in my eyes who prays every day for me

…………...my mother

Dedicated to my unlimited supporting beloved people, my wife and sons Mustafa,

Murtadha and Mujtaba

Dedicated to my brothers and sister for their love and continuous encourage

ACKNOWLEDGEMENTS

ABSTRACT

Trying to improve gas turbines to be flexible to use different fuels requires a big challenge for gas turbine designers when working with current operation stability issues. Flashback is the major challenge for low NOx premixed combustion of high hydrogen content fuels. Flashback in gas turbine combustors is usually assigned to four mechanisms; core flow flashback, combustion instability flashback, boundary layer flashback (BLF) and combustion induced vortex breakdown (CIVB). The last two mechanisms are most common in swirl combustors, which are used to have better operation stability and low emissions.

Improvement of swirl combustors against CIVB has been studied extensively to improve the combustion stability. The most promising solutions of CIVB are limited because the improvement against CIVB worsens the system against boundary layer flashback.

Boundary layer flashback is theoretically based on the Lewis von Elbe's formula for laminar flame, with formulas also used in turbulent flames (with some reservation) by most recent studies. However, the majority of studies take the flame side of the formula, parameters such as fuel type and blends, pressure and preheat temperature, and try to improve the understanding of the boundary layer flashback hoping to find ways to reduce its onset. However, the effect of the burner nozzle has not been studied in many types of research, especially the internal nozzle surfaces. Therefore, this work aims to study the effect of regular surface roughness on the boundary layer flashback in a 150 kW tangential swirl burner.

The first part of this study is a numerical simulation using the in-house code Hydr3D to simulate the flow over riblets with different geometries (blade, triangular, scallop, diamond, lotus and sharkskin). The numerical results demonstrate that the blade riblets were the best at reducing the boundary layer thickness and consequently showed the best drag reduction around 11% compared to the smooth surface while the sharkskin geometry was the worse in drag reduction with only 0.5%.

Although the blade showed the best drag reduction, its weak structure and complex machine specifications make the scallop, lotus, and diamond and sharkskin riblet to be chosen for manufacturing on small discs. The scallop riblet on the nozzle was manufactured using wire electrical discharge machining (WEDM).

The second part of the study was isothermal experimental tests for manufactured surfaces. The flow structure was measured using a 1D LDA. The results show that the riblets alter the flow structure near the wall and increase the velocity gradient which helps the flow to reach a velocity 0.99 from mainstream velocity at y+ <10 compared to y+>30 for a smooth surface.

The third part of the study was obtained with combustion and isothermal experiments using two different stainless steel woven meshes that served as a liner for the nozzle burner. A 50μm and a 150μm wire diameter meshes were used. The isothermal test showed that the 150μm mesh denoted the best shift of the velocity gradient close to the wall. The combustion experiments showed that the two meshes help to improve system against the boundary layer with the 150μm being the best.

Thus, it was demonstrated that BLF could be reduced using microsurfaces, which in conjunction with other techniques, have the potential of increasing optionality, an essential feature for fuel flexibility in Gas Turbines.

PAPERS PRODUCED FROM THIS THESIS

- *Experimental Study to Enhance Resistance for Boundary Layer Flashback In Swirl Burners Using Microsurfaces*. Proceedings of ASME Turbo Expo 2017: Turbomachinery Technical Conference and Expansion June 26-30, 2017, Charlotte, NC, USA.

- *Experimental Study to Enhance Swirl Burner against Boundary Layer Flashback*. 9th International Conference on Applied Energy, ICAE2017, 21-24 August 2017, Cardiff, UK.

- *Investigation of Boundary Layer Flashback Enhancement in Swirl Burner Using Woven Wire Mesh*. 8th European Combustion Meeting. Dubrovnik, Croatia adria combustion institute.org; 2017.

- *A Study of Fluid Flow Characteristics Using Micro-Structured Surfaces Produced by WEDM*. 4M/IWMF2016. Denmark 2016.

TABLE OF CONTENTS

LIST OF FIGURES

xix

LIST OF TABLES

NOTATIONS

Alphabetic Symbols

$(FAR)_s$	Stoichiometric Fuel To Air Ratio	-
AFR	Air Fuel Ratio	-
A_g^+	Dimensional Spacing Parameter	m
C_f	Coefficient Of Friction	-
C_s	Smagorinsky Constant	-
C_w	True Constant (WALE model)	-
D	Pipe Diameter	m
d_q	Quenching Distance	m
E	Electro-mechanical force	v
E'	Instantaneous Electro-mechanical force	v
g	Streamwise Velocity Gradient At The Wall	1/s
g_c	Critical Velocity Gradient At The Wall	1/s
$g_{c,l}$	Critical Laminar Flame Speed	m/s
$g_{c,t}$	Critical Turbulent Flame Speed	m/s
h	Riblet Height	m
h^+	Dimensionless Height (Riblet)	-
h_p	Protrusion Height	m
L	Pipe Length	m
Le	Lewis Number	-
LHV	Lower Heating Value	kJ/mol
P_0	Pressure Of Incoming Mixing Fuel	Bar
Re_d	Reynold Number Based On Pipe Diameter	-
R_{ef}	Flame Péclet Number	-
Re_L	Reynold Number Based On Length	-
Re_x	Local Reynold Number	-
Re_{xcr}	Critical Reynold Number	-
Re_Θ	Reynold Number Based On Mean Flow Velocity (Riblet)	-
S	Swirl Number	-
s	Riblet Space	m
s^+	Dimensionless Space (Riblet)	-
S_f	Flame Speed	m/s
S_f	Flame Speed	m/s
S_L	Laminar Flame Speed	m/s
S_T	Turbulent Flame Speed	m/s
t	Riblet Thickness	m
t^+	Dimensionless Thickness (Riblet)	-
T_0	Temperature Of Incoming Mixing Fuel	C^0
T_{ip}	Burner Tip Temperature	C^0
T_u	Temperature Of Unburnt Gases	C^0
U	Local Velocity (Numerical)	m/s
u(y)	Axial Velocity	m/s
u^*, u_τ	Friction Velocity	m/s
u_∞	Free Stream Velocity	m/s

u_i, u_j, u_k	Velocity Components	m/s
U_m	Mean Velocity (Numerical)	m/s
y^+	Wall Units	-
z^+	Wall Units	-

Greek symbols

μ_0	Dynamic Viscosity Of Unburnt Fuel	$N\ s/m^2$
V	Kinematic Viscosity	m^2/s
δ_b	Balancing Distance From Wall	m
δ_{ij}	Kronecker Delta	-
δ_q, d_q	Quenching Distance	m
P	Fluid Density	Kg/m^3
τ_w, τ_0	Shear Wall Stress	N/m^2
φ	Yaw Angle	^{0}
$\Phi, \emptyset$	Equivalence Ratio	-
Φ_{FB}	Equivalence Ratio Close To Flashback Condition	

ABBREVIATIONS

AIP	American Institute Of Petroleum
ANSYS Fluent	CFD Software Package
ARCCA	Advance Research Computing At Cardiff
ASME	American Society Of Mechanical Engineering
BL	Boundary Layer
BLF	Boundary Layer Flashback
CCD	Charged Couple Device
CCGT	Combined-Cycle Gas Turbine
CFD	Computational Fluid Dynamics
CH_4	Methane
CIVB	Combustion Induced Vortex Breakdown
CMM	Optical Coordinate Measuring Machine
CNC	Computer Numerical Control
CO	Carbon Monoxide
CO_2	Carbon Dioxide
CRZ	Central Recirculation Zone
Da	Damkohler Number
DNS	Direct Numerical Solution
EDM	Electrical Discharge Machining
EIA	Energy Information Administration
FWI	Flame–Wall Interaction
GAW	Global Atmosphere Watch
GHG	Greenhouse Gases
H_2	Hydrogen
HFCs	Hydrofluorocarbons
IBM	Immersed Boundary Method
IC	Internal Combustion Engine
ICCD	Intensified Charge Coupled Device
k-ε	Turbulent Kinetic Energy(K)- Turbulent Dissipation (Ɛ) Model
LDA	Laser Doppler Anemometry
LDV	Laser Doppler Velocimetry
LES	Large Eddy Simulation
LHV	Lower Heating Value
LMR	Local Mesh Refinement
LNG	Liquefied Natural Gas
LOA	Lift Off Alignment
NG	Natural Gas
NO_X	Nitrogen Oxide
PFCs	Perfluorinated Compounds In Teflon And Stain-Resistant Products
PIV	Particle Image Velocimetry
PLIF	Planar Laser-Induced Fluorescence
PMT	Photomultiplier Tube
PTV	Particle Tracking Velocimetry
RAM EDM	Electrical Die Sinking
RANS	Reynolds Average Naiver Stock

SEM	Synthetic Eddy Method
SO_X	Sulphur Oxides
SST	Shear Stress Transport
TKE	Turbulence Kinetic Energy
UHC	Unburned Hydrocarbons
UNFCCC	United Nation Framework Convention On Climate Change
VCD	Vortex-Controlled Diffusers
WALE	Wall Adaptive Local Eddies
WEDM	Wire Electrical Discharge Machining
WMO	World Metrological Organization
XFOIL	Law Reynold Number Airfoil Design And Analysis Code

CHAPTER 1

INTRODUCTION

The work presented in this thesis fits in the wider issue related to energy consumption. It is expected to enable the use of alternative fuels in power plants combustion systems and to lead to an increase in their efficiency and to a reduction in their emissions.

Energy, the key which drives the life on this planet, is everywhere and powers anything. Individuals and society increasingly depend on its abundance, convenience, and potential. It is stealth in every detail of life, moves our bodies; operates our transport and factories and turns our night to day. The idea of a power outage or no port to charge a battery for mobile or stay without energy for one hour becomes a nightmare.

An energy crisis is coming on the horizon due to intensification in global energy demand, extracted more fossil fuels to generate power and transport all in parallel with the steady increase in population. The challenges rise to cover everyday need and limitation of fuel sources. The emissions from factories, transport, and power plants are thought to be the leading cause of greenhouse gases which lead to the more severe climate change problem Coyle and Simmons (2014).

1.1 Fossil Fuel and Alternative Fuels

Mankind has always needed energy; first food was the way to survive and to fuel the body and life. As humankind developed, development was based on wood to set fire and cook. The fire ignited more needs melting iron and copper to make weapons and hunting tools. More and more needs came to light during centuries. With every development and more prosperity in life, there was a greater necessity for new sources from food consumption to fuel.

1.1.1 Fossil Fuel

Fossil fuels are fuels that result from natural processes such as the anaerobic decomposition of buried dead organisms through exposure to heat and pressure in the Earth's crust for an extended period. The age of such organisms and their resulting fossil fuels is typically millions of years, sometimes exceeding 650 million years Wikipedia contributors (2015).

1.1.1.1 Coal

Coal is a regular and conventional solid fuel. Since the industrial revolution, it has become the primary source of energy generation. Because it is a complex and heterogeneous sedimentary, it is characterised by a wide variety of properties and compositions. It is an essential fuel for power generation with more than 41% of coal used in electricity generation. It is also used widely in coke industry. Environmental regulations, SO_x /NO_x problems, ash disposal, the acid rain, greenhouses effects and safety issues in coal mining and economic transporting will guide the future of using coal as the primary source of energy Sunggyu Lee (2014).

1.1.1.2 Petroleum

Crude oils are naturally occurring substances derived from the decomposition over thousands of years of plants and animal organic matter under high elevated temperature and pressure. They are compound of hydrocarbon combinations. Due to their complex composition, crude oils have very wide range of physical/chemical properties. Depending on their density, crude oils can be classified into a range from light to heavy crude oil. All crude oils contain carbon, hydrogen, sulphur, nitrogen, oxygen, minerals and salts in varying proportions depending on their source The American Petroleum Institute (2011). EIA estimates that global petroleum and other liquid fuels inventory build will average 1.0 million b/d in 2016. Inventory builds are likely to continue into 2017, but at a decreasing rate, averaging 0.3 million b/d for the year EIA (2016b).
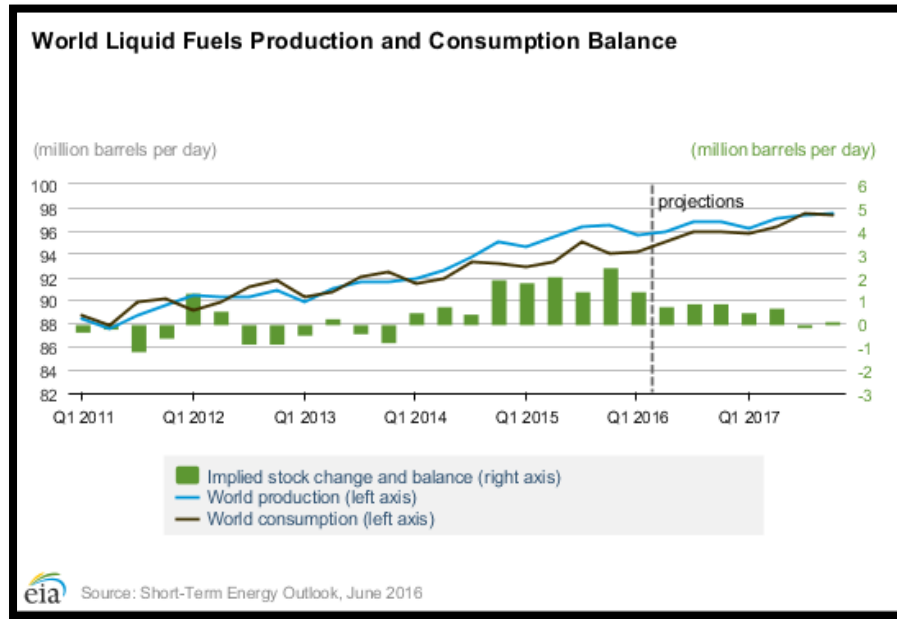
Figure 1-1 Global Petroleum and Other Liquids Consumption.

1.1.1.3 Natural Gas

Natural gas comprises gases captured in oil deposits, whether liquefied or gaseous, consisting mainly of methane. Depending on their origin, there is "non-associated" gas that comes from fields producing hydrocarbons only in gaseous form and "associated" Gas produced in combined with crude oil as well as methane recovered from coal mines (colliery gas). Natural gas can be found in huge qualities. It has the lowest carbon intensity, emitting less CO_2 per unit of energy generated compared to other fossil fuels. It burns efficiently and cleanly, with very few non-carbon emissions. High compressibility and low viscosity of natural gas are essential characteristics that help in development and production.

1.1.1.4 Shale Gas

The trapped gas in rock formations is known as shale gas. Shale formations in which thermogenic gas has been trapped occur up to 2 to 3 km below the Earth's surface, which may vary depending on geological effects. The gas has been caught up in irregular fissures rather than in large lurking vertical wells. Thus optimal production needs to work horizontally Norton Rose Fulbright (2013).
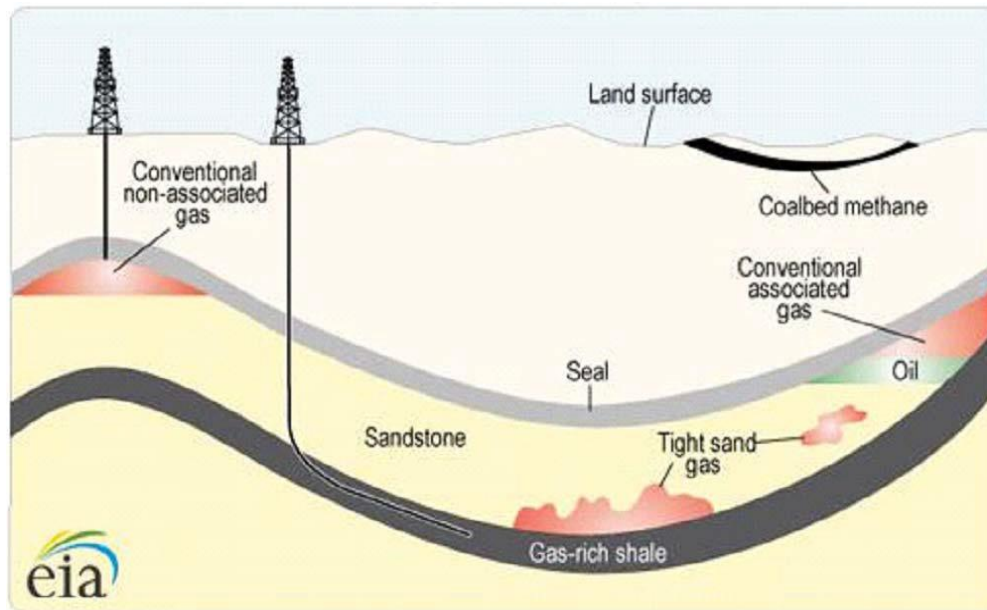
Figure 1-2 Shale gases Energy Information Administraions (2013)

1.1.2 Alternative fuel

Alternative fuels originate from resources other than fossil fuels. Some are produced domestically like ethanol, which is derived from corn or vegetable crop, reducing the dependence on imported oil, and other are derived from renewable sources such as hydrogen. Reduction of emitted pollution to air from the use of alternative fuels is one of their great boosting their application to replace the fossil fuels Oner and Altun (2009).

1.2 Climate change and Greenhouse effect

Scientific studies make greenhouse gases responsible for climate change. Green-house gases (sometimes known as GHG) are gases in the atmosphere that can absorb and emit radiation over the thermal infrared range. It is believed that this process is the main cause of the greenhouse effect. The primary greenhouse gases in the atmosphere are water vapour, carbon dioxide, nitrous oxide, methane, and ozone. Life on Earth has evolved under a greenhouse-like atmosphere. Main greenhouse gases effects can be seen on the temperature of the Earth. Earth's surface warms due to short-wave solar radiation that passes through the atmosphere. The Earth then radiates energy to the

atmosphere as long-wave infrared radiation. Gases in the atmosphere (water vapour, carbon dioxide, methane, nitrous oxide, and ozone) are transparent to incoming solar radiation, but they absorb and re-emit some of the outgoing long-wave radiation warnings up the Earth's surface and its lower atmosphere. This natural greenhouse effect helps to warm the Earth by as much as 33 ∘C, which makes life on Earth possible Kates et al. (2003).
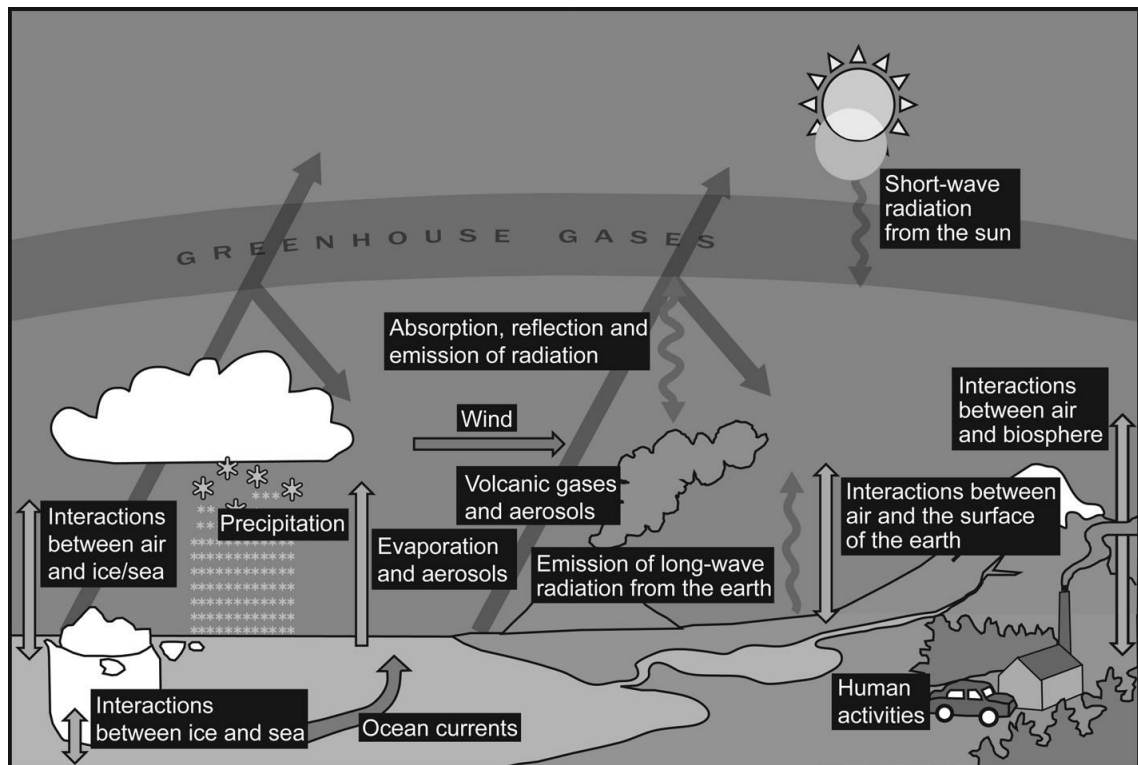
Figure 1-3 Climate parameters Energy Information Administraions (2013).

Efforts to define the reasons behind climate change and put in place solutions go in two directions: scientific and political, which are not all time on the same side, especially when scientists accuse large economies of neglecting the environmental price caused by profitable heavy industries. The first theoretical model for estimating the effect of increasing atmospheric concentrations of carbon dioxide on global temperature was formulated by the Nobel Prize Swedish chemist Svante Arrhenius in 1896. His estimation was that an average increasing of 5-6 ^0C in temperature would occur if the CO_2 concentration were doubled. Also, he used term "hothouse" to describe the heat-trapping properties of atmosphere CO_2 which is later known as greenhouse gases. Effects took about a century to raise the alarm. In 1988 the USA experienced the worst

summer in its history; a heat wave with drought weather supported the theories of climate change which were suggested during the last decays. Sharp growing in population and their needs for transport, electricity and living resources puts more pressure on nature to fulfil. Most of these activities involve using energy in different ways which mean burning more fuel to run factories, power plants and transport leading to more emitted gases to the atmosphere, especially CO_2, Methane, and Nitrous oxide. Figure 1-4 shows the percentage of each gas emitted in the UK during 2013
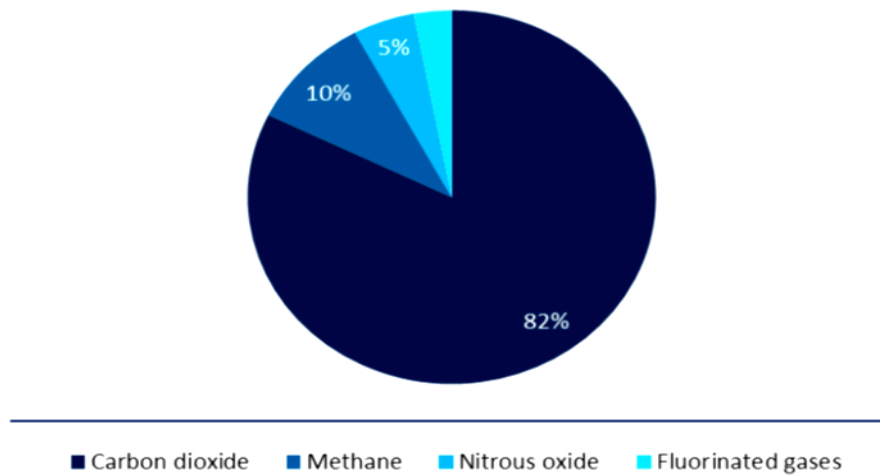
Figure 1-4 Greenhouse gas emissions by gas, UK and Crown Dependencies 2013 (%) UK Government (2013).
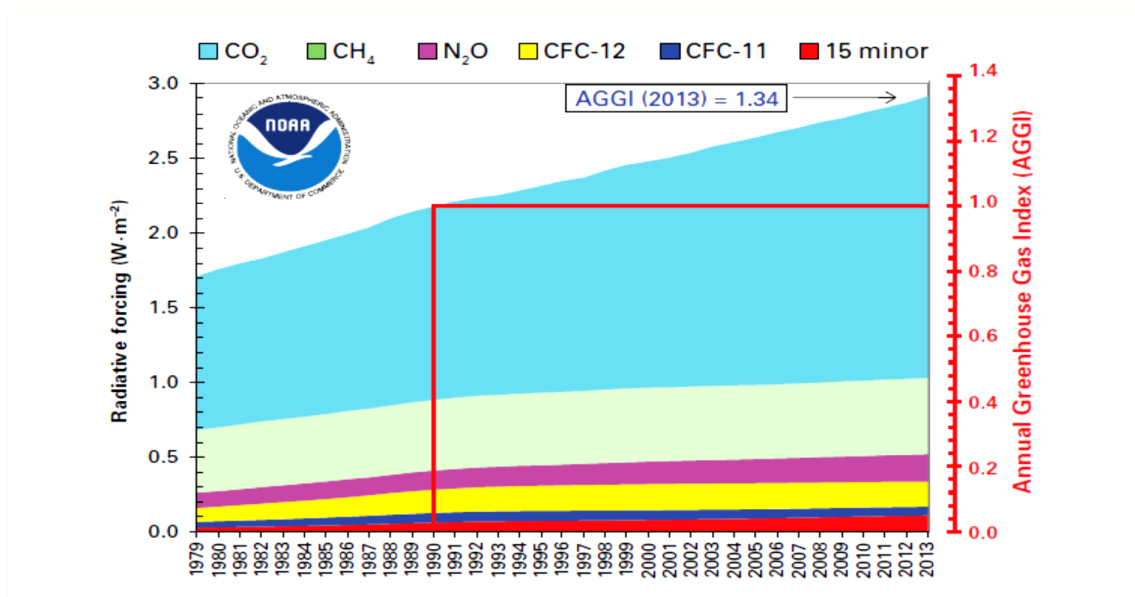
Figure 1-5 Atmospheric radiative forcing WMO/GAW (2014).

Similar studies are published around the world to specify ratios of emitted gases to the atmosphere. Figure 1-5 shows that all GHG will increase every year around the world and CO2 the main greenhouse gas. Sources of CO_2 are mainly fossil fuels, cement, and land-use change while CO_2 sinks are land and oceans.

Figure 1-6 shows the CO_2 budget, an environmental calculation for CO_2. This budget increases every year. It reached 32 ($\pm$2.7) $GtCO_2$ / yr in 2010, with an increase up to 3 % between 2010 and 2011 and around 1 – 2 % between 2011 and 2012. In 2013, global CO_2 emissions from burn fossil fuel (and cement production) were 36 gigatonnes ($GtCO_2$); which is 61% higher than in 1990 (the Kyoto Protocol 1997) and 2.3% more than 2012 Global Carbon Budget (2014).
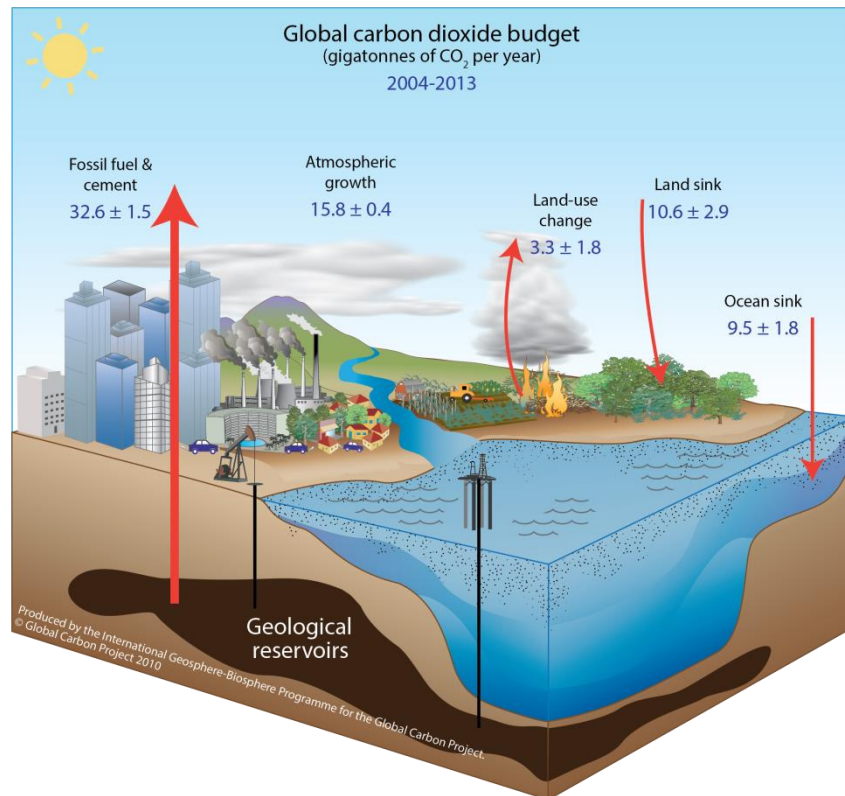
Figure 1-6 Perturbation of the global carbon cycle caused by anthropogenic activities, averaged globally for the decade 2004–2013 (GtCO2/yr).

1.3 Solution

Studies every year that call for action to reduce GHG emitted to the atmosphere increase daily. Such calls force two close related challenges; the first one is to develop more alternative sources of clean or friendly energy, which need enormous investment and funds. Adaptation to the use of clean energy sources requires considerable money since the initial cost for such projects usually is high. Figure 1-7 shows the amounts of investment in renewables through the last decade.
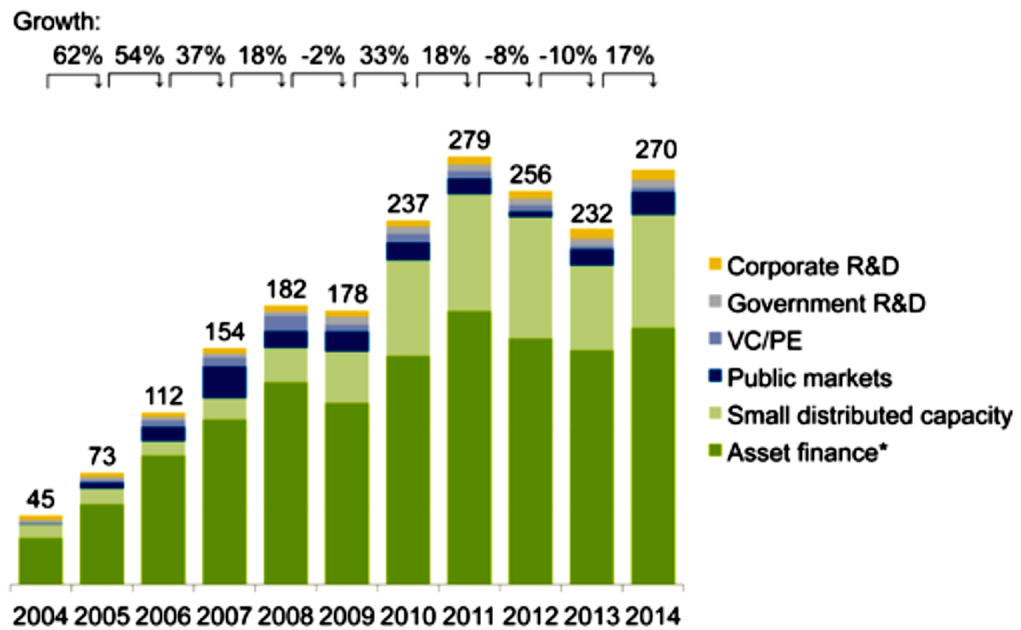
Figure 1-7 Global new investment in renewable energy by asset class, 2004-2014, $BN
UNFCCC (2015)

The second challenge is political. Since accumulative scientific evidence led to accuse the big industrial countries of manipulating the climate of the planet, the politicians prefer to point out to the researchers who put some doubts on linking industry and the energy sectors to climate change. This situation is still the main snag that tackles the efforts to have an enforceable conviction to reduce GHG emissions. In 1997, the United Nation Framework Convention on Climate Change (UNFCCC) negotiated a treaty at the city of Kyoto, Japan, came into force on February 16th, 2005, which is known as the Kyoto Protocol. The Kyoto Protocol is a legally binding agreement. Under which industrialised countries ought to reduce their collective emissions of greenhouse gases by 5.2% as compared with the year 1990, (which is represent 29% cut, when compared

to the emissions levels that predicted by 2010 without the Protocol,). The aim is to reduce overall emissions from six greenhouse gases - carbon dioxide, nitrous oxide, methane, sulphur hexafluoride, HFCs, and PFCs - calculated as an average over the five-year period of 2008-12 UNFCCC (2015). The fruit of this protocol can be seen in the annual reports of CO_2 emissions published periodically by specialist institutes (Energy Information Administration 2013). Fig 1-8 shows lower electricity-related carbon dioxide emissions reflecting lower carbon intensity and electricity use.

U.S. electric power carbon dioxide emissions (2000-2013)
million metric tons (MMmt) of carbon dioxide
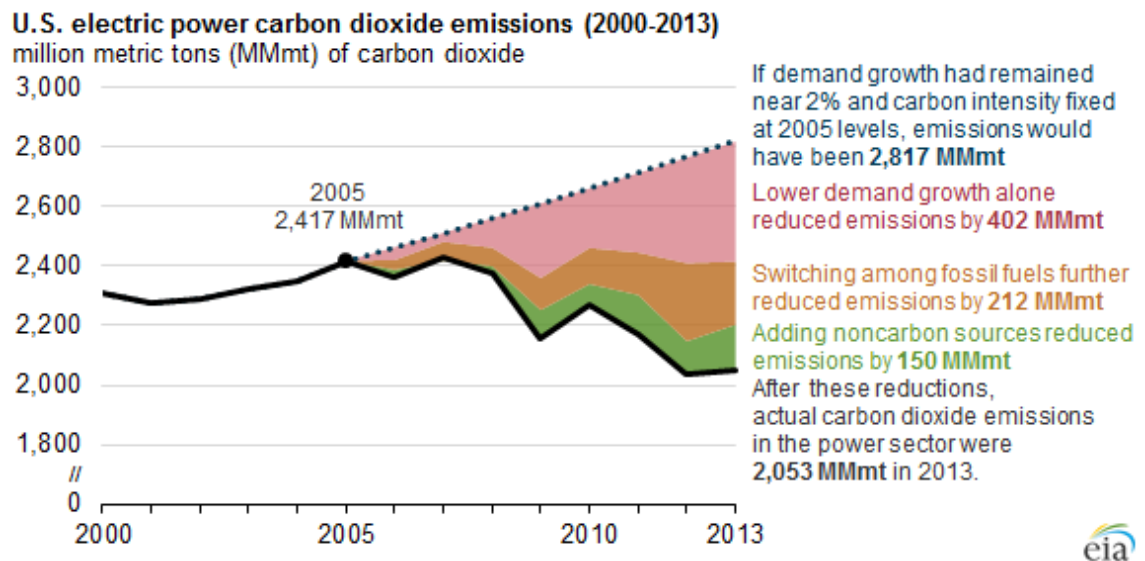
Figure 1-8 Lower electricity-related carbon dioxide emissions are reflecting lower carbon intensity and power use Energy Information Administraions (2013).

It is obvious that times showing annual reductions in GHG around the world are still far away but are not impossible. To accelerate such process, there are many integrative steps in the energy sector, leading sector of GHG emissions:

- Improve the combustion systems in existing gas turbine power plants, upgrade of mid-age gas turbine power plants and retire the old ones.

- Optimise of boilers, generators and carbon capture systems in power plants.

- Invest more in modern technology to use alternative fuels.

- Invest and support research that tries to find advanced materials to improve the efficiency of fuel combustion.

1.4 Gas Turbine Power Plants

The concepts of gas turbines became known by many engineers by the end of 19th century. The simple gas turbine cycle was considered as the first successful electric power-generating machine to go into commercial operation. In 1939 A. B. Brown Boveri in Baden, Switzerland designed and installed in the power station in Neuchâtel, Switzerland ASME (2015). Today, gas turbines are the most widely used power generating technology. A gas turbine is a type of internal-combustion (IC) engine. IC burns an air-fuel mixture producing hot gases that rotate the shaft to generate power. Gas turbines can use a variety of fuels, including fuel oils, natural gas, and synthetic fuels. The increase of gas turbines in recent years has been achieved by three main points Giampaolo (2006):

- Advance materials that have made possible the utilisation of high-temperature gases in the combustor and turbine components.

- Employment of computers in the simulation and design of turbine aerofoils, combustors, and turbine blade cooling configurations.

- Accumulative background of thermodynamic and aerodynamic knowledge.

1.4.1 Principles

A traditional gas turbine engine is comprised of three primary sections connected to the same shaft: 1) the compressor 2) the combustion chamber (or combustor) 3) the turbine. The compressor is classified into two types: axial and centrifugal. The higher flow rates and efficiencies put the axial flow compressors in the forefront of power generation. Axial flow compressors consist of multiple stages of rotating and stationary blades (or stators) throughout which air is suctioned in parallel to the axis of rotation and gradually is compressed as it passes through each stage. The air accelerated through the rotating blades and diffusion by the stators raises the pressure and reduces the volume of air. Despite the fact that no heat is added, compression of the air also leads the temperature increase. Figure 1-9 shows an axial gas turbine for an auxiliary power unit Baskharone (2006).

The combustion system (combustion chamber) typically is made up of a ring of fuel injectors (nozzles) that inject a study amount of fuel into the combustion chambers where the fuel mixes with the compressed air. The compressed air and fuel can be pre-mixed, or the compressed air can be supplied directly to the combustor. Under constant
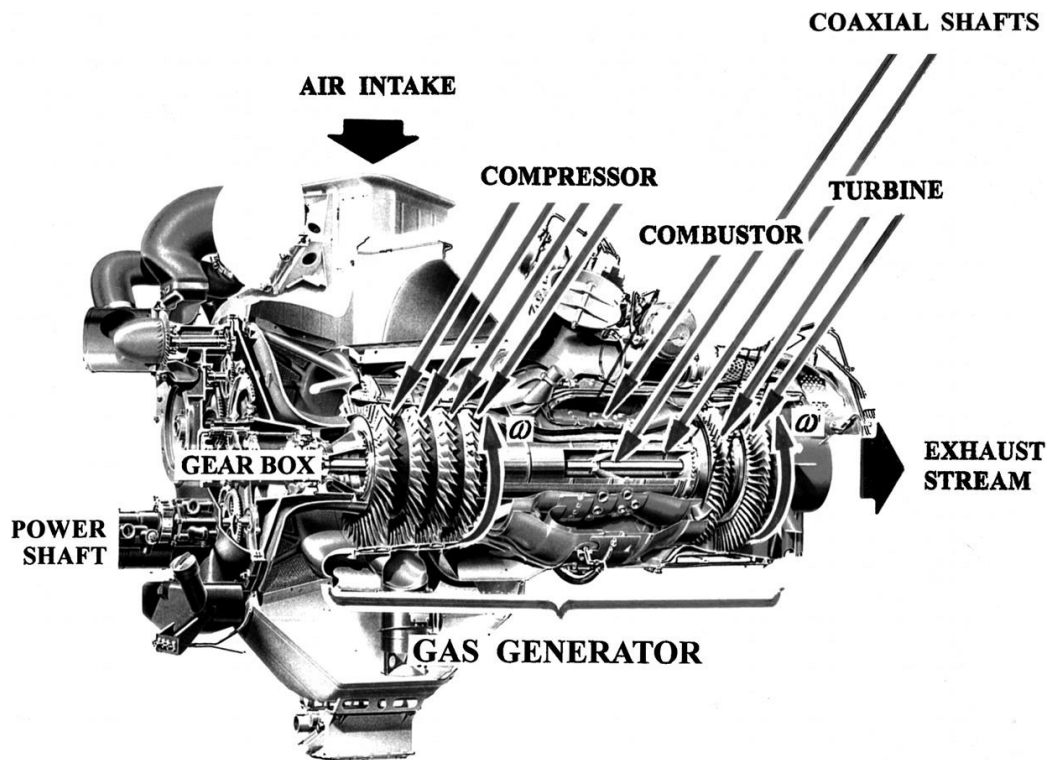
Figure 1-9 Auxiliary power unit, GTCP 660-4 Auxiliary power unit COSPP (2010).

pressure conditions, the fuel-air mixture ignites with temperature that exceed 2000^0 C; the combustion produces a high temperature, a high-pressure gas stream enters the turbine section, where the gases expand rapidly and cause rotation of the shaft.

The turbine has a number of stages, each with a row of stationary blades (or nozzles) to guide the expanding gases followed by a row of moving blades. As a result of rotation, a part of the shaft power is used to drive the compressor to suck in and compress more air to sustain continuous combustion. The other part of the shaft power is used to drive a generator to produce electricity.

1.4.2 Efficiency

As a thermal machine, gas turbines efficiency is the main performance parameter that is considered for the economic and environmental purpose. If we take in mind that the fuel

will still represent 50 to 70 % of annual plant budget any increase of unit efficiency even a tiny one- will reduce fuel consumption and emissions BROGLIO (2014). The efficiency of gas turbines has developed through past years. The first simple cycle had 18% thermal efficiency, with less than 540°C turbine inlet temperature and the exhaust temperature a little over 260 °C. Nowadays, thermal efficiency reaches 40% in a simple cycle, with turbine inlet temperatures of 1500°C and exhausts up to 630°C. A combination of better alloys, combustors, coatings, higher turbine inlet temperatures, compressor ratios, advanced heat transfer technology, better cooling and a whole lot
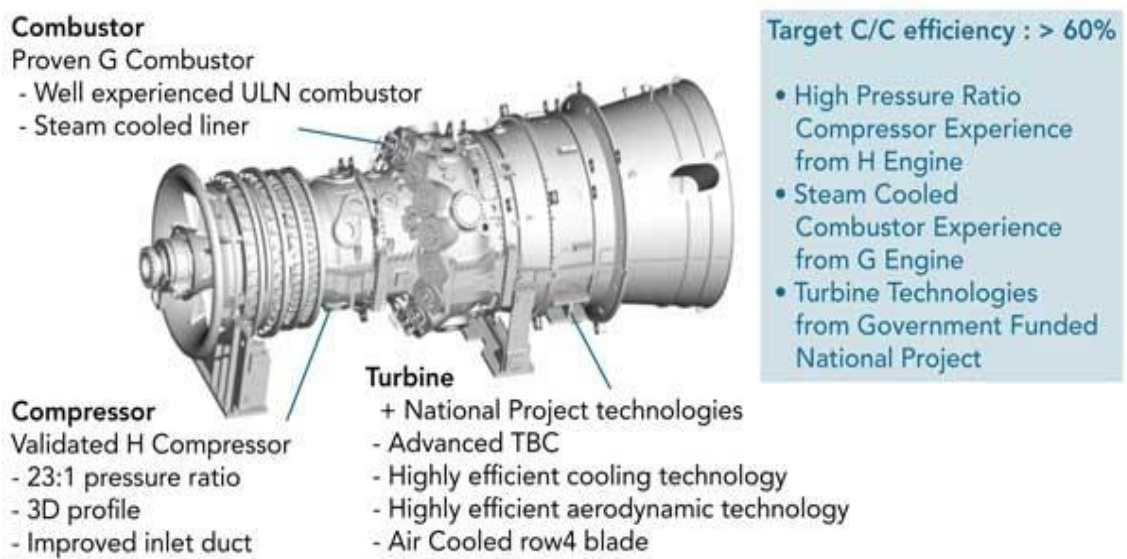
Figure 1-10 Mitsubishi's 'J Class' gas turbine - on course for 60% efficiency in combined-cycle operation (COSPP 2010).

more of devices are employed to produce and develop high-efficiency gas turbines. Furthermore, an improved compressor and turbine aerodynamic designs, improved seals, better clearance control, and larger engines higher gas turbine efficiency can be obtained COSPP (2010).

Over the last few decades, great advancement in technology meant a significant increase in efficiency through raising the gas turbine inlet temperature, with concurrent reduction of investment costs and emissions. The CCGT electrical efficiency is expected to increase from the current 52–60% (LHV) to some 64% by 2020 Seebregts (2010).

1.4.3 Alternative Fuel and Stability

Most of the gas turbines are using the natural gas as a fuel. During the last few decades, the using lean premixed combustion of natural gas has been developed to achieve low NOx and minimal cycle efficiency drawbacks Taamallah et al. (2015). Alternative methods of lowering NOx such as fuel staging, inert species dilution as well as exhaust gas clean-up in a non-premixed combustion system. Also to be limited in their NOx emission, these methods usually are associated with increased operating and basic costs as well as efficiency penalties Gazzani et al. (2014), contrary to premixed combustion. However, operating a combustor in a lean premixed mode brings its own challenges Sreenivasan and Raghu (2000). It raises operability concerns because of the increased risk of combustion instability, as well as possible higher CO emissions, leading to a potentially narrow window of safe, stable and clean operation regarding both CO and NOx. Promising methods for reducing emissions, combined with the high efficiency, fast ramp rate, and relatively low cost makes gas turbines – especially in a combined cycle configuration – one of the best candidates to enable a transition toward a low carbon-based power mix Gazzani et al. (2014). Such methods the hydrogen is produced as a by-product. Hence the gas turbine combustion system would need to be operated using a synthetic gas (a mixture of H2, CO, and CH4 mainly) or potentially pure hydrogen. But, this option faces two major issues: first, is the design of gas turbine itself since most of the designs focused and optimised to use natural gas as a fuel. Second, the issue is the variation in the fuel composition which leads to operability issues Richards et al. (2001). Although Hydrogen and syngas are considered as promising fuel, high instability operation risks also addressed, such as a flashback. Hydrogen and other fuel blends can cause main issues with many swirl combustors, due to the considerable variation in flame velocity with such fuel blends compared to natural gas Syred et al. (2012).

1.5 Summary

Humanity should work hard to find a more sustainable way of life. The sources are limited, but the human brain capabilities are not. The main challenge is to find the ways to improve the exploitation of natural resources efficiently without putting more pressure on nature. Hydrogen and alternative fuels appear to be a promising solution,

however combustion systems need to be improved in terms of stability and operational risks, especially regarding blow off and flashback. More specifically, developing combustion systems more robust to flashback issues will qualify them for the safe and effective use of Hydrogen and alternative fuels in power plants, which would cut emission rates significantly.

1.6 Objectives

This thesis seeks to:

- Achieve wide operation window foe existing burner using the effects of new aerodynamic micro profiles for implementation in GTs, especially to reduce flashback and improve the flame stabilities.

- The study tries to introduce a solution to BLF that enable to switch between different fuels.

1.7 Thesis structure

This work divided into eight chapters which are as follow:

Chapter One: The introduction chapter gives a summary of the fuels that are used in power plants, energy generation, and climate change. A review of comprehensive reports from governmental and organisations agencies that are active in climate change issues is presented. And the need for solutions enabling the use of alternative fuels in power plants is highlighted.

Chapter Two: This chapter firstly presents a review of combustion systems in gas turbines and combustion process stability. Then flashback phenomena are discussed, with emphasis on wall flashback. A good trace of previous works on wall flashback is also performed.

Chapter Three: In this chapter, a brief description of the boundary layer in fluid flows is performed. A promising technique for boundary layer control using structures inspired by nature is then described.

Chapter Four: This chapter gives a full description of the experimental rigs and their components. Numerical studies are reviewed and details of the in-house simulation tool developed in Cardiff University (LES code Hydro3D) are presented.

Chapter Five: This chapter describes the manufacturing techniques and strategies that are used to produce surfaces structures inspired by nature.

Chapter Six: In this chapter, the in-house Hydro 3D code is used to simulate the flow over three essential geometries. Once correlation with published experimental works is ensured, new geometries, which could be manufactured, are tested to reduce the boundary layer thickness and improve the system resistance towards flashback.

Chapter Seven: Isothermal experiments using air as working fluid are described. Results are discussed and compared with other published previous works.

Chapter Eight: Conclusions and future work.

CHAPTER 2

LITERATURE REVIEW

The combustion of hydrocarbons fuel and the gas turbine combustion system will be described first in this chapter. Then, fuel application will be presented and finally, the classification of flames and previous related experimental and numerical studies will be reviewed. In gas turbines, the output power is controlled by the heat input that comes from burning fuel in the combustion chamber using the compressed air from the compressor. The main fuels used in gas turbines are hydrocarbon fuels. Kerosene and natural gas are examples of liquid and gaseous fuels. Natural gas is widely used in industrial gas turbines.

The excessively high temperature in the combustion chamber could cause a reduction in the life of the turbine components, so it should be controlled to avoid such drawback. The combustion process takes place in three distinct parts; normally, the fuel is burnt in the primary zone to release heat from the fuel. Additional air is provided in an intermediate zone to complete the combustion. Finally, more air is provided to reduce the combustion chamber exit temperature to that required for the turbine in a dilution zone.

2.1 Combustion of Hydrocarbon Fuels

Hydrocarbon fuels do not burn in air spontaneously at atmospheric conditions. To provoke such fuels to be burnt, they should be heated to high temperatures. Heated hydrocarbon fuels usually have a strong reaction with oxygen to form carbon dioxide and water, thus releasing heat. The carbon and hydrogen content of the fuel determine the necessary amount of air to complete combustion. The ratio of fuel mass to air mass for complete combustion is called the stoichiometric fuel-air ratio. Fuel-air mixtures are lean mixtures when they have excess air and rich mixtures when they have excess fuel. The stoichiometric fuel-air ratio can be calculated by using the equation below Razak (2007):

16

$$(FAR)s = \frac{12.01x+1.008y}{137.33(x+\frac{y}{4})} \quad \dots\dots\dots\dots\dots\dots\dots\dots\dots\dots\dots\dots\dots\dots\dots\dots\dots \quad (2.1)$$

Where, x and y represent carbon and hydrogen in a hydrocarbon fuel respectively. So for complete combustion of 1kg of methane, 17.12 kg of air are needed. Combustion in the excess air will lead to the presence of oxygen in the products.

2.2 Gas Turbine Combustion System

Figure 2.1 shows the typical combustion chamber system that consists of the following components and zones:

1- Diffuser.
2- Primary zone.
3- Intermediate zone.
4- Dilution zone.
5- Fuel nozzle
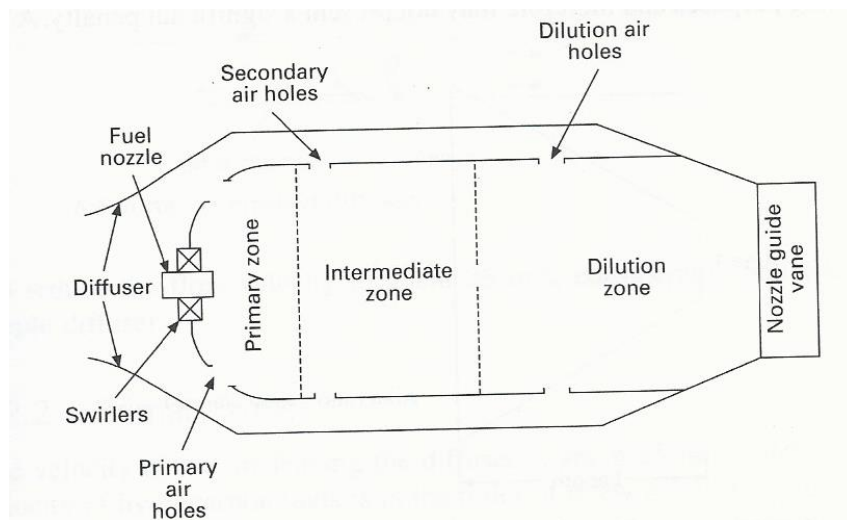
Figure 2-1Schematic representation of a typical combustion chamber

2.2.1 Diffuser

The diffuser is used to reduce the flow velocity in a way that helps to start the combustion process since the compressed air provided from the compressor comes at high speed which could blowoff the flame. A simple diffuser is a straight walled divergent duct. The diffuser length is an important parameter for the diffuser performance. The optimum length should achieve diffusion in the shortest length with

minimum losses in pressure. In aero-engine applications, short diffusers called vortex-controlled diffusers (VCD) are used.

2.2.2 Primary zone

When the air leaves the diffuser and enters the primary zone, the air velocity is around 25 m/s. The flame speed of hydrocarbons is between 5-7 m/s Razak (2007). Such a difference makes burning fuels very hard and will lead to flame extinction. Thus, combustion needs time to be well established which requires sufficient reduction in air velocity to ensure a stable process which could achieved using primary zone.

2.2.3 Intermediate zone

In this region, air is provided in small amounts to reduce the temperature of the combustion gases which leave the primary zone with a temperature around 2000K. Also, this further interaction provokes these gases to complete the formation of carbon dioxide and water. Otherwise, unburned hydrocarbons (UHC) and CO would pass to the dilution zone and appear as pollutants indicating a poor combustion.

2.2.4 Dilution zone

The purpose of the dilution zone is to cool down the combustion gases to meet the thermal specification of the turbine blades by mixing the hot gases with additional amounts of air.

2.3 Fuel Application

Different kinds of fuels are used to operate gas turbines. A short review of the most common types of fuel will be discussed next.

2.3.1   Natural Gas (NG)

Natural gas is considered the second-most common fuel for electricity generation behind coal. Natural gas-fired generation first surpassed coal production on a monthly

basis in April 2015 EIA (2016b). For example, USA the largest consumer of natural gas around 25% of world, natural gas-fired generation has exceeded coal-fired generation since then and is likely to continue to exceed coal production through the remainder of the decade, eventually providing 34% of the United States's electricity generated this year. Coal's has a share of the 2016 U.S. electricity generating mix around 30% with nuclear 19% and renewables at 15% EIA (2016a). Figure 2.2 shows this trend.

Monthly net electricity generation, all sectors (Jan 2011 - Dec 2016)
million megawatthours per day
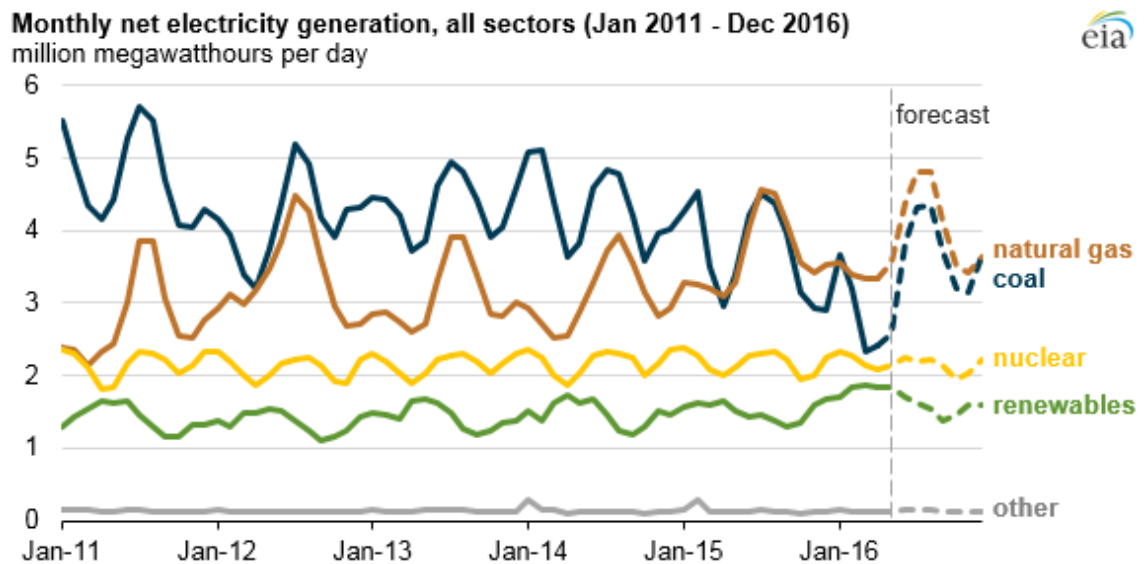
Figure 2-2 Monthly net power generation in the US, Source Short term outlook 2016 EIA.

Notably, the share of energy production that natural gas provided is expected to fall for many years after 2016 as it contends with renewables. Also, as a consequence of natural gas prices rise. In EIA's Annual Energy Outlook 2016 Reference case EIA (2016b), the natural gas generation share declines until about 2020 and then grows steadily over the next two decades. Natural gas is projected to regain the largest proportion in the electricity mix by 2022 and maintain that position up to 2040.

2.3.2 Liquefied natural gas (LNG)

In recent years, liquefied natural gas become a gradually important source of energy throughout the world. Using liquefied natural gas to increase capacity is either under consideration via infrastructure modification. The difference in a number of properties between liquefied natural gas and pure natural gas is a result of its production process; Potential low-calorific constituents are volatilized by liquefaction process. The

production process causes changes in the gas composition, with increased fraction of higher hydrocarbons and higher heating value Volker Poloczek (2008).

2.3.3 Syngas

Syngas is a fuel gas mixture in which hydrogen represents the main component, carbon monoxide, and very often some carbon dioxide. Syngas provides increased flexibility for the use of available energy source. Syngas can be extracted from a wide variety of coal grades, but also from biomass, petroleum coke, and refinery residues. Purified synthetic gas not only increases the flexibility of useable energy source, but it also enables the use of this energy source in gas turbines targeting electricity, heat production, and CO2 sequestration & storage. The difference between syngas and low-BTU gas is that a low-BTU gas does not have any hydrogen (H_2) fraction beyond the standard values. By contrast, syngas has one major component, and that is hydrogen (H_2). H_2 is provided by the gasification process and is a function of feedstock and syngas conditioning upstream the gas turbine. The nature of H_2 is that it has the highest reactivity Schobert and Schobert (2013).

2.4 Classification of Flames

Most essential studies of flame combustion are performed using gaseous or pre-vaporized fuels. Although the flame can propagate through a static air-fuel mixture, it is often to stabilising the flame at a fixed point by supplying fuels via a continuous flow of a combustible mixture. Therefore, flames can be classified into two main categories—*premixed flames* and *diffusion flames*—based on the mixing of fuel and air. In case, the fuel and air are fully premixed before they enter the combustion zone, the flame known as a premixed flame. On the other hand, if the fuel is kept separate until is burned, the flame is known as diffusion flame Swaminathan and Bray (2011). Also, depending on the prevalent flow velocities, both types of flame can be further classified as *laminar* or *turbulent*.

In some cases, complications can appear, especially in practical systems burning liquid fuels. When the fuel is not completely vaporised before entering the flame zone,

heterogeneous spray combustion may take place. Here, a different diffusion flame from burning individual evaporated fuel droplets may be superimposed on a premixed turbulent flame zone. However, the combustion process is described as homogeneous if both reactants are in the same physical state Lefebvre and Ballal (2010). In this work, a premixed flame will be considered.

2.4.1 Laminar and Turbulent Premixed Flames

By definition, in a premixed flame, the gaseous fuel and oxidant are homogeneously mixed before combustion. The burning velocity of flame is the rate at which a plane combustion wave will move through a combustible gaseous mixture; it is determined partly by the rate of chemical reaction in the thin flame zone, and by heat and mass transfer from the flame to the unburned gas. The burning velocity of flame is affected by flame radiation and by flame temperature, also by local gas properties such as viscosity and diffusion coefficient, pressure, temperature, and AFR. It was found that the laminar burning velocities of stoichiometric mixtures of many hydrocarbon fuels burning with air have a typical value around 0.43 m/s at normal atmospheric temperature and pressure Pallav et al. (2014).

On the other hand, the turbulent flame speed more complicated, where more parameters can effects on its value such as turbulent intensity, back pressure and flame thickness, and still a topic of interest to the combustion community Lin et al. (2013). The turbulent flame speed changed with gas type, the turbulent Reynold number and pressure Taamallah et al. (2016).

2.5 Combustion Instabilities

The major challenge for any successful, safe and reliable premixed fuel burner design, especially for H_2-rich fuels is to achieve a stable flame position Benim and Syed (2015a). However, the operability issues represent the main challenges, and the most critical issues are Lieuwen et al. (2008b):

-       *Blow off* refers to the situation when the flame physically extinct. Different systems are used to ensure flame anchoring to combustors such as rapid expansions or

bluff bodies in the flow. Regardless the stabilisation method, there is a certain range of conditions where the flame can stabilise.

- *Autoignition* refers to the situation when the fuel mixture ignites spontaneously upstream of the combustion chamber.

- *Combustion instability* refers to harmful oscillations driven by fluctuations in the combustion heat release rate.

- *Flashback* refers to the situation when the flame propagates upstream of the region where it is supposed to anchor and into premixing passages that are not designed for high temperatures. However, the flashback in gas turbine combustors is usually assigned to four mechanisms:

1- **Flashback due to combustion induced vortex breakdown:** this kind of flashback requires a swirling flow in the mixing zone and occurs due to the interaction of heat release with swirling flows, which leads to the transition of the vortex breakdown characteristics Kröner et al. (2003). The breakdown condition depends upon the swirl number. Vortex breakdown states are presented for high swirl numbers, S>~1. No breakdown occurs for low swirl numbers, S<~0.5 Lieuwen et al. (2008b). The basic phenomenon leading to the sudden flow transition is that the flame contributes to vortex breakdown, and therefore generates a region of low or negative flow velocity ahead of it. The flame advances forward, causing the location of the vortex breakdown region to advance farther upstream into the mixing zone. This process continues as the flame proceeds farther and farther upstream. In this case, flashback can occur even if S_T is everywhere much less than the flow velocity in the isothermal case Lieuwen et al. (2008b).

2- **Boundary layer flashback:** in the boundary layer, the flow gradually reduces towards the wall due to the no-slip wall boundary condition. Thus, even for high freestream velocities, it is possible that the flame speed outbalances local flow rate in the boundary layer Benim and Syed (2015b).

3- **Core flow flashback:** this kind of flashback occurs when the flow velocity falls below the flame speed in the core area. During the normal operation of the gas turbine, this mechanism rarely occurs because of the freestream velocity in the

air-fuel supply system much higher the turbulent flame speed Lieuwen et al. (2008a).

4- **Flashback due to combustion instabilities:** this kind of flashback occurs when the interaction of acoustic modes, flow structure and the energy release of the flame can lead to acoustic velocities in the order of the flow velocity. In such a situation, the flow effectively stagnates during each acoustic cycle, allowing for an upstream propagation of the flame into the fresh gases Wierzba and Kar (1992).

Plee and Mellor (1978) reported in a review of combustor flashbacks that apart from the flashback mechanisms mentioned above, the flashback could occur due other reasons for upstream flame stabilisation. Since Lewis and Von Elbe (1934) introduced their theory of the flame propagation, the four above mechanisms have been studied extensively from many perspectives. To intensify on the primary goals of this search, only the BLF studies will be represented with some details.

2.6 Boundary Layer Flashback (BLF)

2.6.1 Critical Velocity Gradient Model in Laminar Flames

Lewis and Von Elbe (1934) studied the flashback phenomenon through systematic boundary layer flashback (BLF) tests with perfectly premixed, laminar methane–air flames at atmospheric pressure and temperature. The fully developed flow and the flames were burning in the free atmosphere on top of Pyrex glass tubes with inner diameters between 3 mm and 16 mm to obtain reproducible flashback limits. Since it was important to control the temperature of the burner rim, the tube was left to cool down after each flashback Lewis and von Elbe (1943). Flashback was provoked by decreasing the flow velocities in the boundary layer through reducing the flow rate or approaching more stoichiometric conditions. Based on these experiments, they developed the idea of *critical velocity gradient* near the wall. Due to its high importance and its extensive application in flashback research, the model is described here in detail as in figure 2-3.
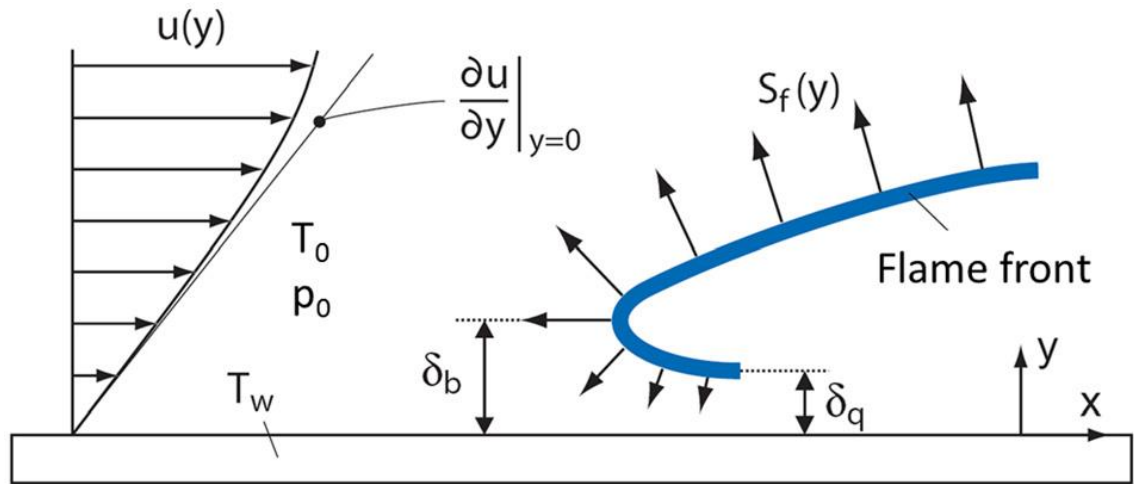
Figure 2-3 Critical gradient model (flow from right to left) Baumgartner et al. (2016).

On the left side of Figure 2-3, the undisturbed laminar velocity profile u(y) of the incoming mixture flow above a flat plate is sketched along with the velocity gradient g at the wall. T_0 and P_0 denote the temperature and the pressure of the approaching flow, and T_W is the temperature of the wall. On the right side, the shape of the flame during BLF is shown. The arrows represent the flame speed S_f (y), which is always perpendicular to the flame surface. Similarly to the flow velocity, the flame speed also decreases toward the wall because of heat losses to the cold wall and primary recombination processes. Eventually, inside of the quenching distance δ_q, the chemical reactions are entirely quenched, and the flame speed vanishes Wohl (1953). The streamwise velocity gradient at the wall is given by,

$$g = \left.\frac{\partial u}{\partial y}\right|_{y=0} = \frac{|\tau_w|}{\mu_0}$$ ………………………………………………………..…………… (2.2)

In Eq.2.2, τ_w is the wall shear stress of the two-dimensional boundary layer, and μ_0 is the dynamic viscosity of the unburnt mixture at P_0 and T_0. According to this model, BLF is initiated when the flame speed S_f at a particular balancing distance δ_b from the wall exceeds the corresponding axial velocity u(y) at this position.

$$S_f(\delta_b) = g_c \delta_b$$ …………………………………………………………………….. (2.3)
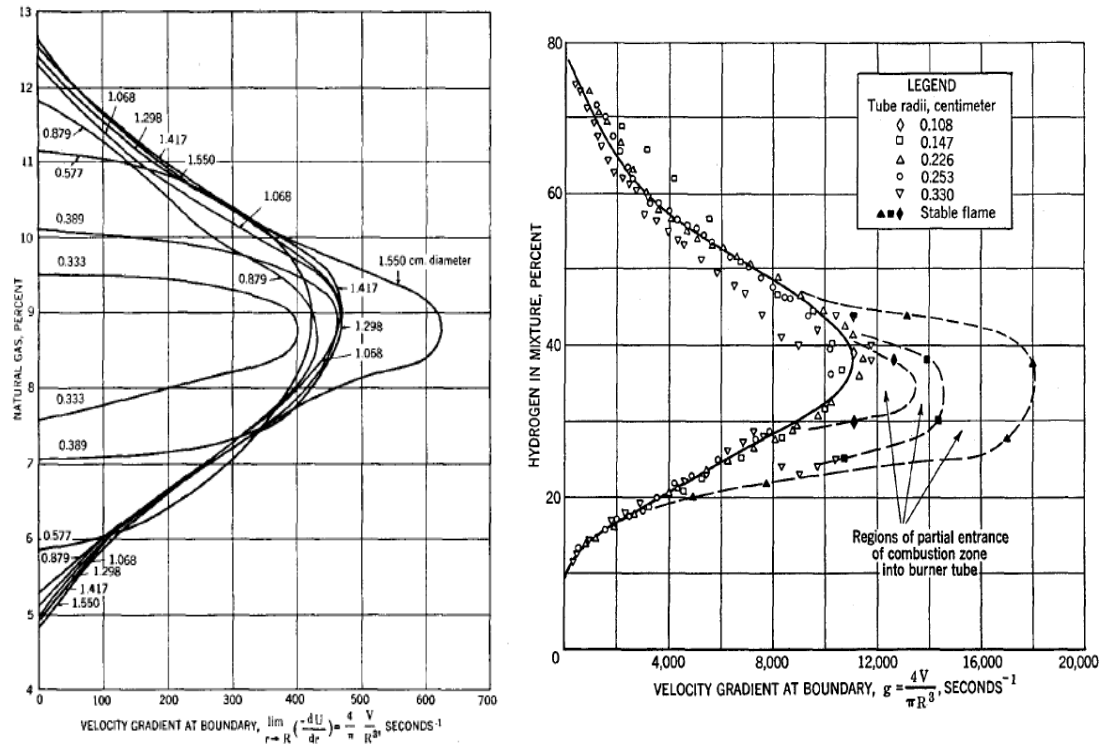
Figure 2-4 Critical velocity gradients for laminar flames: natural gas-air mixture at room temperature and pressure Lewis and von Elbe (1943)(left), H_2-air flames in cylindrical, water-cooled, unconfined tube at room temperature and pressure von Elbe and Mentser (1945)(right).

Where g_c is the critical velocity gradient at the flashback limits. Eq. 2.3, assumes a linear shape of the velocity profile between wall and δ_b. The distance δ_b is also called penetration distance Wohl (1953). For the evaluation of g_c in Eq.2.3, Lewis and Van Elbe assumed an isothermal flow profile, so the model does not take into account the hydrodynamic interaction between flame and flow. Furthermore, it must be pointed out that Eq.2.3 is not capable of predicting g_c because $S_f(y)$ is influenced to an unknown extent by heat exchange with the wall and by flame stretch effects. Thus, the critical gradients must be determined experimentally for different fuels, mixture compositions, temperatures, pressures, etc. Baumgartner et al. (2016).

The critical velocity model represents the cornerstone for later flashback studies, and some correlations were suggested based on analysing different parameters. von Elbe and Mentser (1945) investigated the H_2- air mixtures using a water cooled burner. They showed that the critical velocity gradients strongly increased when hydrogen is used instead of natural gas.

Figure 2-4 shows the critical velocity gradients for laminar natural gas-air mixtures in the cylindrical tube at room temperature and H_2-air flames in cylindrical, water-cooled, unconfined tube at room temperature and pressure. For H_2 –air mixture the solid line represents the limit for flashback along the full length of the tube, while the dashed lines border the limits of the region where flashback occurred provoked by tilted flames. The figure also shows that using hydrogen instead natural gas increases the critical velocity gradient sharply. Also, they revealed that the tilte flames could be stable for configurations with the cool wall, small tube diameters, and mixtures with low burning velocity. The H_2 –air mixtures in Figure 2-4 show that a tilted flame was followed by flashback except for very lean or very rich mixtures. The pressure loss along the tube due to wall friction and the pressure difference across a one-dimensional flame were suggested as a reason for such behaviour.

In later studies Wohl (1953) it was concluded that the pressure dependence of g_c for the laminar flow was directly proportional to atmospheric or higher pressure, from which he derived expressions for quenching distances. Further experiments were conducted in which tube walls were heated to the same temperature of the fresh preheated propane-air mixtures. He imputed the raising of critical velocity gradient with increasing temperature for two reasons; increase in laminar burning velocity and decrease of the heat loss to the wall. The heat loss decrease occurs as a result of a smaller change in flame temperature for a given increase in the preheat temperature, this increase causes a decrease in heat transfer between the unburnt mixture and the wall. Also, he compared experimental penetration distance δ_b for a laminar flashback with half the value for experimental quenching distances in tubes. The resulting ratio was

$$\frac{2\delta_b}{d_q} < 0.5 \quad \dots\dots\dots\dots\dots\dots\dots\dots\dots\dots\dots\dots\dots\dots\dots\dots\dots\dots\dots\dots\dots\dots\dots\dots\dots\dots\dots\dots\dots\dots\dots\dots\dots\dots\dots\dots\dots \text{(2.4)}$$

Dugger (1955) deemed back pressure of the flame is possible, thus affecting parameters related to the penetration distance δ_b. The back pressure is likely to decrease the local velocity gradient in front of the flame during flashback such that the real value for δ_b is increased.

Berlad and Potter (1957) showed similar ratios range between 0.4 to 0.8 for a broad range of fuels. They revealed that these ratios are depending on the actual value of g_c.

Fine (1959) conducted an experimental study to evaluate the temperature dependence of the critical velocity gradient for H_2-air mixtures at sub-atmospheric pressure to:

$$g_{c,H_2-air} \sim T^{1.5} \qquad \dots\dots\dots\dots\dots\dots\dots\dots\dots\dots\dots\dots\dots\dots\dots\dots\dots\dots\dots\dots \text{(2.5)}$$

Equation 2.5 shows the critical velocity gradient is independent of pressure within the measured pressure. Also, the study shows the relation is the same for laminar and turbulent flows.

Khitrin et al. (1965) presented an experimental study on the dependence of laminar wall flashback on preheated temperature at atmospheric pressure. He explained that the data with reference to g_c on the value of S_L for methane-oxygen mixtures. They showed that the critical velocity gradient is proportional to the square of the flame speed for varies compositions at a constant temperature and linearly proportional to flame speed for varying temperature at constant composition. The authors mentioned that behaviour was produced by the thermal diffusivity of the methane-oxygen mixture which stays essentially constant at constant preheat temperature, but increase simultaneously with S_L if the preheat temperature raises.

Fine (1958) used a water-cooled burner tube to conduct experiments for the critical velocity gradient for various fuels. He tested a range of pressures from subatmospheric to atmospheric pressures at room temperature. Tube diameters and flow velocities were chosen to achieve laminar as well as turbulent flow conditions. For laminar H_2-air mixtures between $\Phi=0.95$ to 2.25, the measurements revealed a pressure dependence of the critical velocity gradient of about

$$g_{c,H_2-air} \sim p^{1.35} \qquad \dots\dots\dots\dots\dots\dots\dots\dots\dots\dots\dots\dots\dots\dots\dots\dots\dots\dots\dots\dots \text{(2.6)}$$

However, the author stated that this equation was inaccurate for equivalence ratio Φ much less than unity without revealing any values. Equation 2.6 showed to be applicable in both laminar and turbulent flow conditions. Fully developed flows were assumed for the studied cases above. Such an assumption is not accurate as most of the

time the geometries (large length/diameter ratio L/D) are not large enough to develop the flow to reach fully developed conditions.

France (1977) studied developed flow conditions on the velocity at the wall during a flashback. He used a water-cooled tube and monopod burners with ratios L/D=0.1 to 100 and various fuel-air mixtures. He reported that the flow velocities at wall flashback decreased if the flow was not fully developed. The reason behind that is due to the wall friction at the inlet section usually is at its maximum and subsequently decreases in the downstream direction.

Fuel flexibility and variability are other parameters which have been studied due to the increasing interest in using different alternative fuels for environmental and economic reasons Lieuwen et al. (2008b).

Fox and Bhargava (1984) used a water cooled tube burners with a diameter of 7mm to measure adiabatic flame speed and critical velocity gradients for gas-air mixtures from biomass gasification products. The results showed that the values of g_c are in the same range as those for natural gas.

Davu et al. (2005) experimentally measured g_c for various hydrocarbons and hydrogen fuel blends (syngas) using tube burners with three different diameters (6, 7 and 10.6mm) without cooling. They concluded that g_c could be determined using S_L as well as the Lewis number (Le) of the different mixtures.

Dam et al. (2011) used the same Davu tube burners to present experimental measurements of the critical velocity gradient and flashback behaviour of H_2–CO and H_2–CH_4, external excitation, and swirl on the flashback behaviour for flames of these fuel mixtures were studied. They concluded nonlinearity of the boundary layer flashback propensity of H_2–CO and H_2–CH_4 flames change with the increase in H_2 contents in the mixture. Also for H_2–CH4 flames, g_c values increase with an increase in H_2 concentration of fuel-lean mixtures. An increase of H_2 in the mixture for fuel mixtures above 9% concentration did not significantly affect the critical boundary velocity gradient.

Shaffer et al. (2013) conducted an experimental study to analyse the coupling of flashback with burner tip temperature, leading to models for flashback propensity. They used a jet burner configuration with interchangeable burner materials (quartz and stainless steel) along with automated flashback detection, rim temperature monitoring and inline heater providing preheated air up to 810 K. They stated that results showed flashback propensity of a quartz tube been about double of that of a stainless tube, and they suggested a polynomial model based on analysis of variances. The model shows that if the tip temperature is introduced as a parameter, better correlations are obtained.

Duan et al. (2015) extended Shaffer et al. (2013) work with further analysis on data they had and classified them into five groups: operational parameters, unburnt conditions, ambient conditions, rig properties and others. They developed a physical model suggesting the significance of preferential diffusion (Le), heat loss (T_u/T_o), thermal coupling effect (T_{ip}, T_u) and flame Péclet number (R_{ef}).

One main issue with the work mentioned above is that, despite the fact that gas turbines combustors rarely use laminar flows, most of these studies still use laminar flows to develop an understanding of flashback mechanisms. In addition, the effect of the burner surface roughness is generally ignored, in particular in laminar flows. Work focusing on turbulent flow is reviewed in the next paragraph.

2.6.2 Critical Velocity Gradient Model in Turbulent Flames

Although the critical gradient concept was originally developed for laminar flames, it is also generally applied to turbulent flames. Using the model in turbulent flame studies is common. Bollinger (1952) investigated a mixture of H_2-oxygen in tube burners of different materials and cooling configurations at atmospheric pressure and temperature. He used the laminar velocity gradient model of laminar flashback in turbulent cases. However, the wall shear stress should be calculated from a suitable expression for turbulent flows. For tube flows, the wall shear stress is calculated from the following equation Schlichting (2000):

$$\tau_w = 0.03955\rho\bar{u}^{7/4}\nu^{1/4}d^{-1/4} \quad \dots\dots\dots\dots\dots\dots\dots\dots\dots\dots\dots\dots\dots\dots\dots\dots\dots\text{. (2.7)}$$

Where ρ, is the density and ν are the kinematic viscosity of the flow. The resulting shear stress from equation 2.7 is used in equation 2.1 to calculate the turbulent velocity gradient. The equation 2.7 shows that the tube diameter d has a limited effect on the shear stress value, while $\bar{u}$ has a higher influence on the velocity gradient at wall (g) value. In laminar flow the gradient at the wall was calculated from the Poiseuille paraboloid and varied in order of g~$\bar{u}$, while in turbulent flow the velocity gradient at wall calculated from equation 2.7 was higher. Bollinger showed that the critical velocity gradients for turbulent flames are larger than for laminar flames. Also he, showed in another set of experiments at elevated pressure (14.6 bar) that higher pressure strongly increased the flashback propensity, and he reported that the tip temperature of the burner has a large effect on flashback tendency.

Wohl (1953) referred to two publications which report flashback measurements in tube burners which used H_2- iso –octane –air and propane- air mixtures as fuels. They used different tube diameters in the range of 0.46cm to 2cm. Reynolds numbers based on diameter in the range of 2790 to 5550. Both studies showed that the wall flashback occurred at significantly higher flow velocities than for laminar conditions. Ratios of turbulent critical velocity to laminar critical velocity $\frac{g_{c,t}}{g_{c,l}} \approx 3\ at\ \emptyset \approx 1.1$ for atmospheric propane-air mixture were reported. Whol explained that the higher velocity gradient was a result of wall turbulent flashback taking place outside the laminar region of the velocity profile, were turbulence increases the flame speed. However, most searchers do not adopt this explanation and adopt the interpretation that flashback occurs in the laminar sublayer.

Bollinger and Edse (1956) investigated the effects of several experimental parameters on turbulent wall flashback in partially cooled tube burners using H_2-O_2 mixtures. Different tube diameters between 0.2cm to 1.4cm were used. The authors calculated the penetration depth δ_b using equation 2.2 and showed that compared to the laminar sublayer thickness the δ_b is much smaller. Also, they reported the range of critical velocity being between 20000 1/s to 70000 1/s.

Fine (1958) investigated pressure effects on laminar and turbulent flashback limits. With Reynold numbers around 5500 in a tube burner using H_2-air mixtures the author

suggested turbulent flames are stabilised in the laminar sublayer during wall flashback. Also, he showed that ratios of turbulent critical velocity to laminar critical velocity $\frac{g_{c,t}}{g_{c,l}} \approx 3 \: at \: \emptyset \approx 1.5$ hold H_2-air mixtures at atmospheric condition. The temperature effects were studied by the same author later Fine (1959) based on the critical velocity gradient for H_2-air mixtures, suggesting the equation 2.3 and referring to it is usage for laminar and turbulent flames.

Khitrin et al. (1965) investigated turbulent wall flashback in temperature controlled rim burners using H_2-air mixtures with different tube diameters from 1.8cm to 3.8cm. They observed wall flashback at high Reynold numbers Re_d=20000. No critical velocity gradients were reported in their work.

Schafer et al. (2003) carried a fundamental study on the upstream flame propagation of a turbulent kerosene flame at atmospheric pressure. The study involved various mixtures, fluid dynamics parameters, temperatures and equivalence ratios. Laser Doppler velocimetry (LDV) system was used to collect data at the outlet of the premixed duct to discuss the flashback phenomena in term of the critical velocity. Flashback was observed in the premixed duct of a combustion chamber which comprised a centre body for flame stabilisation. The premixing duct consists of two parts, a 0.4 m quartz glass tube and a metal plenum flange. Velocity distributions at the inlet to the combustor are measured in the yz-plane at x= 0.003m through a small opening of 0.01 m between the plenum and the glass cylinder. LDA instead of LDV (Laser Doppler Anemometry) was used since the latter is a point measuring technique. The author reported critical Reynolds number between 3000-6500 for his rig geometry to induce flashback, and conclude that for the wall boundary layer flashback the gradient theory is appropriate to predict upstream flame propagation. Their data for critical velocity gradient shows again that the penetration distance is smaller than the respective thickness of the laminar sublayer.

Eichler and Sattelmayer (2011b) investigated the boundary layer flashback in a quasi-2D system using different methane-hydrogen-air mixtures and an intensified charge-coupled device (ICCD). In this study, the authors used an 187mm width duct. A ramp used in the rig forms the lower duct (diffuser) wall; the duct length is 570mm, and the

upper part was made of quartz to gain an optical access to the test section. The authors reported that his result deviated substantially from published data for tube burner flashback and imputed those results to the combination of safety-critical flame positions and the influence of an adverse pressure. Finally, the authors conclude that the concept of a critical velocity gradient as a measure of flashback propensity in turbulent boundary layers has to be modified to take into account the outer region of the boundary layer.

Eichler et al. (2012) investigated the turbulent boundary layer flashback limits for fully premixed hydrogen-air flames at atmospheric mixture temperature and pressure. Two different rigs were used in this study; i.e. a tube burner and a quasi-2D turbulent channel flow. Furthermore, two confined flame holding configurations were utilised; i.e. a small backward-facing step inside the duct and a ceramic tile at high temperature, which was mounted flush with the duct wall. The authors reported that the distribution of the flame backpressure and the flame position itself are key parameters for the determination of meaningful turbulent boundary layer flashback limits, which emphasise the author conclusions in a previous study.

Shaffer et al. (2013) conducted an experimental study to investigate the fuel composition effects on flashback using a confined jet flame. The authors reported the use of various fuel compositions of hydrogen, carbon monoxide, and natural gas after being premixed with air at equivalence ratios corresponding to constant adiabatic flame temperatures (AFT) of 1700 K and 1900 K. The authors stated that the result could be used to drive a correlation between the fuel composition and reaction AFT parameters, and (1) the flashback velocity gradient and (2) injector tip temperature. However, the correlation needs more physics to bond the fuel composition impacts on flashback propensity at the engineering level. On the other hand, one of important conclusion from Schlieren intensified OH* images is that flashback begins near or in the boundary layer regardless of whether the confinement is in place or not, suggesting that the flashback mechanism is linked to the boundary layer mechanism which illustrates that flashback is dynamic in nature with random behavior.

Sayad et al. (2015) visually investigated different flashback mechanisms for H_2/ CH_4 mixtures in a variable-swirl burner using high-speed OH* chemiluminescence imaging. The authors reported testing different H_2 mole fractions (0.1-0.9) in the tested premixed fuel mixtures and using swirl numbers from 0.0 to 0.66. For the boundary layer flashback, the results showed that at the stable condition the flame was located at the shear layer, getting shorter with increasing the equivalence ratio. However, at the same attachment points, the flame started propagating gradually against the upcoming flow at an equivalence ratio equal to the flashback equivalence ratio, which indicates that the flashback started in the low-velocity region of the BL.

Baumgartner et al. (2016) described the transition from the stable flame to a flashback in a generic H_2–air combustion system and developed a physics-based model for the description of the transition. The authors used high-speed particle image velocimetry (PIV) and high-speed planar laser-induced fluorescence (PLIF) to get accurate results. They noticed that the velocity profile of the burner flow is distinctly distorted by the presence of the flame inside the premixing duct when approaching the flashback conditions and the flow directly upstream of the flame is retarded and deflected around the leading flame tip. The experimental results propose a new flashback model. According to the new flashback model, the heat transfer to the burner rim and the flame speed are the main drivers for the onset of flashback. One of the important conclusions of this study is that flashback processes started approximately 3mm downstream of the burner exit, and the leading flame tip propagated upstream along the boundary layer with some vertical offset from the burner wall. Thus, they concluded that for the unconfined flame the existing critical gradient model does not correctly account for the shape and the position of the stable system. They added the flame speed and the heat transfer between the flame base, leakage flow, and burner rim to the new model. Therefore the new model is closely linked to burner rim temperature.

Ebi and Clemens (2016) investigated boundary layer flashback of swirling turbulent lean-premixed methane-hydrogen-air flames in a model combustor featuring a mixing tube with a centre body. The authors presented results using high-speed chemiluminescense imaging, stereoscopic and tomographic particle image velocimetry, and a three- dimensional flame front reconstruction technique to reveal the time-

resolved, volumetric velocity field in the vicinity of the flame front during a flashback. They detected two different ways of flame front propagation upstream along the centre body wall. The first mechanism which is not dominant concerns small scale bulges counter-propagating into the upcoming flow in a similar way to channel-flow flashback. The second mechanism is produced by large scale flame tongues swirling in the bulk flow as they propagate in the negative axial direction along the centre body wall, which modifies the approaching flow. In large scale flame tongues, a deflection of streamlines ahead and around the flame tip causes a predominantly swirling motion including a region of negative axial velocity for the leading side of the flame tongue to propagate into the system, and such a negative axial velocity does not relate to boundary layer separation or the recirculation bubble. The presumed elevated pressure region causing the streamline deflection that extends well into the burnt gas was suggested as the cause of the effect.

Sattelmayer et al. (2016) conducted an experimental study on the interaction of flashback originating from flame propagation in CIVB, BL and low bulk flow velocity on a rig operated with hydrogen-air mixtures at ambient pressure and preheated air. The authors reported the use of an experimental rig which has been aerodynamically optimised through many previous studies to have good flashback limits; the rig has a conical swirl followed by a mixing section and a diffuser as an option. The swirl is made from a thick-wall hollow cone; four circumference slots were made symmetrically to inject fuel tangentially, a central hole was used to inject air axially producing unswirled jets in the centre of the flow to improve the system against CIVB. The authors concluded that trying to optimise the system against one flashback mechanism leads to another type of flashback, as a consequence, flashback limits are worsened. Also, the radial momentum of the fuel jets in the swirl prevent further improvements that suggested tailoring of the radial fuel distribution in the swirl.

In most recent study, Hoferichter et al. (2017) presented analyses to predict the boundary layer flashback limits in confined flames using boundary layer separation theory. The suggested model is based on Stanford's criterion for boundary layer separation which showed to be successful to predict BLF limits at ambient and preheat condition. Moreover, it was noticed that the high turbulent velocity fluctuation near the

burner wall increases the tendency for flashback. Thus, in order to avoid flashback it is required that the local premixed flow speed is higher than the flame speed. This concept is true for all flashback mechanisms except for the CIVB, where the flame starts to generate a conical flame bubble in the center of the downstream flame zone.

In summary, studies focusing on boundary layer flashback in turbulent flames have been studied extensively. Parameters such as type of flow (diffusion or swirl), system pressure, fuel preheat, using of bluff body, central or radial air injection to alter the velocity gradient near the wall were used. However, as in the laminar flames studies the effects of the burner surface roughness has not been considered, which represent a gap that this work try to answer.

2.6.3 Numerical Studies in BLF

Probably the first numerical study on boundary layer flashback was the study of Lee and T'Ien (1982) in which they presented a numerical study to simulate wall boundary layer flashback. They studied premixed methane-air flames at $\Phi=1$ confined in a circular duct. Their study was a two-dimensional study using cylindrical coordinates with the assumption of constant heat capacity mixture, ideal gas behaviour and Lewis numbers equal to a unity. The transport coefficients of the mixture were functions of temperature. The chemical reaction was assumed to be a single-step global reaction with an Arrhenius-type rule for the production rate. Two velocity profiles at the inlet were prescribed parabolic (wall velocity gradients), and tube radius, respectively, and the wall temperature was constant at the inlet temperature of the mixture. A false transit method solver was used which required steady final condition assumptions. Thus, the simulation converged to the flow condition at which the flame was barely stable just before flashback. The simulation showed the deviation of critical velocity gradients from small diameters to flashback limits of larger tubes for which critical gradient becomes independent of diameter. The flame had a curvature in its structure of the order of the flame thickness, which points to the general importance of non-equidiffuision effects on such flames. Close to the wall at the flame bottom, unburnt mixtures diffused into the reaction zone. Also, the study showed that the expansion of gases behind the flame caused a high-pressure field in front of the flame such that streamline were

divergent. Using two different inlet velocity profiles showed a clear difference in stabilised flame shapes which concluded that not only the velocity gradient at the wall but also the curvature of the velocity profile is an important factor for wall flashback.

Mallens and De Goey (1998)Mallens and De Goey (1998) conducted an experimental and numerical study to determine the critical velocity gradient for laminar CH_4-air mixtures. In the experimental part of this study, a cooled rectangular burner and uncooled tube burners were used. The assumption of fully developed flows was checked at the exit of the burners using an LDA. The numerical solution was used to simulate a two-dimensional domain with a parabolic velocity gradient at the inlet and isothermal walls at the temperature of the mixture. The studied domain contains the exit, the rim and extends to some distance of the combustion zone. The chemical reaction was assumed to be a single-step global reaction with an Arrhenius-type rule for the production rate. They tried to implement a different approach than Lee and T'Ien (1982) in their model, where the critical velocity gradient of the mixture at the wall was taken at the point when steady-state solvers did not converge anymore. The authors reported a 10% deviation between experimental and numerical results. Based on the results, they concluded that the quenching phenomenon is governed by heat loss to the wall and not by radical recombination or surface chemistry.

Kurdyumov et al. (2007) investigated experimentally and numerically the flashback in an uncooled burner that using propane and methane as a fuel. The numerical procedure first investigated a small diameter tube to avoid the uncertainty in specifying the boundary condition at the boundary between the computational domain and the free stream, then when the boundary condition was precisely specified the tube diameter was increased until a diameter was reached beyond which the flame flashback remain unchanged. The authors used an assumption to simplify the treatment where they neglected the radiation heat transfer, bulk velocity, influence of body force, viscous dissipation and compressible work. They also assumed that the specific heat of the mixture was constant with temperature change, thus the ideal gas law can be applied. The focus of the study was on the effects of tube radius and incoming velocity profile on the flashback limit and the flame structure. They concluded that not only the wall

velocity gradient can describe the limiting conditions but also the velocity profile near the wall is important which is one of the motivations of the present work.

Gruber et al. (2010) conducted a numerical study of a turbulent flame–wall interaction (FWI) using a three-dimensional direct numerical simulation (DNS) and detailed chemical kinetics. The study focused on investigating the effects of the wall turbulent boundary layer on the structure of a hydrogen–air premixed flame, near-wall propagation characteristics and spatial and temporal patterns of the convective wall heat flux. The authors suggested that the near-wall coherent turbulent structures play a major role in the convective wall heat transfer by pushing the hot reactive zone towards the cold solid surface.

Eichler and Sattelmayer (2011b) investigated experimentally and numerically the turbulent boundary layer flashback in a quasi-2D system using different methane-hydrogen-air mixtures. In the numerical part, they modelled the diffuser flow and used isothermal flows to calculate the shear wall stress. The shear wall results were compared to experimental results for the same study. In general, the authors reported that the numerical results came in line with the experimental results.

Gruber et al. (2012) investigated numerically the transient upstream propagation (flashback) of premixed hydrogen–air flames in the boundary layer of a fully developed turbulent channel flow. In this DNS study, the configuration consists of non-anchored premixed H_2–air flames propagating upstream in the boundary layers of turbulent Poiseuille flows at two different pressures. The authors choose a high rich H_2- air mixture at $\Phi=1.5$ and low pressure (1 and 2 atm.) to understand high flame speed combined with short channel transit time. Their results showed a presence of near wall regions of reverse flow immediately ahead of the upstream-propagating flame that is convex towards the reactants. Also, they suggested that the Lewis-Von Elbe boundary layer flashback model is largely inadequate, and the presence of near-wall regions of reverse flow ahead of the flame sheet has effects on flashback speed. The actively contributes to flame acceleration (together with wrinkling due to (Darrieus–Landau) DL instability and turbulence), with an important role in maintaining high flame propagation velocities. Finally, they suggested for a correct representation of the tiny

near-wall reverse flow patterns, a considerable modelling issue for hybrid LES–RANS (Reynolds-averaged-Navier–Stokes) models that employ simplified descriptions of the boundary layer.

Lietz et al. (2014) conducted a large eddy simulation LES study to model the flashback of the turbulent flame through the low-velocity boundary layers in the premixing region. The authors used a suite of LES calculations with different model formulations and filter widths to consider a turbulent channel flow, for which high-fidelity direct numerical simulation (DNS) data already existed. They used two different mesh sizes (Δ/Δ_x =8, 16) to explore its effects on flame propagation. Also, they tried three models of front flame shape (Direct flamelet model, Algebraic flame surface density model and Filtered tabulated chemistry for LES). The results showed that LES computations are very accurate in predicting the structure of the turbulent flame front but they have a large discrepancy in the propagation velocity of the flame front. The flamelet model gave the best representation to flame compared to the other models.

In most recent numerical work, Gruber et al. (2015) conducted direct numerical simulations of freely- propagating premixed flames in the turbulent boundary layer of fully-developed turbulent channel flows using a new model to describe the mean shape of the turbulent flame during a flashback. The authors stated that the numerical study considered the fuel mixture condition through the Damkohler number where they used Da~0.7 for the lean fuel mixture and Da~1.2 for a rich mixture. The flame model for numerical simulation was based on a balance of mean flow and the propagation of the interface towards the flow, where the steady state mean flame propagation was taken from CHEMKIN PREMIX and applied to the flame flow taking into account the main features of flashback. They showed that the suggested model can capture the mean shape of the turbulent flame brush for both lean and rich mixtures, but they emphasised that the model needs further work to be validated in high Reynold numbers to represent near wall velocity profile.

From the experimental and numerical work on boundary layer flashback in laminar and turbulent flame, the main conclusion so far is that the flame penetrates the upcoming fuel near the wall depending on the low velocity gradient near the wall. The best way to

reduce the risk of occurring BLF is reduce the boundary layer thickness and bring the low velocity gradient as close as possible near the wall to increase the heat transfer and ensure extinguishing the flame before the BLF occurring. And while this could be achieved through the use of bespoke surface structures, it appears that this has generally been ignored in previous studies.

In this thesis, a promising technique to control the boundary layer thickness and drag reduction is investigated, which is using regular roughness to alter and enhance the flow near surfaces, especially with developing in manufacturing techniques that make manufacturing a micro shapes on surfaces is possible. The next chapter will describe the main concepts of boundary layer and fluid drag reduction and will describe the sharkskin techniques and will review the studies in this topic.

CHAPTER 3

LITERATURE REVIEW 2

BOUNDARY LAYER

In this chapter the main concepts of laminar and turbulent boundary layer will be described, also fluid drag reduction is presented. A method of controlling the boundary layer and drag reduction will be introduced. Finally, previous works on controlling boundary layer and drag reduction using regular roughness will be reviewed. When a fluid moves alongside a body with different velocity, a thin layer is generated with a gradient velocity towards the fluid flow stream. This layer is known as the boundary layer. In this chapter, fundamentals and principles of the boundary layer and some controlling techniques are presented.

3.1 Introduction

Historically, the boundary layer was first defined by Ludwig Prandtl in a paper presented on August 12, 1904, at the third International Congress of Mathematicians in Heidelberg, Germany Schlichting (2000). Simply, he divided the flow into two regions to simplify the fluid flow equation solution. The first region is inside the boundary layer, dominated by viscosity and creating the majority of drag experienced by the boundary body. The second region is located outside the boundary layer where viscosity effects can be neglected without significant diverting on the solution. Viscosity in real fluids plays a significant role in flow characteristics. As the fluid moves past the object, the molecules right next to the surface stick to the surface. The molecules just above the surface are slowed down in their collisions with the molecules sticking to the surface. These molecules in return slow down the flow just above them. The farther ones move away from the surface with fewer collisions being affected by the surface. This creates a thin layer of fluid near the surface in which the velocity changes from surface velocity to the free stream value away from the surface as shown in figure 3-1
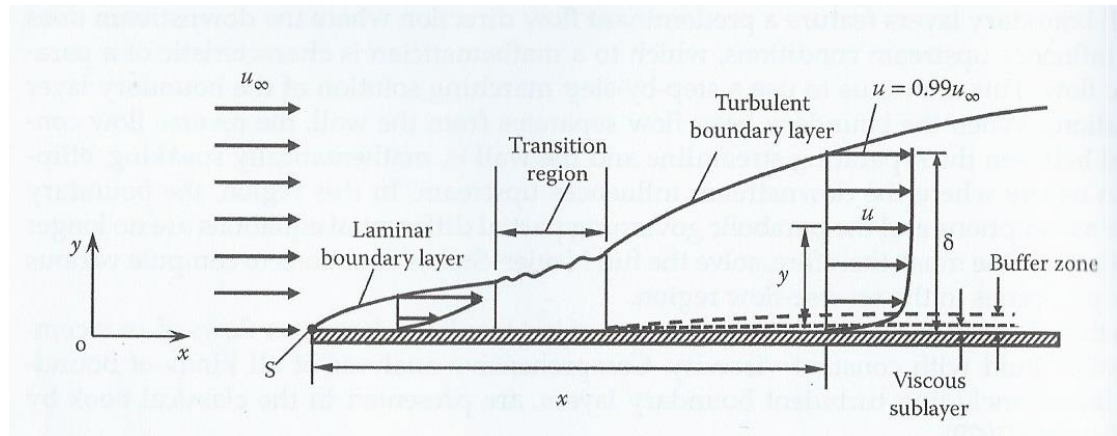
Figure 3-1 Boundary layer over a flat plate Sultanian (2015).

3.1.1 Boundary Layer on External Flows:

Figure 3-1 shows a fluid flow with mainstream velocity u_∞ blowing over a flat plate. As the flow touches the plate at its leading edge, a stagnation point, S, is formed. Due to no slip conditions, the fluid has zero velocity at the plate boundary. The velocity changes from zero to the free stream velocity, u_∞, over a very small thickness in the stagnation region, which makes the plate suffer from the highest shear stress in the region. As shown in the figure the laminar boundary layer starts from the stagnation point and grows in the direction of the flow. In the laminar region, the viscosity is considered the major effective parameter. Its effectiveness appears on the distribution of the shear stress (maximum at the wall and zero at the upper limits of the boundary layer). However, the laminar boundary layer is generated beyond the stagnation point (leading point S) regardless if the free stream condition is laminar or turbulent Sultanian (2015).

As the laminar boundary layer increases in thickness, it becomes unstable due to the momentum transfer from free stream to the boundary layer and transitions to a turbulent boundary layer after a certain length. The turbulent boundary layer consists of three regions. The inner region closest to the plate surface is known as a viscous layer or what is known as a laminar sublayer. Next, to the viscous layer comes the buffer zone which has a mix of laminar and turbulent behaviour. The region above the buffer zone to the end of the boundary layer (typically when the flow velocity is 0.99 u_∞) features a fully turbulent behaviour. In this region, the velocity distribution along the flat plate is

almost uniform, and its gradient is highly confined to the buffer zone. Also, vorticity and the shear stress are much greater than in the laminar boundary layer.

3.1.2 Laminar Boundary Layer in Internal Flow

The flow is considered internal flow whether it is a pipe flow or flow between two parallel plates. In both cases, the boundary layer starts to grow at the entrance. For the pipe flow, this layer starts to grow all around the pipe surface in contact with the fluid. Outside the boundary layer, the fluid is still unaffected by viscosity and may be treated as potential flow with a uniform velocity which increases along the pipe axis. The boundary layer keeps growing further in the downstream direction, which is known as the entrance length, figure 3-2 until it reaches the pipe axis and stops growing any further. Beyond this point, the boundary layer fills the whole pipe diameter, and a developed pipe velocity profile is formed. The profile of the developed velocity is parabolic and unchanged for the rest of the pipe.

$$V_z(r) = 2V\left[1-\left(\frac{r}{R}\right)^2\right]$$
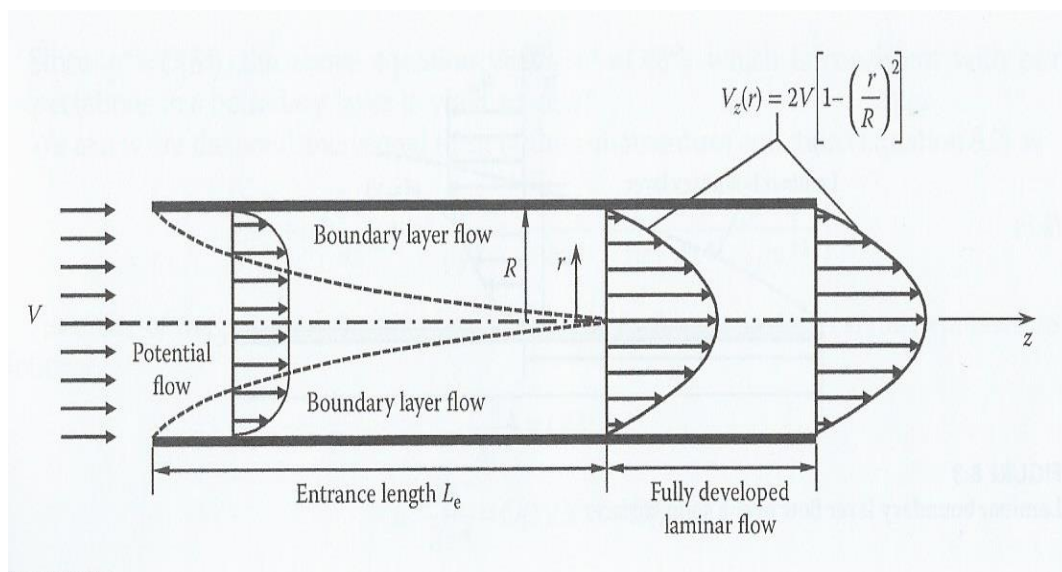
Figure 3-2 Boundary layer in the pipe (internal flow) Sultanian (2015).

Such flow is known as fully developed pipe flow. However, in internal flows the whole flow in the fully developed region is affected by viscosity unlike the external flow, where the growing boundary layer has two regions, one is affected by viscosity, and the outer region is where the viscosity effect can be neglected.

3.1.3 Laminar Boundary Layer Approximation

To deal with the boundary layer and to solve fluids flow in boundary layers, Navier-Stoke's and continuity equations are applied with some assumptions. The equations are derived by applying momentum conservation of Newton's second law to a compressible, isotropic, Newtonian fluid element. Also, Navier- Stoke's equations for the shear stress tensor, which result from Navier- Stoke's equations, are used for the solution by neglecting body forces. The resulting equation is

$$\frac{\partial}{\partial t}(\rho u_i) + \frac{\partial}{\partial x_j}(\rho u_i u_j) = -\nabla p + \frac{\partial}{\partial x_j}[\mu\left\{\frac{\partial u_i}{\partial x_j} + \frac{\partial u_j}{\partial x_i} - \frac{2}{3}\delta_{ij}\frac{\partial u_k}{\partial x_k}\right\}] \dots\dots\dots\dots (3.1)$$

Where u_i, u_j and u_k (i,j and k =1,2,3), are the velocity components in the corresponding direction (i.e. u_1=u, u_2= v, u_3= w) denoting the velocity components in x,y and z-direction respectively, ρ is the density of the fluid, p represents the pressure, μ is dynamic viscosity and δ_{ij} is the Kronecker Delta. To simplify the equation more, it should assume some helpful assumptions. An essential assumption is that the boundary layer thickness δ is thin compared to a characteristic length scale L of the geometry. This assumption is valid only when the Reynold number ($Re_L=\rho$ u_∞/L) is very large respect to the free stream velocity u_∞ and L. Then by using L, u_∞ and a reference pressure p_0 to nondimensionalized the equation 3.1 and neglecting other terms, the resulting equations are multiplied by $1/Re_L$ or $1/Re^2_L$, to derive the boundary layer equation. For two-dimensional flows with variable density and dynamic viscosity, the momentum boundary layer equation is:

$$\rho\frac{\partial u}{\partial t} + \rho u\frac{\partial u}{\partial x} + \rho v\frac{\partial u}{\partial y} = -\frac{dp}{dx} + \frac{\partial}{\partial y}(\mu\frac{\partial u}{\partial y}) \dots\dots\dots\dots\dots\dots\dots\dots (3.2)$$

Equation 3.2 is a second order partial differential equation and is used with the 2D continuity equation:

$$\frac{\partial u}{\partial x} + \frac{\partial v}{\partial y} = 0 \dots\dots\dots\dots\dots\dots\dots\dots\dots\dots\dots (3.3)$$

To compute the distribution of u and v in the boundary layer for the laminar condition, at large Re, the solution becomes unstable due to transition to the turbulent condition. But the turbulent boundary layer equations could be derived from Reynolds-Averaged

Navier- Stoke (RANS) equations using the same assumptions as used in equation 3.2, which then includes turbulent shear terms.

3.2 Derivation solution for the boundary-layer equations

The boundary layer equations are a set of partial differential equations that need to be solved to explain a number of fluid behaviours like a drag, wake, separation, .tec. The solution depends on the boundary layer type if it is laminar or turbulent.

3.2.1 Analytical solutions (Blasius' solution)

In general, the laminar boundary layer equations will form a system of partial differential equations which can, in principle, be solved numerically. It is also possible under particular conditions to work out the solution analytically in certain cases. In the case of an incompressible flow over a flat plate at zero incidences, the Blasius solution can be derived. The plate starts at and extends parallel to the x-axis and will have a semi-infinite length. The free stream velocity will be constant. It follows from equation (3.2) that a constant condition will result in a constant pressure at the edge of the boundary layer. This will result in the x-component of the momentum equation for the boundary layer equations. The solution of laminar boundary layers on the horizontal flat plate was obtained by Prandtl's student of H. Blasius in 1908. For two-dimensional, steady, incompressible flows with zero pressure gradients, the governing equations of motion are reduced to;

$$\frac{\partial u}{\partial x} + \frac{\partial v}{\partial y} = 0 \quad\text{..} (3.3)$$

$$u\frac{\partial u}{\partial x} + v\frac{\partial u}{\partial y} = v\frac{\partial}{\partial y}\left(\mu\frac{\partial u}{\partial y}\right)\text{..} (3.4)$$

With boundary conditions,

$at\ y = 0,$ $u = 0,$ $v = 0$

$at\ y = \infty,$ $u = u_\infty\ or\ U,$ $\frac{\partial u}{\partial y} = 0$ $\text{..................................} (3.5)$

Blasius proved that the velocity, *u/U*, should be similar for all values of x when plotted against a nondimensional distance from the wall; the boundary thickness, δ, was chosen to nondimensionalized the distance from the wall. Thus the solution is of the form

$$\frac{u}{U} = g(\eta) \qquad \text{where} \qquad \eta \propto \frac{y}{\delta} \quad \dots\dots\dots\dots\dots\dots\dots\dots\dots\dots\dots\dots\dots \text{(3.6)}$$

Blasius proved that $\delta \propto \sqrt{\frac{vx}{U}}$ and set,

$$\eta = \frac{y}{\delta(x)} = y\sqrt{\frac{U}{vx}} \quad \dots\dots\dots\dots\dots\dots\dots\dots\dots\dots\dots\dots\dots\dots\dots \text{(3.7)}$$

Introducing the stream function, ψ, where

$$u = \frac{\partial \psi}{\partial y} \qquad and \qquad \mathrm{v} = -\frac{\partial \psi}{\partial x} \quad \dots\dots\dots\dots\dots\dots\dots\dots\dots\dots\dots\dots \text{(3.8)}$$

Substituting for *u* and v into equations (3.3) and (3.4) reduces the equation to one in which ψ is the single dependent variable. Defining a dimensionless stream function as,

$$f(\eta) = \frac{\psi}{\sqrt{vxU}} \quad \dots\dots\dots\dots\dots\dots\dots\dots\dots\dots\dots\dots\dots\dots\dots \text{(3.9)}$$

So by substituting equations (3.9) and (3.8) in the equation (3.4) and differentiating the velocity components the final shape of equation (3.4) is:

$$2\frac{d^3 f}{d\eta^3} + f\frac{d^2 f}{d\eta^2} = 0 \quad \dots\dots\dots\dots\dots\dots\dots\dots\dots\dots\dots\dots\dots\dots \text{(3.10)}$$

With boundary condition,

$$at\ \eta = 0 \qquad\qquad\qquad f = \frac{df}{d\eta} = 0$$

$$at\ \eta \to \infty \qquad\qquad\qquad \frac{df}{d\eta} = 1 \quad \dots\dots\dots\dots\dots\dots\dots\dots\dots\dots \text{(3.11)}$$

Equation (3.10) is a third −order nonlinear ordinary differential equation, which is also known as Blasius equation. The boundary conditions in equation (3.11) are sufficient to determine the complete solution of equation (3.10). Figure 3-3 shows the solution of Blasius boundary equation.
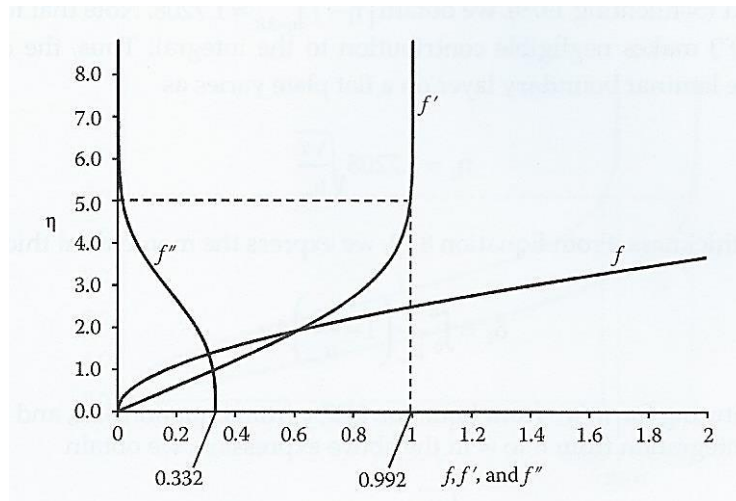
Figure 3-3 Solution of Blasuis boundary layer equation Sultanian (2015).

Figure 3-3 shows an important result which is that at $\eta = 5$, u = 0.992U. Now by defining the boundary layer thickness, $\delta(x)$, at each distance x along the y direction where u become 0.99 of the free-stream velocity U, equation (3.7) yields,

$$5 = \delta(x)\sqrt{\frac{U}{vx}}$$

$$\delta(x) = 5\sqrt{\frac{vx}{U}} = \frac{5x}{\sqrt{Re_x}} \dotfill (3.12)$$

This result is accepted as an exact solution of the Blasius boundary layer (3.10) for boundary layer thickness.

The wall shear stress can be expressed as

$$\tau_w = \mu \frac{\partial u}{\partial y}\bigg]_{y=0} = \mu U \sqrt{U/vx}\, \frac{d^2 f}{d\eta^2}\bigg]_{y=0}$$

Then

$$\tau_w = 0.332 U \sqrt{\rho\mu U/x} = \frac{0.332\rho U^2}{\sqrt{Re_x}} \dotfill (3.13)$$

And the wall shear stress coefficient, C_f, is given by

$$C_f = \frac{\tau_w}{\frac{1}{2}\rho U^2} = \frac{0.664}{\sqrt{Re_x}}$$ .... (3.14)

From equations (3.12, 3.13 and 3.14) it is clear that the boundary layer thickness, δ, wall shear stress, τ_w, and skin friction coefficient, C_f, are dependent on the length Reynold number, Re_x, to the one-half power. These results characterise the behaviour of the laminar boundary layers on a flat plate.

3.2.2 Approximation solution

Approximation solutions of the boundary layer equations can be obtained from the Momentum-Integral Equation in combination with making an educated guess for the velocity profile. The Momentum-Integral Equation initially contains too many unknowns to solve the equation. So a cubic or quadratic velocity profile is used to simplify the solution.

3.2.3 Numerical solutions

Numerical solutions of the boundary layer equations are based on replacing derivatives by finite-difference approximations. This approximation is called discretization. Generally speaking, the numerical solution methods are common where the domain containing the boundary layer is divided into small elements: the so-called grid. This grid consists of grid points which are formed by the coordinate lines. At the grid points, the unknown velocity components u(x,y) and v(x,y) are determined. We can use this method since we know the x- and y-components of the velocity at a starting line namely the leading edge (x=0) of the horizontal plate. The full details of the numerical method that is used in this work will be explained in the next chapter.

3.3 Transition in Boundary layer

The flow in most engineering applications is turbulent. This means that the flow has an irregular fluctuation (mixing or eddy motion) in its mainstream. In general, the value of Re, combined with initial boundary condition plays the main role in boundary layer transition from laminar to the turbulent condition. On a flat plate with sharp edge subjected to a uniform flow, the transition take places at the distance x from leading edge when Re_{xcr} is in range 2×10^5 to 3×10^6. In internal flows, the Re_{cr} between 2300 – 4000 depends on the initial boundary conditions.

The transition from laminar to a turbulent condition not necessary occurs in a specific single point. Typically, the transition begins at random locations on the plate in the vicinity of Re= R_{excr}. Then the disturbance grows rapidly downstream until the entire width of the plate is covered with a turbulent flow. And as the laminar boundary layer, the turbulent boundary layer could exist on both external and internal flows.

3.4 Turbulent Boundary Layer

The boundary layer on a plate is laminar close to the leading edge and turns turbulent downstream around transition point x_{cr} which can be calculated from critical the Reynold number Re_{xcr}, where Schlichting (2000)::

$$Re_{xcr} = \left(\frac{Ux}{v}\right)_{cr} = 5 * 10^5$$ ……………………………….……… (3.15)

In turbulent flow, the velocity components and other variables (e.g. pressure, density, if the fluid is compressible, temperature - if the temperature is not uniform) at a point fluctuate with time in an apparently random fashion. In general, turbulent flow is time-dependent, rotational, and three-dimensional, which makes the exact solution impossible. In this way only momentum and continuity equations describe fluid velocity (u,v,w) and pressure p distribution (Navier -Stokes equation):

$$v. \nabla v = -\frac{1}{\rho}\nabla p + v\Delta v$$ …………………………………………………… (3.16)

$$\nabla. v = \frac{\partial u}{\partial x} + \frac{\partial v}{\partial y} + \frac{\partial w}{\partial z} = 0$$ …………………………………………… (3.17)

To solve the equations above, the flow physics should be considered as the flow velocity components and pressure is fluctuating. In most engineering application the interest focused on the average, mean values of velocity, pressure, shear stress, etc., this approach leads to a new form of each parameter where each parameter is represented in terms of a mean and fluctuating parts. i.e. $= \bar{u} + \acute{u}$, $v = \bar{v} + \acute{v}$, etc., where the bar (”-”) denotes a time average, and prime (” ′ ”) indicates fluctuation about the time–averaged, mean quantity. Applying this to equation (3.16) will lead to complicated Navier-Stokes equations. For example the equation of the flow in x direction will be;

$$\bar{u}\frac{\partial \bar{u}}{\partial x} + \bar{v}\frac{\partial \bar{u}}{\partial y} + \bar{w}\frac{\partial \bar{u}}{\partial z} = -\frac{\partial \bar{p}}{\partial x} + \frac{\partial}{\partial x}\left(\mu\frac{\partial \bar{u}}{\partial x} - \rho\overline{\acute{u}^2}\right) + \frac{\partial}{\partial y}\left(\mu\frac{\partial \bar{u}}{\partial y} - \rho\overline{\acute{u}\acute{v}}\right) + \frac{\partial}{\partial z}\left(\mu\frac{\partial \bar{u}}{\partial z} - \rho\overline{\acute{u}\acute{w}}\right)$$

…...(3.18)

The three correlation terms $-\rho\overline{\acute{u}^2}$, $-\rho\overline{\acute{u}\acute{v}'}$, $-\rho\overline{\acute{u}\acute{w}}$ are called *turbulent stresses,* $\tau_{tur,}$ because they have the same dimensions and occur right alongside the newtonian (laminar) stress terms $\tau_{lam} = \frac{\partial u}{\partial x}$, actually, they are convective acceleration terms (which is why the density appears), not stresses, but they have the mathematical effect of stress and are termed almost universally in the literature. *The turbulent stresses are unknown a priori* and must be related by experiment to geometry and flow conditions. The problem of how to relate the $-\rho\overline{\acute{u}^2}$, $-\rho\overline{\acute{u}\acute{v}'}$, $-\rho\overline{\acute{u}\acute{w}}$ to the the mean velocities $\bar{u}, \bar{v}, \bar{w}$ has occupied a lot of people for a long time. In pipe and boundary-layer flows, the stress $\rho\overline{\acute{u}\acute{v}}$ associated with the direction y normal to the wall is dominant, and we can approximate it with excellent accuracy to a simpler streamwise momentum;

$$\bar{u}\frac{\partial \bar{u}}{\partial x} + \bar{v}\frac{\partial \bar{u}}{\partial y} + \bar{w}\frac{\partial \bar{u}}{\partial z} = -\frac{\partial \bar{p}}{\partial x} + \frac{\partial \tau}{\partial y} \dots\dots\dots\dots\dots\dots\dots\dots\dots\dots\dots\dots\dots\dots \text{(3.19)}$$

Where

$$\tau = \mu\frac{\partial \bar{u}}{\partial x} - \rho\overline{\acute{u}\acute{v}} = \tau_{lam} + \tau_{turb} \quad \dots\dots\dots\dots\dots\dots\dots\dots\dots\dots\dots\dots \text{(3.20)}$$

In the outer layer τ_{turb} is two or three orders of magnitude greater than τ_{lam} , and vice versa in the wall layer. These experimental facts enable us to use a crude but very effective model for the velocity distribution $\bar{u}(y)$ across a turbulent wall layer. To solve equations (3.19) and (3.20), the flow is divided into three regions:

1- Wall layer: the viscous shear is dominant.
2- Outer layer: the turbulent shear is dominant.
3- Overlap layer: both types of shear are important.

Also, some parameters are introduced to connect these layers mathematically. For the wall layer, Prandtl deduced in 1930 that $\bar{u}$ must be independent of the shear–layer thickness, so a new presenter is suggested which is known as friction velocity u*:

$$u^* = \left(\frac{\tau_w}{\rho}\right)^{1/2} \quad \dots\dots\dots\dots\dots\dots\dots\dots\dots\dots\dots\dots\dots\dots\dots \text{(3.21)}$$

Although, it is not actually a flow velocity but because it has an m/s unit it is termed as velocity. Friction velocity is used to create a non-dimensional term;

$$u^+ = \frac{\bar{u}}{u^*} = \emptyset\left(\frac{yu^*}{v}\right)$$ …………………………………………………..…………. (3.22)

Equation (3.22) is called the ***law of the wall***, and it is found to satisfactorily correlate with experimental data for a smooth surface for $0 \leq yu^*/n \leq 5$. Therefore, the thickness of the viscous sublayer is roughly 5. The viscous sublayer gets thinner as the mean velocity increases. Consequently, the velocity profile becomes nearly flat and the velocity distribution becomes more uniform at very high Reynolds number (very low viscosity).

Von Karman in 1933 deduced that *u* in the outer layer is independent of molecular viscosity, but its deviation from the stream velocity, *U,* must depend on the layer thickness, δ, and other properties which could be combined in the non-dimensional form;

$$\frac{U_{max} - \bar{u}}{u^*} = \emptyset\left(\frac{y}{\delta}\right)$$ …………………………………………………. (3.23)

 Where *u** is friction velocity, the deviation of velocity from the centerline value $U_{max} - \bar{u}$ is called the *velocity defect* or retardation of the flow due to wall effects. Equation (3.23) is called the *velocity defect law* for the outer layer.

Both the wall law equation (3.22) and the defect law equation (3.22) are found to be accurate for a wide variety of experimental turbulent duct and boundary-layer flows. In 1937 C. B. Millikan showed that if the overlapped layer velocity varies logarithmically with y, which means that the wall layer and outer layer are overlapped smoothly, the result is;

$$u^+ = \frac{1}{k}lny^+ + B$$ ……………………………………………………..……………. (3.24)

For the full range of turbulent smooth wall flows the dimensionless constants k and B are found to have the approximate values k = 0.41 and B = 5.0. Equation (3.24) is called *the logarithmic overlap layer*. Figure 3-4 shows the experimental verification of the inner-, outer-, and overlap- layer laws relating velocity profiles in turbulent wall flows.
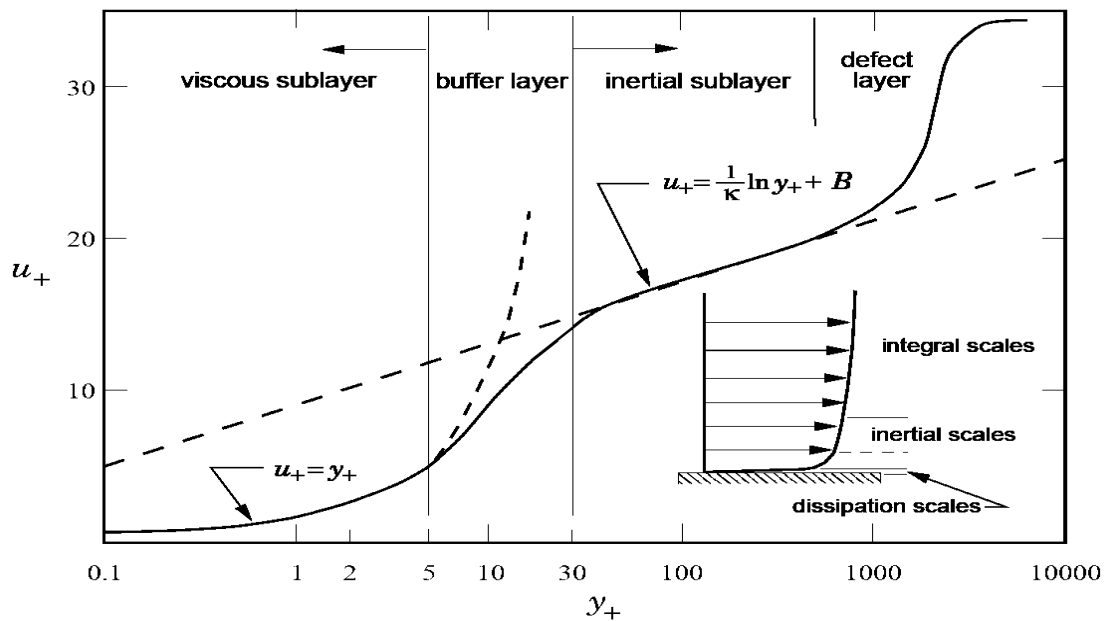
Figure 3-4 Experimental verification of the inner-, outer-, and overlap- layer laws relating velocity.

One of the main negative effects linked with the presence of a boundary layer is the resulting drag force, which often needs to be overcome in engineering applications and therefore can lead to the need for more power or energy consumption.

3.5 Fluid Drag reduction

A brief description with some details for the fluid drag mechanism, which include skin friction and pressure drag, will be introduced in the next few pages. Also, the description will define the drag reduction mechanisms and the mechanism which is used to reduce the drag in this work.

3.5.1 Drag Mechanism

In fluid flows, a drag comes in several forms; the most common are the pressure drag and friction drag. The pressure drag is the drag related to the amount of required energy to move the fluid from front to back of an object, such as air moving around a cylinder. This kind of drag may be reduced with streamlined shapes, such as in submarines or airfoil designs in aircraft. The friction drag or what is alternatively known as viscous

drag is caused by the interaction of the fluid and a surface parallel to the flow, which creates friction and which means resistance. Another reason for the friction drag is the attraction between molecules of the fluid. Moving away from the surface, the interaction between the surface and the fluid decreases and the velocity of the molecules increases until it reaches the mean fluid flow velocity. This behaviour is known as velocity gradient. Higher viscosity fluids have higher drag due to the higher attraction between fluid layers, which then leads to increase skin friction Sultanian (2015).

3.5.2 Drag Reduction Techniques

There are two types of techniques available for drag reduction- passive and active techniques. Passive techniques require no energy input into the flow. Therefore, any drag reduction obtained from the application of this type of techniques will be net benefits apart from the costs of system installation and maintenance. Active techniques, however, require certain energy input, for example, to move the fluid/body interface and to suck or blow the fluid through it. Since the level of drag reduction achieved by employing the active techniques is usually higher than that from the passive techniques, it is possible to obtain a greater gain by using the former procedure.

3.5.3 Sharkskin

Evolution and species adaptation to survive have inspired engineers to introduce abnormal solutions for some complex engineering problems. Mimicking of nature has led to developing many designs that represent cornerstones for many industries such aeroplanes, automobiles, ships, and buildings. From the available vast list of examples, fast swimming sharks grab the attention of mechanical engineers on how fast and clean they are. It is believed that sharks stay clean due to their micro-structured, ribletted skin and a mucous layer as in Figure 3-5 Martin and Bhushan (2016a). Lower drag is also an evolutionary advantage necessary for sharks since it allows sharks to swim faster to catch their prey. Thus, drag reduction by shark skin is one of the main issues drawing attention and interest for most types of fluid flows in engineering applications such as aerospace, submersibles ships and gas/liquid pipelines, especially because of the energy crisis Kwon et al. (2014).

Shark-skin-inspired surfaces for aircraft applications have been studied by the National Aeronautics and Space Administration (NASA) and the German Aerospace Center Walsh and Anders Jr (1989). In ships, these energy efficient surfaces were applied to the hulls of US boats in the 1984 Los Angeles Olympics and 1987 America's Cup Bechert et al. (1997). Furthermore, they have been incorporated into the Speedo FastSkin® swimsuit worn by Michael Phelps in the 2008 Beijing Olympics when setting records and winning gold medals. These suits had drag reduction effects of up to 4% in men and 3% in women and were subsequently outlawed by the International Swimming Federation (FINA) supposedly due to their drag reduction benefits derived unfairly by some swimmers Martin and Bhushan (2016a).
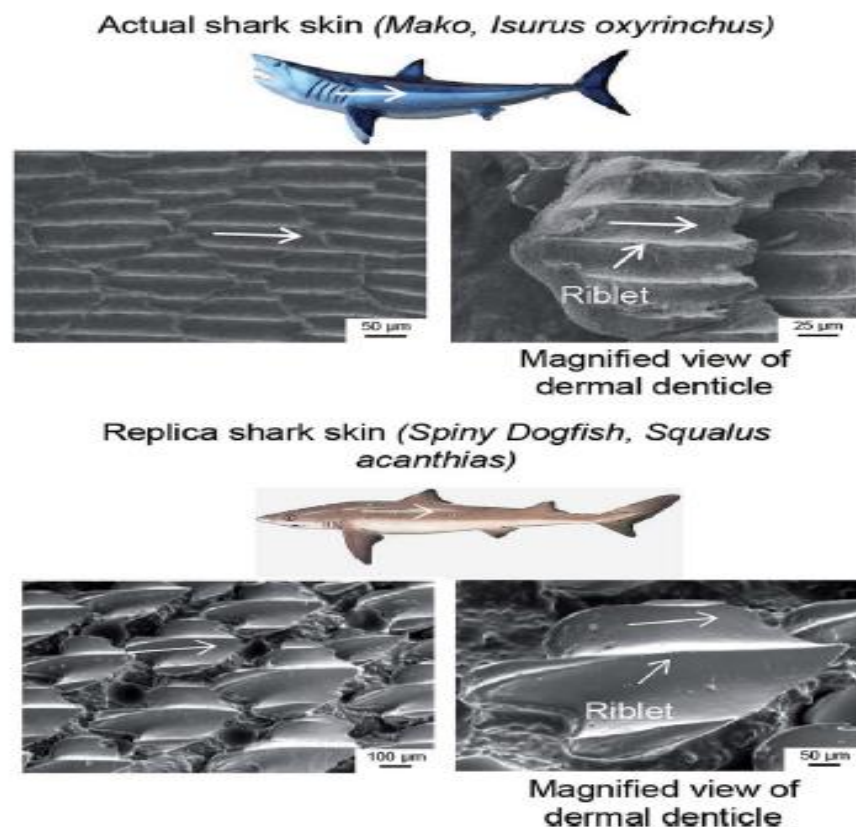
Figure 3-5 Scanning electron microscopy (SEM) micrographs of shark skin samples. The Mako shark has riblets that have little gaps and no offsets Martin and Bhushan (2016a).

3.5.4 Shark Skin Geometry

Shark skin dermal denticles and riblets are exhibit rather complex three-dimensional geometries and configurations. Therefore fabrication of such microstructured features is challenging. Additionally, to study the dimensional effects of riblets in fluid flows, experiments with varying sizes of relatively durable fluid-tolerant riblets are necessary. However, due to the micro sized nature of the riblets, this poses difficulty in producing cost effective riblet samples, especially for larger sample sets Bixler and Bhushan (2013a). In response, the assumingly most important characteristics of the riblets have been identified, and then samples have been fabricated for experimentation. Riblet sizes range from species to species and from location to location on sharks. For reference, the Spiny Dogfish shark Squalusacanthias has triangular shaped riblets with a base width of 100 to 300 μm, summit radius of about 15 μm, the height of 200 to 500 μ m, and spacing of 100 to 300 μm Bixler and Bhushan (2013a). Using actual riblets as an inspiration, simplified artificial riblet samples include various combinations of the blade, sawtooth, scalloped, and bullnose geometries with continuous and segmented (aligned and staggered) configurations. It is believed that actual shark skin most closely resembles scalloped riblets with a staggered segmented configuration.
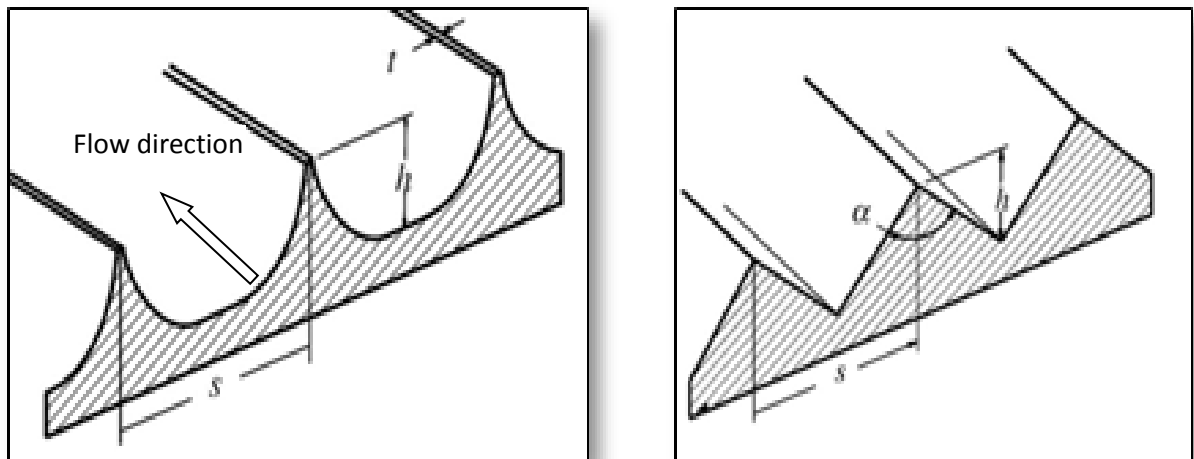
Figure 3-6 some riblet shapes that are used in drag reduction studies Martin and Bhushan (2014).

Many riblet shapes have been numerically and experimentally tested since the first introduction of the using riblet to reduce the drag by Lachmann G. V. (1961). But there are some essential parameters and dimensions that are common between these shapes. Figure 3-6 shows the important geometry parameters in two common shapesfor riblets,

s, h, and t denote the riblet spacing, the riblet height and riblet thickness (for some shapes). To compare different shapes it is usual to use the riblet aspect ratio (h/s).

There is another form of geometrical dimensions used to optimise the riblet performance and to compare between different shapes. This is denoted by the $^+$ symbol, which allows for better comparison of experiments with various riblet geometries and flows conditions. Minimising energy losses can be accomplished with riblets that effectively lift and presumably pin the turbulent vortices. However, the viscous drag or skin friction increases at higher Reynolds number. Similarly, Reynolds numbers based on riblet parameters can also be calculated, which are useful for riblet optimisation. The Reynolds numbers based on spacing and height of the riblets are defined as Bechert et al. (1997); Bechert et al. (2000); Lee and Lee (2001):

$$s^+ = \frac{su_\tau}{\vartheta}$$ ....(3.25)

$$h^+ = \frac{hu_\tau}{\vartheta}$$ ....(3.26)

$$t^+ = \frac{tu_\tau}{\vartheta}$$ ....(3.27)

where, u_τ is the wall shear stress velocity and ϑ is kinematic viscosity.
Considering kinetic energy, the wall shear stress expression ($\tau_o = (\rho/u_\tau)^2$) provides the wall shear stress velocity as Bixler and Bhushan (2013b):

$$u_\tau = \left(\frac{\tau_0}{\rho}\right)^{1/2}$$ .... (3.28)

Where ρ is the fluid mass density. Determining optimal riblet dimensions for various flow conditions is possible by considering dimensionless parameters. Therefore, the optimised riblet spacing for a given fluid can be determined by rewriting Equation (3.25), where $s^+ = \frac{su_\tau}{\vartheta}$. This equation indicates that for a constant s + value, the required riblet spacing for maximum drag reduction increases as kinematic viscosity (ϑ) increases. Appropriate s $^+$ values may be determined by varying the riblet spacing with a

constant flow velocity or vice versa, where varying velocity is generally more feasible Bixler and Bhushan (2013b); Martin and Bhushan (2016a).

3.5.5 Previous Work

Experimentally, an early report on riblets effects on flow was presented by Michel from NASA's Langley Research Center in 1970's. He found that the ribbed surfaces can effectively reduce the wall friction Zhang et al. (2011). This has opened up new ways for drag-reducing technology.

Walsh et al. (1984) investigated several different types of groove geometries and found that the optimum shapes for drag reduction have a sharp peak protruding into the flow and have a height and spanwise spacing of the order of the viscous sublayer thickness. The best drag reduction occurred when $s^+<30$ and $h^+<25$, for a V- groove riblet. Net drag reduction was large by 8% for two configurations: V-groove with $s^+ = h^+ =12$ and scalloped riblet with sharp tips and large valleys with $s^+=16$ and $h^+=8$.

Bacher and Smith (1986) used a free surface water channel and a high-speed camera to visualise the flow over streamwise triangular riblets. The riblets were 1.5mm in span space (s) and 1.5mm in height (h) with 0.21 m/s stream velocity, which gave optimal nondimensional riblets geometries $s^+=h^+=15$. The results showed that the streaks generated above the riblet surface are wider than those of a flat plate, and the flow within the riblet valley is slow and serene. The authors summarise that the secondary vortices at the riblet tips weaken the streamwise vortices and prevent the streamwise streak formation, which limits the turbulent momentum exchange in the lateral direction.

Choi (1989) studied the near wall turbulence structure over smooth and riblet wall surfaces under zero pressure gradient conditions using a wind tunnel. They used a rectangular riblet with the tapered top; the riblet's thickness is 0.5mm in the base, and 0.2 in top the riblet high (h) is 1.6mm and space (s) are 2.5mm and 3m/s the mean stream velocity. For these specific geometries, he found that the restriction of spanwise movement of the longitudinal vortices was the main mechanism for drag reduction over

riblet surfaces by comparing the near-wall structure over grooved and smooth surfaces. He concludes that the optimisation of riblets should be possible by maximising the effectiveness of this restriction of the spanwise movement.

Vukoslavcevic et al. (1992) used hot-wire anemometry to investigate the effect of stream wise-aligned riblets on the mean and fluctuating streamwise velocity distribution at $Re_\Theta \approx 1000$. He showed that the local shear stress in the riblet valley was sufficiently lower than on flat plate and the turbulence was rarely penetrating deep into the riblet valley.

Park and Wallace (1994) conducted an experimental study using an open return low-speed wind tunnel to compare the drag reduction over a smooth plate surface and a riblet surface. The 5mm base thickness and 10mm span between two peaks and 40° triangular riblets in the cross-sectional area made from low thermal conductivity fibreglass were used in this study. They used single and four sensors hot-wire probes anemometry to measure the streamwise velocity profile on V-shaped riblet grooves with $s^+=28$ and $h^+=14$. In the single probe, the stream velocity was 1.29m/s and in four sensors probe the velocity was 2.4-2.9 m/s to achieve Re_Θ between 1200 and 2500 respectively, for comparison with other studies. They reported having 4% drag reduction compared to a smooth surface that has the same surface area; also they suggest that those riblets reduce the vertical flux of streamwise momentum within the riblet valleys.

Suzuki and Kasagi (1994) investigated the turbulent structure of flow over V-shaped riblet surface manufactured on the aluminium plate using a turbulent water channel and 3D particle tracking velocimetry (PTV) system. They used scalloped riblet with 3.2mm space (s) and 2.5mm height (h). They reported that the redistribution mechanism of the turbulent kinetic energy from the streamwise component to the spanwise one was considerably suppressed in the region above the riblet valley; also they mentioned that under a neutral drag condition, a cross-stream secondary flow was apparent near the ribs leading to enhancement of the turbulent momentum transport and deterioration of the drag-reducing effect of the riblet.

Djenidi and Antonia (1996) used a closed circuit constant-head water channel and Laser Doppler anemometer (LDA) system to experimentally obtain the drag reduction over V-shaped riblets with (s^+=25 and s^+=75). They showed that there was a drag decreasing in the s^+=25 case and a drag increasing in s^+=75; also the near-wall secondary flow motion was much weaker for drag-reducing than that for the drag-increasing case.

Bechert et al. (1997) used an oil tunnel to extend a previous theoretical work Bechert et al. (1986). The studied riblets were trapezoidal grooves with wedge-like ribs and an extendable lateral space between 2 – 10mm. Although the study was focused on utilisation of an oil channel, the large scale of the riblets helped in obtaining shear stress measurements which were necessary to establish the connection between the oil tunnel and wind tunnel data. A new parameter t/s (riblet thickness to space) was used in this study, and the results showed that thinner riblets have higher drag reduction. Also, the results showed that the riblet high to space ratio h/s has a dominant role in drag reduction. The best results were obtained at h/s around 0.6. For commercial use in the aircraft industry, the authors reported that they had 8.2% drag reduction by using a riblet that has trapezoidal grooves with a wedge-like ribs geometry.

Bechert et al. (2000) extended the previous work; the authors reported using both the wind tunnel and oil tunnel to experiment with a group of 3D riblets with different geometries and compared the results with the 2D results. The best drag reduction achieved by these geometries was around 7.3% compared to a flat plate. However, the drag reduction using 3D riblets was less by 1.7% when compared to 2D. In contrast, the optimum drag reduction for short 3D-riblets occurs at a lower rib height than for longer 3D-riblets or for infinitely long 2D riblets. No explanation is given by the authors for this.

Lee and Lee (2001) used a closed type subsonic wind tunnel and a PIV system to investigate experimentally the near-wall flow structures of a turbulent boundary layer over semi-circular riblet grooves with 3mm peak to peak space (s) and 1.5mm peak to valley height (h). Two cases, low and high free stream velocity 3 m/s and 5m/s respectively, are considered, which caused a drag decrease and drag increase (s+=25.2 and s+=40.6) respectively. The result showed that in the case of s+=25.2, the large-scale

streamwise vortex stays above the riblets because the average streamwise vortices are larger than the riblet spacing and the spanwise motion has been restricted more or less by the riblet tips. However, the streamwise vortices sizes in case of $s^+=40.6$ are smaller than the riblet spacing. Therefore, they can easily penetrate into the riblet valleys which increase the wetted area and increased the drag as a consequence. Also, they visualised the flow using the synchronised smoke-wire technique with a high-speed camera under the same experimental conditions; they found that the normalised RMS velocity fluctuations and turbulent kinetic energy were small near the riblet surface as compared with a flat surface.

Koeltzsch et al. (2002) used a high-speed wind tunnel and a special pipe system which is very low sound and vibration influence to measure the velocity field over convergent and divergent riblet patterns in turbulent pipe flows using hot-wire anemometry. Two pieces of special riblet film were used to coat the internal wall of the pipe, the riblet height (h) and spacing (s) were taken equal ≈ 225 μm, which provides $s^+ = h^+=19$ in wall units. The riblet films were arranged obliquely, with a yaw angle $\varphi=-45^0$ in one-half of the pipe and $\varphi=+45^0$ in the other. The authors concluded that close to the wall the time-averaged streamwise velocity decreases, and the velocity fluctuation u_{rms} increases over the convergent riblets. The opposite was found on divergent riblets. Their explanation was that in the convergent riblet, the coming fluid move away from the wall is slower because of continuity. Thus a local decrease in streamwise velocity U and an increase in u_{rms} are observed. This phenomenon is inverse in divergent riblets.

Dean and Bhushan (2012) studied the drag reduction over a riblet in a rectangular duct experimentally. Blade riblets with different h/s ratios (h/s =0.3, 0.5 and 0.7) were tested combined with different Reynold numbers (4000-20000). Although the results showed that the pressure drop in the flow was very small and in some cases was similar to the flat plate pressure drop, the authors suggested more investigations on different blade shape and compared them with pressure drops on a flat plate that were machined using the same machining process.

Nugroho et al. (2013) used an open-returned blower wind tunnel and hot-wire anemometry to measure the velocity fluctuation in a zero pressure gradient turbulent

boundary layer over converging–diverging riblet-type surface roughness (herringbone shape). The study also investigated the effect of the viscous-scaled riblet height h^+. The authors noticed two opposite behaviours for the local mean velocity, above the diverging region, i. e. the local mean velocity increases while the turbulent intensity decreases, resulting in a thinner overall boundary layer thickness in these locations. The opposite situation occurs over the converging region, where the local mean velocity is decreased and the turbulent intensity increases, producing a locally thicker boundary layer. They explained that this highly directional surface roughness pattern provokes a large-scale spanwise periodicity onto the boundary layer, resulting in a noticeable spanwise modification of the boundary layer thickness. In term of the riblet high, the studied riblet heights h^+ were 24, 19, 13, and 7. They reported that the riblets height effects on maximum spanwise variation for both the mean and standard deviation of the streamwise velocity components, the higher riblets lead to higher maximum spanwise variation.

Bixler and Bhushan (2013b) experimentally investigated the drag reduction over different riblet shapes in different fluids (water and air) in open and close channels by using different measuring methods such as force balance and wake traverses. They reported testing many riblet geometries, fluid velocities (laminar and turbulent flow), fluid viscosities, riblet combinations, channel sizes, wettability, and scalabilities. A triangular cast acrylic riblet was manufactured using laser technology. The riblet of 200-500μm height, 100-300μm base width and 100-300μm of spacing, allowed the authors to investigate wide range of blade h/s and t/s values (0.16 < h/s < 0.62 and 0.18 < t/s < 0.38). The results indicated that lower h/s for the blade and higher h and t for equilateral saw tooth riblets are desirable. However, the s^+ value must be such that the vortices remain lifted and pinned. The change in velocity was taken inclusively by varying Re number between 0-6000. The results showed that at higher Reynolds Numbers, drag reduction improves. Since turbulent flow contains natural vortices, the riblets offer more benefit in turbulent versus laminar flows. In terms of viscosity and pressure drop, both the air and water show the same reduction trends, which lead to the important conclusion that the riblet efficiency is independent of the fluid viscosity. Also, the study investigated channel high and the position of the riblet in the top or bottom surfaces of the channel. The results showed that the high of the channel has no effect on pressure

drop if the riblet was fixed to a bottom surface while it has a significant effect on the pressure drop if the riblet is fixed to the top surface. A connectional model was introduced to explain the results, and the main concept is that the vortex interaction is the main reason for that.

Chen et al. (2014) investigated a drag reduction over herringbone riblets experimentally using water tunnel. The riblet geometry was s = 100 μm, h/s = 0.6, and the Reynold number was between 110,000-470,000. He reported obtaining a maximum drag reduction of p-3D and s-3D herringbone riblets about 17 and 20%, higher than traditional microgroove riblets. Also, a significant change of drag reduction was found by the change of the angle between herringbone riblets and the maximum drag reduction occurred at an angle about 60° close to a real flight feather.

Samira Sayad Saravi (2014) investigated the drag reduction over alternative shape Serrate-Semi-Circular riblets using wind tunnel and hot wire anemometry. The riblets had s^+ =19 and h^+=11. Since the shape suggested is not standard such as blade a new definition of the dimensional spacing parameter (A_g^+) was taken into consideration. The authors showed that the new model achieved 7% reduction in skin friction compared to the flat plate; also they concluded from comparing their model results with other researchers for same s^+ that A_g^+ is a better characterization of drag reduction breakdown than the riblet spacing s^+.

Bixler and Bhushan (2014) experimentally tested three samples of riblets fabricated with photolithography techniques inspired on rice leaf and butterfly wings; they reported using four different samples which are combinations of ribs and pillars with 2-4μm in height and 5μm pillar diameter. Although the study focused on the self-cleaning action in such dimensions, the authors reported a drag reduction with pressure drop measurements and a maximum pressure drop reduction of 23% and 26% for the wing and rice leaf, respectively.

Luo et al. (2016) conducted an experimental study to investigate the hydrodynamic drag reduction of different shape manufactured sharkskin samples using a water tunnel system. The width of the microgroove used was about 50 μm, and its height was about

10 μm. Although the study focused on the stretching fabrication of sharkskin morphology, hydrodynamic tests showed 10-13% reduction in shear stress on sharkskin surfaces compared to a flat plate.

Numerically, Bechert and Bartenwerfer (1989) theoretically investigated the viscous sublayer of a turbulent boundary layer and the origin of the velocity gradient on a surface with fine longitudinal ribs, using conformal mapping. The study covered a number of common geometries like sawtooth profiles with triangular and trapezoidal grooves as well as profiles with thin blade-shaped ribs, ribs with rounded edges, ribs having sharp ridges and U-shaped grooves. They calculated the velocity distribution over various shapes; also they calculated the position of the velocity origin below the riblet tip and termed it as "protrusion height" because it determines how far of the rib tips protrude into the boundary layer. However, they stated clearly that these calculations are certainly valid in pure viscous flows which mean such calculations are valid only within a regime very close to the riblet surface. Another limitation of their calculation was that the protrusion height, which was between 10-20% of the riblet spacing, is valid only for regular riblet shapes with sharp tips such thin blades, sawtooth, riblet with trapezoidal grooves and riblets with the scalloped cross-sectional area. Other geometries need more complicated analyses.

Chu and Karniadakis (1993) used direct numerical simulations (DNS) to simulate a channel flow over riblets using a spectral element Fourier for the method. The riblet was a V-groove shape, and the Reynold number was taken between 500-3500 to cover laminar to turbulent flow conditions. The laminar results showed that the velocity profiles were inflexional in nature which suggests that the instability mechanism which initiates transition over the riblets may be different from that of the smooth wall. The turbulent results showed the same behaviour but the point where the velocity profile was unstable was up to $y^+=26$. Also, they reported having approximately 6% drag reduction at Reynold number 3500 for the surface with riblets compared with a smooth surface. They found that riblets limit the spanwise motion of low-speed wall streaks, decreasing the ejection events.

Haecheon et al. (1993) used DNS to simulate turbulent flows over riblet-mounted surfaces. The riblets were V-shaped with $s^+=20$ and $s^+=40$; they obtained a drag reduction about 5-6% for riblets with $s^+=20$ and drag increase for riblet $s^+=40$. Also, they computed the mean velocity profiles depending on the virtual origin of the wall and showed upward and downward shifts in the log-law for drag-decreasing and drag-increasing cases, respectively. Furthermore, they suggested that the transverse flow near the wall was impeded by the riblets depending on the reduction of the normal and spanwise velocity fluctuations above the riblets which occurred, as a result, the reducing of velocity and vortices' fluctuations as well as Reynolds shear stress above the riblets.

Goldstein et al. (1995) used an immersed boundary technique in a DNS study to model riblet covered surfaces on one wall of a channel bounding fully developed turbulent flows. Two different riblet configurations using two different spanwise resolutions were used; first a short and squat riblet $s^+=18$ and $h^+=5.3$, second a high and more closely riblets $s^+=11.7$ and $h^+=9.4$. They presumed that the useful drag reduction effect of riblets was assigned to the damping of cross-flow velocity fluctuations. Very short riblets do not protrude far enough into the flow to sufficiently damp w (or v) fluctuations. Larger riblets s^+ and h^+ i. e. (10 to 20) do damp w and have a lower drag in the valleys but produce a greater drag near the rib peaks. Ribs that are spaced closely enough not allow the large boundary layer streamwise vortices to settle between them.

Benhalilou and Kasagi (1999) used a nonlinear low-Reynolds number k-ε model together with several turbulent scalar flux representations to numerically study heat and momentum transfer characteristics in a fully developed turbulent channel flow with triangular riblets. The Reynold number was taken to be varied from 3000 to 20000 and $s^+=20$-30 and $h^+=20$-30. The major advantages of the turbulence model they adopted are the abandonment of the reference to the wall topography and the implementation of the shear parameter in the model function, which combined with the Reynold number. Thought to be more useful in capturing the complex flow over the riblets (vortices) and to predict the mean secondary flow that exists in the plane normal to the mean flow direction, these vortices contribute to the inhomogeneity of the flow field in the close vicinity of the riblet surfaces.

El-Samni et al. (2005) they investigated by using DNS the effect of longitudinal thin rectangular riblets aligned with the flow direction of turbulent channel flows. They built their model using immersed boundary method (IBM) technique and tried different spacing (s^+) between 11 and 43 wall units, keeping the height/space ratio at 0.5 and Reynold number based on shear velocity and half channel width at 150. The computational domain utilised from 64x65x144 grid point in the streamwise, wall-normal and spanwise direction, respectively. They used a hyperbolic tangent mesh distribution in the wall-normal direction to calculate the high gradient near the wall, while used uniform meshes for the two other directions. The results showed significant changes in Reynolds stresses as well as the instantaneous field over the riblets. Also, they focused on having the optimum space corresponding to maximum drag reduction and reported that a 17 wall unit was the best. Although the drag calculations showed higher ratios than other works, they recommended using the model but with a finer grid.

Zhang et al. (2011) conducted a DNS study to investigate the drag reduction on sharkskin. A riblet model was built based on a scan of a real biological shark skin. The physical domain was a channel with the smooth upper wall, and the sharkskin riblets were laid on the lower wall, the flow was taken as a fully developed turbulent flow. They used very fine mesh near the wall with total domain grids reaching 1470000 grid points. They concluded that the velocity rapidly changes from the high value on the tip to even negative velocity at Valley (as backflow). Also, the turbulence intensity is much larger on the tip than that in the valley, and the spreading movement of the vorticity is restricted by the grooves of the shark skin, which leads to drag reduction. Also, they tested the angle of attack and reported that the change could lead to the occurrence of tiny backflow on the valley, and the micro-grooves and attack angle of the scale are the main contributions to drag reduction.

Jin and Herwig (2014) investigated the drag reduction and heat transfer behaviour in the channel with a sharkskin surface using DNS. Obstacles (small rectangular), blades and wedges riblet geometries and Reynolds numbers from 2800 to 5600 were tested. They analysed the turbulence close to the wall and concluded certain turbulent structures are lifted off and rearranged, so they proposed a mechanism called lift off and alignment

(LOA) and supported it by analysing entropy generation rates. The calculated drag reduction was around 5%.

DeGroot et al. (2016) used a RANS to study a turbulent flow in groove channels. Sinusoidal grooves parallel to the flow direction were fitted to the upper and/or lower walls of the channel. The authors reported studying the effects of the Reynold numbers, groove wave number and groove amplitude on skin friction. They concluded from the results that the grooves redistributed of the bulk velocity into high-velocity stream direction leading to change the skin friction profile, also the skin friction was reduced significantly in the narrow part and slightly reduced in the wide part of the channel.

Martin and Bhushan (2016a) used a CFD software package ANSYS Fluent 16.0 and the Large Eddy Simulation (LES) model to investigate the optimal design of riblets through studying spacing, height, thickness, gap and offset. They reported that the optimum spacing should be 15-20 wall units to lift up away the vortices with 20-30 non-dimensional units and the height should be around 8-10 wall units to minimise the drag reduction; also, thinner riblets are better because of major drag occurs at the riblet peaks. They used riblets with optimum parameters that they found from previous works i.e. s^+=15-20, h^+=8-10 and t^+ small. They reported that that the blade riblet has the greatest drag reduction around 11.6%, and then scalloped at 5.7%, and then saw shape with 4.1%.

Song et al. (2017) concluded a numerical study to simulate the flow over ovoid non-smooth surfaces. The authors used ANSYS software to conclude the study and used the k-ε turbulent model and a standard wall function correction method. They concluded that the ovoid dimples maintain the stability of the flow due adsorption of the fluid near the wall and had a regular disturbance to the turbulent flow, also increase the boundary layer thickness and reduce the velocity gradient as a consequence.

Radmanesh et al. (2017) used ANSYS and XFOIL (viscous analysis code which is capable of modelling the influence of laminar separation bubbles) to simulate the flow over NACA S5020 covered by different riblet geometries. The authors reported an increase in drag by 4% for non-optimal riblets; also, the drag depended greatly on the

angle of attack the best was at 8^0. They emphasised that riblets performance is dependent on the aerofoil and the optimal span and performance could change significantly by aerofoil.

3.6 Summary

From most of the previous experimental work, it can be seen that the drag reduction using riblets or sharkskin is still open to many questions such as effect of h/s, riblet thickness, riblet tip thickness, angle of riblet aligned. Although the efforts and theories have tried hard to find dimensionless parameters that may be considered as crucial parameters that could be a reference to riblet design, most studies end with that uncertainty of applying the results on other geometries which means needing to manufacture and test every single geometry. The solution may be in the picture of the numerical solution. But numerical studies limits, DNS is appropriate for addressing basic research questions regarding turbulence physics. But the limitations of its computational cost, especially with high Reynolds numbers, prevent DNS from being used as a general-purpose design tool. Another modelling method is LES, which depends on solving large scales of the flow field and filtered out the small scales of the flow field based on turbulence criteria. The disadvantage of this modelling is that it does not consider all scales, omitting the smaller ones.

In this work, a validation of the in-house LES software Hydro3D is carried out to investigate the drag reduction and flow mechanism over blade riblets with different h/s ratios in turbulent channel flows as a first step to using this code in the design of the best riblet pattern that could be manufactured using WEDM (wire electrical discharge machining). To do so, blade riblets, which are the simplest riblet design, with three different h/s ratios are numerically tested. Two of the many advanced tools in Hydro3D, the WALE model, were used to perform the near wall flow, and the LMR (local mesh refinement) also was used to save computational time. More details will be presented in the next chapter.

Using a successful numerical code to design different riblet shapes will reduce the cost of manufacturing by suggesting the optimum designs and allow to manufacture the best performance results without need to test every design. Also, the numerical code will give a chance to gain better understanding of different parameters that could have an effect on the riblet performance such as height, h/s ratio, and thickness of the riblet, Reynold number, and alignment of the riblets etc… which helps reduce the cost of experimental tests and use the manufacturing machines more effectively, as will be described in chapter five.

Special designed experimental rigs and measurement systems will be described in the next chapter, together with the numerical setup.

CHAPTER 4

EXPERIMENTAL AND NUMERICAL SETUP

4.1 Introduction

In this chapter, the two experimental rigs designed specifically for channel flow and for swirling flow are described. The hot wire anemometry and LDA systems that are used in combination with these two rigs are also reviewed. Finally, the numerical set up is introduced. The experimental tests are designed to cover the main goal of study which is to improve swirl combustion system resistance to boundary layer flashback using manufactured surfaces (riblets) as a regular roughness pattern on the internal wall of the burner. To do so, the study benefited from using two different experimental rigs: the first rig is designed to study isothermally the fundamentals of using riblets as a passive technique to reduce the drag in the boundary layer and to enhance the velocity gradient in the boundary layer. While the second rig, which is a swirl combustion system, is used to test the outcome of the first rig under isothermal and combustion conditions using three different nozzles. The nozzles that were used in this rig are nozzles with different surface finishing; the first is normally stainless steel nozzle with smooth surface which is used as a base to compare the other nozzle's performance; the second is a stainless steel nozzle with EDM constructed surfaces. The third is a stainless steel nozzle using a woven stainless steel wire as a liner.

The numerical side of this work uses an in-house code known as Hydro3D. The software is based on an immersed boundary method and can adopt different turbulent models like Smagornisky, WALE or One-Equation model; also Hydro3D is a parallelization code, which means that the numerical zone can be divided to many sub-zones, assigning one or more sub-zone to each processor and save time and computing costs. This enables to employ LMR (Local Mesh Refinement) in which the code can refine the mesh for sub-domains to reduce the computing effort on the most important parts of the domain. The goal of using the numerical simulation in this study is to overcome the high cost and complex manufacturing of riblets with different patterns.

which achieved as will show through next chapters. So the numerical work assesses common geometries of riblets (blades, sawtooth, scalloped, ..etc) in a fully turbulent duct flow to verify the software ability to solve each case and compare it to published work. Next, the numerical solutions focused on the geometries that could be produced using the available EDM machine at hand. Finally, the numerical simulation is used to investigate the effect of riblet alignment on drag reduction.

4.2 Experimental rigs

The experiments were conducted in two different rigs; a duct for straight flows and a swirl flow rig.

4.2.1 Duct Flow Rig

A new rig was specially designed to test cost effectively and accurately multiple regular surfaces under isothermal diffusion flow. The rig design aims at enabling the testing of multiple manufactured surfaces effectively and accurately, while being flexible enough for potential future tests. The rig compromised of a centrifugal fan, a fluid straightener, duct test discs, unit slide and hot wire anemometry. The centrifugal fan is run at 2880 rpm; the maximum air mass delivered by the fan is 3000 l/min. The fan is driven by a 7.5kw, 3 phase motor, and the intake of the centrifugal fan is provided with an air filter to ensure that the delivered air is free from any particle that could damage the hotwire probe. The delivery pipe has two air rotometers each rotometer can measure up to 2000 l/m, but due to the pipe system, the maximum delivered flow is 1500 l/min. The centrifugal fan, rotometers and piping system is shown in figure 4-1.
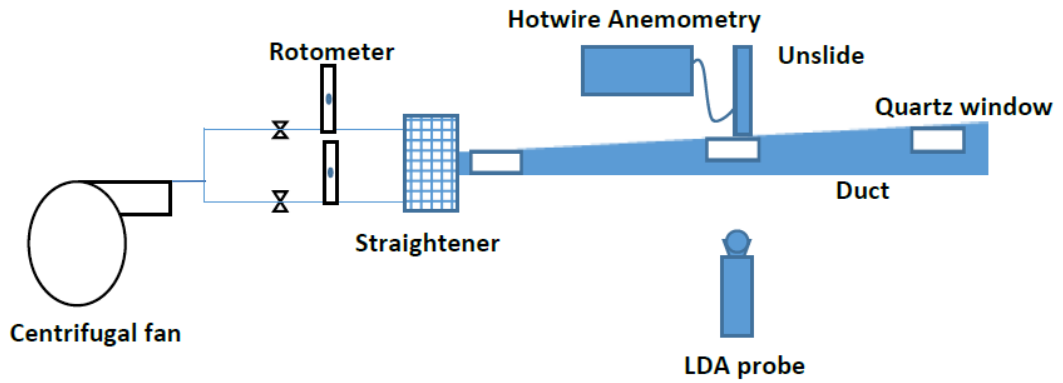
Figure 4-1 Shows centrifugal fan, rotometers, and connections.

The rotometers supply the air to the duct flow system through a couple of 2inch plastic hoses. In order to obtain a uniform flow, the air passes through air straighteners. The air straighteners, which contain a small chamber receiving air from two 2" side holes, force the air to pass through a stainless steel honeycomb to damp and suppress any vortex in the flow. After a short settling distance, a couple of wire meshes are fixed inside the duct to have streamlined Mehta and Bradshaw (1979).
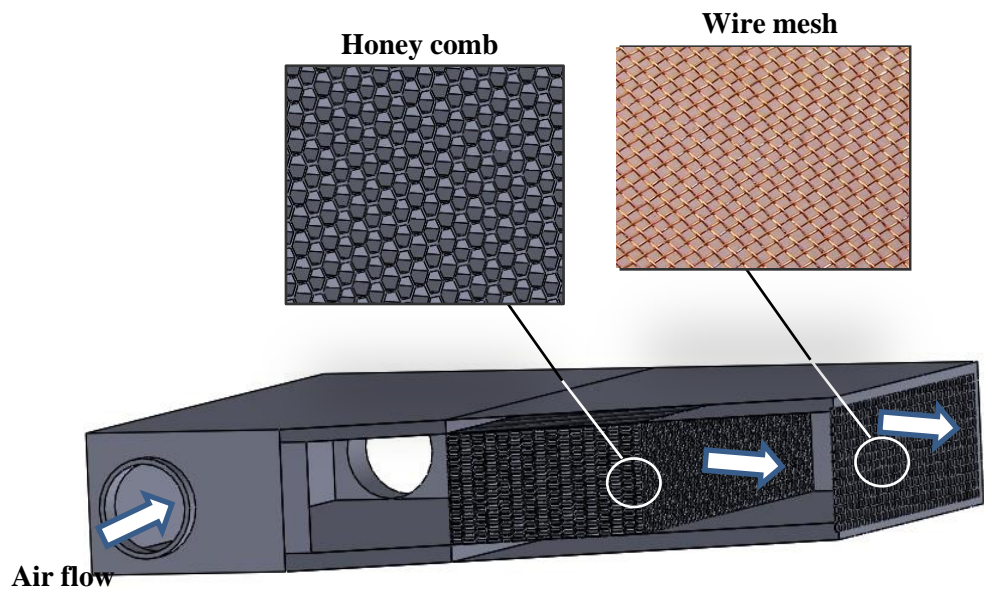
Figure 4-2 Flow Straightener section

The air then enters the duct. The duct is variable in cross-sectional area; at the entrance, the duct dimensions are 15cm x 1.5cm width and height respectively. The ratio of width to heigth is kept more than 10 to ensure that the flow could be treated as two-dimensional flow and to eliminate the wall effectTuncer Cebeci (1977). At the exit, the

dimensions are 20cm x 4.7 cm (when the bottom plate is horizontal) with a total length of the duct in 870mm to ensure fully developed flowTuncer Cebeci (1977). The bottom part of the duct is made of a stainless steel plate pivoted at the inlet and left free to move from the other end to obtain different outlet cross-sectional areas to have good control on backpressure in the case of using the duct in diffusion combustion studies in the future. The sides wall are tapered with three quartz windows located at the beginning, middle and the end of the wall, each window is 2.6cm and 9.6cm in height and width, respectively. These windows give the visual access to three testing section through the duct. Figure 4-3 shows the full detail of the wall.
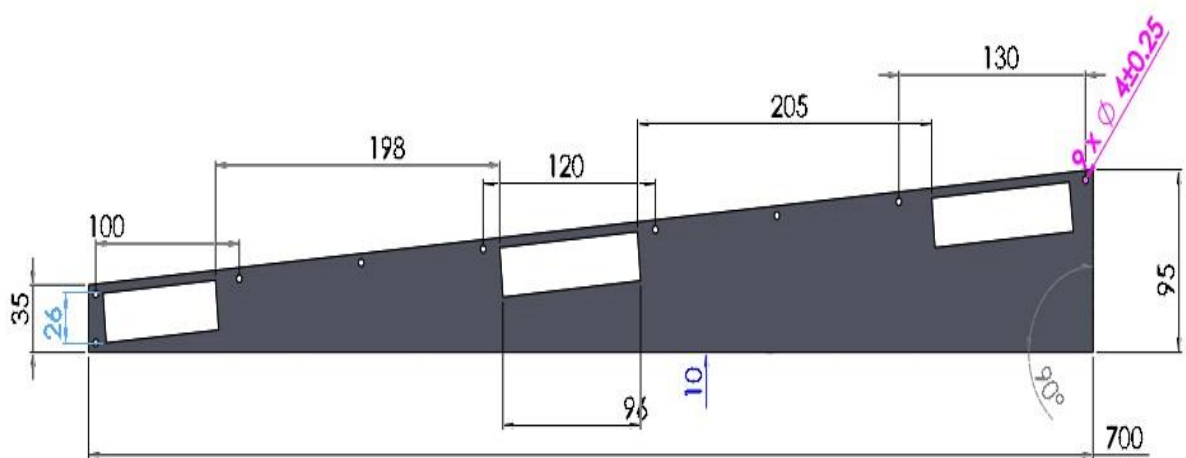
Figure 4-3 shows the dimensions of the side walls and the quartz windows location and dimensions.

The top part of the duct is placed on and fixed to the sides walls in such a way to be inclined upward by 5^0 to avoid the boundary layer separation at high Reynolds numbers J. B. Klemp (1972). The length of the top part is 702mm, and it has three holes in different positions, each hole is 78mm in diameter. The hole positions are chosen to be at the entrance region, partially developed flow region and fully developed flow Tuncer Cebeci (1977). Figure 4-4 shows the top part with holes.
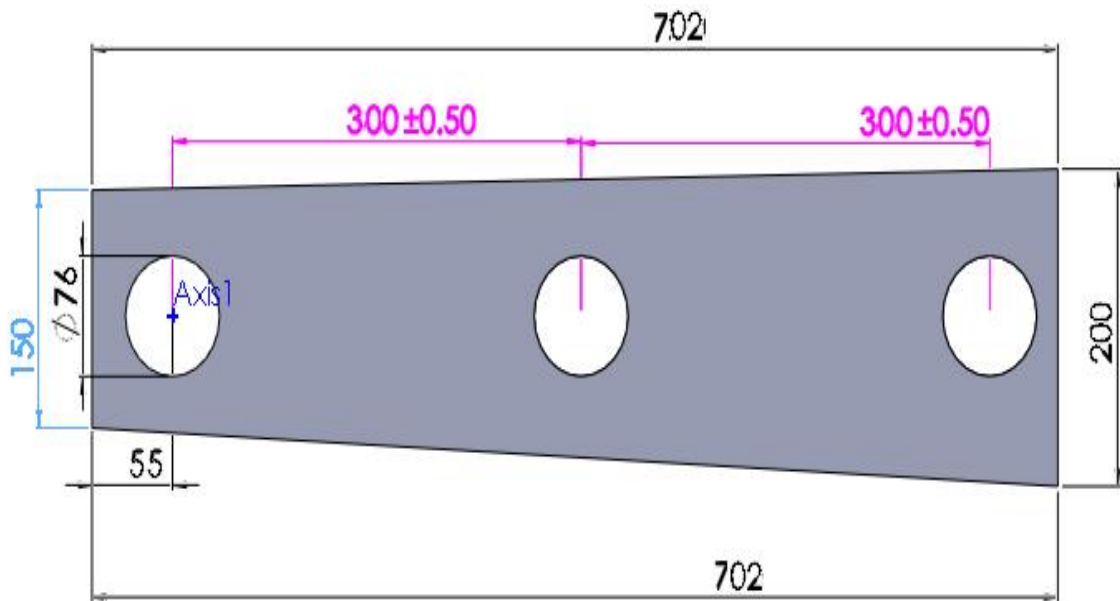
Figure 4-4 shows the top part of the duct and holes.

The test section contains two discs, which are stainless steel. Their diameter is 76mm and 10mm in thickness and a collar 4mm thickness and 82mm diameter to help in fixing the disc into the hole on the top plate. The first disc (or large disc) has 25mm hole to insert the second disc. The disc only has two 4.5mm holes to insert the hot wire probe through it to measure the velocity fluctuations at two positions before and after the manufactured surfaces which are constructed on the second disc. The top surface of the collar has been marked with 8 small grooves to align the second disc to the income flow. To accurately detect the angle of the incoming flow and the microstructure surface a protractor stuck on the top of the large disc as in figure 4-5.
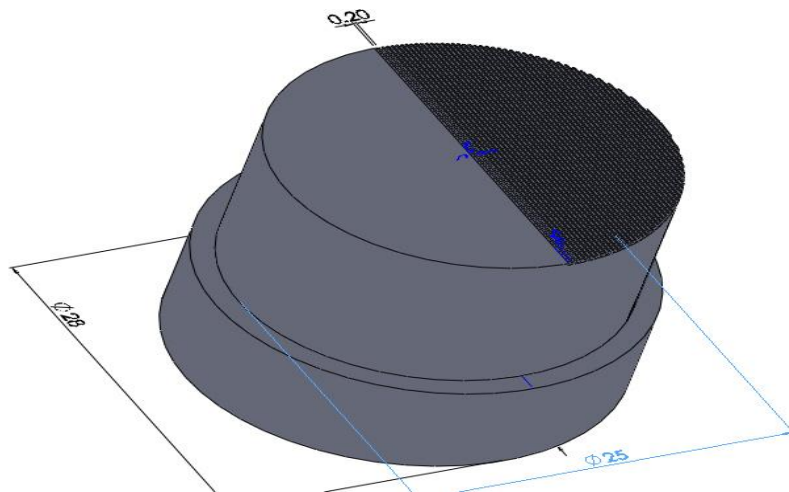
Figure 4-5 shows the smaller disc and the different manufactured geometries: louts (top left), sharkskin (top middle), diamond (top right) and a sketch of smaller disc down with a manufactured surface.

The second disc or smaller disc is inserted into the hole of the larger disc and is used a collar to sit on the larger disc. The disc freely rotates inside the larger disc. The bottom surface of the disc is ensured to be aligned to the bottom surface of the larger disc and the inner surface of the top part of the duct as shown in figure 4-6. This allows the cost effective testing of multiple regular surface roughness.
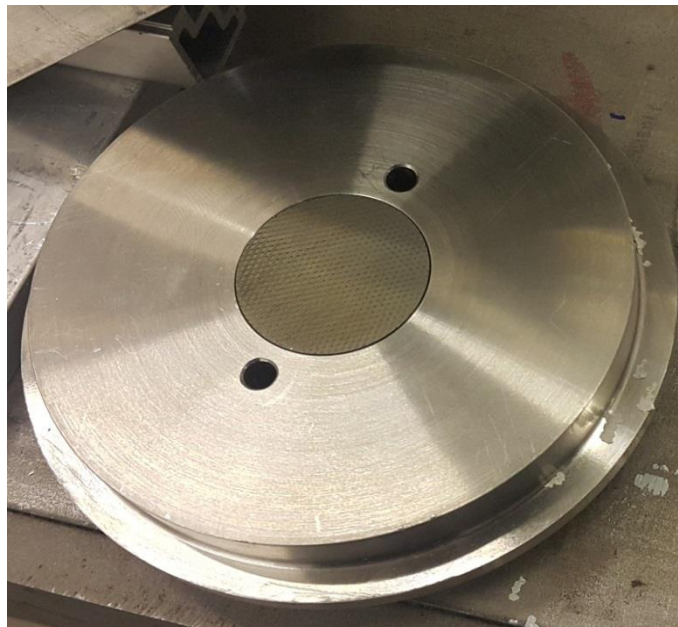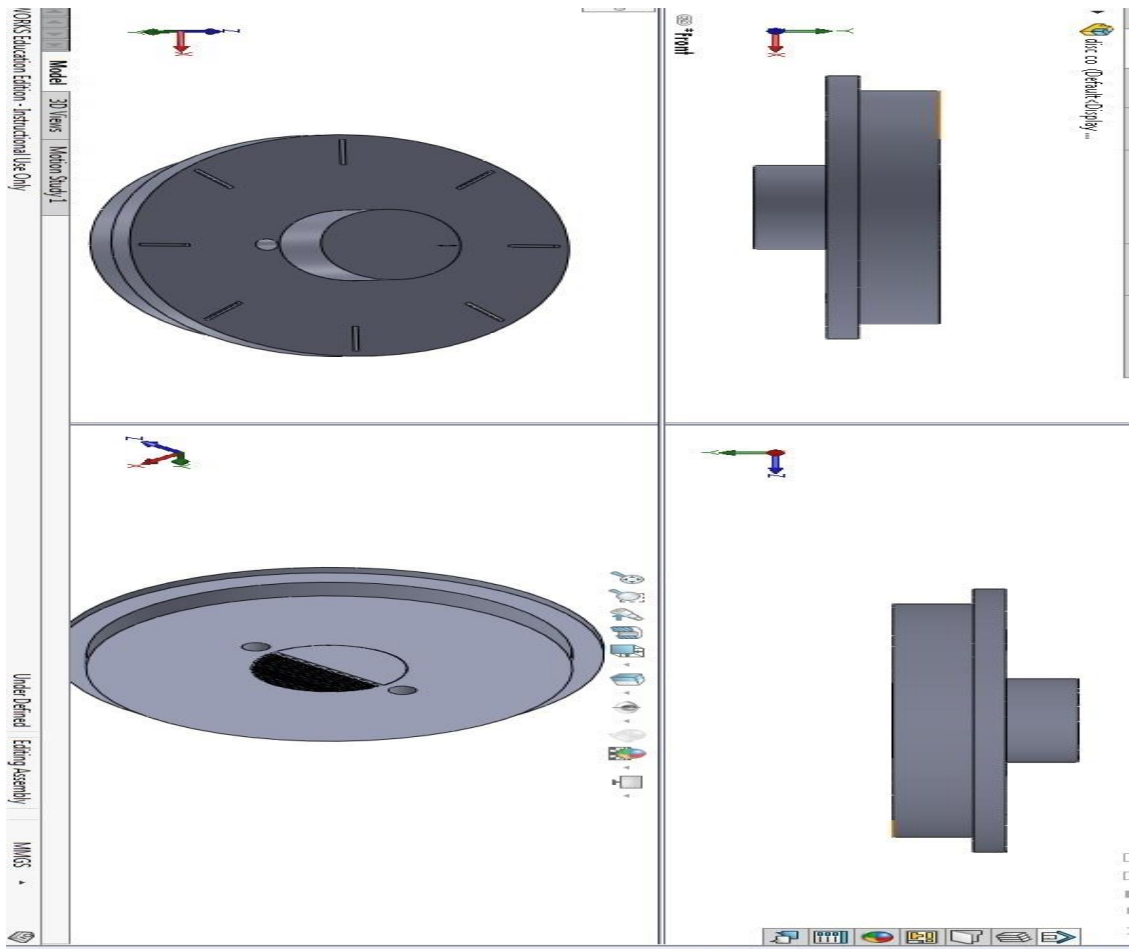
Figure 4-6 Large and small discs are assembled together: small holes for the Hotwire.

Different microstructure patterns have been constructed on the bottom surface of the smaller disc using manufacturing method WEDM (wire electrical discharge machining).

Due to manufacturing abilities limitations and to keep the manufacturing accuracy as high as possible and to handle the cost of manufacturing using WEDM, only small discs were manufactured with WEDM. Figure 4-6 shows the smaller disc and the different geometries that have been made.

The last part is the slide which is used to hold the hot wire probe and move it precisely. The unislide has been the preferred method to produce linear and rotational motion in the scientific instrument and industrial applications since the late 1960's. The unslide used in this work is supplied by LG Motion Ltd LG Motion (2016). The unslide moves 1mm in the vertical direction for each full turn of the leadscrow. The total vertical distance that could be covered is 16cm in the vertical direction, with a minimum achievable distance of 10µm ±2µm LG Motion (2016). Figure 4-7 shows the unslide.

Figure 4-7 LG Motion unslide.

4.2.2 Swirl Flow Rig

A 150 KW Tangential generic swirl burner was used Figure. 4-8. This system has been extensively used to investigate flame characteristics and other combustion features by using different configurations Valera-Medina et al. (2011a); Valera-Medina et al. (2011b); Syred et al. (2014); Fares Amer Hatem (2017). It has two tangential inlets of 67mm diameter which can be changed by using different inserts blocking 25%, 50% and 75% of their total area, giving swirl numbers ranging from 0.913 to 4.5. The burner exit diameter is 76 mm, D, which can be changed by using different nozzle configurations.
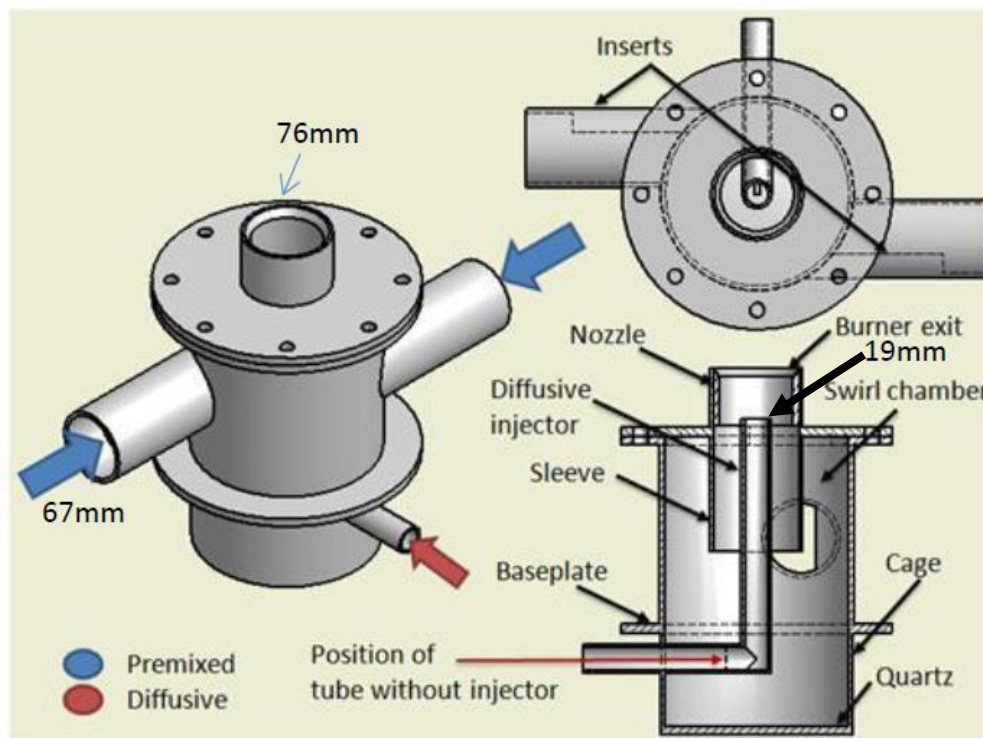
Figure 4-8 Generic tangential swirl burner.

Experiments were done using a 19mm air injector, five configurations two nozzles and inserts without confinement. The nozzles that are used in the experiments are made from stainless steel, and one of them has longitudinal grooves along the inside wall, while the other one is left smooth. The smooth nozzle is used in first place to obtain a standard data set for comparison purpose. Then two different diameter woven stainless steel wire mesh (desribed in more details in chapter 5) are used as liners and installed to the inner wall of the smooth nozzle, as shown in figure 4-9. A centrifugal fan provided

air via flexible hoses, and two banks of rotameters were used to control the air flow and natural gas injection, respectively. Two modes of fuel injection were utilised; a diffusive mode where the fuel is injected via the central injector, and premixed injection where the fuel is injected through the tangential inlets just before the inserts, fuel always being natural gas. The former is used to start up the system, and once a stable flame has been achieved premixing is added to the flame. Diffusive injection is slowly shut down once that stability with high premixed fuel rates has been achieved.
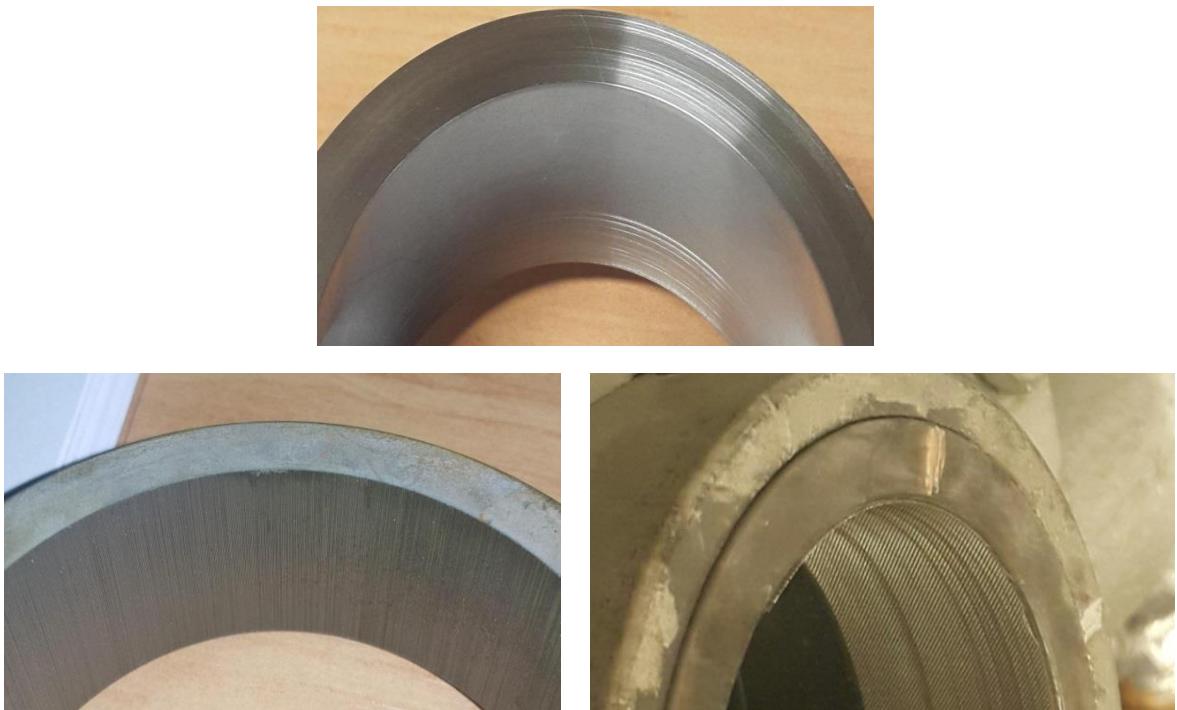
Figure 4-9. Nozzles used in the experiments. Smooth nozzle (top), nozzle with longitudinal grooves machined by WEDM (down left) and nozzle with 150µm wire mesh as liner (down right).

4.2.3 Hotwire Anemometry

To obtain velocity distributions in the channel for the region over testing region, hot wire anemometry was used. Hot wire anemometry has the necessary frequency response, in the range of kHz, and sensitivity at low flow velocities for measurements the high turbulence levels encountered in swirling flow systems.

4.2.3.1 Calibration of Hot Wires for Velocity Changes

All instruments related to the measurement of fluid velocities and heat transfer are linked to several non-dimensional parameters and geometrical factors such as the Nusselt (Nu), Reynolds (Re), Prandtl (Pr), Knudsen (Kn), etc. In the context of a cylindrical thermal anemometer, the equation can be expressed as follows:

Nu = f (Re, Pr, Kn,… geometrical factors) …………………………………………(4.1)

In 1914, King derived a solution for the heat transfer from an infinite cylinder in an incompressible low Reynolds number flow that may be written as:

$$Nu = A' + B' \, Re^{0.5} \quad \text{…………………………………………………… (4.2)}$$

A' and B' are constants. Knowing that the heat loss is equal to the electrical power delivered by the sensor (V^2/R, where R is constant), the geometrical parameters of the wire and the fluid characteristics are constants; then the expression can be reduced to Cambridge (2017),

$$V^2 = A'' + B'' \, U^{0.5} \quad \text{……………………………………………………. (4.3)}$$

Where the new values A'' and B'' are constants. V_0^2 can be replaced by A'' when the velocity of the fluid is equal to zero. In practice, the voltage registered at the anemometer output is the electro- mechanical force E that is applied to the top of the bridge, where the two arms act as potential dividers. So, a more general expression can be written as,

$$E^2 = A'' \, + \, B'' \, U^{0.5} \quad \text{……………………………………………….(4.4)}$$

However, this expression has shown to be unsatisfactory when used over a large cooling range. So, higher order polynomials provide curves that fit the experimental calibration curves E vs. U. The equation commonly used is,

$$E^2 = A \, + \, B \, U^{0.5} + CU \quad \text{…………………………………………….(4.5)}$$

However, the value of U is comprised of 3 different velocity components, so the instantaneous cooling velocity is given by,

$$U^2 = u^2 + G^2W^2 + K^2v^2$$ …………………………………………………………… (4.6)

Where u, w and v represent the three velocity components, and G and K are values dependent on the wire characteristics Agustin Valera-Medina et al. (2008). For flows where turbulence intensities are less than 10% and where one main flow direction predominates, the mean velocity is obtained from the mean voltage level, and the turbulence intensity from the R.M.S. voltage,

$$U = \left(\frac{E^2 - A}{B}\right)^2 \quad and \quad \frac{\left(U'^2\right)^{1/2}}{U} = \frac{4\left(E'^2\right)^{1/2}E}{E^2 - E_0^2}$$ ……………………………… (4.7)

Where U' and E' are instantaneous values. Typically, six different measurements are taken at a given point to obtain the three components of the velocity U and their mutual relation.

4.2.3.2 Equipment Selection

Probes are selected on the basis of (Jorgensen, 2005):

- Fluid Medium
- Number of velocity components to be measured (1, 2 or 3)
- Velocity Range
- Quantity to be measured (velocity, wall shear stress, etc.)
- Required Spatial Resolution
- Turbulence intensity and fluctuation frequency in the flow
- Temperature variations
- Contamination Risk
- Available space around measuring point

The way of selecting one or other can be as follows,

- o Miniature Wires: First choice when analysing air flows with turbulence intensities up to 5-10%. These wires have the highest frequency response and can be repaired easily. These wires are the most affordable.

- o Gold Plated Wires: These can be used when turbulence intensities are up to 20-25%. However, their frequency response is inferior to miniature wires. They can also be repaired.

- o Fibre-film sensors: These can be used for applications in the air, with a lower frequency response than wires. They are more rugged and can be used in less clean air. They can be repaired. If a Heavy-quartz coating sensor is used, this can function for applications in water.

- o Film-sensors: These can be used for applications in air at moderate to low fluctuation frequencies if they are thin-quartz coated. They can be used in less clean air than fibre-sensors. If the coated is a heavy quartz one, they are more rugged than fibre sensors and can be used in applications in water. However, they cannot be repaired.

4.2.3.3 Anemometer Setup

For the hardware, the setup consists of an overheat adjustment (static bridge balancing) and a square wave test (dynamic balancing). When a signal conditioner is part of the array, the hardware setup also includes low pass filter and optional gain settings. The overheat adjustment determines the working temperature of the sensor. The overheat resistor in the system is adjusted so that the wanted sensor operating temperature is established when the bridge is set into Operate. The cold and warm resistors are related using the following equation,

$$a = \frac{R_W - R_0}{R_0} \quad \dots\dots\dots\dots\dots\dots\dots\dots\dots\dots\dots\dots\dots\dots\dots\dots\dots\dots\dots\dots\dots \text{(4.8)}$$

a: Overheating Ratio

Rw: Sensor resistance at operating temperature Tw

R0: Sensor resistance at ambient temperature T0

So,

$$R_W = R_0(1 + a) \quad \dots\dots\dots\dots\dots\dots\dots\dots\dots\dots\dots\dots\dots\dots\dots\dots\dots\dots\dots \text{(4.9)}$$

The recommended value for *a* is 0.8 in air (over temperature approx. 220 ℃) and 0.1 in water (over temperature 30 ℃). So the value can be setup to measure the values with the correct resistance at the desired temperature.

The over temperature $T_W - T_0$ can be calculated as:

$$T_W - T_0 = \frac{a}{a_0}$$

$$\dotfill (4\text{-}10)$$

Where, a_0 is the sensor temperature coefficient of resistance at T_0, which is given by the manufacturer. The probe leads resistance, and the resistance of the support and cable are provided by the manufacturer DISA (1995).
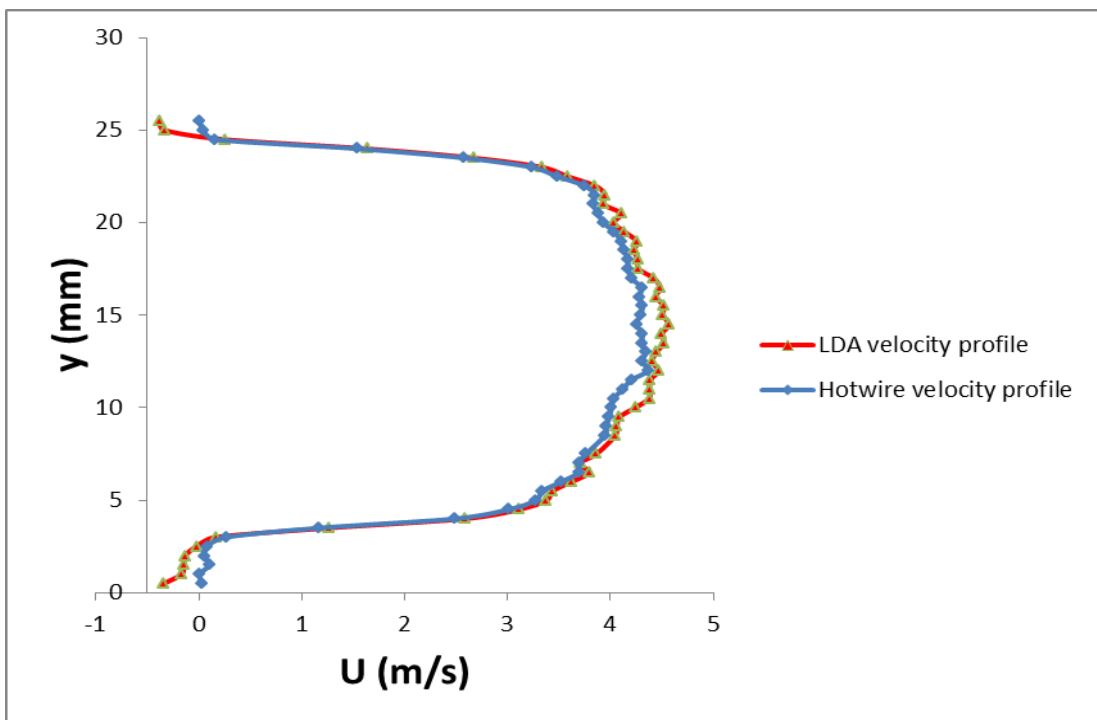
Figure 4-10 Hotwire and LDA velocity profile for 25mm square pipe at 0.3 mm downstream of the exit.

This value is adjusted only once and left untouched during calibration and data acquisition. Only if more accurate measurements are required, this can be done every time that the equipment is turned on. The hotwire system used in this study contains from 55P14 probe, MiniCTA 54T42 and StreamWare Basic software. Probe 55P14 is designed to measure one dimensional velocity. MiniCTA is a single channel anemometer optimized for moderate-speed airflow and low-speed water flow

measurements. Air velocities up to 100m/s and water velocities up to 2m/s can be measured Dynamics (2016). To calibrate the hotwire system used in this study, a primary test of velocity runs using the hotwire anemometer and AF210 anemometer at the same time by varying the mass flow rate to change velocity. The resulting curve used to calibrate the hotwire reading, for more accuracy the hotwire used to measure the velocity of a 25mm square pipe and the same test repeated at the same condition using LDA system with 10um seeding particles and the results are compared to each other as shown in figure 4-10. Since the probe used measured only one dimension velocity the difference between the Hotwire and LDA velocity profile could be noticed near the wall. However, the accurate measurement of flow velocities in the laminar sublayer and the buffer region with CTA probes requires additional efforts. To detect the zero point or the wall point a simple method was used. Since the manufactured surface is inserted into the disc and fixed to the upper wall of the duct, the best way to use the hotwire probe was to make a hole as close as possible to the manufactured disc. Then using a small piece of flat plate the hole was covered. Then the hotwire probe was inserted in the negative y –direction into the channel after being attached it to the unislide, allowing the movement of the probe in small increased until the prong tips make electrical contact with the flat plate. This point will be the surface point or the origin of the boundary layer. From this point, after moving the flat plate away, the probe move further down to the other end of the duct to precisely measure the duct height and mark the duct centerline for calibration purpose.

4.2.4 Laser Doppler anemometry

Laser Doppler Anemometry (LDA) is an optical technique to measure the velocity of particles convicted by fluid flow. The fundamental of the LDA is the shifted the frequency of the scatter light that is reflected by the moving objects. The frequency of the scattered light is shifted by an amount proportional to the speed of the object. So, one could estimate the speed by observing the frequency shift. Flow is seeded with small, neutrally buoyant particles that scatter light. The particles are illuminated by a laser at a known frequency of laser light. The scattered light is detected by a photomultiplier tube (PMT), and an instrument generates a current in proportion to the

absorbed photon energy, and then amplifies that current. The difference between the incident and scattered light frequencies is called the Doppler shift.
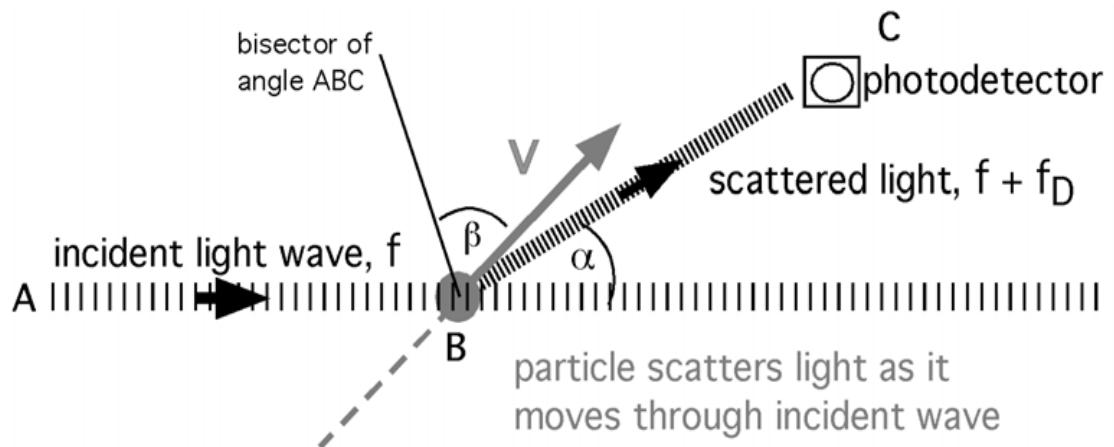
Figure 4-11 A particle moves through an incident light wave of frequency f and scatters light in all directions. The scattered light picked up by the photodetector will be shifted by f_D Durst et al. (1981).

The Doppler shift, f_D, depends on the speed, V, and direction of the particle motion, the wavelength of the light, λ, and the orientation of the observer. The orientation of the observer is defined by the angle α between the incident light wave and the photodetector [PMT]. The direction of the particle motion is defined by β, the angle between the velocity vector and the bisector of ABC as shown in figure 4.11 Durst et al. (1981)

$$f_D = \frac{2V}{\lambda} cos\beta sin\frac{\alpha}{2}$$ …………………………………………………………….. (4-11)

A direct way to estimate f_D is to measure the incident frequency, f, and the observed frequency, f_O, and find the difference. However, the Doppler shift is a very small fraction of the incident frequency, so this results in estimating a small value from the difference between two large values, a process with a high degree of uncertainty. To improve the estimate of f_D, a method using two incident beams has been developed. In this configuration, the incident beam is split into two beams of equal intensity. The beams intersect, and the point of intersection is the measurement volume. Particles that pass through the measurement volume scatter light from both beams. The frequency shift of the light scattered from each beam will be different because the orientation of the two beams relative to the photodetector and relative to the particle's velocity vector

are different as shown in Figure 4-12. That is, α and β defined in figure 4-12 are different for the two beams.

Let the Doppler shift for the two scattered beams be f_{D1} and f_{D2}, *i.e.* the scattered beam will have frequencies $f + f_{D1}$ and $f + f_{D2}$. Because f_{D1} and f_{D2} are both much smaller than f, the scattered light waves have a nearly equal frequency. When waves of equal amplitude and nearly equal frequency are superimposed, the amplitude of the resulting signal periodically rises and falls. This modulation is called a beat. The beat frequency is one-half the differences between the two original frequencies. Thus, when the two bursts of scattered light are superimposed within the photodetector, the resulting signal has a beat with frequency, $|f_{D1} - f_{D2}|/2$. As shown below, the beat frequency will be the Doppler frequency we seek Durst et al. (1981).
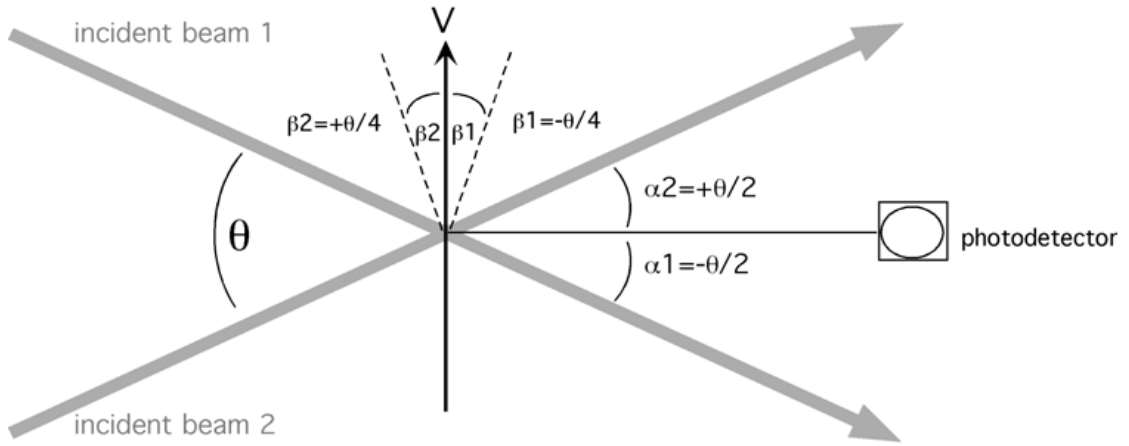
Figure 4-12 Beam and photodetector configuration for forward scatter, differential LDA Durst et al. (1981).

As an example, consider the geometry depicted in Figure 32. Using equation (4-11), the frequency shift for beam 1 is $f_{D1} = (2V/\lambda)\cos(-\Theta/4)\sin(-\Theta/4)$, and for beam 2 is $f_{D2} = (2V/\lambda)\cos(+\Theta/4)\sin(+\Theta/4)$. Because $\sin(-a) = -\sin(a)$ and $\cos(-a) = \cos(a)$, we see that $f_{D1} = -f_{D2}$, which is consistent with the symmetry of Figure 4-13. The beat frequency is

$$\frac{|f_{D1}-f_{D2}|}{2} = \frac{2V}{\lambda}\cos\left(\frac{\theta}{4}\right)\sin\left(\frac{\theta}{4}\right) = \frac{2V}{\lambda}\sin\left(\frac{\theta}{2}\right) \tag{4-12}$$

Comparison of the second term in equation (4-12) with the either f_{D1} or f_{D2} confirms that the beat frequency is the absolute value of the Doppler shift we seek. The same

result can be found for any choice of α, β, and θ *if* V is taken as the velocity component perpendicular to the bisector of beam 1 and beam 2.

Another useful way to interpret the signal recorded by the photodetector is regarding the interference fringe pattern generated at the beam crossing. The fringe pattern, shown in figure 4-13, consists of alternating zones of brightness and darkness. The fringe spacing, d_f, is the distance between sequential bright (or dark) zones.

$$d_f = \frac{\lambda}{2sin\left(\frac{\theta}{2}\right)} \quad \dots\dots\dots\dots\dots\dots\dots\dots\dots\dots\dots\dots\dots\dots\dots\dots\dots\dots\dots\dots\dots\dots\dots\dots\dots\dots\dots(4\text{-}13)$$
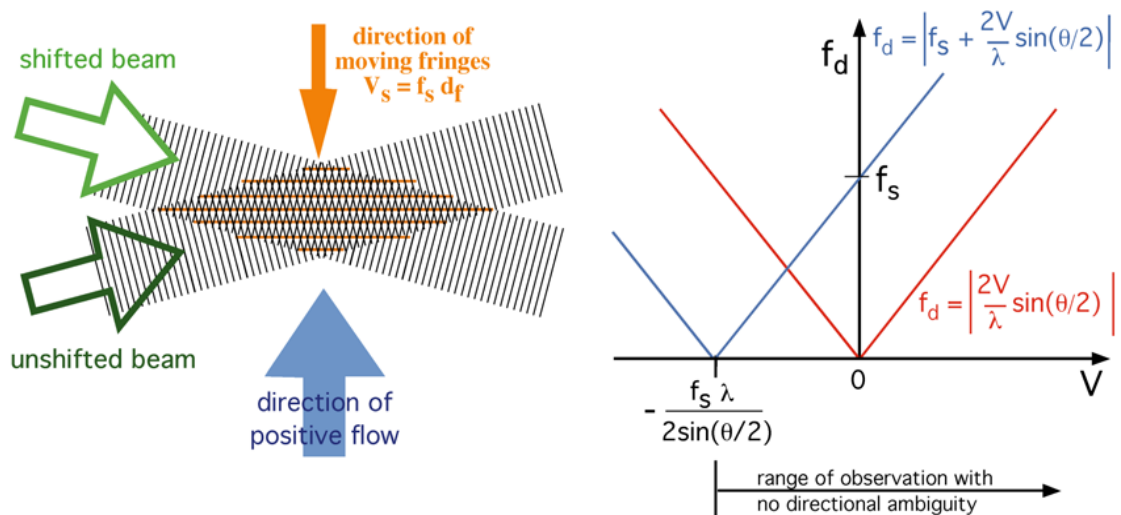
Figure 4-13, Removing directional ambiguity with frequency shifting Dynamics (2013).

As a particle crosses the fringe pattern, the intensity of the scattered light varies with the intensity of the fringes. Thus, the amplitude of the signal burst varies with timescale dF/V, where V is the velocity component perpendicular to the fringe pattern, *i.e.* Perpendicular to the bisector of the two incoming beams. The frequency of the amplitude modulation is thus,

$$\frac{V}{d_f} = \frac{2V}{\lambda} sin\left(\frac{\theta}{2}\right) \quad \dots\dots\dots\dots\dots\dots\dots\dots\dots\dots\dots\dots\dots\dots\dots\dots\dots\dots\dots\dots\dots\dots \ (4\text{-}14)$$

Which, by comparison with (4-12), is the Doppler frequency, f_D. Note that with the two beam system, the Doppler frequency is not dependent on the position of the photodetector, as the angles α and β do not appear in equations (4-14) or (4-12) Durst et al. (1981).

Note that the Doppler frequency depends only on the magnitude of V, not the direction, *i.e.* positive and negative values of V will produce the same Doppler frequency Figure 4-13. To correct this directional ambiguity, the frequency of one of the incoming beams is shifted by a known value, fs. This causes the fringe pattern to move at speed Vs= fs d_f toward the incoming unshifted beam Figure 4-13. The frequency recorded by the photodetector is now

$$f_d = \left| f_s + \frac{2V}{\lambda} sin\left(\frac{\theta}{2}\right) \right|$$ ………………………………………………………..(4-15)

And the sign of V is reflected in fd. That is, a particle moving through the fringes at speed V shifts the detected frequency, f_d, up (positive V) or down (negative V) from fs. To avoid directional ambiguity, $f_s > |(2V/\lambda)sin(\theta/2)|$, as shown in Figure 4-13. Thus, to optimise the system, a different shift frequency will be required for different flow conditions. An acoustic-optical device called a Bragg cell generates the required frequency shift.

4.3 Numerical Solution

As introduced in this chapter, an LES in-house code called Hydro3D is used to calculate and simulate the flow characteristics such as velocity distribution, velocity fluctuations, vortices, shear stress and pressure gradient depends on the studied cases. The Hydro3D has been validated through many internal and external flows Stoesser et al. (2010); Bomminayuni and Stoesser (2011); Kara et al. (2012); Papanicolaou et al. (2012); Kara et al. (2014); Kim et al. (2014); Kara et al. (2015) Kara et al. (2015); Cevheri et al. (2016); Fraga and Stoesser (2016); Fraga et al. (2016).

4.3.1 Numerical model and solution method

The basic equations to be solved are the Navier –Stokes equations. For an incompressible fluid flow the filtered equations are Cevheri et al. (2016):

$$\frac{\partial u_i}{\partial x_i} = 0$$ …………………………………………………………………….(4-16)

$$\frac{\partial u_i}{\partial t} + \frac{\partial (u_i u_j)}{\partial x_j} = -\frac{\partial p}{\partial x_i} + \frac{1}{Re}\frac{\partial^2 u_i}{\partial x_i \partial x_j} - \frac{\partial \tau_{ij}}{\partial x_j} \quad \dots\dots\dots\dots\dots\dots\dots\dots\dots\dots\dots\dots(4\text{-}17)$$

Where x_i and x_j are the spatial location vectors (i.e. x_i and x_j = x, y ,z for i and j = 1,2,3), u_i, u_j (i, j = 1,2,3) are the resolved velocity components in x−,y− and z−directions, respectively, normalized on the reference velocity U, and p is the resolved pressure divided by the density. Re = UL∕ν is Reynolds number, where ν is the kinematic viscosity, and L is the reference length scale Cevheri et al. (2016).

In LES for the incompressible flows, scales smaller than the grid size are not resolved but counted for through the subgrid scale tensor τ_{ij}. Most subgrid scales modelling are based on an eddy viscosity assumption to model the subgrid tensor Nicoud and Ducros (1999a). In this work, the WALE model was used to model the small scale fluctuations. WALE is a model in which the subgrid viscosity is dynamically worked out with the square of the velocity gradient tensor rather than resolved through strain rate in a Smagorinsky-type model. This velocity tensor not only accounts for the effects of both strain and rotation rate of the smallest resolved turbulence fluctuations but also recovers the proper $O(y^3)$ near-wall scaling for the eddy viscosity without requiring the dynamic procedure. Its model coefficient is proved to be a relatively constant value ($C_w^2/C_s^2 \approx 10-12$). Also, the WALE model is invariant to any coordinate translation or rotation and, no test-filtering operation is needed Huang and Li (2010). This makes the model able to calculate zero eddy viscosity in laminar shear flows automatically. The eddy viscosity calculation, the method to couple the pressure and velocity and solving the Poisson equation using Fourth −order accurate approximations is fully explained in Cevheri et al. (2016). Also, Hydro3D is parallelized domain decomposition, dividing the computational domain into a number of smaller sub-domains.

4.3.2 Local Mesh Refinement

In the present work, the computational meshed domain was performed in three levels, coarse to a fine mesh. A 2:1 reduction in mesh size between neighbouring levels was performed on the staggered computational grid to implement LMR in critical areas, Figure 4-14.
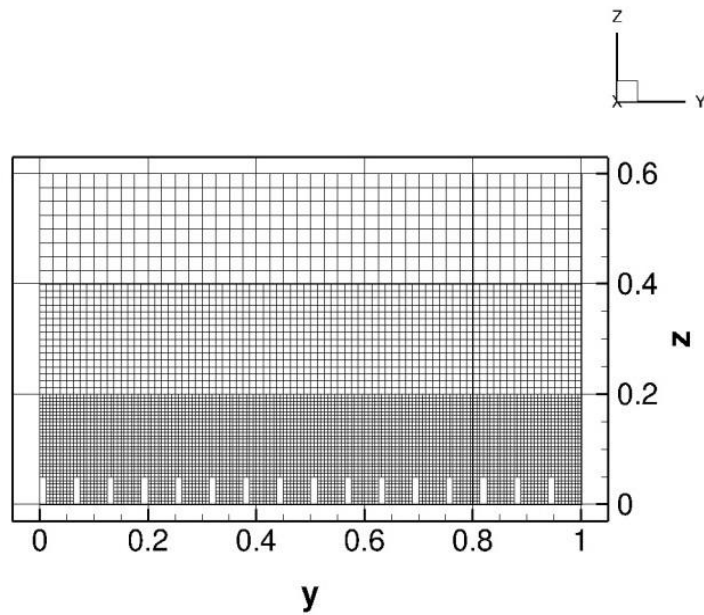
Figure 4-14 Local mesh refinement of the computational domain

Ghost cell method was used to ensure the accuracy of pressure and velocity values in the interface between coarse and fine meshes. In this method, all cell centers exteriors to the body are computed with fluxes at the four surrounding cell edges. For pressure, values from the coarse grid cells are quadratically interpolated. Then another quadratic interpolation to calculate fine ghost pressure is applied. The edge-centered of the fine grids are calculated, and the arithmetic average of the fine-grid pressure is taken as the coarse grid pressure gradient to enforce the continuity of the gradient across the interface. For velocity, the case is slightly more complicated since the calculation and interpolation should be done for the tangential and normal velocities. Full details of the procedure are covered by Cevheri et al. (2016).

4.3.3 Computational Domain and Boundary Conditions

The computational domain was designed to represent a turbulent flow over different riblets which aligned with the direction of the flow. No slip condition was assigned to the bottom boundary of the computational domain. Upper and side boundaries are considered as slip condition to eliminate the wall effect on flow over the studied area of the real duct. The inflow was taken as a fully developed turbulent flow by running the computation for approximately 8 convective time units, which represent the time needed to flow to go through the duct, (tu_τ/δ , where u$_\tau$ is friction velocity, δ is half channel height and t is interval time which is taken as 0.001 sec.) using a periodic condition in inflow to ensure a fully developed turbulent flow. The Reynolds number was calculated based on δ and bulk velocity. For the comparison and to verify the code, Reynold number was varied from 4500 to 13500, which is close to the work performed by Martin and Bhushan (2014). In the streamwise direction (along x-axis), the computational domain span is 10δ and the cross sectional span (y-axis) is ≈ 3.3δ with the wall-normal direction (z-axis) being 2δ. Since, Hydro3D is a parallelization code and to employ LMR, the main computational domain was divided to 36 smaller sub-domains in three levels of refinement. LMR was applied to these sub-domains on bases of 1:2 to move from a coarse mesh for domains far from the wall to a finer mesh in domains near the vicinity to the wall, Figure 4-14. The total meshes at each level are shown in Figure 4-15. Also using immersed boundary method which enables the code to deal effectively with sharp edges and complex geometries combined with LMR and MPI features in Hydro3D make it the best choice to simulate the flow over riblet rather than software packages such as ANYSIS.
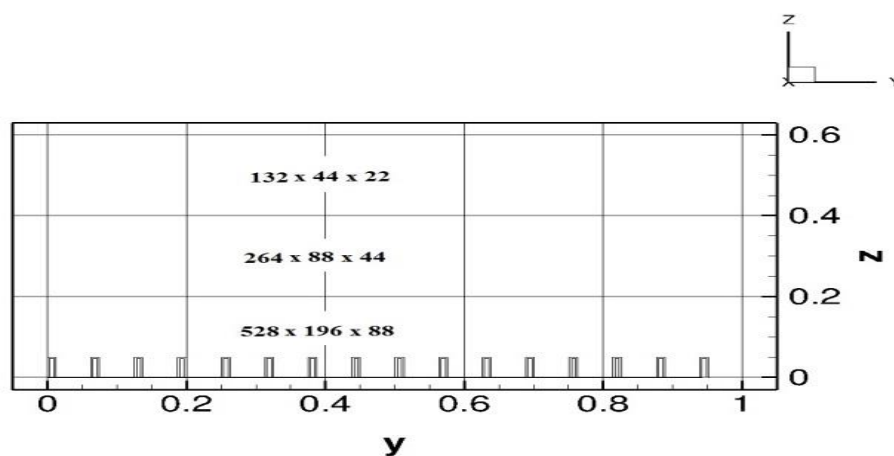
Figure 4-15 Grid resolution

4.3.4 Riblet model

Different models of blade riblets with a different h/s ratio were numerically tested. The riblet height was kept constant for the most models at h=200μm to have a non-dimensional height of $h^+ \approx 10$ as tabled by Martin and Bhushan (2016a) for optimum drag reduction. Also, the blade riblets thickness was kept to a minimum, as the thickness plays a significant role in drag reduction at t= 12.5μm. The space between riblets was varied to have three different s^+ (17, 23 and 34) to test the code results as the optimum s^+ were reported by many researchers from 15-20 Bixler and Bhushan (2013b). The riblet part was partially applied to the computational domain in order to further study the flow before, over and behind the riblets, Figure 4-17.

Figure 4-16 Riblet position in the computational domain.

CHAPTER 5

RIBLET MANUFACTURING METHODS

5.1 Introduction

Nature shows many lessons on the creation of adaptive techniques to survive in harsh or competitive environments. One of these lessons, which inspired the aerodynamics engineers are the drag reduction on sharks using small riblets, covered its skin. Riblet sizes range from species to species and from location to location on sharks. For reference, the Spiny Dogfish shark Squalus acanthias has triangular shaped riblets with a base width of 100 to 300 μm, summit radius of about 15 μm, the height of 200 to 500 μm, and spacing of 100 to 300 μm (Jung and Bhushan (2010). Such dimensions represent a big challenge to fabricate, especially when metallic materials are used. Riblets have been fabricated with a variety of polymers and metals using various fabrication and assembly processes. The actual process depends on many factors, such as costs, geometry configuration, durability, precision, accuracy, base material, experimental set-up, chemical compatibility, and sample set size. Feasible riblet fabrication techniques include using metal shims Bechert et al. (1997), machined acrylic Bechert et al. (1997); Dean and Bhushan (2012), machined aluminium Walsh et al. (1984); (Samira Sayad Saravi 2014), extruded/coextruded polymer Marentic F. J. (1986), embossed polymer Marentic F. J. (1986), soft lithography Jung and Bhushan (2010); Bixler and Bhushan (2012), photolithography Friedmann (2010), wet and dry etching Friedmann (2010)Friedmann (2010)Friedmann (2010)Friedmann (2010)Friedmann (2010)Friedmann (2010)Friedmann (2010)Friedmann (2010)Friedmann (2010) , grinding Denkena et al. (2010), rolling Thome and Hirt (2007), and laser etching Bixler and Bhushan (2013b, 2013a). In general, blade and scalloped riblets are less durable than sawtooth riblets, and continuous riblets are easier to fabricate than segmented. Furthermore, photolithography is preferred for producing the most accurate two-dimensional riblet geometries but can be cost prohibitive Martin and Bhushan (2016a). However, the number of studies that used metallic riblets is a few due to the complexity of manufacturing technology to manufacture riblet on hard

material accurately, therefore most researchers scaled the riblet up to avoid these limitations Walsh et al. (1984); Bechert et al. (1997), or milling medium strength alloy material such as aluminium 6082 Samira Sayad Saravi (2014). However, the target of this work is to apply microstructure geometries inside burner tube, which is by necessity made from high strength stainless steel.

In this chapter, the techniques used to produce bio-inspired regular surface roughness are presented. More specifically, Electrical Discharge Machining (EDM) techniques are reviewed, and novel design and construction methods of different geometry riblets using Wire EDM are described. Finally, a description of stainless steel woven wire meshes is given, as their simple and cheaply produced structure will be tested for the first time to alter Boundary Layer and consequently control flashback.

5.2 Electrical Discharge Machining

EDM processes remove metal by discharging electric current from a pulsating DC power supply across a thin interelectrode gap between the tool and the workpiece. The gap is filled with a dielectric fluid, which becomes locally ionised at the point where the interelectrode gap is the narrowest-generally, where a high point on the workpiece comes close to the high point on the tool. The ionisation of the dielectric fluid creates a conduction path in which a spark is produced. The spark produces a tiny crater in the workpiece by melting and vaporisation, and consequently tiny, spherical "chips" are produced by resolidification of the melted quantity of workpiece material. Bubbles from discharge gases are also produced. In addition to machining the workpiece, the high temperature created by the spark also melt or vaporise the tool, creating tool wear. The dielectric is pumped through the interelectrode gap and flushes out the chips and bubbles while confining the sparks. Once the highest point on the workpiece is removed, a subsequent spark is created between the tool and the next highest point, and so on. Literally, hundreds of thousands of sparks may be generated per seconds J T Black (2013).
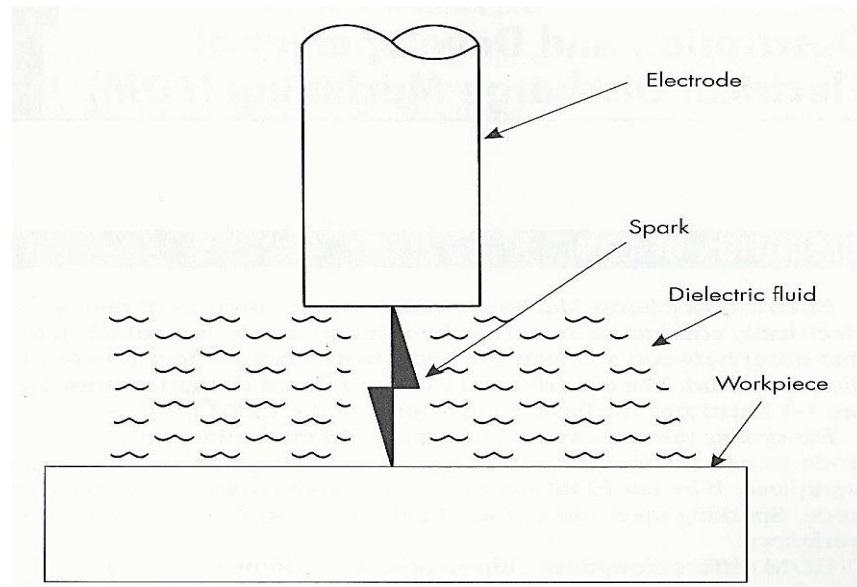
Figure 5-1 Basic components of EDM Jameson (2001)

The EDM process can be used on any material that is an electrical conductor. The melting point and latent heat of melting are important physical properties that determine the volume of metal removed per discharge. As these values increase, the rate of material removal slows. The volume of material removed per discharge is typically in the range of 10^{-6} to 10^{-4} mm^3. Since the process does not involve mechanical energy, the hardness, strength, and toughness of the workpiece material do not necessarily influence the removal rate. The frequency of discharge or the energy per discharge is usually varied to control the removal rates, as are the voltage and current. The rate and surface roughness increase with increasing current density and decreasing frequency of sparks Serope Kalpakjian (2008).

The EDM process has become the workhorse of the tool making industry for the precise machining of the workpiece that can conduct electricity. It can produce holes or cavities of the complex cross-section and to almost any depth in fully hardened steels or tungsten carbide with relative ease Benjamin W. Niebel (1989). In the context of the research presented here, this capability of structuring hard material is essential due to the expected applications in combustion systems, in which the burners operate under high temperature, pressure and acoustics level, especially during the flashback phenomenon.

There are three main types of EDMs that can be used to produce the required structures; the ram, the wire-EDM and the EDM milling. Each is used to produce very small and accurate parts, and the first two can be used to produce large items like automotive stamping dies and aircraft body components. The largest single use of EDM is in die making. Materials worked with EDM include hardened, and heat-treated steels, carbide, polycrystalline diamond, titanium, hot and cold rolled steels, copper, brass, and high-temperature alloys. However, any material to be machined with the EDM process must be conductive.

5.2.1 RAM EDM

In ram EDM, the electrode/tool is attached to the ram which is connected to one pole, usually the positive pole, of a pulsed power supply. The workpiece is connected to the negative pole. The work is then positioned so that there is a gap between it and the electrode. The gap is then flooded with the dielectric fluid. Once the power supply is turned on, thousands of direct current or DC, impulses per second cross the gap, beginning the erosion process as in figure 5-2. The spark temperatures generated can range from 14,000° to 21,000° Fahrenheit. As the erosion continues, the electrode advances into the work while maintaining a constant gap dimension Benjamin W. Niebel (1989).

The finished EDM workpiece can exhibit several distinct layers. The surface layer will have small globules of removed workpiece metal and electrode particles adhering to it, which are easily removed. Ram EDM machines are also known as diesinkers or vertical EDMs. They range in size from table top models to large CNC units. In general, the Ram EDM is preferred for it is features such as the ability to:

- Work on small pieces that could be damaged from excess cutting tool pressure.
- Work on delicate sections and weak material due to no direct contact with the material.
- Work on extremely hard material and very fine tolerance.
- Needless set up time due no tools required.

- No worries of size changing at heat treatment, since the process is burned into hardened materials.

However, A major issue with this EDM strategy is that when trying to produce small features at the micro scale, significant wear occurs on the tool and it's shaping quickly deviates from the original ones Surleraux et al. (2016), which make the production of accurate features difficult. Therefore this technique was not selected to produce the riblet designs required for this PhD study, but for future work, the Ram EDM could have a potential to provide some complex in difficult workpiece areas such as the entrance of the pipes or part of the internal walls or even inclined geometries.

5.2.2 Micro EDM milling

To produce microscale features, μEDM milling tends to be the preferred machining strategy because proven methods exist to mitigate the influence of tool wear on the final result Bissacco et al. (2011).

The low mechanical strength of the micro milling tools makes machining a three-dimensional micro mold using a traditional fabrication method very difficult. The EDM offers a solution from such problem. Although the EDM is precise in manufacturing tiny details, the electrode wear represents the main reason for not using complex tool geometries. However, these problems can be resolved using a simple shaped electrode that moves along a designed 3D tool path. There have been some reports on 3D EDM using a simple electrode Yu et al. (1998).
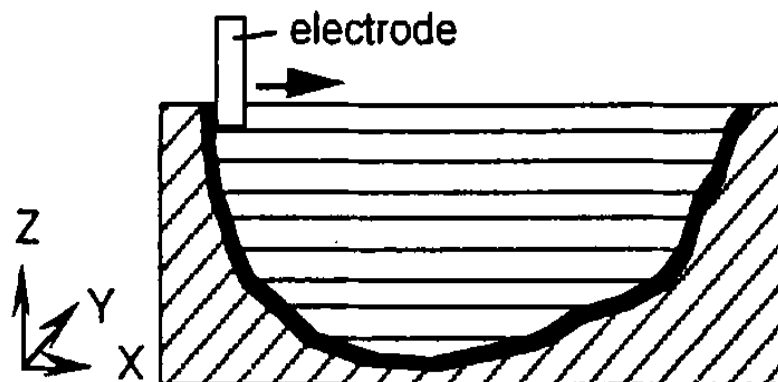
Figure 5-2 Dry EDM working principles Yu et al. (1998).

For the purpose of this PhD study, this technique could produce the relevant structures accurately. However, due to the low removal rate and considering the relatively large surfaces that would need to be textured, this process would not be cost effective and highly time-consuming and was therefore not used in this investigation. However, this would be considered in future works.

5.2.3 Wire EDM

Another EDM strategy that is promising for the production of the structures required for this PhD study is called Wire EDM. This process uses a consumable, electrically charged wire to affect very fine and intricate cuts. The process is particularly useful in cutting fine details in pre-hardened stamping, and blanking dies. A wire drive system constantly presents fresh wire to work, so electrode wear is not a problem. Typical wire diameters range from 50 to 300 μm.
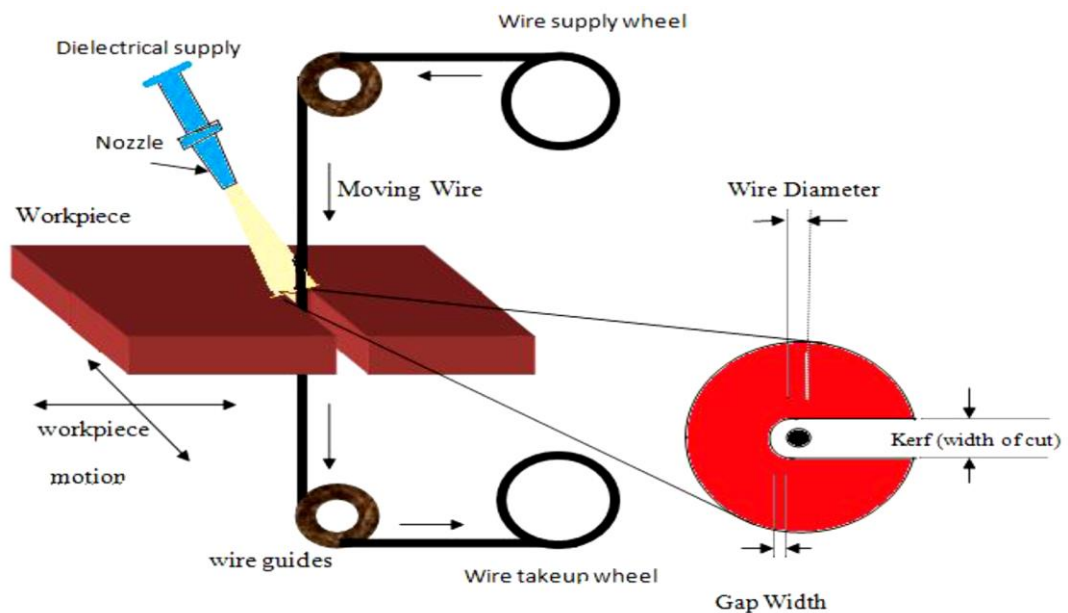
Figure 5-3 Working principles of WEDM Sreenivasa Rao M (2013).

Because the fresh wire is constantly brought to the cutting zone, the wear on the tool can be ignored, and accurate microscale features can be produced in relatively large areas.

However, these wires will produce a kerf slightly larger than their diameter depending on the discharge power used. For example, figure 5-4 shows a 300 μm wire leaving 380 μm kerf, due to an additional gap of 80 μm produced by the electrical sparks.
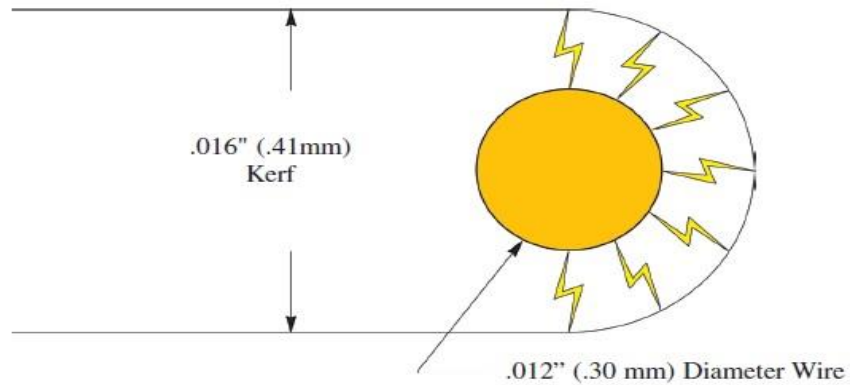
Figure 5-4 Wire kerf Benjamin W. Niebel (1989).

Wire EDM's can run for long periods without operator attention. Also, it can produce a sharp edge on the outside of a corner, but it will always leave a small radius on inner corners as shown in figure 5-5. The size of this radius is determined by the wire diameter plus the spark gap Benjamin W. Niebel (1989). Finally, another important part of the strategy to be considered is that a single machining is usually performed using a combination of cuts following a similar path with the same wire but with varying energies. It would start with higher energy, and consequently larger spark gap, to remove the majority of the material, and finish with lower energies (smaller spark gap) to produce smoother surfaces and achieve tighter tolerances.
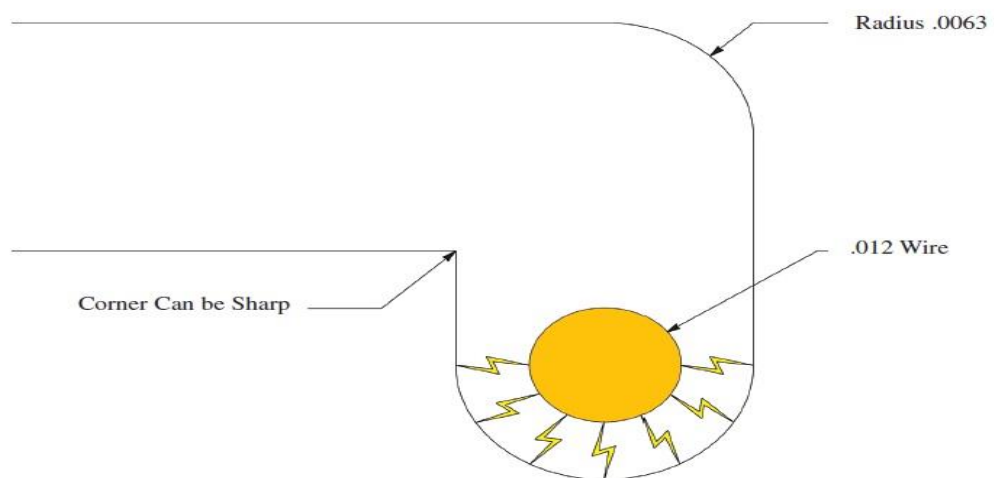
Figure 5-5 inside and outside corners.

This is the EDM strategy that was selected for this investigation. In the next section, a new Wire EDM strategy is described to enable the production of complex 3D textures.

5.3 Design of micro riblet structures for WEDM

The key aim of the project was to replicate the flow effects of shark skin and lotus leaf microsurfaces. Therefore, the main concept was to produce similar shapes to those seen in nature, and that had been numerically tested as shown in the previous chapter.

Due to the WEDM cutting principle, the type of structure it can achieve is limited to ($2^{1/2}$D) features, which means only extrude 2D feature to a third dimension, shown in section 5.3.1. In the following section, a new method using multiple cuts performed sequentially after rotating the part to a specific angle for each cut is introduced to allow the production of more complex 3D structures.

5.3.1 Design of $2^{1/2}$D microstructures

As will be described in chapter 6, the simulation results showed that the blade result has the best drag reduction compared to another shape. However, in practical application, the manufacturing of stainless steel blade riblets are nearly impossible due to the cutting tool geometry which is a wire and also the gap between the wire and the workpiece which is needed for a spark to remove material and the electrode to flush the debris away.
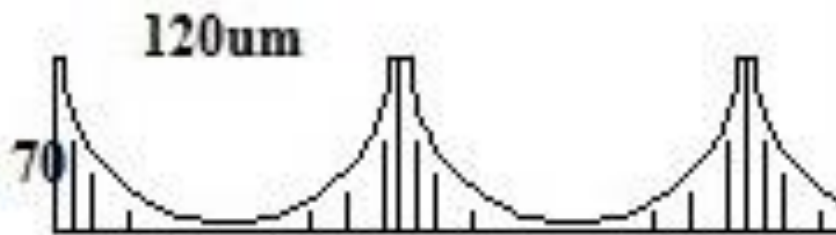
Figure 5-6 scallop riblets.

On the other hand, the blade riblet structure is very weak due to the thin base and high height to base dimension. So from other numerically tested shapes, the scallop riblet has been chosen for manufacture. The scallop riblets are simple shapes like half circles channels aligned together to provide tips and valleys. The wide base of the riblet makes

it more preferable for long term applications. Also, the circular shape of the valley fits with WEDM output figure 5-6.

In riblet design, the key geometries are riblet space (s), riblet height (h) and riblet thickness (t). The first two geometries are the most important since the mechanism of the drag reduction on riblets depends on the size and depth of the valley that riblets made. However, to make the studies on riblet more general and free of geometry restriction, dimensionless geometries are introduced as explained in chapter 3. The dimensionless geometries are $s^+ = \frac{su_\tau}{v}$ and $h^+ = \frac{hu_\tau}{v}$, where u_τ the frictional force and v the kinematic viscosity. So, the design should achieve the drag reduction with optimum geometries could be obtained and taking in accounts manufacturing errors that could happened such as tolerances, power intensity etc... The best drag reduction could be obtained when s^+ in range between 12-21 and h$^+$ around 10 for blade, scallop and saw shape riblets Bixler and Bhushan (2013a). The range of dimensionless geometries gives the opportunity to calculate the range of spaces under constant velocity application or the range of the velocity at constant riblet dimension. In this study the velocity will be ranged from 5-15 m/sec. which mean u_τ range between 0.055425 to 0.142 m/sec. the average riblet space (s) calculated from $s^+ = \frac{su_\tau}{v}$ will be around 110 μm. and average height (h) around 75μm.
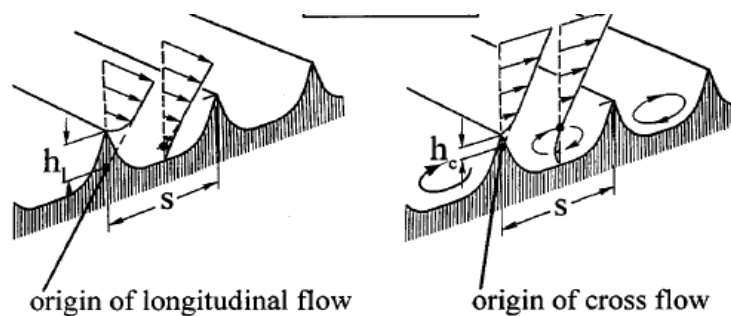
Figure 5-7 Longitudinal and cross flow on a ribbed surface.

Using the single orientation machining, it was possible to test the smallest feature achievable using the design shown in Fig. 5-6, namely 130μm wide riblets. A depth of

65μm was set to maintain an optimal depth-width ratio of 0.5. Fig. 5-8 shows the resulting structure.

Although the numerical results show that the best microstructure shape to achieve highest drag reduction is the blade, the limitation of the WEDM in corners and the kerf make this scalloped design the most basic shape that could be achieved as shown in figure 5-8.
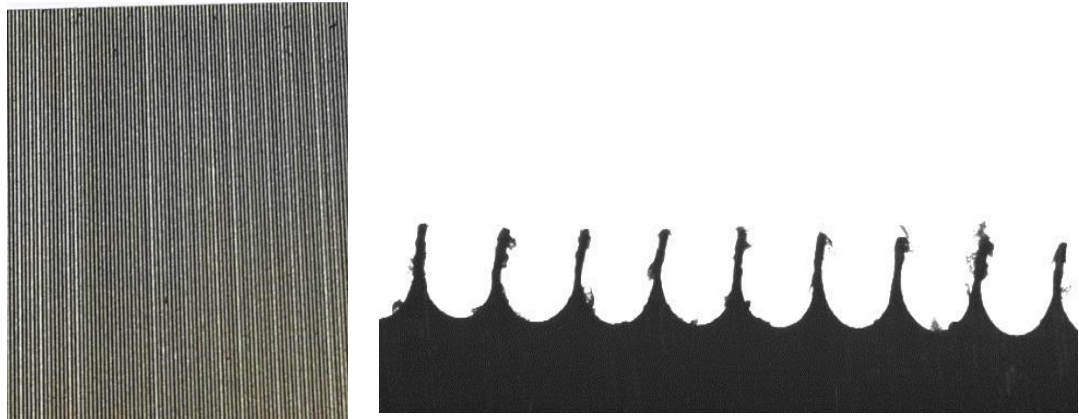
Figure 5-8 the scallop micro structure on stainless steel small disc. Scalloped surface (left), scallop section (right).

This strategy is the standard in WEDM but to produce more complex structure a new approach was designed for multiple workpiece orientations. This approach in described in the next section.

This design considered as the base design for more complex design such as diamond, lotus and shark skin riblets.

5.3.2 Design of 3d microstructures

For the other structures, the aim was to try and replicate the lotus leaf and shark skin textures, with the limitations of the WEDM process, to produce truly 3D structures rather than a 2-1/2D structure. The key reasoning was that drag effects are 3-dimensional and therefore the textures should provide turbulence reduction in both the streamwise and cross-flow directions by being positioned at a suitable angle to avoid energy losses. To achieve this, multiple wire passes were performed after rotating the

circular stainless inserts thus providing some 3-dimensional complexities to the textures or more complex shapes, which are derived from this basic shape, the shape of the textures was defined on Solidworks initially to explore the capabilities of the proposed process. This was achieved by creating a pattern of cuts on the surface of a blank model, then creating additional patterns of cuts on different WEDM machining orientations as shown in figure 5-9. Figure 5-9 shows the key designs that were produced; one inspired by lotus leaves, and two by shark skin with one more complex than the other.
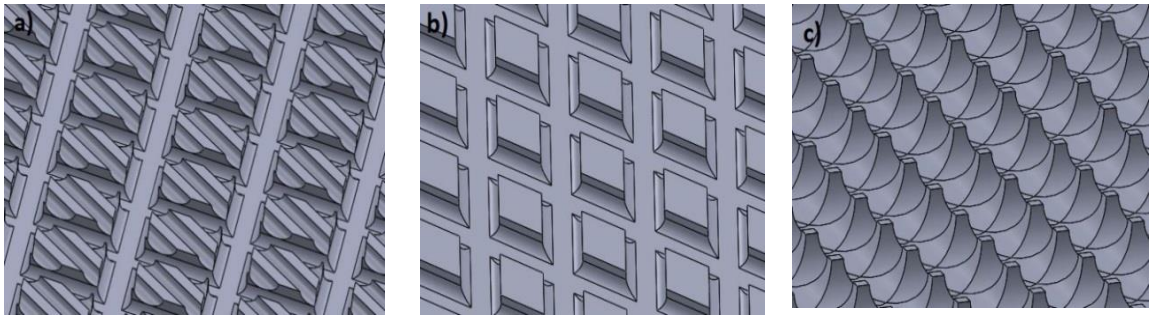
Figure 5-9 Texture designed a) Shark skin, b) Diamond, c) Lotus.

The lotus design aimed to imitate the fine pins of lotus leaves with two close perpendicular cuts. While the diamond and shark skin designs imitate the natural shark skin denticles with the two cuts at 60° to each other; these were deep relative to the width in order to make the denticles protrude more as would be seen with natural sharkskin. The shark skin design additionally has a smaller, 3rd cut through the 30° plane which attempts to model the small riblets on the denticles in nature. By having these complex shapes, it was theorised that they would provide the turbulence reduction in both the streamwise and cross-flow directions, and positioned at a suitable angle they would not cause the benefits at either flow direction to be lost. The key reasoning was that the drag effects are 3-dimensional and therefore the textures should accommodate for this, along with the intention that design features could be identified that would improve 3D riblet design. However, the approximate dimensions of the riblets were derived in first place from the numerical tests, that been done before the manufacturing process. As explained before the numerical simulation approach work into a two-way working method, which verifies the numerical code ability to adopt a solution to the physical approach of the flow over sharkskin textures. By comparing the numerical result with the experimental result for the same basic geometries and from there moving to simulate more complicated geometries, which could be manufactured based on

available machining technology. For most sharks, the riblet scales are 0.2-0.5mm in size and 30-100μm in spacing apart Martin and Bhushan (2016b). Based on these facts and taking into accounts the WEDM machine available in the university a wire with 100μm in diameter was used. The aim was to produce a groove as narrow as possible. For the lotus texture, this was kept at 130μm with a depth of 65μm. However, due to the need of deeper grooves for the diamond and shark skin textures, the grooves were set at 260μm width with 130μm depth. This was particularly important for the shark skin texture as it would have the 3rd cut, for which the grooves could not be smaller than the Lotus texture's grooves. These maintained the optimal depth-width ratios of 0.5 Bechert et al. (1997). The spacing between grooves was minimised for Lotus, being 25μm, while for the diamond the spacing was 280μm which was also used for the shark skin. The 3rd, smaller set of cuts on the shark skin was set to align grooves at positions of 25%, 50% and 75% along the denticles.

The number of wire EDM processes that could be run at different orientations was also considered, with three as a reasonable maximum that could attain the desired geometries. It was also considered that if trying to keep the grooves at the size and spacing where meaningful drag reduction could be achieved, a 4th cut would reduce too much metal, resulting in a texture that could be fragile.

5.4 Manufacturing strategy for selected design

5.4.1 Workpiece Design

The basic idea of experimental work is to put manufactured surfaces with microstructures in the small duct and blow air through the duct. Using hotwire anemometry and LDA system to track the changes in near wall sublayer, to do so it essentially to have a necessary length required to build a boundary layer thickness that could be accessible by LDA at the same time the length of the micro-surface should be kept as minimum as possible to reduce the cost. As the velocity inside the duct is taken to be 5-15 m/s depends on flow rates, the Re number will be around 4300-13000. Due to the high cost of constructing micro structuring the constructed part should be at the minimum length and to reduce the effect of the wire stress on the outcome shape Liang

and Liao (2014). From another hand, the constructed surface should be as long as possible to build a boundary layer with a thickness that covers the structure, by assuming that the minimum thickness is 1 mm at the minimum velocity 5 m/s. from equation (5-1) Lautrup (2003):

$$Re_\delta = \frac{U\delta}{v} \approx 5\sqrt{Re_x} \qquad\qquad (5\text{-}1)$$

Where, Re_δ is Reynolds number based on boundary layer thickness, U is the stream velocity in m/s, δ boundary layer thickness, v is kinemativ iscosity of fluid and Re_x is local Reynolds number. From the equation (5-1) the minimum Re_x needed to build up 1 mm boundary layer thickness is about 4100, since $Re_x = \frac{Ux}{v}$, the minimum length is:

$$x = \frac{vRe_x}{U} \approx 15 \text{ mm}$$

This value was rounded to 25mm to use a standard material size and a diameter that could be more easily manufactured. To produce this, a 30mm diameter stainless steel bar was cut into lengths of 27mm, and all but the last 10mm was narrowed to 25mm. The texture could then be manufactured on the 25mm face. This allowed the part to sit within the larger disc; into which a 25mm hole was cut with a tolerance to ensure a tight fit but that it was easy to insert/remove parts. Figure 5-10 shows the insert and the large disc.

Figure 5-10 manufactured surface insert and the large disc.

5.4.2 WEDM using single workpiece orientation

A Ø 100µm wire was used as a cutting tool, and due to the discharge gap the smallest achievable feature identified was 130µm. A small gap is linked to a smaller discharge energy and consequently to the smaller removal of material and longer machining times, making it almost impossible to cut through the bulk of a workpiece.

Thus, for each produced structure, the inserts top surface was first machined "flat" with the highest energy to efficiently align the top surfaces to the wire axis, a process which requires the removal of a significant amount of material as shown in figure 5-11.
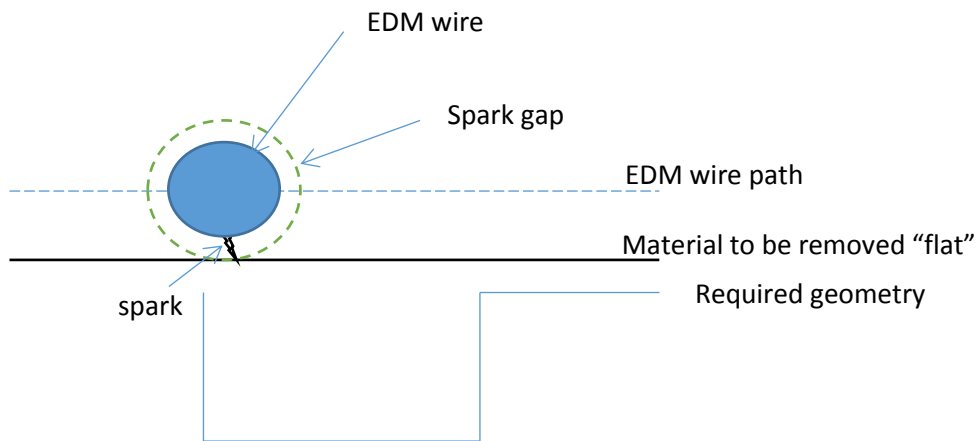
Figure 5-11 Wire path in "flat" process.

Six other "flat" cuts were then performed with gradually smaller energy and smaller discharge gaps to achieve a better surface finish as shown in figure 5-12. A final cut following the required profiles was then performed with the smallest energy with a targeted roughness around 200nm Ra, assuming this would ensure that the flow would be affected mainly by the tested geometries and not by the roughness. An average surface roughness of 200nm Ra measured using a White light interferometer.

EDM wire

Spark gap

EDM wire path
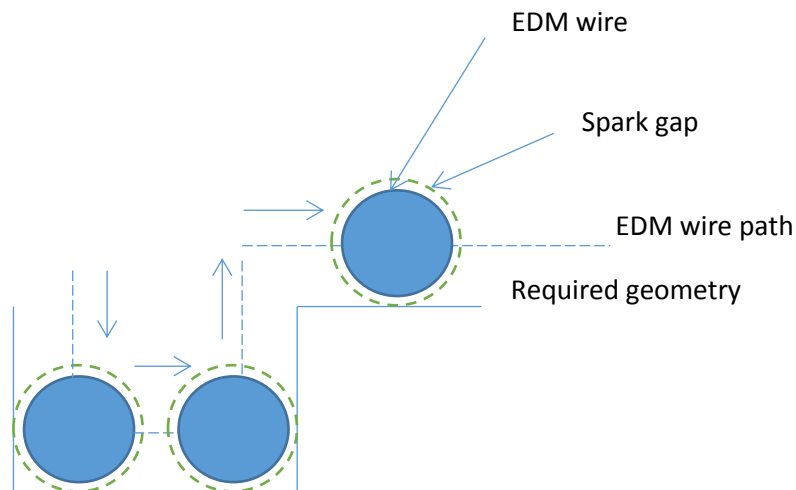
Required geometry

Figure 5-12 Wire path during the cutting process.

However, because the WEDM using electrical sparks to remove material without direct contact between the wire and the workpiece the minimum obtained geometry will equal wire diameter plus the two spark gaps. Also, the wire will leave unremoved material at the sharp corners as shown in figure 5-13.

Corners left due the wire
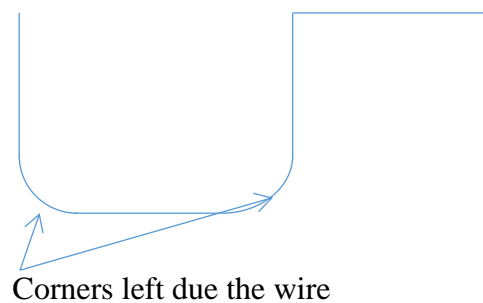
Figure 5-13 left material at the corners after WEDM process.

The final obtained geometry was a scalloped surface with grooves 110-130μm in space and 100μm in depth and the thickness of 8-15 μm as shown in figure 5-14.
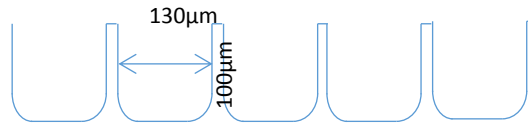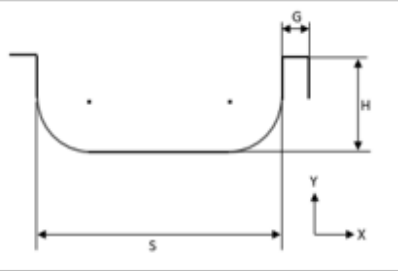
Figure 5-14 final geometry obtained.

While this was simple as it only required four lines of code per groove/riblet, the scale of these in comparison to the workpiece meant that there were many instances, the maximum being 182 for the lotus texture. Also, if any amendments needed to be made to a line of code, the whole program would have to be rewritten. To make code writing quicker, an excel spreadsheet was specifically produced in order to automatically generate the code based on the simple parameters. It was built to accommodate a range of variables:

☐ Width of groove

☐ Width of riblet

☐ Depth of groove

☐ Number of instances

☐ Offset from edge for the program to initialize

Figure 5-15 G Code for diamond: a) The spreadsheet producing code from variable inputs b) the generated code in plotter

5.4.3 WEDM using multiple workpiece orientations

To accurately define the angles of machining to obtain the textures desired, a jig was designed and manufactured. It needed to fix the insert in place at a variety of angles and for setting and changing the angle to be a straightforward procedure. The resulting design involved the insert having two M4 screw holes on the top; one in the centre and the other offset by 8mm figure 5-16.
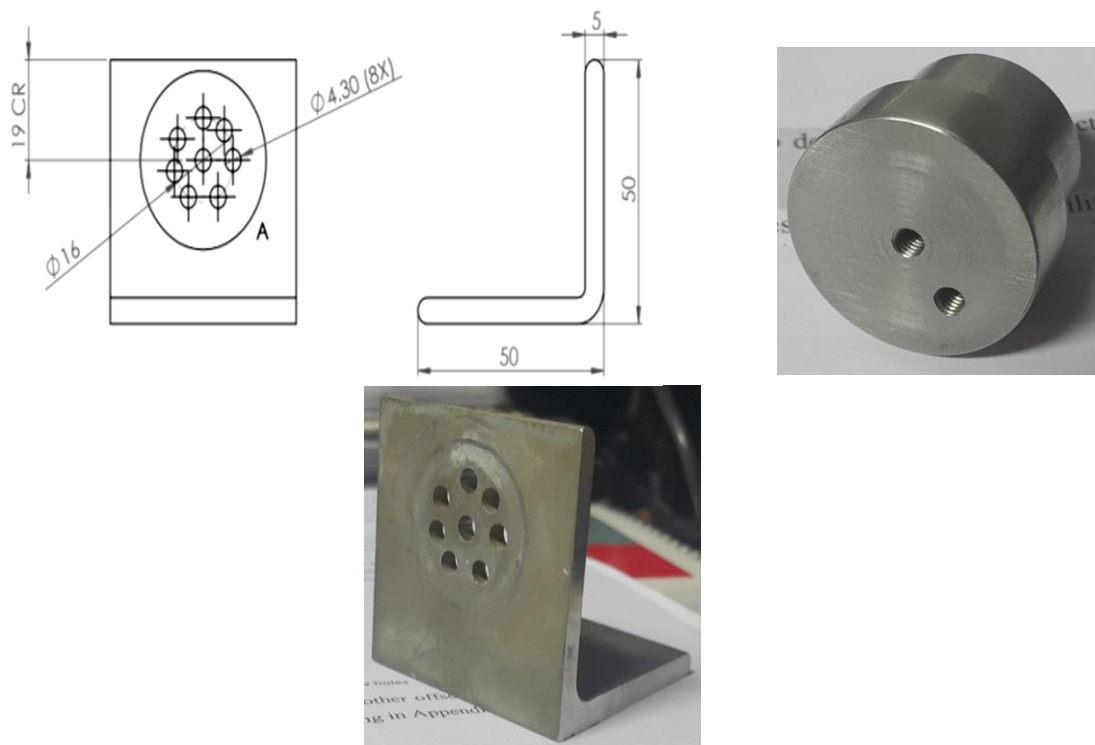
Figure 5-16 Angle jig design

The jig itself comprised of an L-shaped piece of stainless steel, with a set of holes on one face. There was a centre hole, and then a range of holes along the 8mm circumference which could be used to set a range of angles figure 5-16. Angles were positioned at 15° intervals as this would allow access to some interesting and diverse shapes.

Due to the holes being 4.3mm on this small circular array, it was not possible to have the holes all in order up to 90° (i.e. going clockwise 0° then 15° then 30° and so on), as they would overlap and interfere with each other. This could lead to the material around this area wearing away after usage. Therefore, some holes were relocated to the

opposite sides because the cut goes right through the face of the workpiece making any cut symmetrical Figure 5-17. For example, there is no need to define 150° as 30° will produce the same effect, and using the same logic, 75° could be defined with a hole at 105°.
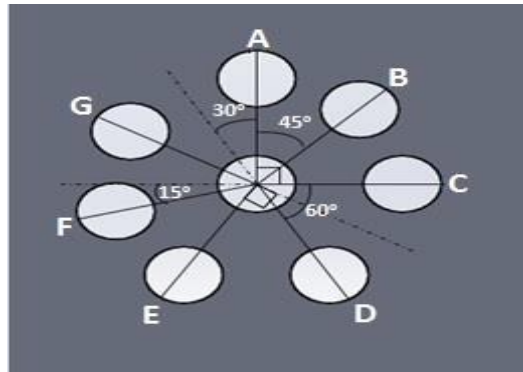
Figure 5-17 the layout of holes.

The angles available with the jig were 0°, 15°, 30°, 45°, 60°, 75° and 90°. While some of these were not required for this project, they were included on the jig to allow for future research to utilise a wide range of angles.
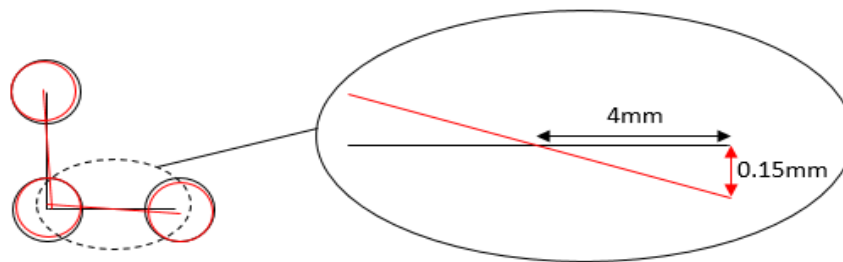
Figure 5-18 potential of error when setting the position of parts.

The holes are cut with 4.3mm diameter, meaning if one of the M4 screws is aligned centrally then there will be a 0.15mm radial gap surrounds it. This was to give tolerance to ensure screws could easily be applied and removed. However, it meant there would be a potential precision error with the angles set figure 5-18. Using trigonometry, this produces a 2.15^o rotational displacement for each setting, but as making an angle between two cuts is two settings, this could become a maximum of 4.3^o.

The insert screwed onto the jig with the centre screw fixing the insert in position and the offset screw being used to set the angle desired. When changing angles, the centre screw was retained with the offset screw removed then reapplied once the part was rotated. This ensured easy fixing and secured the part when changing the angle.

5.5. Analysis of manufacturing Results

The manufactured parts were measured with an Optical Coordinate Measuring Machine (CMM), a Mitutoyo Quick Vision Accel Pro. This equipment connected to a PC workstation and used a high resolution charged coupled device (CCD) camera with magnification to observe the microstructure. The given accuracy by the manufacturer is 1.5μm Mitutoyo (2012).

The first manufactured geometry was the scallop as explained before. Two scallops patched on a flat plate and stainless steel rod was manufactured with different sizes; the first one was a square patch with 87mmx87mm in width and height respectively and the second one was a 25 mm circular patch on rod diameter. For the patch on a flat plate, The close pictures to the structure at the upper and lower edge of the plate show a difference in depth of the structure, also a difference in riblet tip, where more sharp tips seen in lower edge as shown in figure 5-19. The difference between up and down of the output shape mainly caused due to stress on the cutting wire. The stress generated due to moving electric spark between the start and end of the working piece of the cutting tool (wire) Liang and Liao (2014). The dimensionless space (s^+) and depth (h^+) varies on the shear velocity at the wall. However, for scallop geometry, the variation in dimensionless geometries was not big and still in optimum values range except the lower edges at high velocities, where the wide space between riblets could lead to habitat a local flow vortices causing an increase in drag.

| Up | Down |
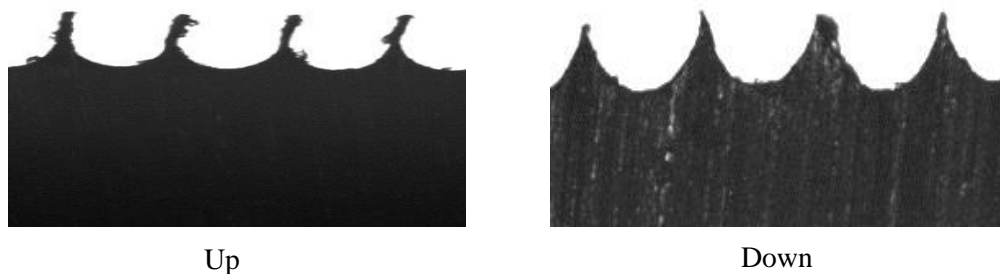
Figure 5-19 up and down structure of the scallop geometry.

However, the second patched of scallop was manufactured on 25mm circular part to reduce the manufacturing cost and to avoid the change in dimensions. The small

dimension of the new part limited the stress force in the wire, which results in no significant changes between the upper and lower edge of the patch. Table 5-1 shows the dimension of the two scallop patches the error in manufacture of scallop riblet were around 8% in width and 11% in depth and 32% for thickness.

Table 5-1 the dimension of the scallop riblets.

No	Patch dimension (mm)	Width (μm) avg.	s^+	depth (μm) avg.	h^+	Thickness (μm) avg.	t^+
1	87 x87 upside	110	11.5-24	70	8-20	20	2.8-6
1	87 x87 down	130	13.5-35	100	11-25	10-15	1.4-3
2	25 mm diameter	110	11.5-24	80	9-22	20	2.8-6

The other complex geometries (Diamond, lotus and sharkskin) were investigated in more details. The diamond texture figure 5-20 produced visually correct, with the distinctive shape clearly visible. However, there were some discrepancies in the geometry Table 5-2.
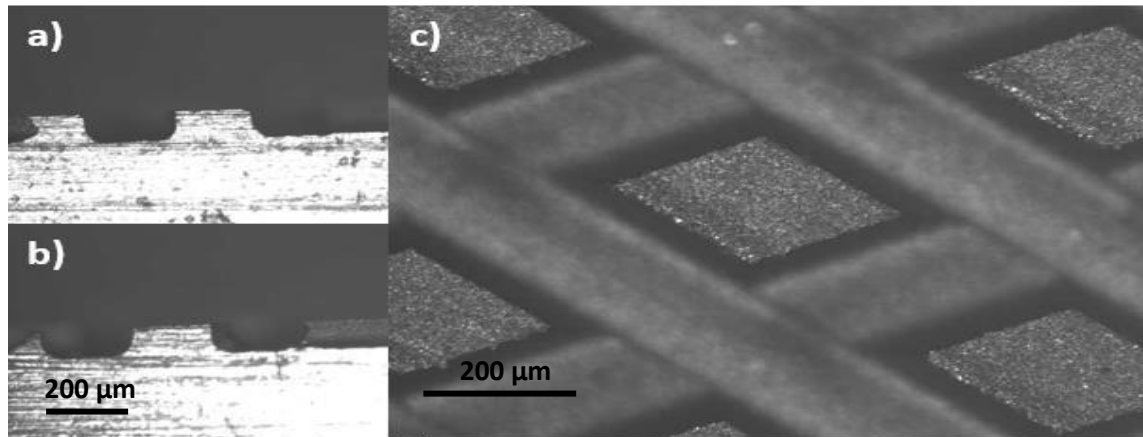
Figure 5-20 Dimond surface in different cuts a) 1st cut b) 2nd cut c) top view

Although these were consistent for each cut, and if this is repeatable, it could be corrected in the CNC program. The key issues that could affect the effectiveness of the texture produced on the flow were a difference in the groove depth between the two cuts, and the grooves themselves being much wider than intended. The larger groove causes the fluid vortices to go deep inside the riblet valley and increase the wetted area and increase the drag reduction as a consequence, especially at high fluid velocities. The only data available for diamond riblet are extracted from a numerical simulation.

However, the boundary layer thickness was measured using hot-wire anemometry and show good matching with numerical results at low velocities, both shows a reduction in boundary layer thickness around 5%, but the results diverted at high velocities. The diverting in velocity profile (boundary layer thickness) is a result of the sharp edges of the diamond geometry which lead to separate the flow and generate vortices that settled inside grooves and increase the chaotic of the flow.

Table 5-2 Measurement taken from Diamond

Diamond		Intended	Measured	% error
1st cut	Width of groove (µm)	260	306.2	17.7 %
	Depth of groove (µm	130	144.6	11.2 %
	Width of riblet (µm	280	247.6	11.5 %
2nd cut	Width of groove (µm)	260	312.2	20.1 %
	Depth of groove (µm	130	124.5	4.2 %
	Width of riblet (µm	280	241.9	13.6 %
	Angle Between cuts (deg)	60	61	1.7 %

In terms of geometric accuracy, the lotus texture figure 5-21 had the least magnitude of error, apart from the significant reductions in the riblet widths Table 5-3. The design did aim for fine pins, which were achieved, although figure 5-21c shows how many of these did not materialise or may have been too fragile. To the right of this figure, the peaks of
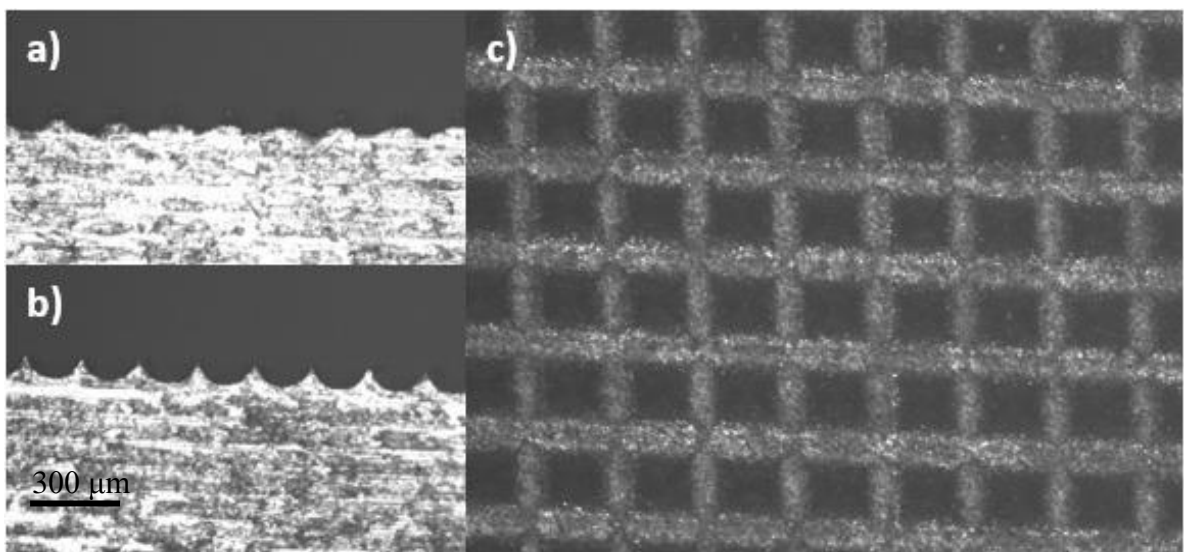
Figure 5-21 Lotus surface in different cuts a) 1st cut b) 2nd cut c) top view

the pins are visible, but this is not the case at other points in the figure 5-21b. As for the diamond geometry, the data available was only from numerical solution. Furthermore, the simulated geometry is slightly different from the manufactured one where the depth increased to 85µm to avoid code crashing. However the experimental results were more close to the numerical results as compared to the diamond geometry results as will be shown later in chapter 7, but the structure was weak, and many usage damages are seen in the patch.

Table 5-3 measurements taken from Lotus texture

Lotus		Intended	Measured	% error
1st cut	Width of groove (µm)	130	143.6	10.5 %
	Depth of groove (µm	65	49.3	24.2 %
	Width of riblet (µm	25	10.7	57.2 %
2nd cut	Width of groove (µm)	130	151.4	16.5 %
	Depth of groove (µm	65	65.8	1.2 %
	Width of riblet (µm	25	7.3	70.8 %
	Angle Between cuts (deg.)	90	86	1.7 %
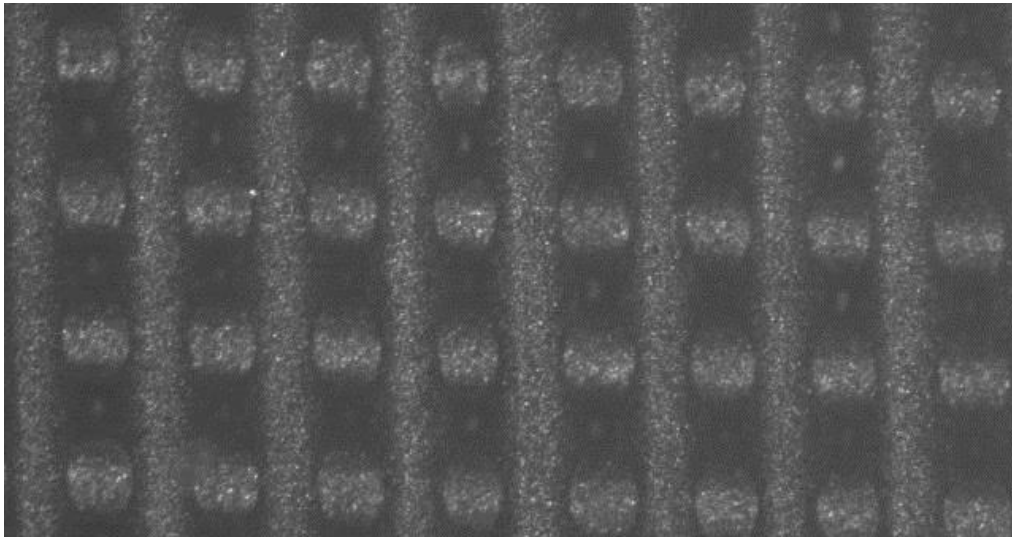
Figure 5-22 Top view of Lotus texture at the edge of work piece.

Aspects observed on the lotus texture that did not feature on the diamond were that towards the edges the texture had degraded, and the riblets/pins were heavily worn. Also as seen with the diamond texture, there was a depth difference between the cut. For the lotus texture, this was around 40µm. Manufacturing of the shark skin texture

was not as successful as diamond and lotus figure 5-23. The geometry was out by a high degree of error in almost every measurement Table 5-4, and it was unrecognisable visually. There was a height difference of 20μm between the two main cuts, and the depths of the grooves were only half what they should have been. The isothermal experimental results in small duct flow show that the obtained geometry shows more dragging to the flow and cause more turbulence and represents more roughness compare to the flat plate. The increasing in turbulence attributed to the large error in manufacturing.
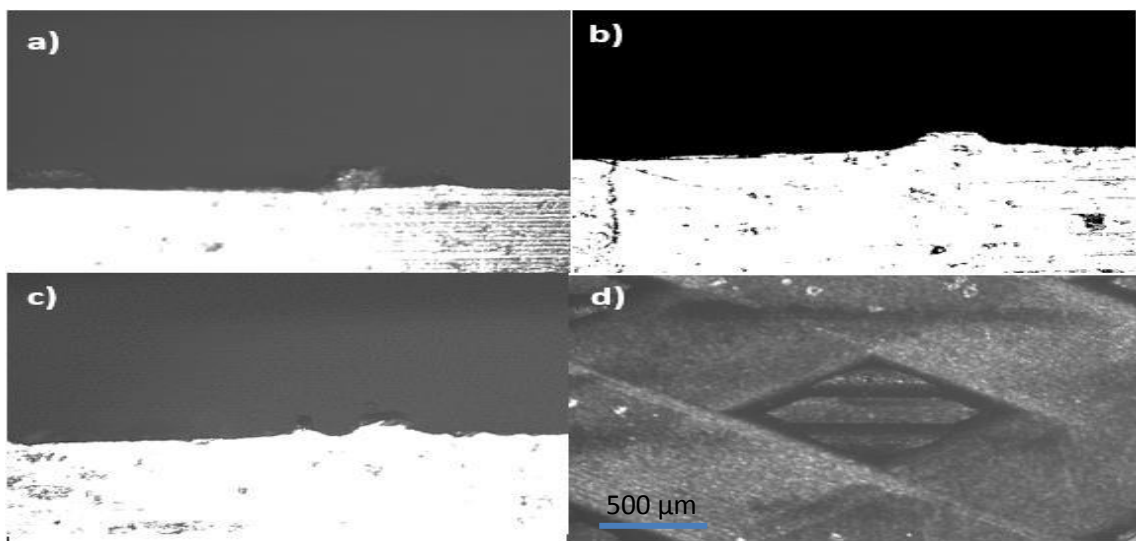
Figure 5-23 Shark skin texture under microscope a) Profile of 1st cut, b) Profile of 2nd cut (contrasting applied to improve visibility), c) Profile of 3rd cut, d) Top view

Table 5-4 Measurement taken from shark skin.

Shark		Intended	Measured	% error
1st cut	Width of groove (µm)	260	589.2	126.6%
	Depth of groove (µm	130	81.4	37.4 %
	Width of riblet (µm	520	219.8	57.7 %
2nd cut	Width of groove (µm)	260	375.8	44.5 %
	Depth of groove (µm	130	66.4	48.9 %
	Width of riblet (µm	520	225.8	56.6 %
3rd cut	Width of groove (µm)	130	113.6	12.6 %
	Depth of groove (µm	69	72.0	10.8 %
	Width of riblet (µm	95.16	90.2	5.2 %
	Angle Between cuts 1& 2 (deg)	60	61	1.6 %
	Angle Between cuts 1 & 3 (deg)	30	28	6.7 %

There was also an effect on the edge Figure 5-24, where it appears that the 3rd cut went into the grooves of the first two cuts, despite the fact that this cut was only designed to be half as deep.
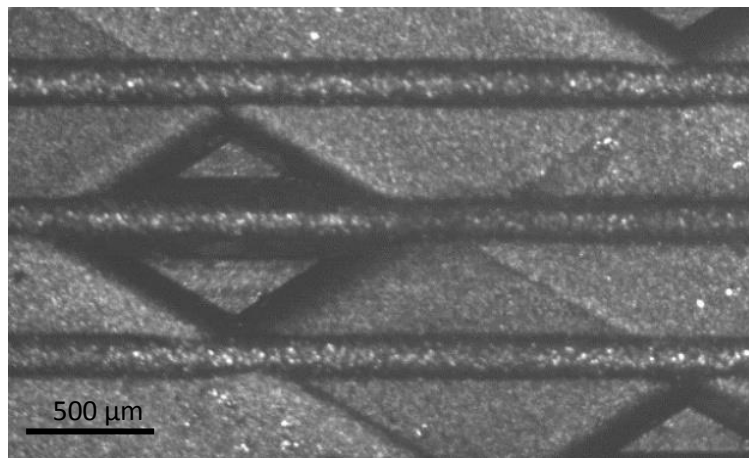
Figure 5-24 Top view of the edge of the shark skin texture.

The geometrical results above were used to evaluate which geometry could be constructedd inside the burner nozzle, also the numerical results were evaluated based on the manufacturing limitations which suggest that the scallop riblet is the most reliable choice.

5.6 Riblet Construction on Nozzle

Achieving the goal of this study requires applying riblet manufacturing process to the burner nozzle. From the numerical and experimental results obtained from different geometries and study the limitations of geometries, the scallop geometry is the best to construct. However, the construction of the scallop riblet shows that the length of the patch is very important to avoid the manufacturing error due to stress, which leads to change in space and depth of the riblet between top and bottom of the workpiece. Based on results the height of the nozzle was chosen to be no more 25mm. A stainless steel burner nozzle was cut. The internal diameter was 59 mm and height was 50mm, then the nozzle was cut horizontally into two pieces 25mm each; one piece was milled to increase the internal diameter to 61mm, the other piece was manufactured with WEDM to construct a patch of scallop riblet to the entire inner wall, and the final internal diameter was 61mm too as shown in figure 5-25.

The two nozzles were fitted to combustion rig in combustion lab. Due to the safety issues, only isothermal tests were conducted. The flow in combustion rig is swirl flow, which is very complicated flow, and using the same concepts of channel flow is not accurate and the numerical code support only the channel flow. So the solution was to experimentally measure the flow using the two nozzles and compare the results to find
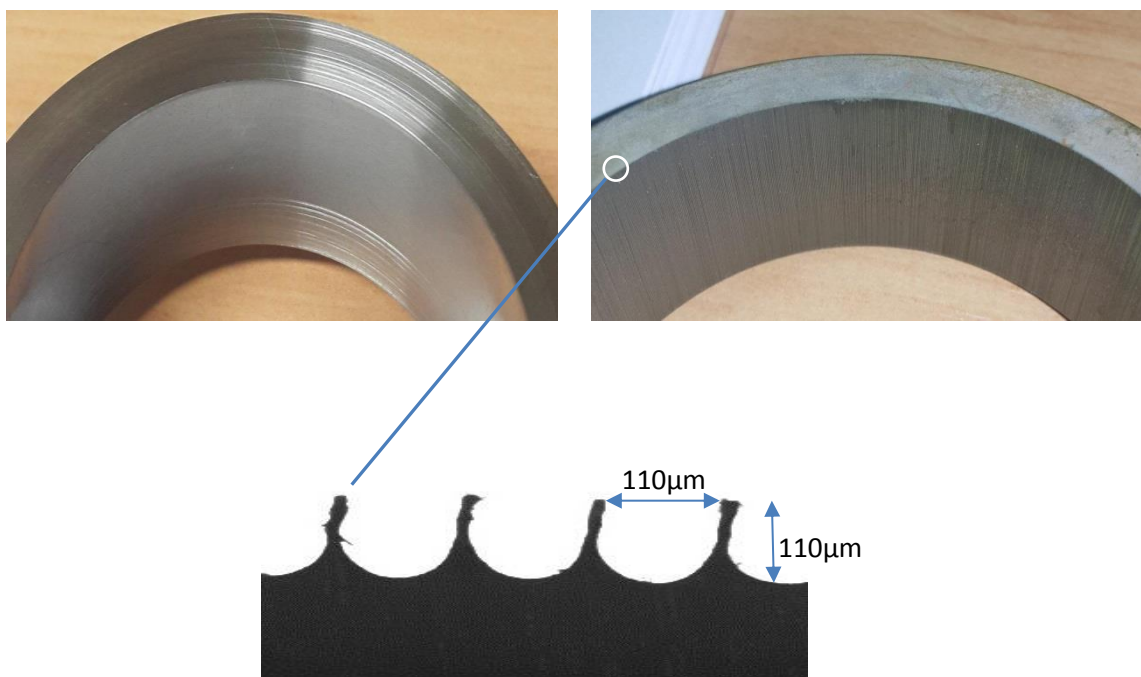
Figure 5-25 the burner nozzle: no riblet (up left) with scallop riblet (up right) the resulting structure (down).

out the effects of the riblet. The results show good improve in velocity gradient near the wall which supports the idea of this work. The full results and discussion will introduce in details in chapter seven of this thesis.

5.7 Wire mesh

The numerical results of the diamond and lotus geometries are promising for the reduction of boundary layer. However, these structures can be costly to produce and it can difficult or even impossible to introduce them inside a nozzle.

However, this led to a novel idea. It was noticed that the surfaces of wire meshes presented some structural similarities with diamond and lotus geometries. It was therefore decided to test woven stainless steel meshes, as they are relatively simple to manufacture and would resist high temperatures.

Two woven stainless steel grids or micro meshes were used. The mesh wire diameters were 50 μm and 150 μm and same pitch. The grids make a liner as shown in figure 6-26; the liner thickness was scanned by Shared Labs Europe LTD (2017). The wire mesh structure provides small solid holes that trapped the air inside and helped to make a fluid cushion that separates the high-velocity region and the wall. Using trapped air
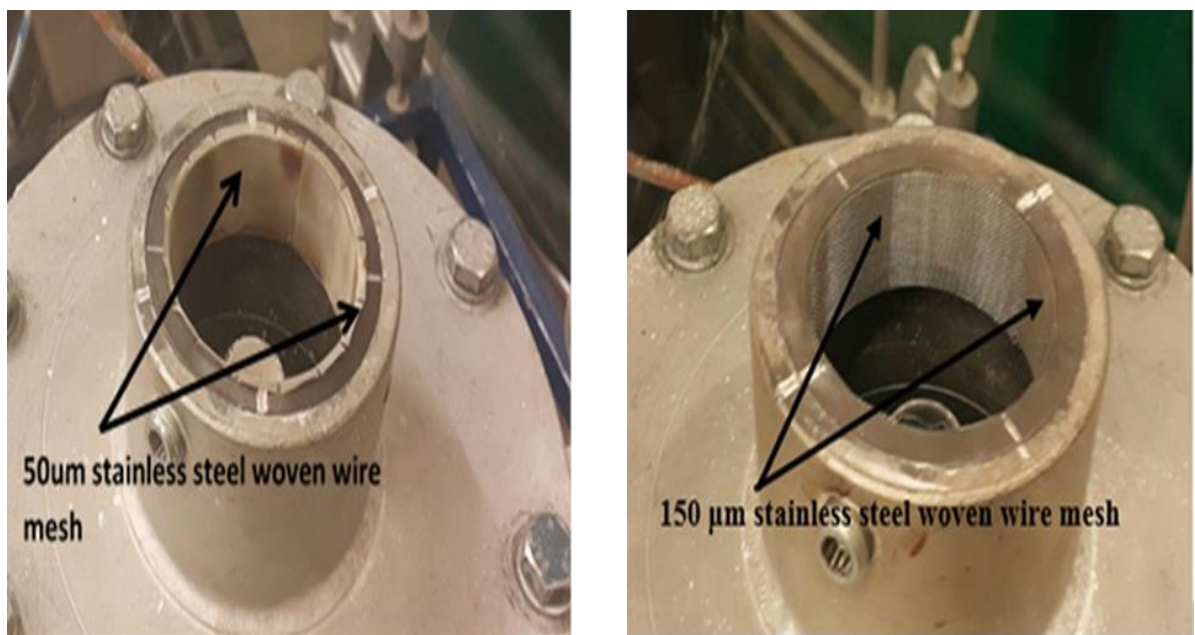
Figure 5-26 nozzle stainless steel woven wire liner.

bubbles to reduce drag is reported by Kwon et al. (2014). Figure 6-27 shows the geometrical scan of the wire mesh with 150 μm by Shared Labs Europe LTD (2017).
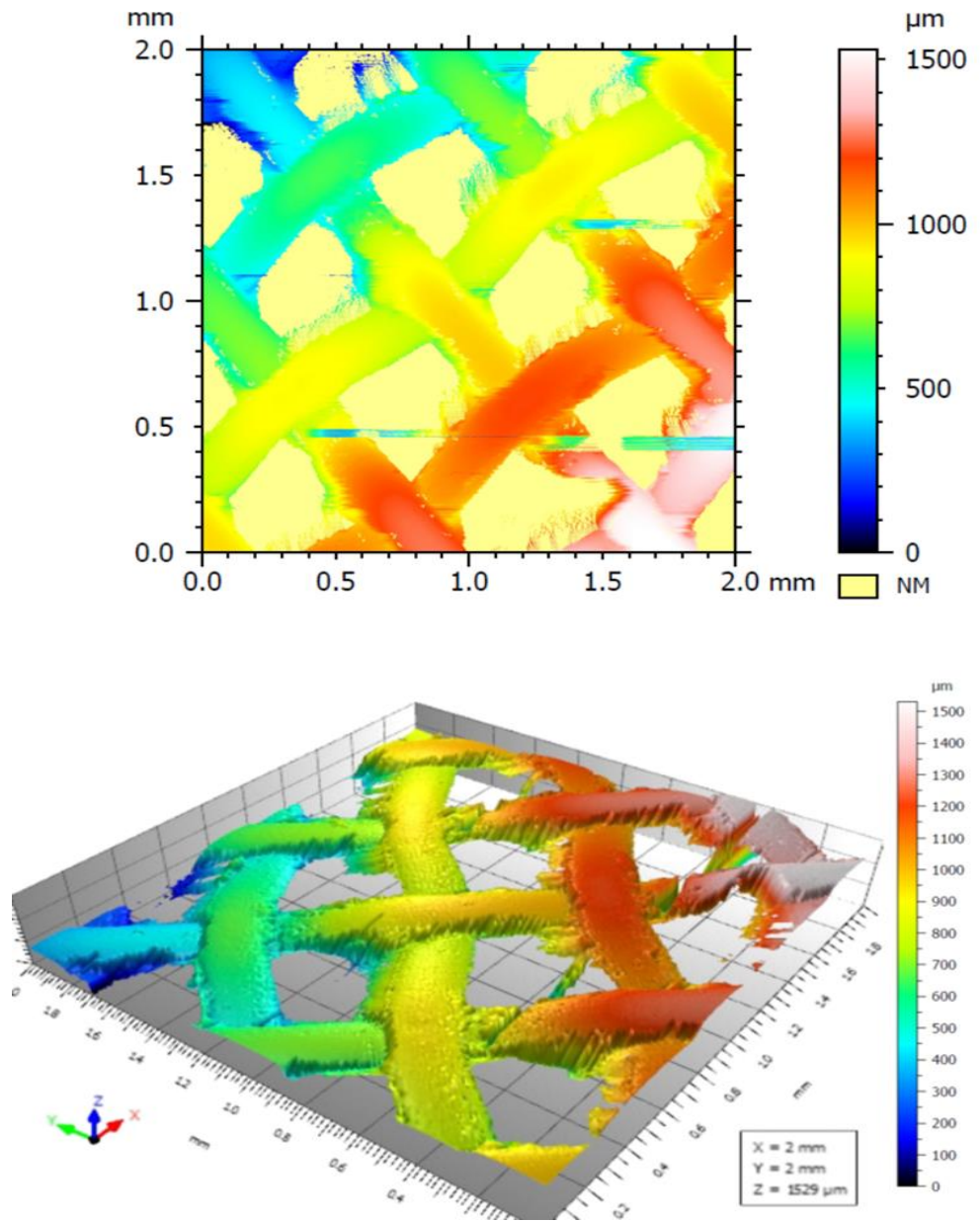
Figure 5-27 geometrical dimension scanned by

5.8 Summary

WEDM was used to produce different micro structured patterns on 25mm discs. A jig was especially designed to help in producing more complicated patterns more efficiently and cost effectively. Also, a scallop riblet pattern was constructed on the burner nozzle using WEDM. Finally, as the more complex patterns could not be produced inside the nozzle by WEDM, a novel idea using stainless steel woven wire meshes with different wire diameters was implemented to introduce regular roughness with more complex structures inside the burner nozzle.

CHAPTER 6

NUMERICAL RESULTS

6.1 Introduction

As described in chapter four, Hydro3D was used to investigate characteristics of a flow passing over different riblet shapes. In this chapter, the results will be assessed based on the way that logically connects all numerical and experimental tests.
The investigated riblet shapes were divided into three groups:

1- Verification group: two basic and widely reported riblet geometries (blade and saw shape (triangle)) were tested under the same condition of an experimental study by Bixler and Bhushan (2013a) to verify the code accuracy.

2- Modelling group: based on the manufacturing technologies available at the University and it's limitations, a scalloped design was numerically tested and was compared to the verification group results.

3- Manufactured group: a scalloped geometry and three other geometries that are extended from scallop design (diamond, lotus, and sharkskin) were numerically and experimentally tested.

6.2 Computational Domain and Input Parameters

The computational domain was taken as a small duct with 3.0cm x 1.0cm x0.6cm in length, width and height respectively. Then, the main domain was divided into 36 sub-domains. Dividing the main domain will help Hydro 3D features to work effectively. The first feature is the LMR (Local Mesh Refinement), which enables to refine the mesh near solid surfaces or near the wall. The second feature is the parallelisation, which divides a computational domain to small sub-domains and processes each sub-domain or group of sub-domains by a single processor at the same time. A riblet patch

was located at 1.0 cm from the inlet and has the same width of the channel as shown in figure 6-1.
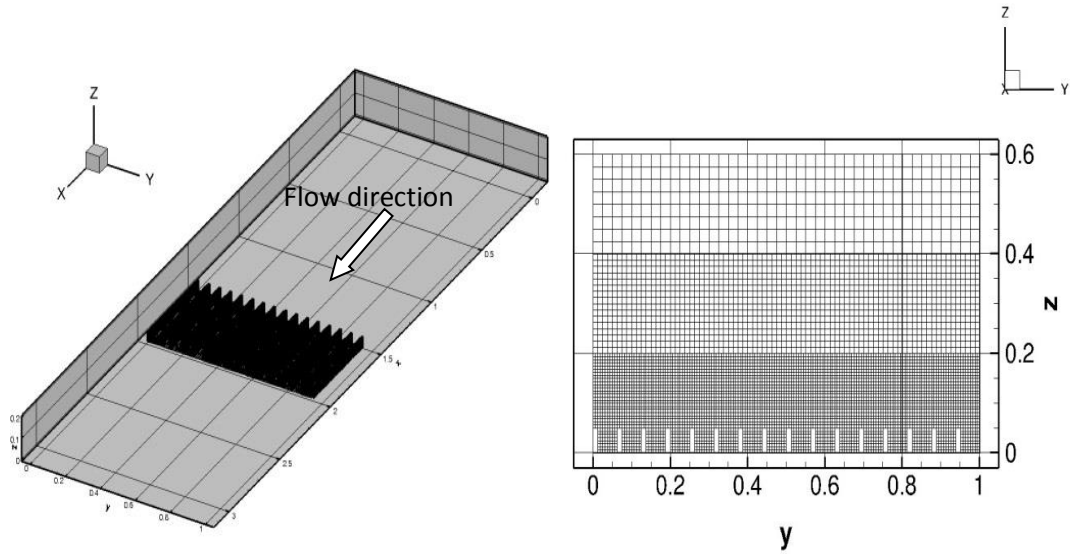
Figure 6-1 The computational domain: patch position (left) and LMR (right).

During the runs, the slip condition was applied to the top and both sidewalls, while the no-slip condition was applied to the bottom wall. Parameters such as bulk velocity, mesh size (dx, dy, and dz), density, Reynold number, the number of iteration and convergence were inputs to the code using a control input file. The input velocity profile could be chosen as simple inflow, $1/7^{th}$ power law, prescribed profile or Synthetic Eddy Method (SEM). A prescribed velocity input profile was used in this study to mimic a fully developed flow; a simple inflow with the periodic condition was used first to generate the prescribed inflow file. For the standard numerical calculation, the code runs first to simulate the flow over a smooth surface at different Reynold numbers. For each Reynold Number, a data base was generated. The boundary condition was assumed to be simple inflow at the inlet and a no-slip condition at the bottom while the rest of the boundary was taken to be a periodic condition. The code runs up to 100,000 iterations to obtain fully developed flow effects. The resultant velocity profile file was stored to be used later when the riblet was applied into the computational domain. Other output results such as the three-dimensional velocity distribution contour, velocity gradient, viscosity, turbulent terms, etc., were taken as a standard to compare each case. The code was run on ARCCA, the supercomputer located at Cardiff University, using 2 nodes

with 16 processors in each node. The average run time for each case was 3-7 days depending on the tested geometry.

6.3 Smooth surface (flat plate)

6.3.1 Introduction

In many studies, studying the flow over a flat plate is the first step to understanding the mechanism of flow developing over different geometries under different conditions. The flow over flat plates is usually used to introduce the study of boundary layer development and transition from laminar to the turbulent boundary layer. The results of turbulent flows inside a channel will be presented and discussed in order to develop an understanding of the riblet performance afterwards. In boundary layer principles, the flow of fluid over solid surfaces or bodies will provoke boundary layer development, depends on which initial conditions such as velocity, viscosity and the geometry of the surface. Thus, the boundary layer will be said laminar or turbulent. However, the laminar boundary layer transits to turbulent if the surface is long enough under the condition of continuity of fluid flow at the same main velocity. The transition from laminar to turbulent occurs because of the movement of the fluid particles in the lateral and normal direction of the main flow. These movements absorb the energy from the main flow and dissipate it as a thermal energy as drag force or as a friction force at the surface Schlichting (2000). This chaotic movement is responsible for energy dissipation in the fluid flow and transition of the boundary layer from laminar to turbulent, which is not preferable in most of the engineering applications. On the other hand, these random movements make it too difficult to analyse the turbulent flow and obtain exact solutions to describe the engineering application. Moreover, the cost of precise measurement techniques and complexity of some application has forced researchers to develop numerical solutions to solve the fluid flow. Direct Numerical Solution (DNS) is preferred in fluid flow solutions, but the computational cost of DNS limits its potential, especially at high Reynold Numbers. For turbulent flow, the most difficult part of obtaining a numerical solution is to apply a turbulence model that adapts to the near wall viscous layer where most of the numerical techniques fail. These difficulties could be partially overcome using LES with proper turbulence models such as Wall Adaptive Local Eddies (WALE) or k-ε with enhanced wall function or k-ω with Shear Stress

Transport (SST). In this study, an LES with WALE turbulence model will be used to simulate the flow over a smooth surface.

6.3.2 Velocity Distribution

Figure 6-2 shows the axial velocity distribution (U/Um), where U is the local velocity in the x-direction and Um is the bulk velocity at the inlet, along with the channel. The channel dimensions are represented in wall units (x^+, y^+, z^+) for comparison purposes. The results show the laminar sublayer, buffer zone, and turbulent layer. The laminar sublayer, where the effects of viscosity are obvious starts from the wall and extend to $z^+=5$; at $5< z^+ <30$ the wall effects are weakened due to the momentum transfer from the turbulent layer and the fluid particles have more energy to escape from the viscous layer. With an increase of Reynold Number, the momentum will increase significantly near the wall. The increase in the momentum near the wall will allow the boundary to withstand a larger unfavourable pressure (positive pressure gradient). This positive pressure results in higher wall shear stress and drag Schlichting (2000). At $z^+>30$, the boundary layer reaches its thickness, the effect of the wall completely vanished and the velocity reached the mainstream velocity value as shown figure 6-3.
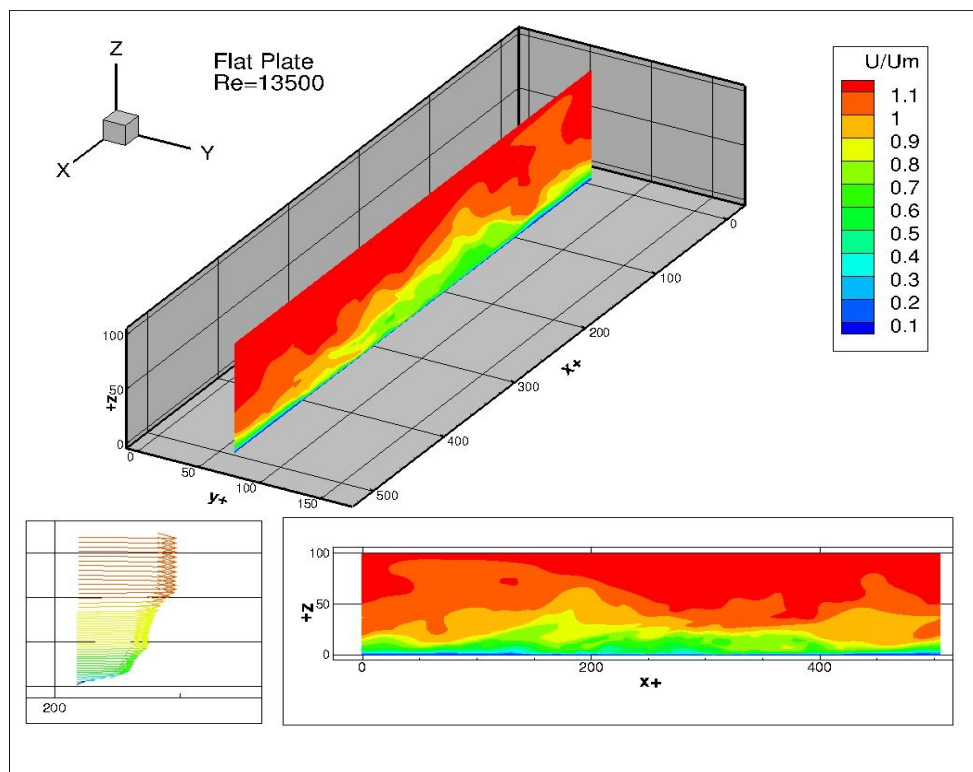
Figure 6-2 axial velocity distribution over flat plate.
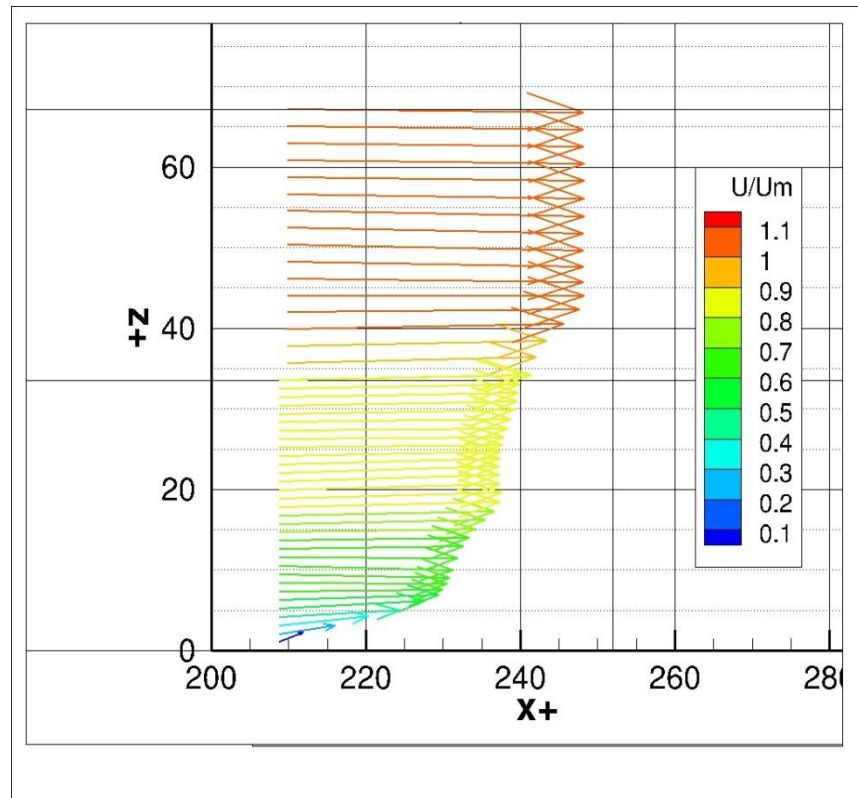
Figure 6-3 x-component velocity distribution in the boundary
layer.

In turbulent flows, the fluid motion is in the form of a three-dimensional movement, lateral and vertical motions have their impact on turbulence intensity and boundary layer transition processes from laminar to turbulent. With the increase of the Reynolds number or the surface length, small vortices generated near the wall cause streak motion in the lateral direction across the flow Kline et al. (1967). Although these streaks are small inlays under the main flow stream, their back and forth movement will cause more instability for the flow. The formation of these vortices increases with increasing Reynold Number due to high momentum transfer; also these vortices are generated near the wall causing more shear stress and drag. The transition of the lateral streaks involves a coalition or destruction of energy transfer to the flow generating new vortices. In figure 6-4, the lateral velocity distribution is presented in different positions of the channel (entrance, middle and exit); the lateral velocity changes its position across the flow. In figure 6-5, the study state lateral velocity at the same position at different time intervals shows the coalition or destroying in the lateral streak.
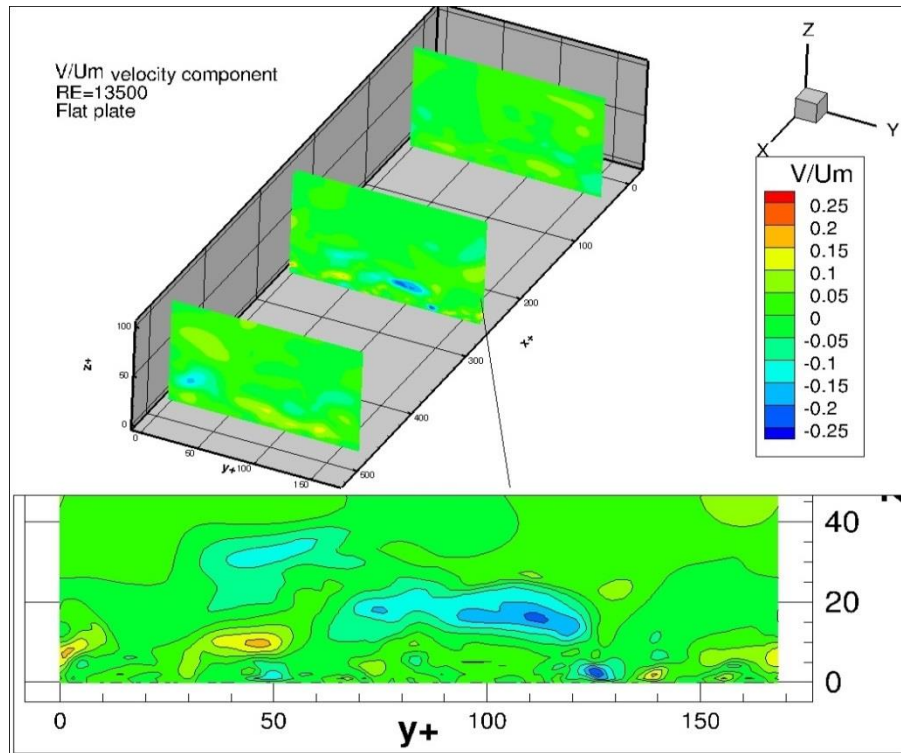
Figure 6-4 Lateral velocity in different position. (up) The slides are at $x^+=2$, 242 and 485, which are represent start, middle and the end of the domain. (down) the slide at $x^+=242$
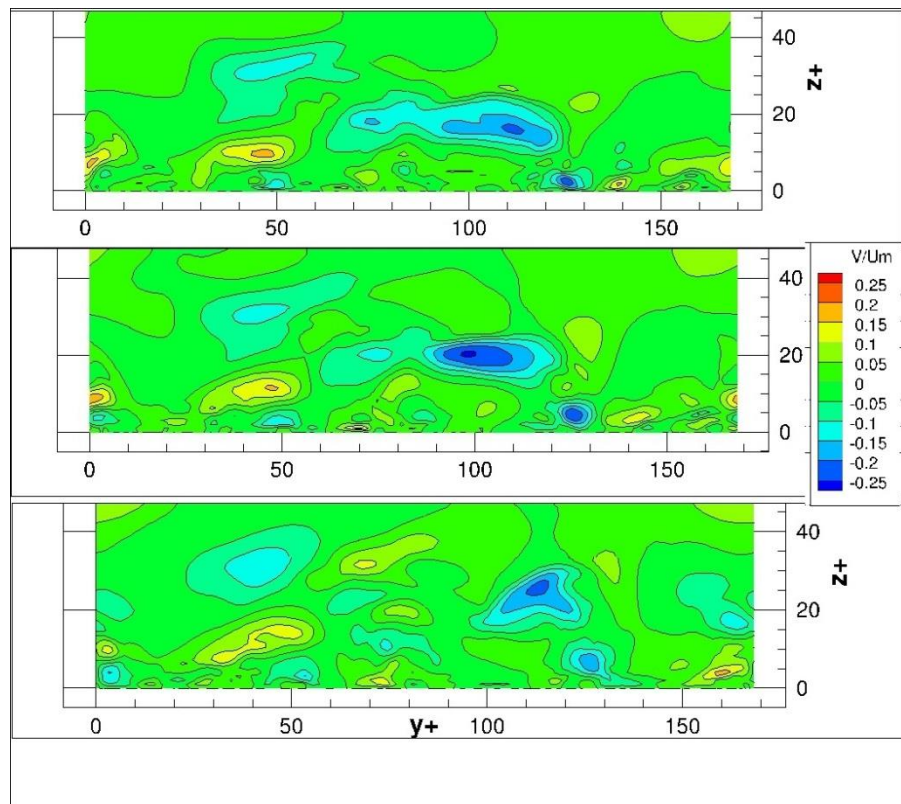
Figure 6-5 lateral velocity in different time. The slides are at $x^+=242$.

The turbulence in the buffer zone also represents ejecting vortices in the normal direction far from the wall. This ejection occurs as fluid motion in the normal direction. This motion is strong in the buffer zone and is dissipated in the mainstream or absorbed by the lateral streak Tuncer Cebeci (1977). In figure 6-6 the formation of vortices near the wall is followed by their injection towards the mainstream, with new vortices generated.
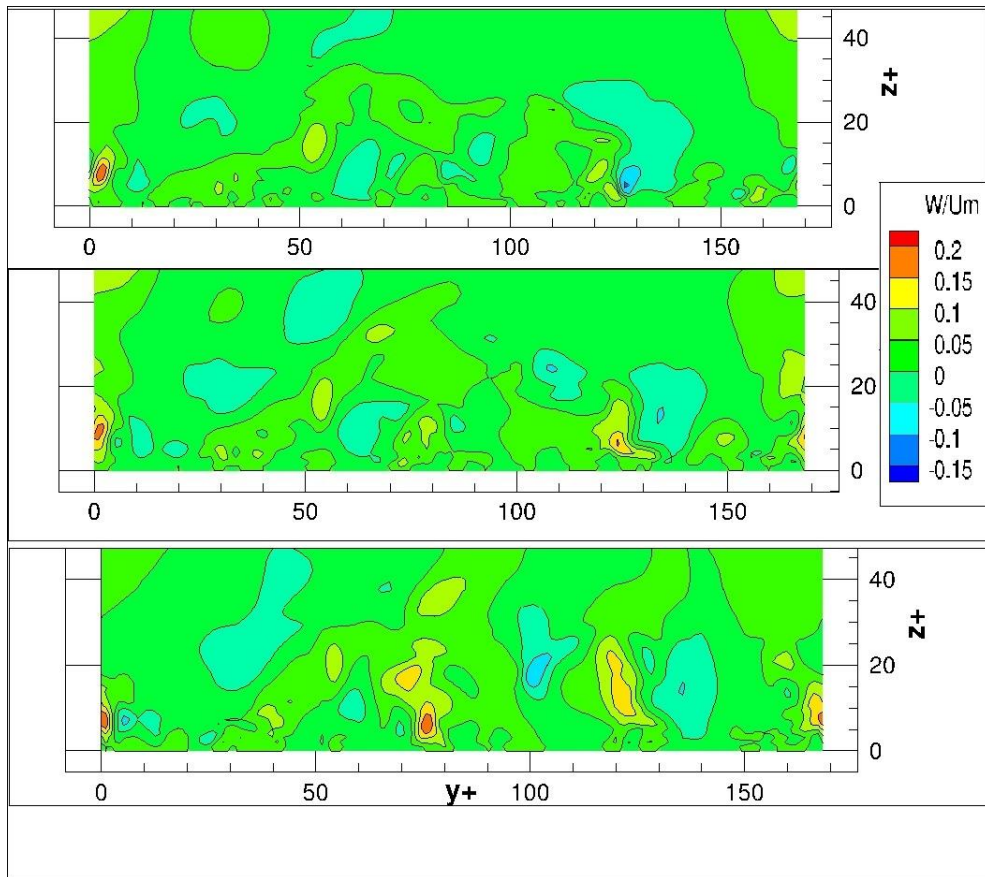
Figure 6-6 velocity distribution in normal direction at different time intervals. The slide at $x^+=242$.

The vortex diameter is related to the strength of the turbulence at the point, where the vorticity is generated, and the Reynold number. Computational studies have suggested that the average vortex diameter for these condition around 30^+ , with experimental studies showing average vortex diameters around 40^+ Lee and Lee (2001). In this study, the vortex diameter was found in a range of 25-35 wall units as shown in figure 6-7.
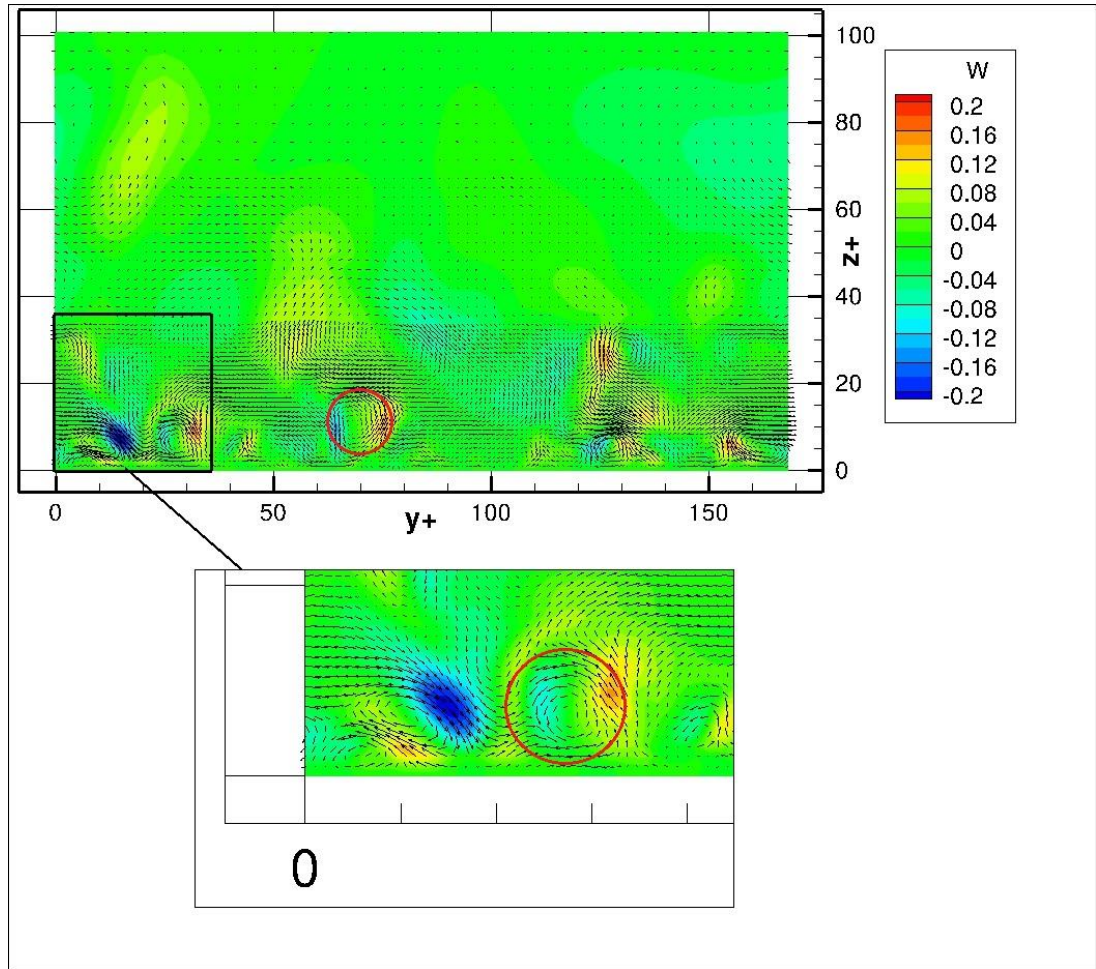
Figure 6-7 vortex diameter at x$^+$=242.

6.3.3 Drag Reduction

In flows over flat plate, the wall shear stress (τ_0) formula that describes the friction coefficient is:

$$c_f = 0.074(Re_L)^{-1/5}$$ …………..……………………………..……………………..(6-1)

And the wall shear stress can described as :

$$\tau_w = 0.332 \, U^{3/2} \sqrt{\frac{\rho\mu}{x}}$$ …………………………………………………..(6-2)

Where, ρ, v, u and d are fluid density, kinematic viscosity, mean stream velocity and pipe diameter or hydraulic diameter, respectively. In figure 6-8, the wall shear stress for the smooth surface is calculated from equation 6-3. The wall shear stress increases with the increase of Reynold numbers. Three velocities were taken as 5, 10 and 15 m/s, which represent 4500, 9000 and 13500 Reynold number, respectively.
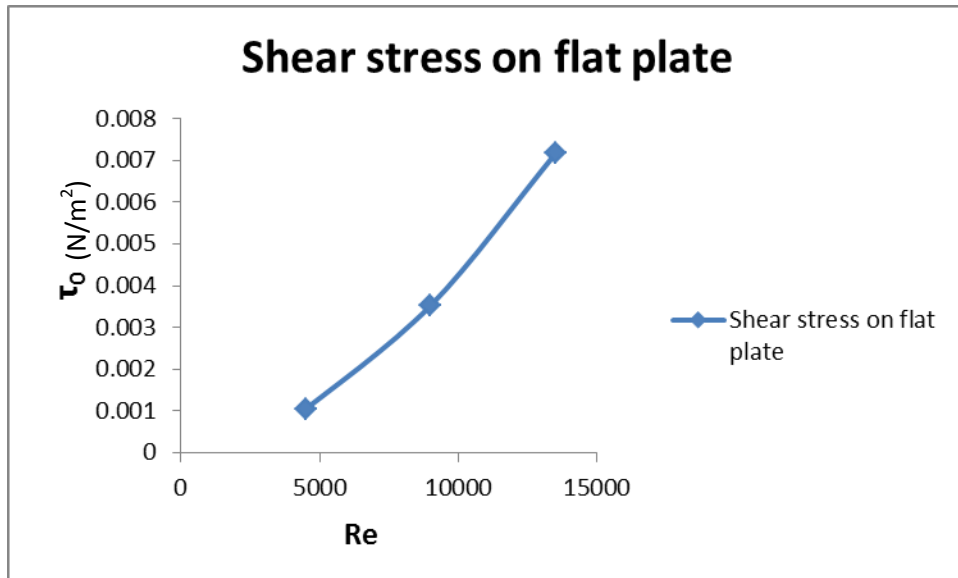
Figure 6-8 Shear stress on flat plate at different velocities.

Figure 6-9 presents the turbulence kinetic energy (TKE) for different Reynold numbers. The numerical results show that TKE increases with the increase of Reynold number. In turbulent flows, the physical quantities are represented in terms of mean and fluctuating parts. i.e. $= \bar{u} + \acute{u}$, $v = \bar{v} + \acute{v}$, etc., where the bar ("- ") denotes a time average, and prime (" $\prime$ ") indicates fluctuation about the time–averaged, mean quantity. The TKE represent the measure of the intensity of turbulence. Thus, the increase in mean velocity will increase the fluctuating part in the equation of velocity field, and since the TKE represents the fluctuating part, it will increase as a consequence.
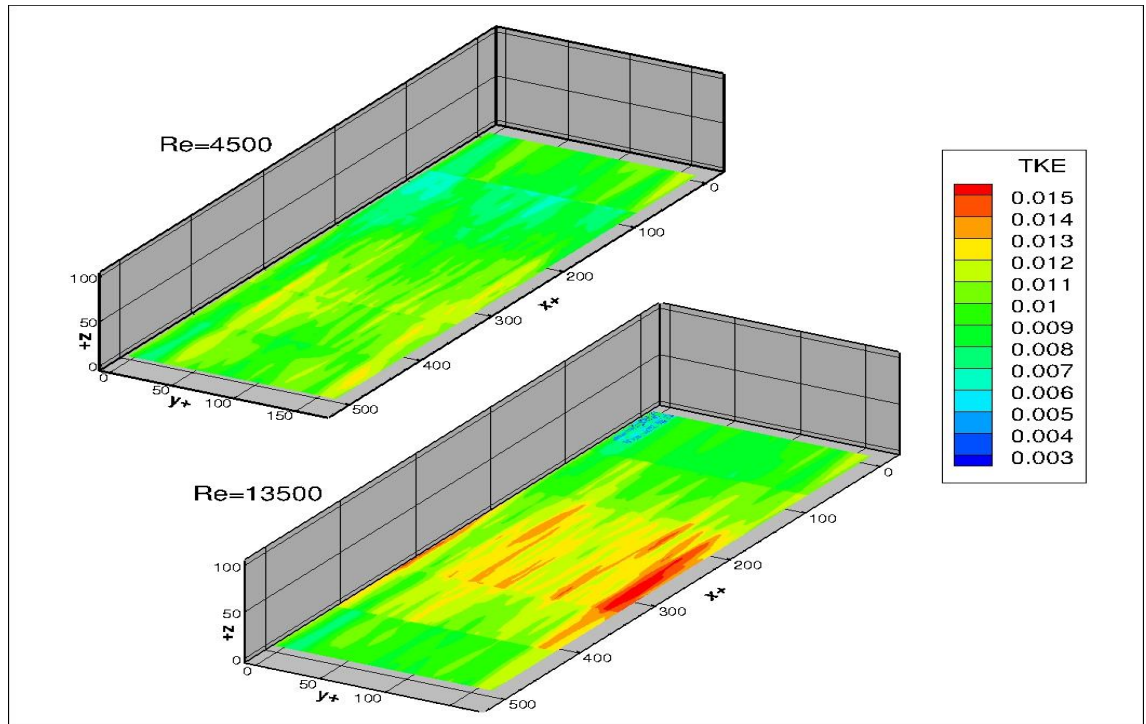
Figure 6-9 Turbulent kinetic energy over a smooth surface at different Reynold number at $z^+ = 1$ for both cases.

Figure 6-10 shows the shear stress on a flat plate over the wall. The middle zones, where the LMR is applied, and the mesh is close to the wall in the normal direction, show high shear stress as a result of fine grid. However, the shear stress at these zones is important for the next result because the riblets are located in the same zones.
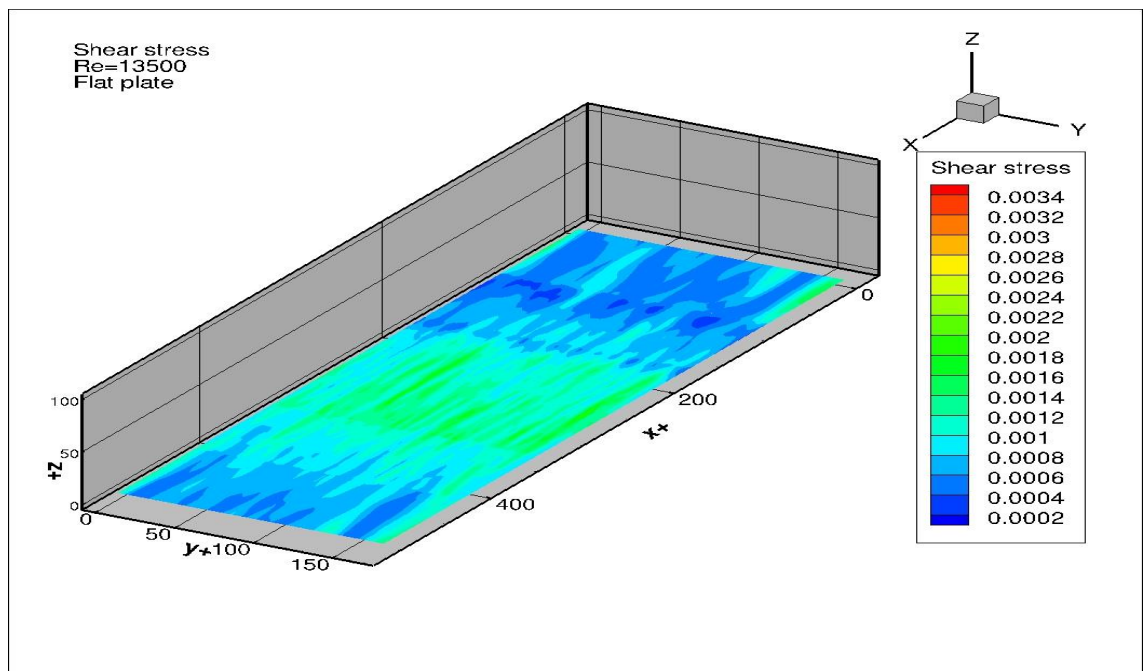
Figure 6-10 shear stress on flat plate Re=13500 at $z^+=1$.

To validate the simulation, the code was run using two different turbulence models, i.e. WALE and Filtered Smagorinsky. The non-dimensional mean streamwise velocity ($u^* =$ u/u_τ) over the smooth surface was compared to each other as in figure 6-11. The same results are obtained by Nicoud and Ducros (1999b). The dashed lines represent the linear law and log-law. The log law formula is ($u^+ = 2.4$ $\ln y^+ + 5.5$). The Filtered Smagorinsky and present work with WALE turbulence model are in good agreement, which validates the simulation. The validation results showed that Hydro3D code is valid with good accuracy for the prediction of flow over smooth surfaces, so the code will used next to simulate the flow over the verification riblet group.
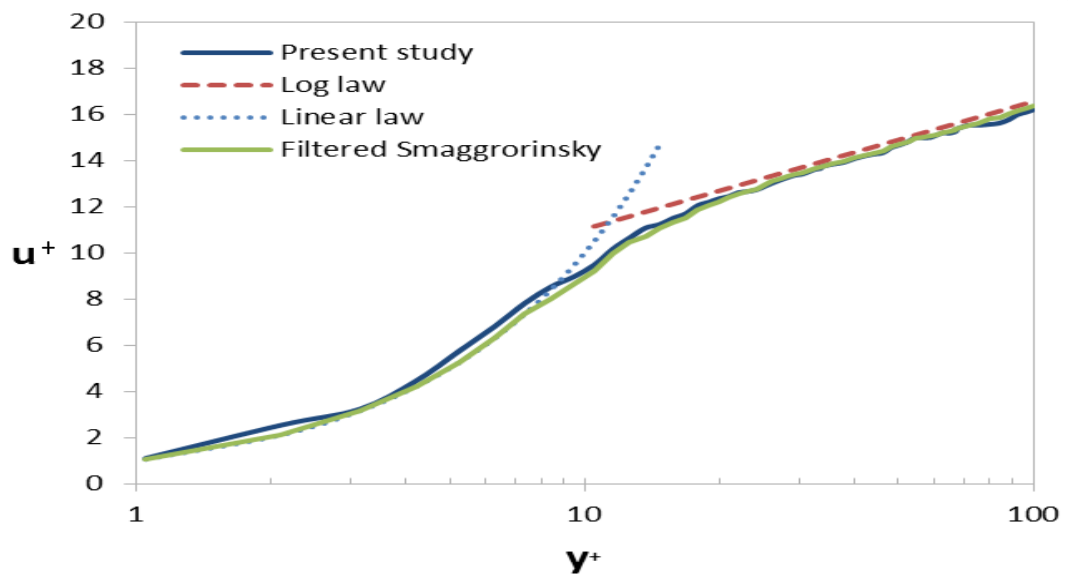
Figure 6-11 comparison between Filter Smagorinsky and WALE. The log low and linear low as Nicoud and Ducros (1999b).

6.4 Verification Group

6.4.1 Blade Riblets

To study flow over riblet surfaces first we need to specify the main parameters. The simplest design of riblet is the blade riblets. In such geometry, the ratio of the riblet height to space (h/s) and velocity are the main parameters. To optimise the riblet design, the physical dimensions are represented as dimensionless variables by normalising them and denoting each parameter with a superscript + to refer it as dimensionless. The riblet size in real life in the range of 200-500 μm and the depth between 70-200 μm Bixler and

Bhushan (2012). Also, most experimental studies have reported that the best drag reduction is obtained from blade riblet with (h/s) between 0.6 - 0.8. Therefore, the basic blade design to test in Hydro 3D code was a patch of blade riblets located in the middle of the channel under fully developed turbulent flow conditions. The riblet height is 200 μm and space was varied between 200μm and 400μm, to obtain different (h/s) ratios as shown in figure 6-12. However, the focus was on the study of the velocity change over certain geometries; the surveyed velocity was between 1.0 m/s to 20.0 m/s. This geometry is related to the manufacturing equipment available to use at Cardiff University. From results figure 6-12, the blade with h/s=0.7 was chosen for further studies. The blade geometry was 200 μm height and 280μm in space. Although this geometry does not give the optimum TKE reduction, the results show that the wider spacing produces higher TKE and lower protrude positioning which means that the high-velocity flow contacts more area and leads to more shear stress and drag. Meanwhile, the narrower spacing shows slower fluid motion or even backflow with a higher protrude positioning which means the backpressure raises with velocity increase and cause more pressure drag.
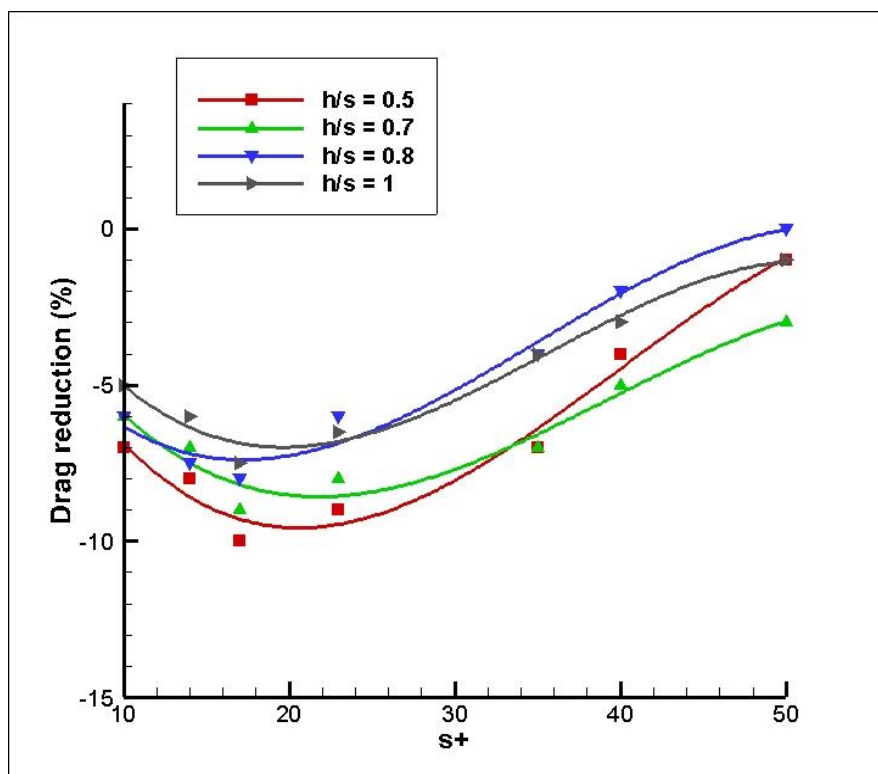
Figure 6-12 Drag reduction for different velocities (in term of s^{+}).

6.4.1.1 Velocity Distribution

Figures 6-13, 6-14 and 6-15 show the streamwise velocity distribution over the blade riblet at different Reynolds number. The results show that the velocity distribution is affected by Reynold numbers where the velocity distribution becomes larger and the high speed come closer to the wall with increasing the velocity which means increase in velocity gradient near the wall. This behaviour could explain why the wall shear stress increases with the increase of velocity. Also, the velocity contour shows that with velocity increase the high-speed flow enters deeper between the riblets, which mean the more wetted area in contact with high velocity leading to changing profile and sublayer, more wall shear stress and more drag as a consequence.
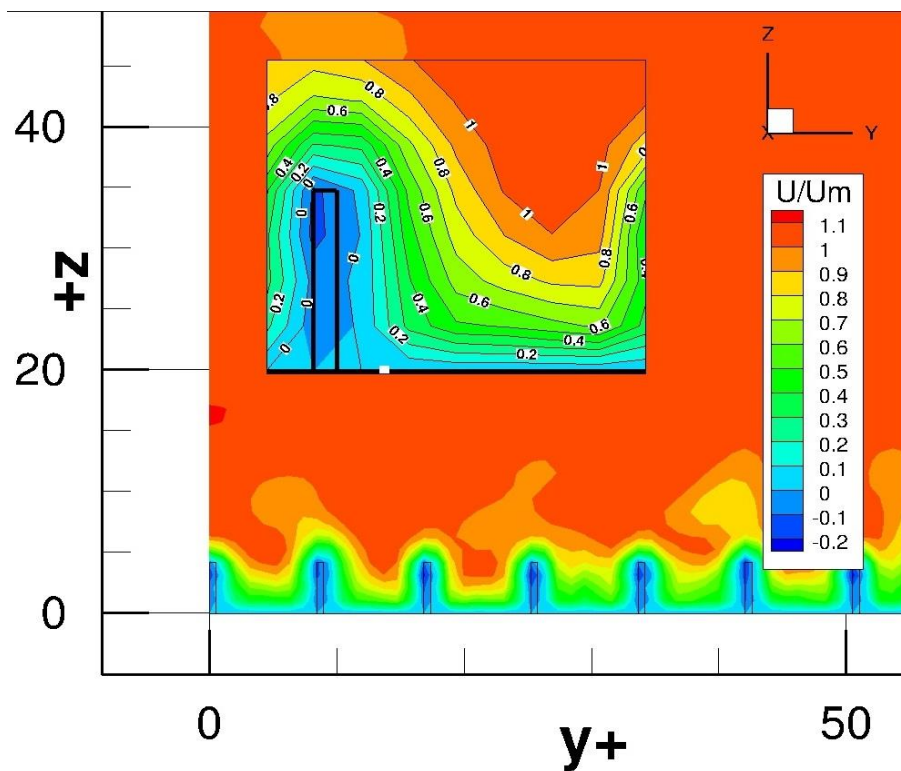
Figure 6-13 streamwise velocity distribution Re=4500
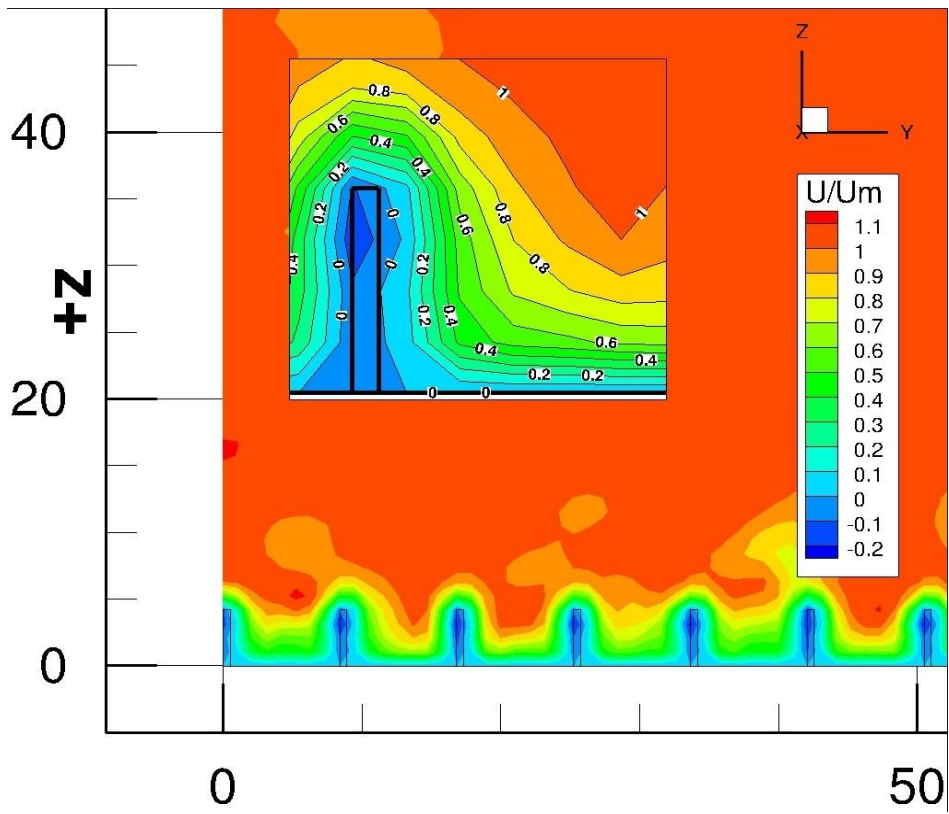
Figure 6-14 streamwise velocity distribution Re=9000
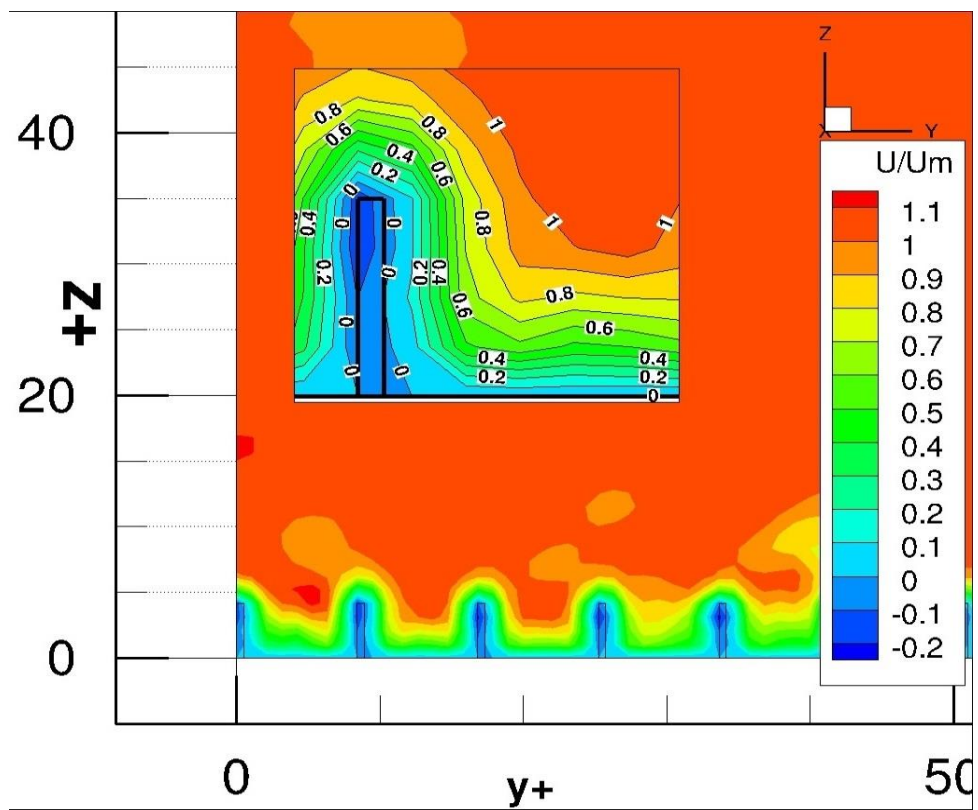
Figure 6-15 streamwise velocity distribution Re=13500.

Due to the small changes in the results and the general pattern which not exceeds 5% for different Re, only the results of blade riblet with (h/s=0.7) at Re=13,500 and h= 4 wall units and s around 6 wall units are presented in fellow. The streamwise velocity distribution and a boundary layer profile are presented in figure 6-16. Two interesting outcomes are shown in figure 6-16. First, the velocity in the streamwise direction becomes more uniform and less chaotic compared to flow over the smooth surface which is shown in figure 6-2. This uniform behaviour of streamwise velocity refers to a decrease of lateral and normal velocities which are responsible for provoking the turbulence in the laminar flow to transit to turbulent conditions. Second, the backflow, which is normally located behind the riblet and also at the internal tip of the riblet downwards to the riblet root, where the flow generates tiny backflow zones due to the blade thickness as shown in profile B in figure 6-17. However, the backflow zones combined with the low velocity are important to locate the apparent origin, which is a virtual elevation where the boundary layer starts.
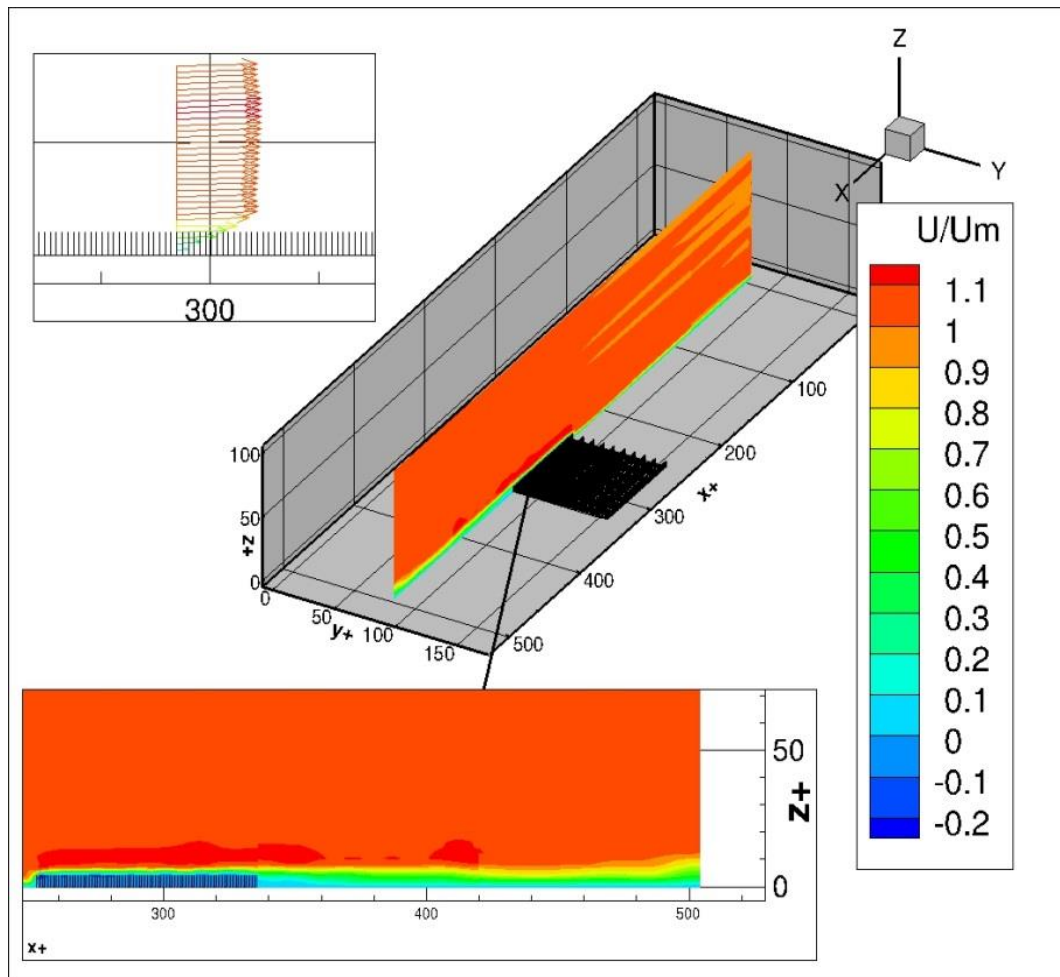
Figure 6-16 Streamwise velocity distribution with boundary layer profile at y^+ =78.
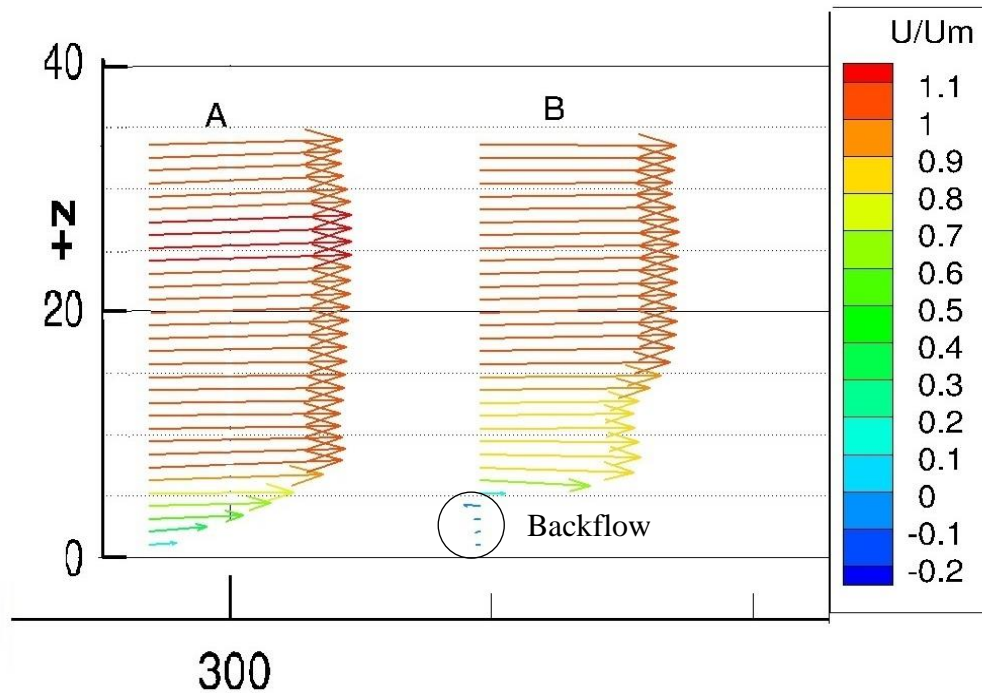
Figure 6-17 Boundary layer profile; Profile A velocity profile in the smooth surfaces between two blade riblets at y^+ =82 and x^+ =295. Profile B velocity profile near blade wall at $y^+ = 85$ and $x^+ = 315$.

Figure 6-17 shows the boundary layer profile for the flow at two different positions across the riblet. Profile A shows the boundary layer at the middle distance between two blades and the profile B shows the boundary layer profile close to the blade riblet wall. From these two profiles, the effect of riblets on reduction the wall effect on boundary layer is noticed. These effects are obtained by trapping the flow between the riblets and reducing its velocity which provides a fluidic bed that prevents the coming flow from contacting the trapped flow. Moreover, the riblets will channel the trapped fluid and force it to move in the streamwise direction restricting the momentum in a cross or normal direction, which reduces the amount of momentum, transferred from the outer layer to the viscous layer, thus reducing the friction drag as a consequence. Comparing the boundary layer profiles in figure 6.17 to the boundary layer over smooth surfaces shown in figure 6.3, it is clear that for a smooth surface the streamwise local velocity needs about 20 wall units (z^+) to reach 80% from the bulk velocity and 40 wall units to reach the margin of the outer layer, while it needs only 5 wall units to reach 80% from bulk velocity and 8 wall units to reach the outer layer at U/Um=0.99. this results are due to the smaller effective flow area through the channels. These results demonstrate that

134

the riblet has a strong influence on the velocity distribution in the outer region by strengthening the streamwise velocity against the lateral and normal velocity.

Figure 6-18 shows the lateral velocity over blade riblets. The riblets work as guide channels for the flow and restrict the lateral movement. Although the number and strength of the lateral velocities have higher values in riblet surfaces than in the flat plate, the fact that the freedom in moving in the cross direction is highly restricted makes their effects a high impact to drag reduction. Moreover, these trapped lateral vortices will cause a slowing down in velocity inside the channel in the streamwise direction as shown in figure 6-15.
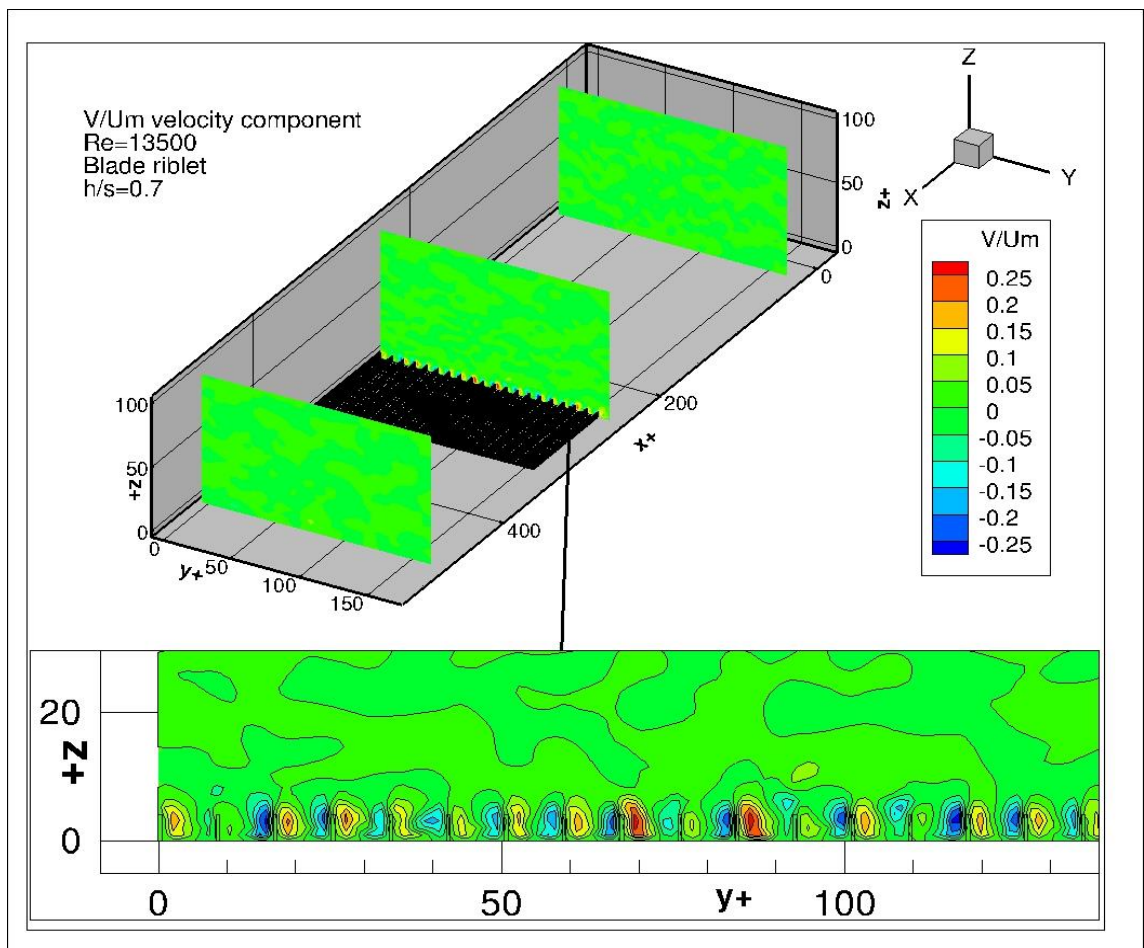
Figure 6-18 lateral velocity over blade riblets at $x^+ = 242$.

Figure 6-19 shows the normal velocity component. The restriction of the lateral velocity inside the blade riblet spaces reduces significantly the ejecting process. The normal velocity gradient, shown in figure 6.19, represents the normal behaviour of the flow over the sharp edge where the flow develops small pockets with high velocity in the

normal direction. These pockets vanish quickly when mixed with the nearby flow. However, the ejecting vortices are reduced in the normal direction which leads to making the flow far from the riblets more uniform due to the lack of lateral and normal disturbance.
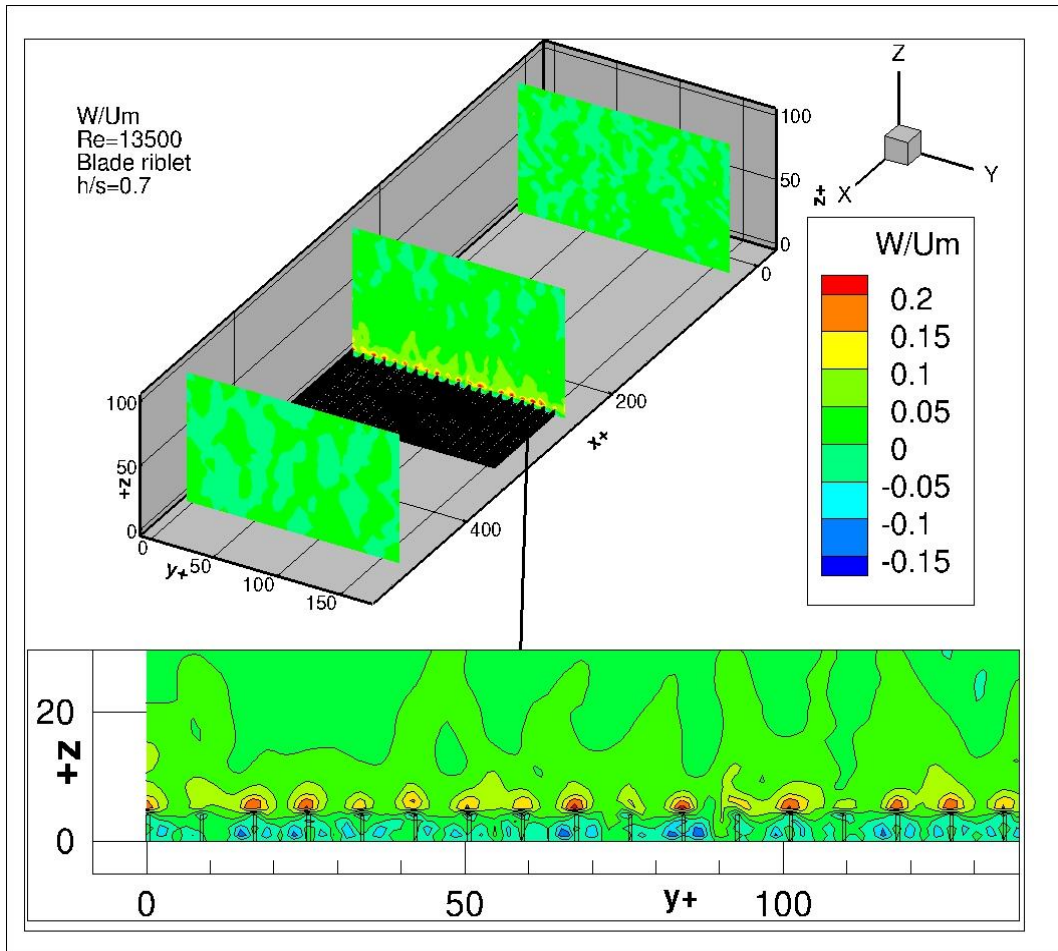
Figure 6-19 normal velocity over blade riblets at x^+ =242.

6.4.1.2 Drag Reduction

Figure 6-20 shows the turbulent kinetic energy in the computational domain. The effect of riblets on turbulent kinetic energy is clear. The blade riblets geometry make mini channels, the smooth surface between any two riblets make a channel. These channels have trapped the flow causing a huge reduction in turbulence. The reduction in turbulence is a result of the restriction in lateral and normal velocity. Although the velocity at the entrance of the channels has high fluctuation the flow slow down inside the channel.
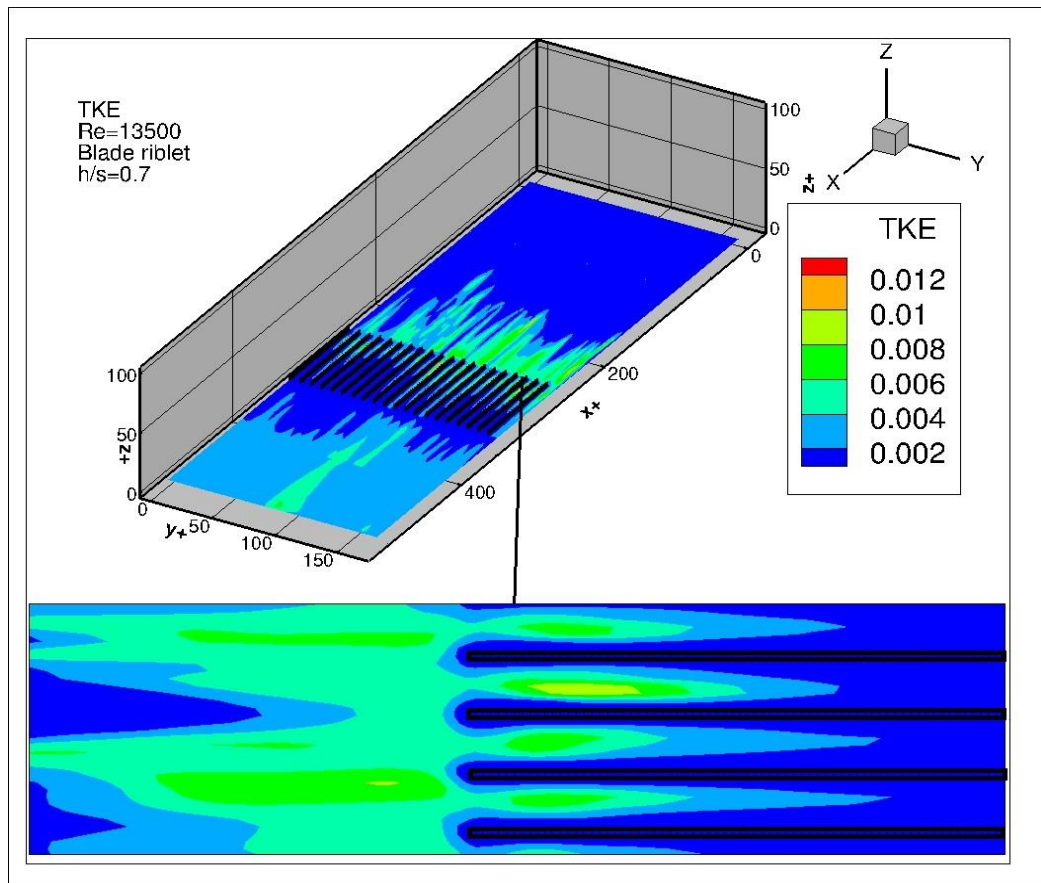
Figure 6-20 turbulent kinetic energy over blade riblets at $z^+ = 1$.

Figures 6-21 and 6-22 show the shear stress at the root and the tip of the blade riblets, respectively. The shear stress in riblet surfaces appears in three positions, at the smooth surface between riblets and also at the sidewalls and tip of the riblets. Although there is a more wetted area in the riblets and the maximum shear stress is higher than the flat plate, the velocity gradient at the riblet and the sidewall is too low, and only at the tip of the riblet, the velocity gradient will be high. Also, maximum shear stress locates in front of the riblet due to its non-aerofoil shape, with a total area that is affected by the high shear much less than in the flat plate.
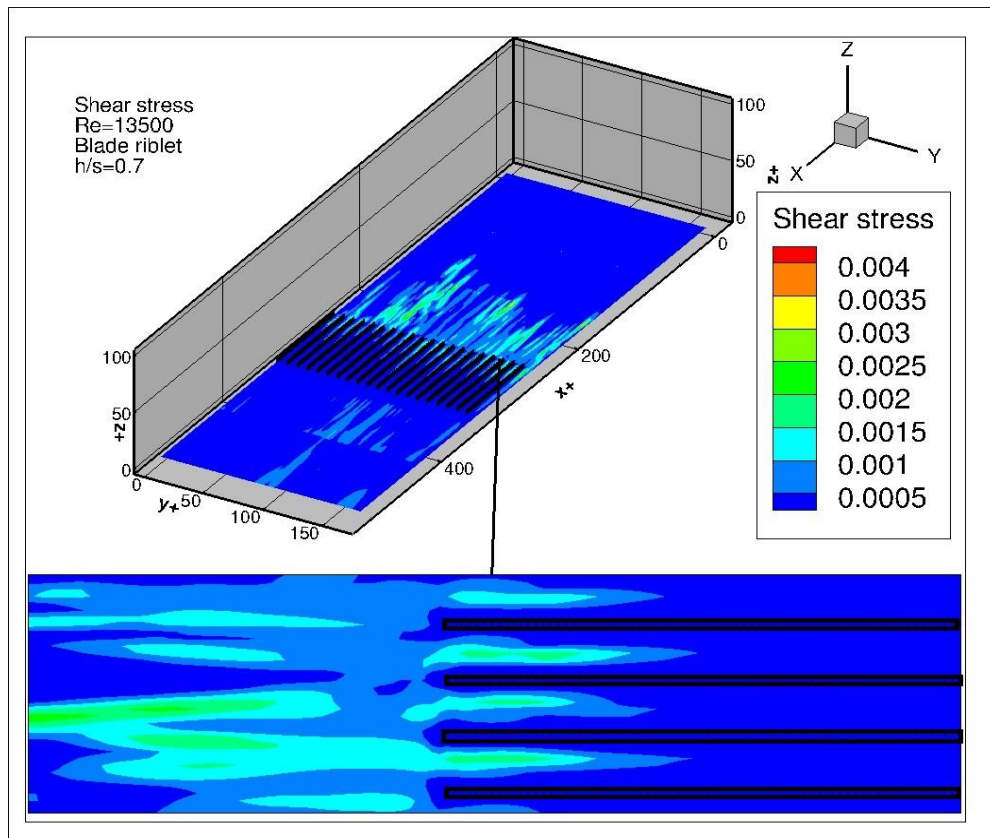
Figure 6-22 shear stress at the root of the blade riblets at $z^+ = 1$.
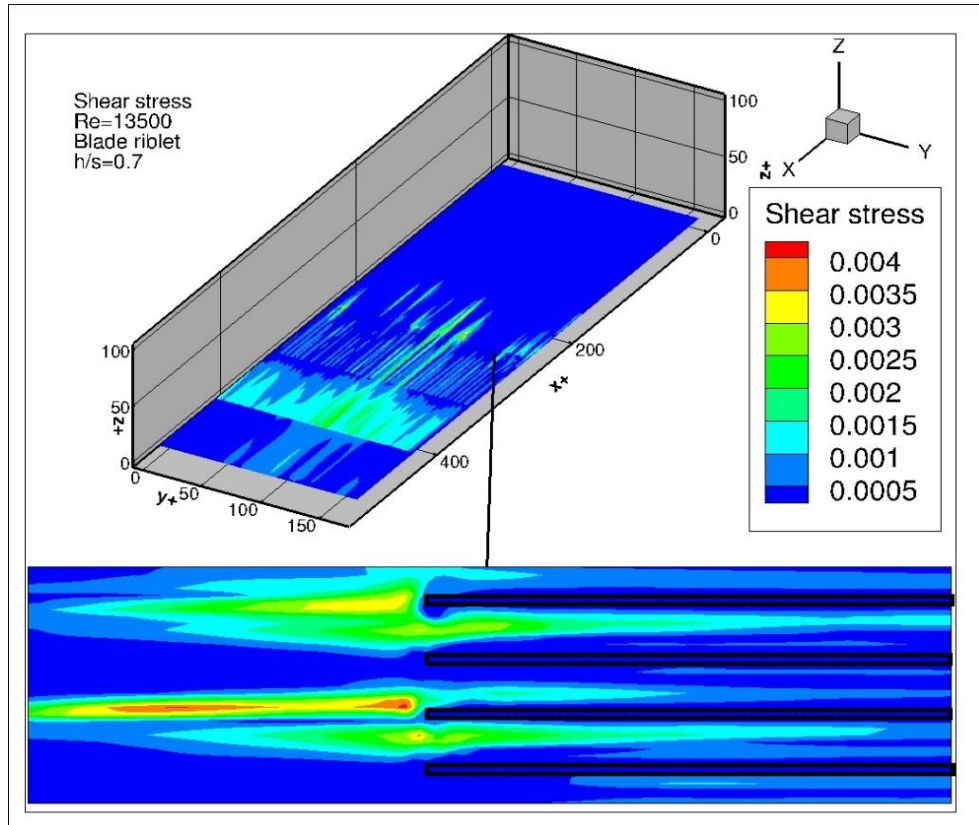
Figure 6-21 shear stress at riblet tips at $z^+ = 5.5$.

6.4.2 Triangular Riblets

The flow was also simulated over triangular riblets. The riblets were 250μm in height, and the space between tips was 250μm, so the h/s ratio was 1.0. The tip was taken to be flat to copy the tip of the blade riblet. The main difference in triangle geometry is the variable thickness of the riblet, where the base is wide, and the tip is similar to the blade riblets. This geometry will cause more resistance to the incoming flow as a consequence of reduces open of the cross section of the valley, which provokes more drag. The results show a significant increase in TKE; the typical increase obtained was 500% compared to blade riblets. Also, the maximum shear stress at the riblets tips increased by 1000% compared to blade riblets, the shear stress at the root of the riblet was lower. However, the net drag will not be as bad because the area that is exposed to high shear stress is too small at the tip of the triangles with most of the riblet exposed to low shear stress. Figures 6-23, 6-24 and 6-25 show TKE and the shear stress at the tip and root of the triangular riblets. These are just samples of the tests, with more details in Appendix A.
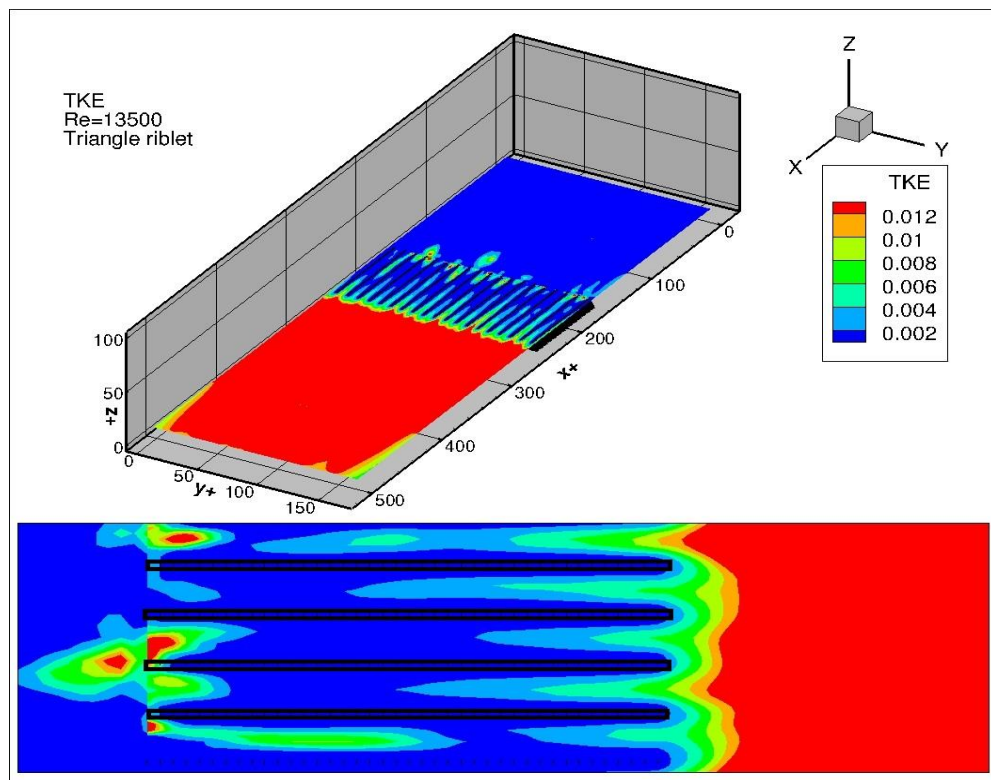
Figure 6-23 turbulent kinetic energy over triangular riblets at $z^+ = 5.5$.
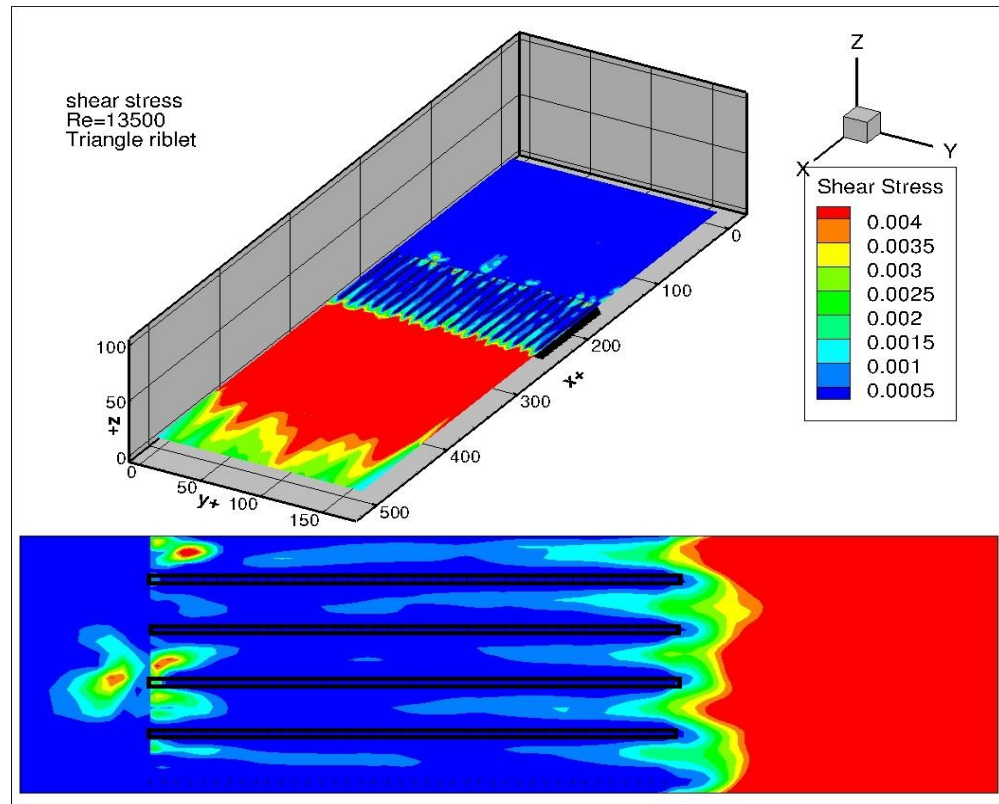
Figure 6-24 shear stress at the tip of the triangle tips at $z^+ = 5.5$.
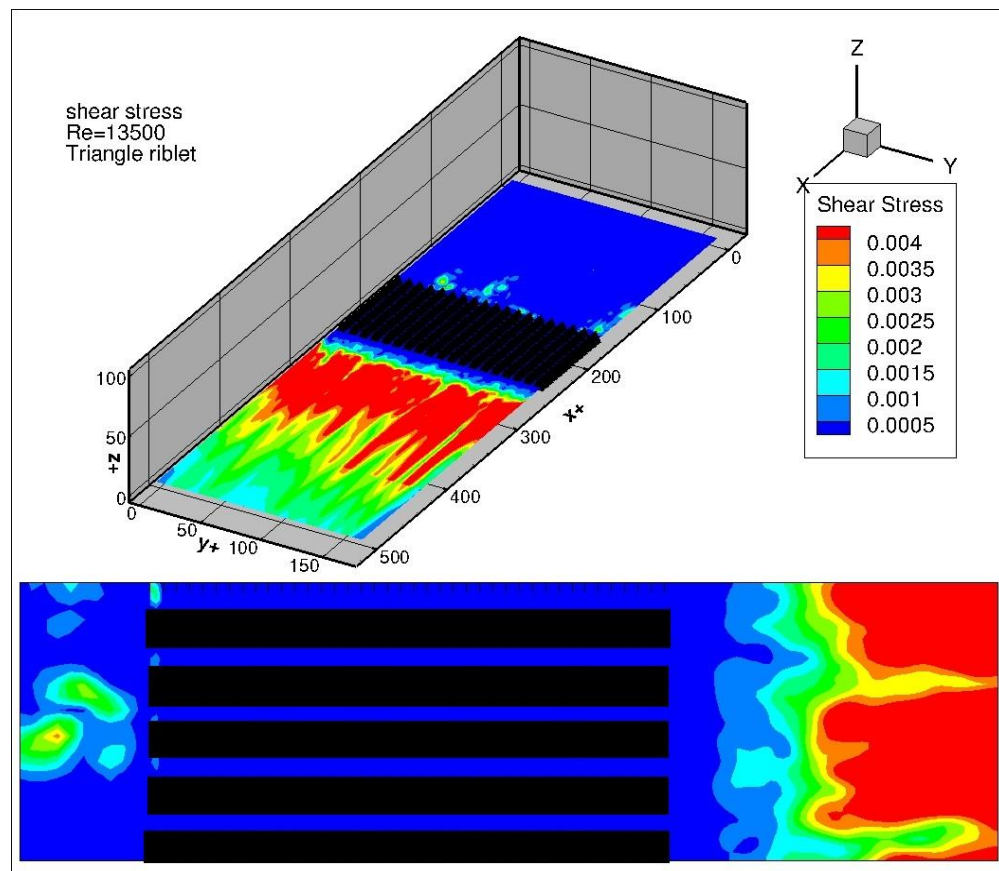
Figure 6-25 shear stress near triangle riblet root at $z^+ = 1$.

The shear stress results of the blade and triangular riblets were compared to the experimental results of triangular and blade riblets published by Bechert et al. (2000); Martin and Bhushan (2014), respectively. The shear stress was calculated by adding the average shear stress on the wall and the shear stress at the blade tips. The averaging shear stress was calculated by extracting the shear stress values at the first layer close to the wall and its averages values. Then the values of the shear stress are averaged and added to the average values on the wall. The comparison shows a good agreement between the experimental and Hydro 3D results. The figure 6-26 shows the agreement between the experiments and simulations. The results showed good agreement at a range of $s^+ \approx 15\text{-}35$, and the trend of the experimental results was well captured by the simulation results. At higher s^+, no experimental result was available, but the simulation suggests a smoother increase in drag. At high s^+ the increase in drag depends on both space and velocity. If s^+ is changed using an increased space at a constant velocity, most of the drag comes from the shear stress which increases with an increase in space due to vortices entering in the valley, thus increasing the wetted area. The increase in s^+ comes from an increased velocity in constant space; the drag is a combination of shear stress and pressure drag due to back pressure and slow motion at the valley Bixler and Bhushan (2014).
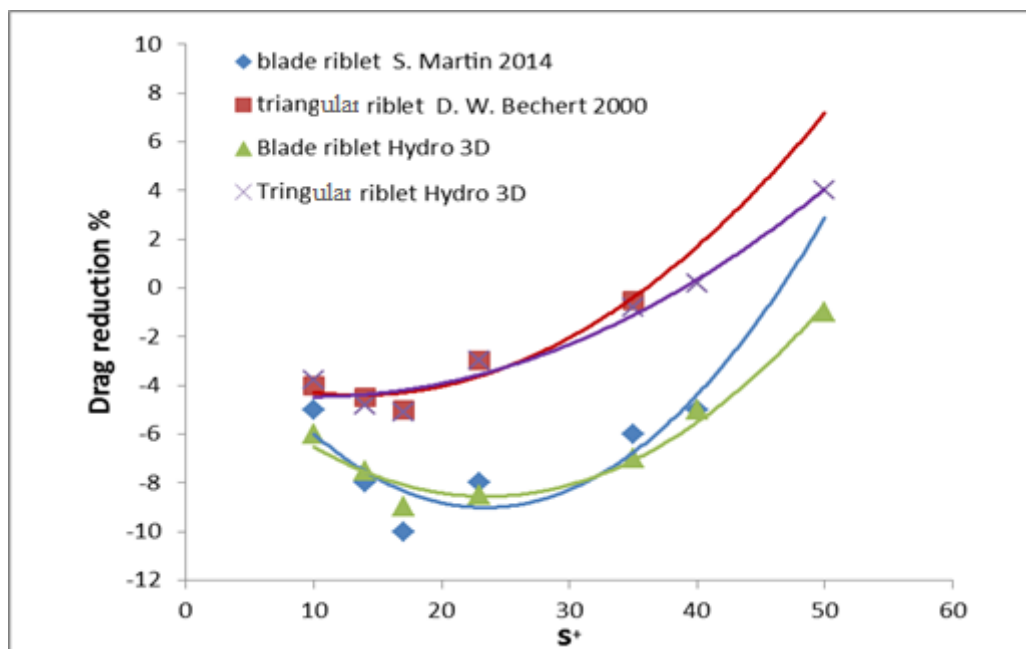
Figure 6-26 simulation and experimental results comparison.

The blade riblets and triangular riblets results of drag reduction show that the blade riblet performance is better than other geometries. The main difference between these two geometries was the base width since other parameters were kept almost the same. However, manufacturing blade riblets is considered inefficient due to the weakness of the structure of the blade, especially when the thickness plays an important role on riblet performance and needs to be kept as minimum as possible Martin and Bhushan (2016a). On the other hand, the triangular riblets show an increase in drag with an increasing the velocity. The triangle riblets show high-pressure build-up around 22.4 Pa/m, while the blade riblet shows a negative pressure around 30 Pa/m and the flat plate has a pressure build up around 0.8 Pa/m. Such results could explain the lower performance of the triangular riblets compared to blade riblet. The increase in pressure or positive pressure will lead to an increase in the instantaneous acceleration motion near the wall which increases the skin friction K. S. Choi (1996). Figure 6-26 showed that Hydro3D code is valid for the use in simulation of flow over complex geometries such as riblets.

6.5 Modelling Group

6.5.1 Scallop Riblets

The difficulties of manufacturing blade riblets and their weak strength in a harsh environment such as combustion chambers, combined with poor drag reduction of triangle riblets lead to investigate another geometry which can adapt the strength of the triangular riblets and the good drag reduction performance of blade riblets. Scallop riblets, a geometry that could be manufactured using the manufacturing machines available at Cardiff University, were examined. The geometry can be described as a group of half circular channels aligned together as shown in figure 6.27. Scallop riblets have experimentally reported producing drag reduction between blade riblet and triangle riblets Bechert et al. (1997).
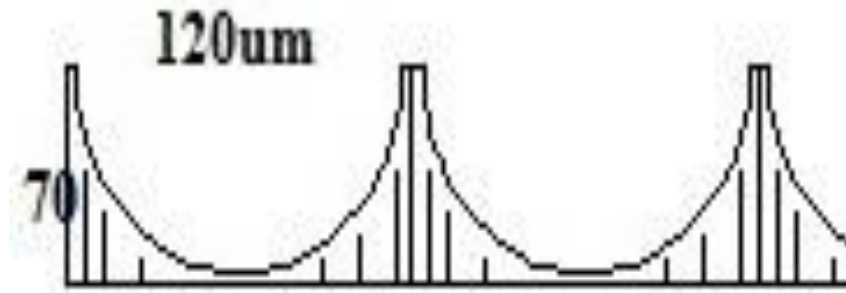
Figure 6-27 scallop riblets.

This geometry has a feature that could be extend to other geometries that will be discussed later. Understanding the limitation of the available manufacturing resources and the features of the WEDM machine at the University necessitate requires the geometry numerically first. Three different h/s were tested, i.e. 0.6, 0.8 and 1. The 0.6 geometry gives a good performance in term of TKE and Shear stress. From this point, the scallop riblet with 120 μm in space and 70μm was chosen. However, the manufacturing process produced a slightly different geometry. The final manufactured scallop riblets have h/s =0.72, h=80 and s=110. To evaluate the effects of the new dimensions, a numerical simulation for the new geometry after small modifications was carried out and gave almost the same results, which will be discussed later. Also, although the h/s ratio is different between the simulation of the manufactured scallop riblets and the simulation of the target shape (shown in Figure 6.27), the numerical results show no significant difference.

6.5.1.1 Velocity Distribution

Figure 6-28 presents the streamwise velocity component. The results show that the geometry of the riblets has a significant effect on the streamwise velocity profile. The wide base of the riblet changes the valley area from narrow at the base to wide at the tip. Narrow valleys cause a slowing down in velocity in the direction of the flow.
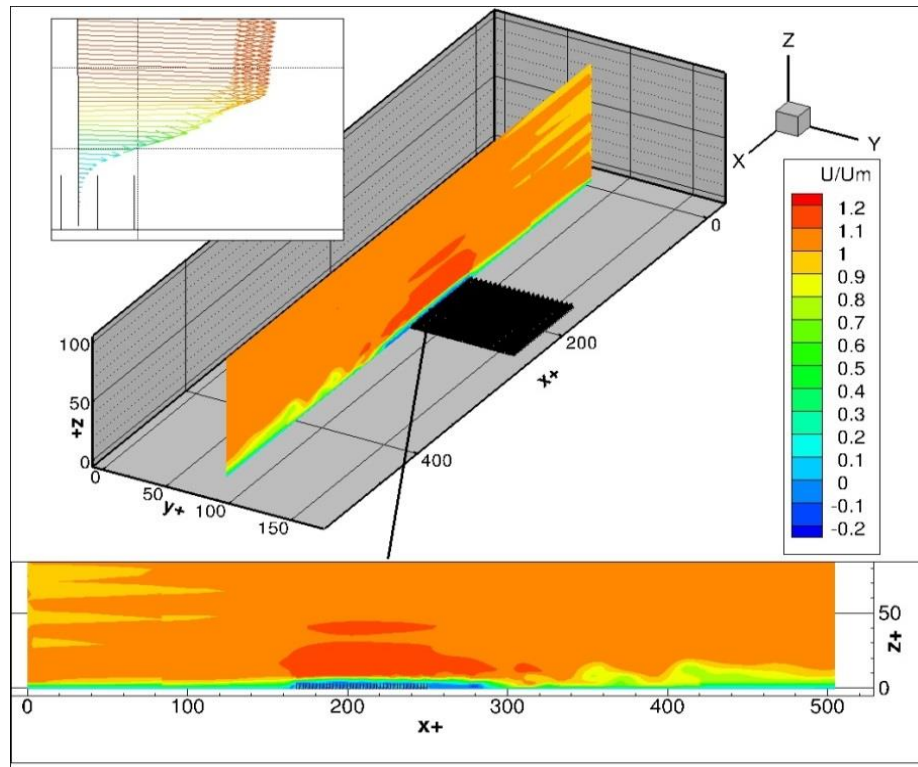
Figure 6-28 streamwise velocity distribution over scallop riblets at $y^+ = 78$.

The flow at the entrance of the valleys generates vortices in lateral and normal direction, these vortices cause in blockage the flow at the entrance of the valleys and slow down the flow. Moving up towards the riblet tip, the valley becomes wider, and the velocity gradient starts at protrusion height (hp). The protrusion height is a virtual distance down the riblet tip where the velocity profile obeys the linear law. The protrusion height depends on the riblet geometry and the mainstream velocity, i.e. a higher h/s ratio means lower h_p, and a higher velocity means lower h_p. Thus h_p has an inverse relation to s^+. The scallop results show that h_p is around 0.25h down the riblet tip as shown in figure 6-29. Similar results were obtained by Bechert and Bartenwerfer (1989).
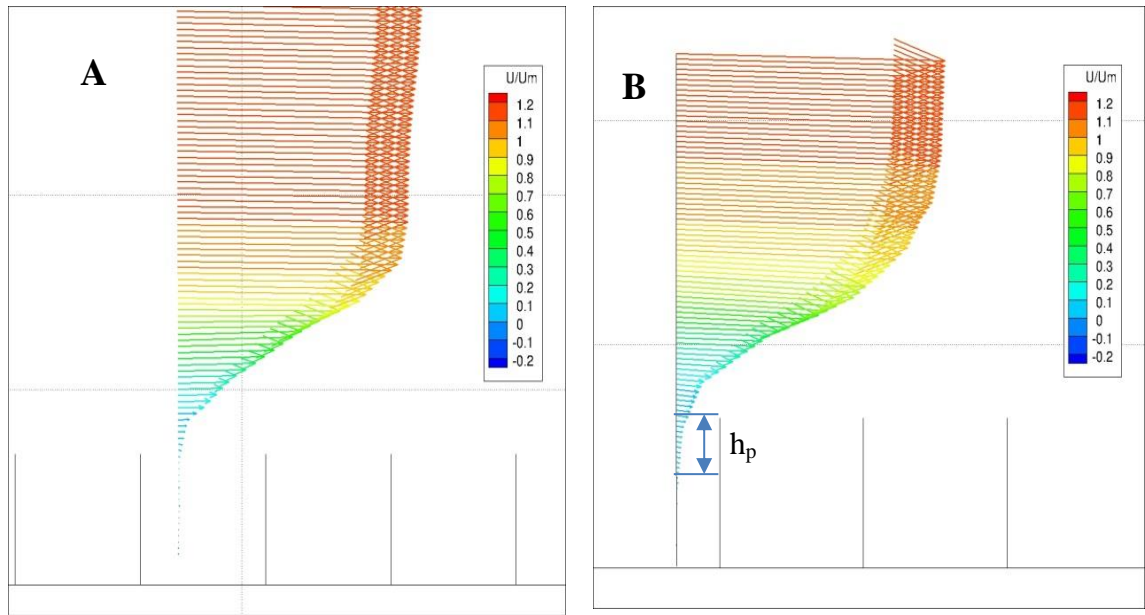
Figure 6-29, streamwise velocity profile (boundary layer) A) near riblet tip at y+ = 85 and x+ = 295, B) in the middle of the valley at y+ = 83 and x+ = 295.

Figure 6-29 shows the stream velocity profile over a scallop riblet at two different positions. Position A is located near the riblet tip, where the boundary layer profile starts at a level very close to the tip height. Position B is located in the middle of the valley, where the boundary layer profile starts at an of level 0.25-0.3 down the tip of the riblet. This difference in position will cause a velocity differential between the adjacent boundary layers across the valley and an increase in the shear stress over the riblet tips. However, the shear stress inside the riblet's valley is reduced significantly due to the low velocity gradient inside them.

Figure 6.30 presents the streamwise velocity distribution close to the riblets tips. The results show the velocity distributions inside the valleys and over the riblets. The results in figure 6.30 show low velocities inside valleys and the core of the high velocity is lifted over the riblets. Compared to blade riblets, the high-velocity core expands to cover 4-5 riblets at the same time, which considers as a possible reason for increase the shear stress in the thin shear layer flow Martin and Bhushan (2014, 2016a).

Figure 6-31 shows the velocity gradient over the scallop riblet. The high-velocity gradient is located at the riblets top because the flow with high velocity is in contact with riblets tip; inside the valley, the flow is moving at low velocities less than 10% from the mainstream velocity. Therefore, the wall effect on velocity gradient is low.

Moving towards the main flow stream, the velocity gradient increase which means an increase in shear stress. This result a high shear layer located in the mainstream close to the riblet tips.
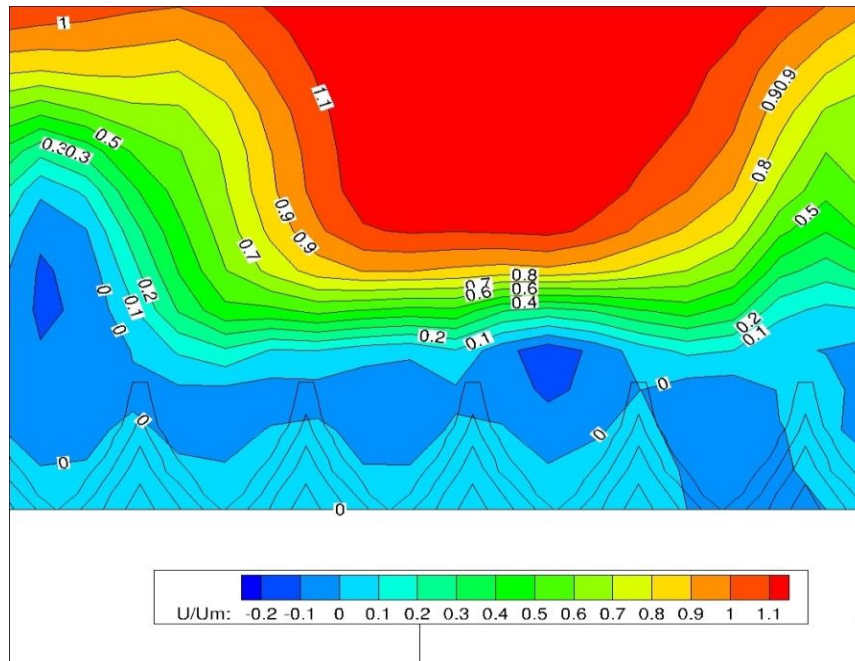
Figure 6-30 streamwise velocity gradient over scallop riblet.
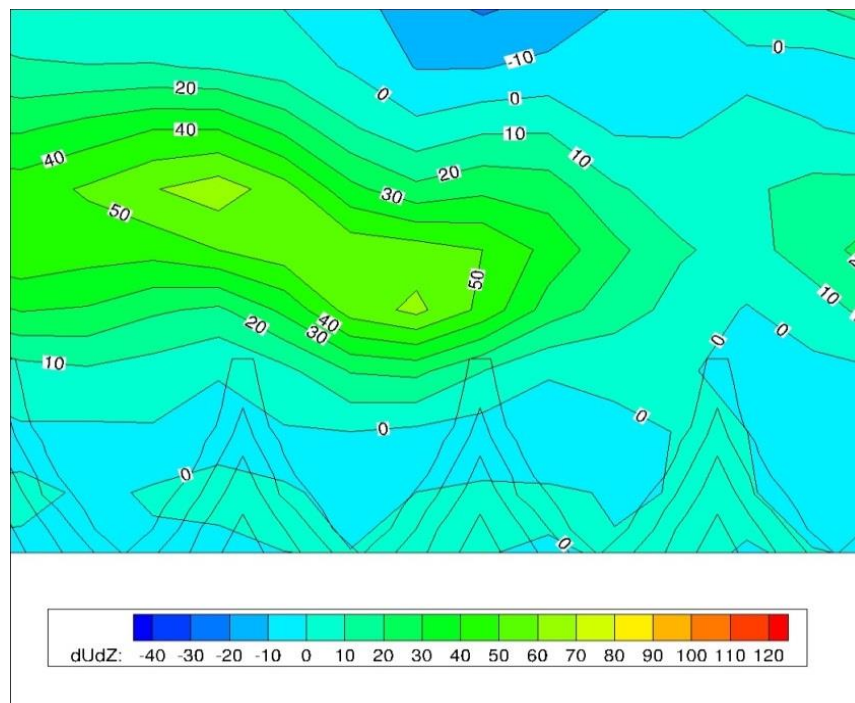
Figure 6-31 streamwise velocity gradient over scallop riblets
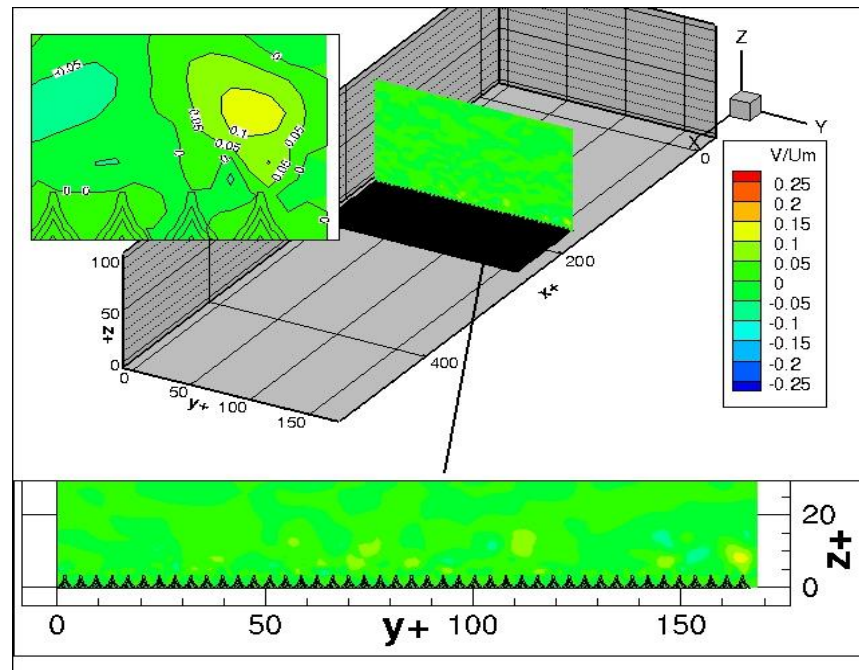
Figure 6-32 lateral velocity distribution over scallop riblets at $x^+ =242$.

The low streamwise velocity inside the valley (around 10% from mainstream velocity) and height of h_p have significant effects on the lateral and normal velocity of the flow. Figure 6-32 shows the lateral velocity over the scallop riblet. The extension of the viscous wall layer will prevent the formation of lateral vortices that will appear in the flow over smooth surfaces or blade riblets. This leads to a reduction of the lateral motion, which means less momentum will transfer to the near wall region and reducing the skin friction significantly over the riblet area.

Figure 6-33 shows the lateral velocity contour close to the riblets. The results show that the high lateral velocity core (20% from mainstream velocity) is shifted up towards the main flow stream which significantly reduces the high momentum flow close to the wall and reduces skin friction. However, the formation of lateral vorticities in the free stream will increase the ejection of the vortices in the normal direction which appears as normal velocities in the normal direction. The increase in the normal velocity will increase the shear stress in the thin shear layer. Figure 6-34 shows the normal velocity distribution over the scallop riblets. The formation of normal velocity regions means more mixing between high and low velocities. Although this mixing will cause more momentum transfer and more chaotic and high TKE, the area affected by this high TKE is still less than in smooth surfaces.
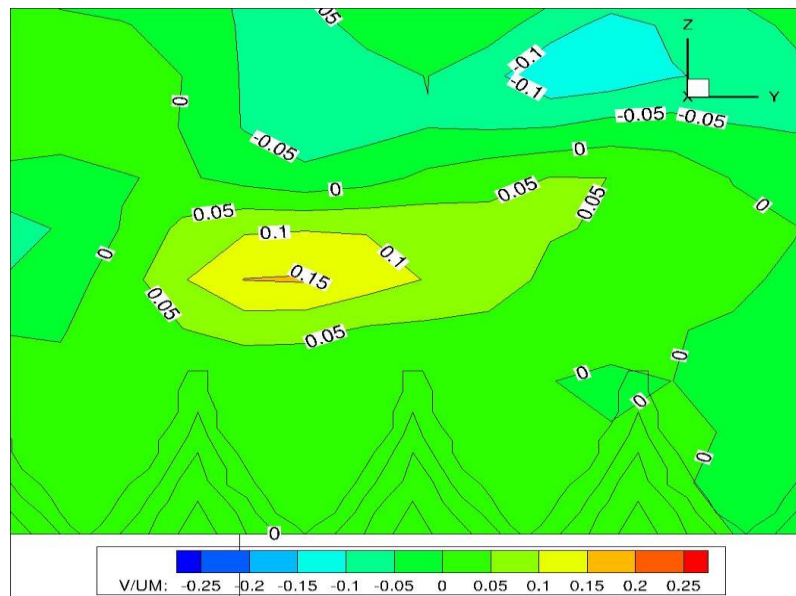
Figure 6-33 lateral velocity contour over scallop riblets at x^+ =242 close image.
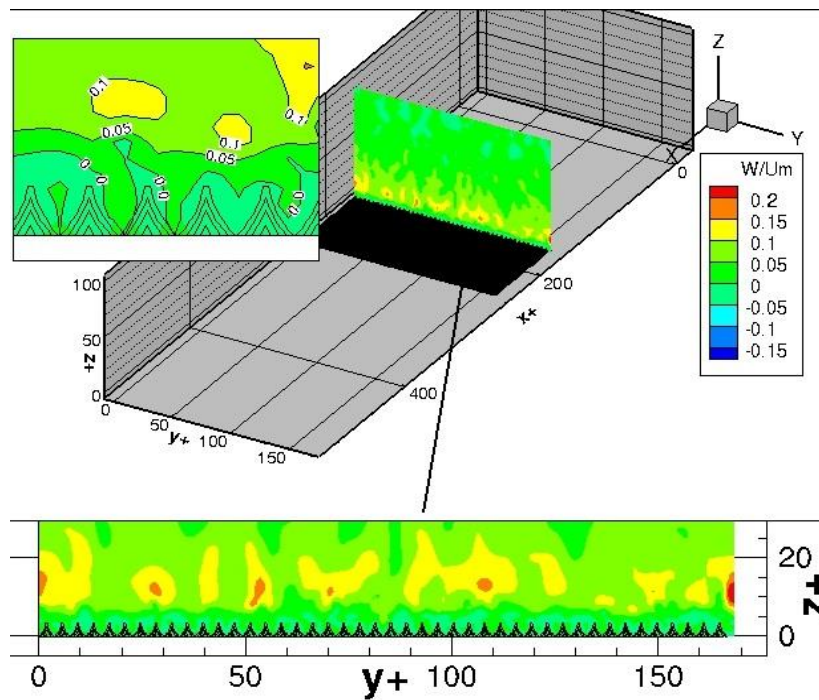
Figure 6-34 normal velocity distribution over scallop riblets at x=242.

6.5.1.2 Drag Reduction

Figure 6-35 shows the TKE over the scallop riblets. TKE over scallop riblets at the riblet tip was reduced as a result of the reduction in the lateral and normal velocities at this level and below. However, the significant increase in TKE energy was calculated in the free stream at a higher level from the tip and in front and behind the riblets. The increase in TKE in front of the riblets is due to the riblet thickness at the base, where the flow is forced to stagnate and change its direction, generating high TKE spots. Meanwhile, the increase in TKE behind the riblets is due to the mixing of the flow that leaves the valleys at low velocities. Moreover, the separation in the flow part that was attached to the riblet tip surface also increased the TKE behind the riblets.
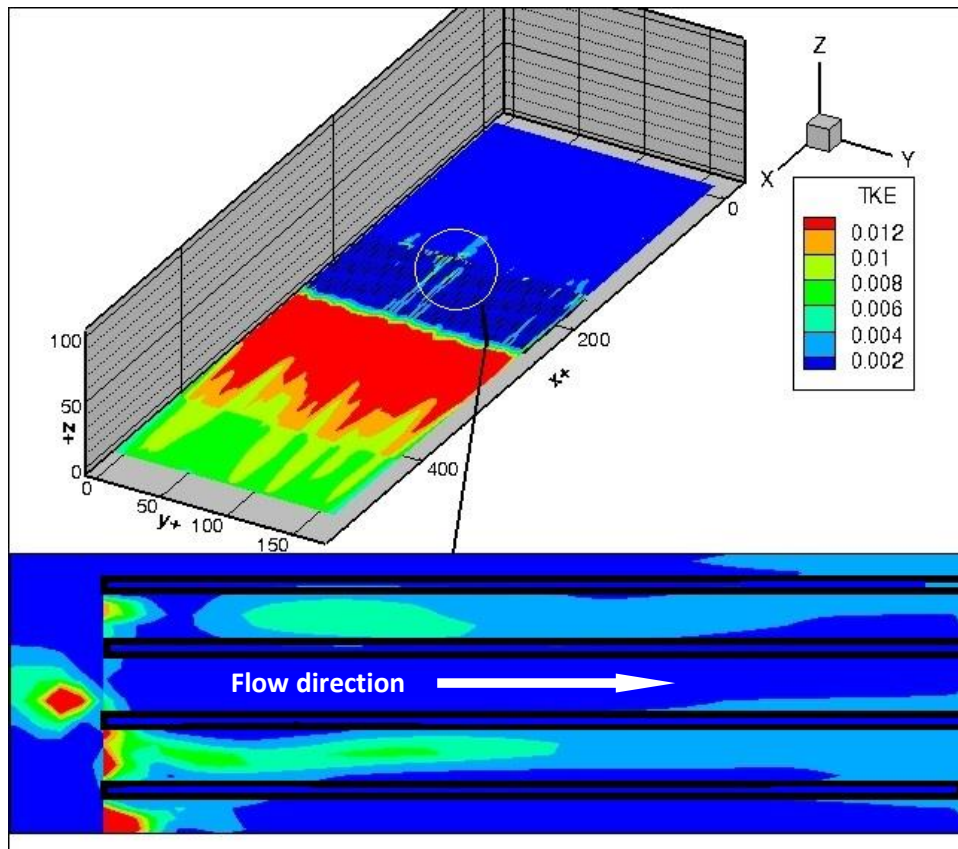
Figure 6-35 TKE over scallop riblets at $z^+ = 5.5$.

Figure 6.36 shows the shear stress over the scalloped riblets. The shear stress contour at the riblet tip is reduced due to the reduction in velocity components and TKE. As the same concepts of the TKE, the shear stress shows low values (compare to a smooth surface at the same position) over the riblets and moderate values in front the riblets and

high values behind the riblets. However, the shear stresses values at the front of the riblets are still lower these that of smooth surfaces despite the riblets thickness. The low velocities above these layers reduce the effects of the increase in wet area due to riblet thickness. By contrast, the shear stress behind the riblets is mainly skin shear stress. These high values are due to the high mixing rates between high and low-velocity flows. The low shear stress over the riblets is obtained as a result of the low velocities and low velocity fluctuating in the valleys. Also, the pressure build up in scallop riblets is less than the pressures build up in triangular riblets, the fact that helps to reduce pressure drag.
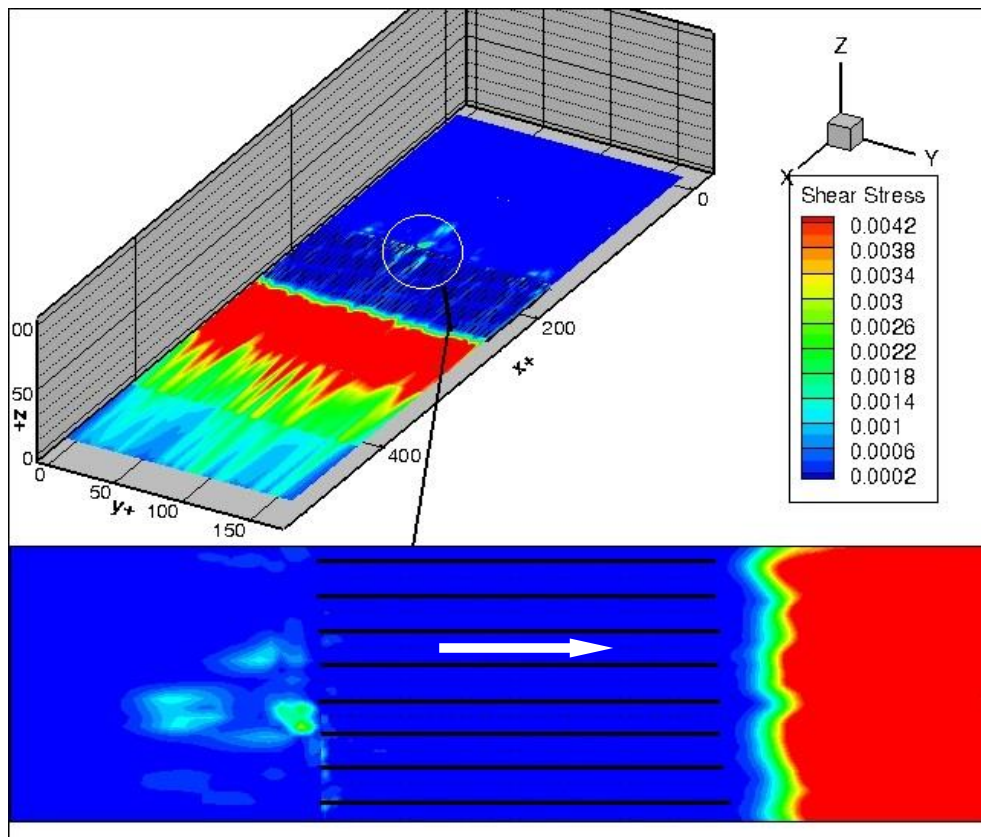
Figure 6-36 Shear stress over scallop riblets $z^+ = 5.5$.

6.6 Manufacturing Group

Modified scalloped riblet geometries, for example, diamond, lotus, and sharkskin, were also numerically tested to improve and gain more drag reduction. The results show no significant improvement and sometimes worsen the results in the case of shark skin. This suggests no real gain compared to the extra costs of manufacturing these geometries.

Table 6-1 shows drag reduction regarding wall shear stress for the patch of the riblets and the pressure gradient for the verification group and the modelled group. Drag reduction results were taken only for the zones that contain the riblets and compared to the same zones smooth surfaces. For each case, the shear stress was averaged in two levels, i.e. at the base of the riblets, and the tip of the riblets and the obtained results were considered to be the value of the shear at that level. The pressure gradient was calculated by dividing the pressure along the riblets over riblet length. The pressure was averaged using pressure values at the beginning and end of the zones. The results show that the blade riblet is the best in drag reduction and pressure gradient, and the triangular riblet is the worst between all tested geometries. However, the fact that the blade riblet construction is very weak and has manufactural difficulties suggests using scallop riblets as a compromising solution.

Table 6-1 drag reduction and pressure gradient for different surfaces tested.

Surface	h/s	s μm	h μm	s^+	Drag reduction %	Pressure gradient Pa/m
Smooth surface	-	-	-	-	-	0.8
Blade riblet	0.7	280	200	17	10.29	-30
Triangle riblet	1	250	250	15	2.9	22.4
Scallop riblet	0.7	110	80	17	6.7	14.7
Diamond riblet	0.5	320	155	18	6.1	14.0
Lotus riblets	0.6	250	135	16	6.6	13.5
Shark skin riblet	0.4	520	230	17	0.5	1.5

CHAPTER 7

EXPERIMENTAL WORK

7.1 Introduction

The experimental work in this thesis is divided into three groups. The first group was carried out on the channel rig, where the isothermal flow blew through the duct, and the velocity near the wall is measured using hot wire and LDA systems. The second group is isothermal experiments on a swirl burner with different nozzle surface condition (smooth, scallop structure and stainless steel grid as a liner). The final group is combustion experiments on the nozzle with 150μm stainless steel wire mesh.

7.2 Isothermal Diffusion Flow

The numerical results from Hydro 3D with the manufacturing considerations led to choosing the scallop riblet and other designs derivatives from scallop riblets as geometries that could be constructed and experimented. The experimental tests were carried out on an experimental rig that was described in Chapter 4. The chosen geometries were constructed as small circular inserts fixed on large disks, which flushed to the internal surface of the upper wall. Two measurement systems were used to measure the velocity distribution near the wall over the riblets. The velocity distribution was measured first using hotwire anemometry for two cases, i.e. smooth surface and scallop riblets. The sensitive construction of the wire – probe (55P14) limited the distance close to the wall could be reached without destroyed the probe. The closest reached distances from the wall were 50μm for the smooth surface and 125μm from the scallop riblets, below these distances the probe destroyed three times. For certainty purpose the following steps were applied:

- The tests were repeated five times for each geometry.
- The results for each geometry were averaged.

- The test that shows most odd results that exceed 5% from the average values was dropped.

- The rest values were averaged again to obtain one set of results for each geometry.

Like the numerical results, the experimental results show the same trend. For the flat plate, the velocity profile shows linear distribution at $z^+<5$, where the viscous wall sublayer plays the major role. Then the influence of the presence of the wall starts to be weaker at $5< z^+< 30$, and the effect of the mainstream significantly appear at $35< z^+$.

For the riblet surfaces, regardless of the geometry, due to the technical necessity, the results recording starts at $z^+\approx5.5$. The results show that the scallop, diamond, and Lotus surfaces have a similar impact on the velocity distribution, especially in the area at $6 < z^+ < 30$, where the geometries caused a sharp increase in mainstream velocity compared to the mainstream velocity values for a flat plate. This behaviour supports the explanation that a reduction in lateral and normal velocities is observed due to flow over the riblets. The increase in streamwise velocity near the wall has its drawback, which is the wall shear stress. However, the area in contact with high velocity for the riblets surfaces is less than for the flat plate, thus reducing the wall shear stress as a consequence. For example, the scallop riblet has an area in contact with the high velocity is around 0.7 compared to the area of the flat plate.

From the error bars in figure 7-1, the best results are the lotus geometry. However, the Lotus geometry is difficult to construct inside the nozzle because of the limitation to access the workpiece using EDM machines. The other option is to use RAM EDM, but the improvement in the results of the lotus geometry compared to the scallop geometry do not justify the extra cost and time of switching to RAM EDM.
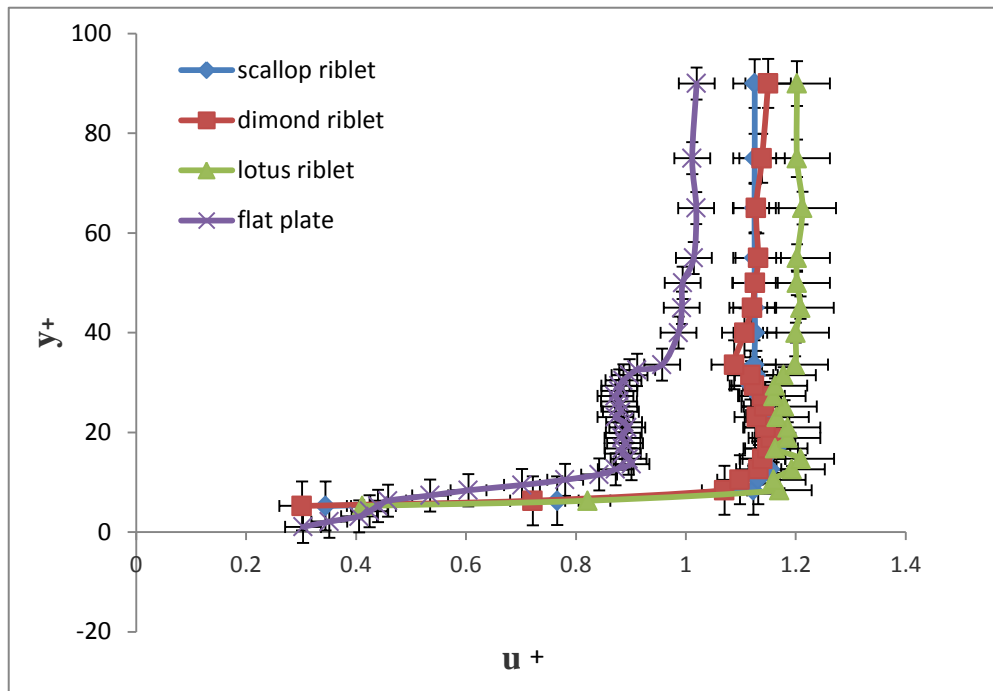
Figure 7-1 error bars for the experimental velocity profile (boundary layer) for different geometries using hotwire.

Since the hotwire probe has been used in velocity measurements with difficulty to measure velocity over wide area surface, one-dimensional LDA system used to measure a sample area over the smooth and riblet surfaces. The area covered by LDA was 1.0 cm
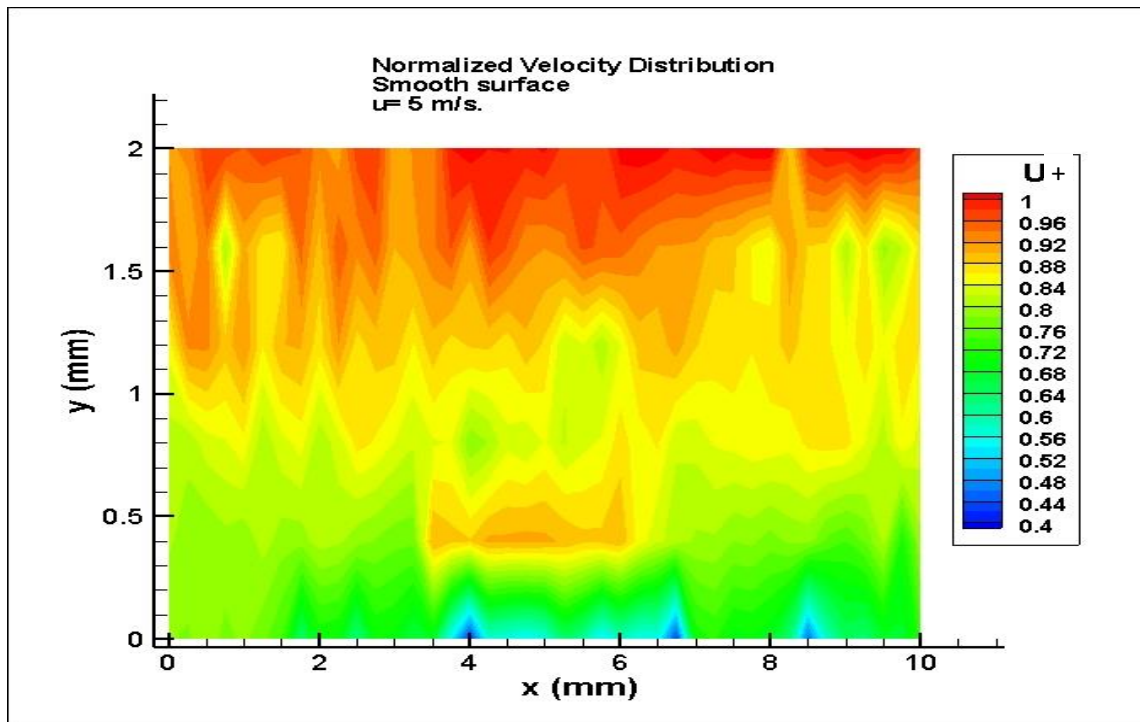
Figure 7-2 The normalised stream velocity distribution for a smooth surface. The measuring area starts at 0.3 mm from wall.

(along with the surface) x 0.2 cm (normal to the surface). The closest distance to the wall reached by the LDA was 0.3 mm. Figure 7-2 show the normalised stream velocity distribution for a smooth surface.
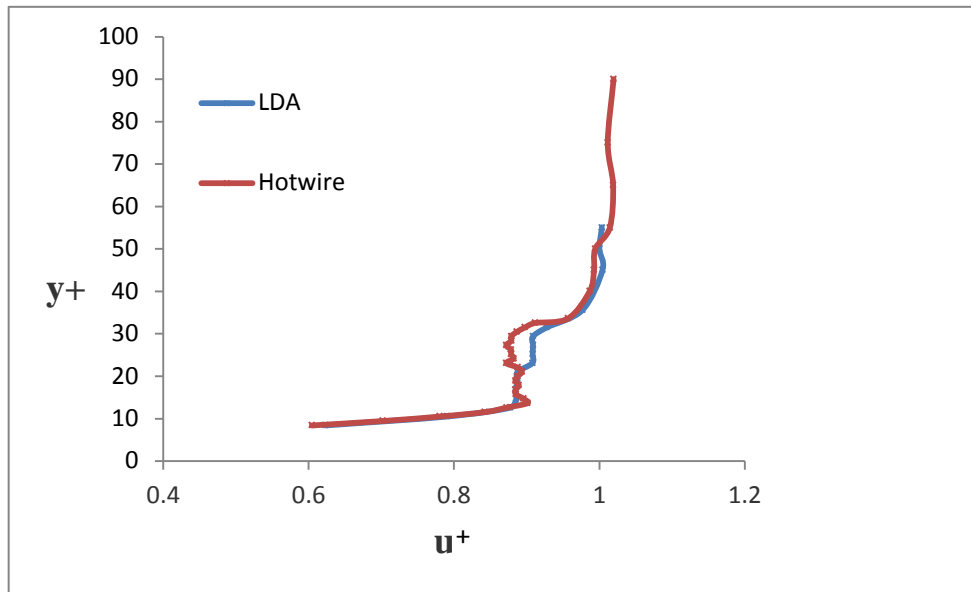
Figure 7-3 LDA and Hotwire results comparison for the smooth surface.

LDA results for the smooth surface show the normalised velocity ($u^+= u/U$) varies from low values around 0.6 at a distance around 0.3 mm from the wall, which represents $y^+ = 8$, reaching the streamwise velocity value at 2 mm from the wall which represents $y^+ \approx 50$. Comparing the LDA results to hotwire results show that the behaviours or trends of velocity profiles are similar, as shown in figure 7-3. The small change in velocity profile between Hotwire and LDA could be as a result of using seeding in LDA measurements Melling (1997).
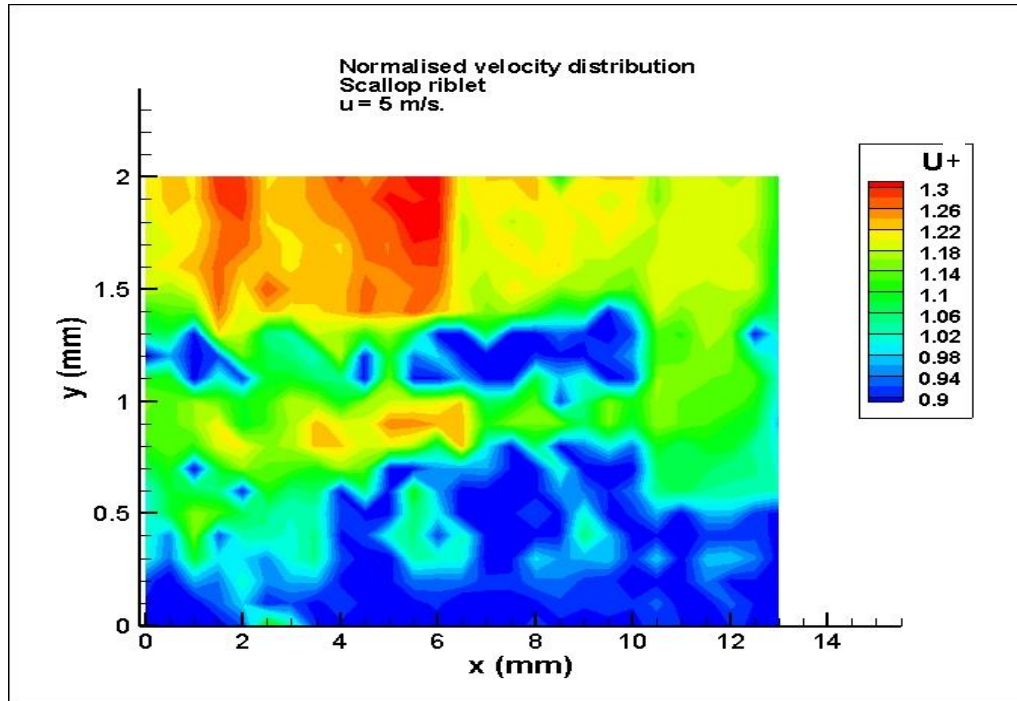
Figure 7-4 the normalised streamwise velocity profile for scallop riblets.

Figure 7-4 shows the normalised streamwise velocity profile for scallop riblets. The results show the difference in streamwise velocity between the smooth surface and the scallop riblets. The velocity values are higher in the case of the scallop everywhere compared to the smooth surface. These results confirm the hotwire results and the numerical results. Although reach close to the smooth surface or the riblet surface was not achieved to have a better understanding of the flow behaviour at the riblets, the settled seeding particles show interesting results.

The seeding particles deposit as a thick layer on the smooth surface while the seeding particles are significantly removed from scallop surfaces as shown in figure 7-5 and figure 7-6. These surfaces are called antifouling surfaces. The antifouling surfaces are the surfaces that have the ability to invest its share and the fluid flow to avoid any contamination or dirtiness Bixler and Bhushan (2014). The self-cleaning effect shows that the velocity in streamwise direction is increased near the scallop tips which prevent the seeding particles from a deposit on the riblet surface, while on the smooth surface the amount of seeding those deposits was much higher due to the low velocities near the wall.
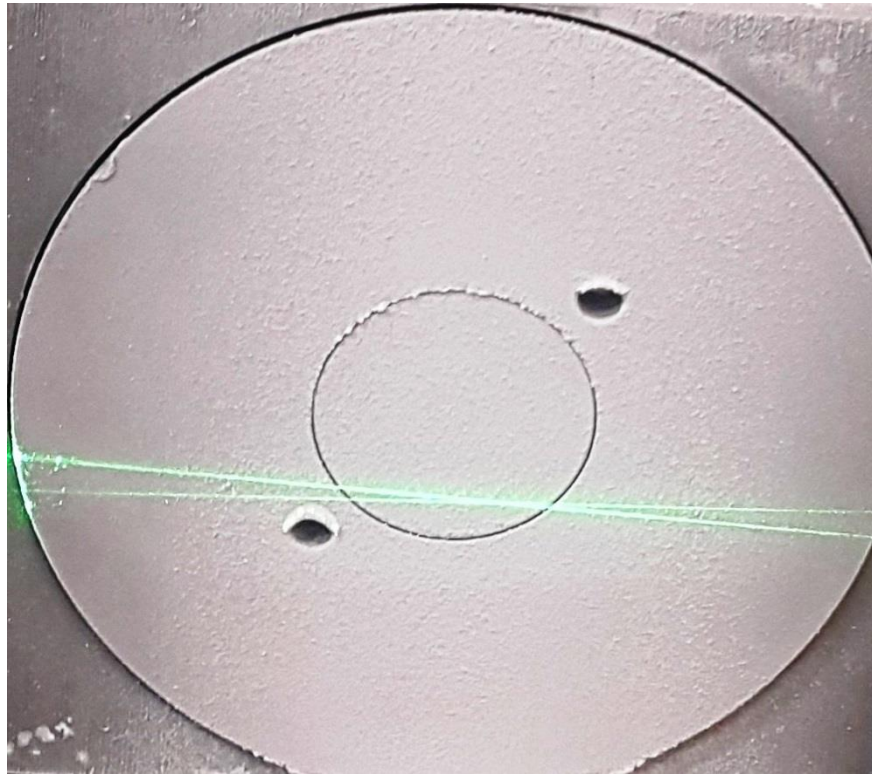
Figure 7-6seeding deposit on smooth surface.

Figure 7-5 seeding deposit on riblet surface (scallop surface).

Hotwire experimental results of the isothermal diffusion flow showed that scallop, diamond and lotus geometries have close results in term of velocity profile with some leading for the Lotus geometry. Also, understanding of the limitation of the existing WEDM (wire electrical discharge machining) machine and to reduce the range of LDA experiments the scallop riblet was chosen as riblet surface to carry out LDA tests. LDA results emphasise the correlation between hotwire and numerical results. The main difference between scallop riblets and diamond and lotus riblets is that the scallop riblets have long extended surfaces along the flow stream direction while the lotus and diamond riblets have isolated shape like hills. From one hand, the short extended surfaces will reduce the area in contact with high velocity flows which reduces shear stress. On the other hand, the isolated geometries will generate more high local velocity region at each riblet tip.

7.3 Isothermal Swirl Flow

The next step was using WEDM to construct scallop structure inside burner nozzles and test them in swirling flows. Swirling flows have more complicated structures compared to diffusion flows. The total mainstream velocity has three components, a velocity component in the axial direction, a velocity component in the radial direction and a circumferential component. The streamlines are spiral in the downstream direction, so the turbulent structures are subject to the mixed effects of centrifugal force due to the streamline curvature and flow skewness caused by the non-uniform spiral pitch in the flow Kitoh (1991). Despite the significant skewing in the flow body, a thin shear layer close to the wall still exists where the flow does not skew much and obeys the ordinary law of the wall Bradshaw (1971). In swirl flows close to the wall the velocity shows a very steep velocity gradient which does not exist in the other regions. This thin shear layer plays a similar role as the boundary layer in diffusion flows Kitoh (1987). Wall shear stress plays a significant role in swirl decay which influences the flow downstream the exit Steenbergen and Voskamp (1998). To assess the effect of the burner wall roughness on the flow six configurations were tested. The configurations are a smooth nozzle, a nozzle with scallop structure and a nozzle with stainless steel wire meshes as liners. These three nozzles were tested with central air injection and without air injection. Figure 7-7 shows the LDA results of axial velocity distribution at

0.3mm downstream the nozzle exit with no central air injection. The internal wall of the nozzle is located at 0.0, and the centre of the nozzle is located at 1.0. The velocity distribution near the wall is shown in the zooming part of the figure 7-7. Also, the figure shows the CRZ in the middle of the nozzle.
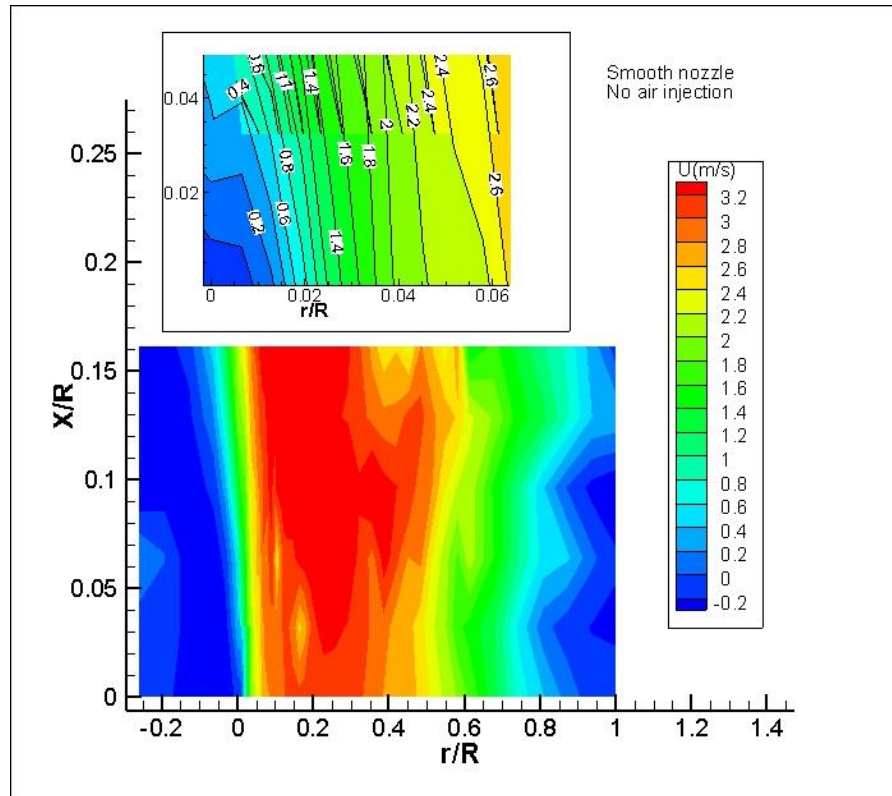
Figure 7-7 axial velocity distribution in smooth nozzle with no centeral air injection

In flashback studies, the CRZ is not preferable due to its role in driving the CIVB. Injecting air in the centre of the nozzle could help in improving the system against CIVB Sattelmayer et al. (2016); Hatem et al. (2017). However, it provokes the BLF to force the flame to try to penetrate the flow near the wall where low-velocity regions exist although the injected air causes sharp velocity gradients near the wall. Figure 7-8 shows axial velocity distributions for a smooth nozzle with central air injection. Injecting air in the centre of pipe pushes the high axial velocity towards the nozzle wall, which means the skewing effect of swirling flow moves closer to the wall as concluded from comparison the zooming part of the figures 7-7 & 7-8. The distribution suggests that the effect of the high axial velocity region comes closer to the wall as a result of the central air injection.
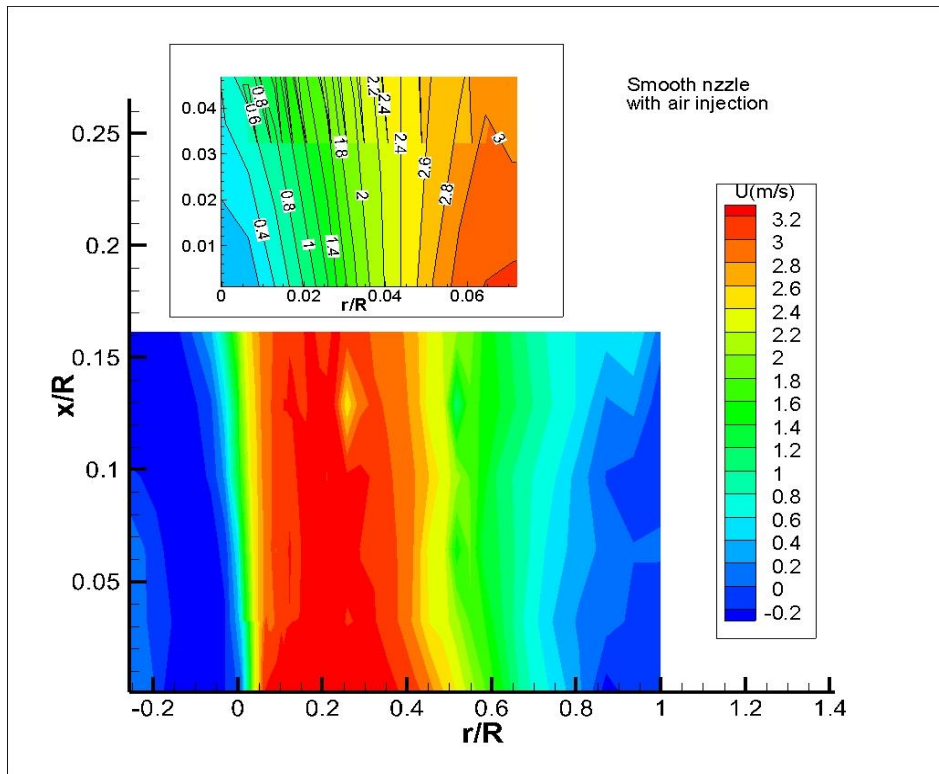
Figure 7-9 axial velocity distribution in smooth nozzle with air injection.
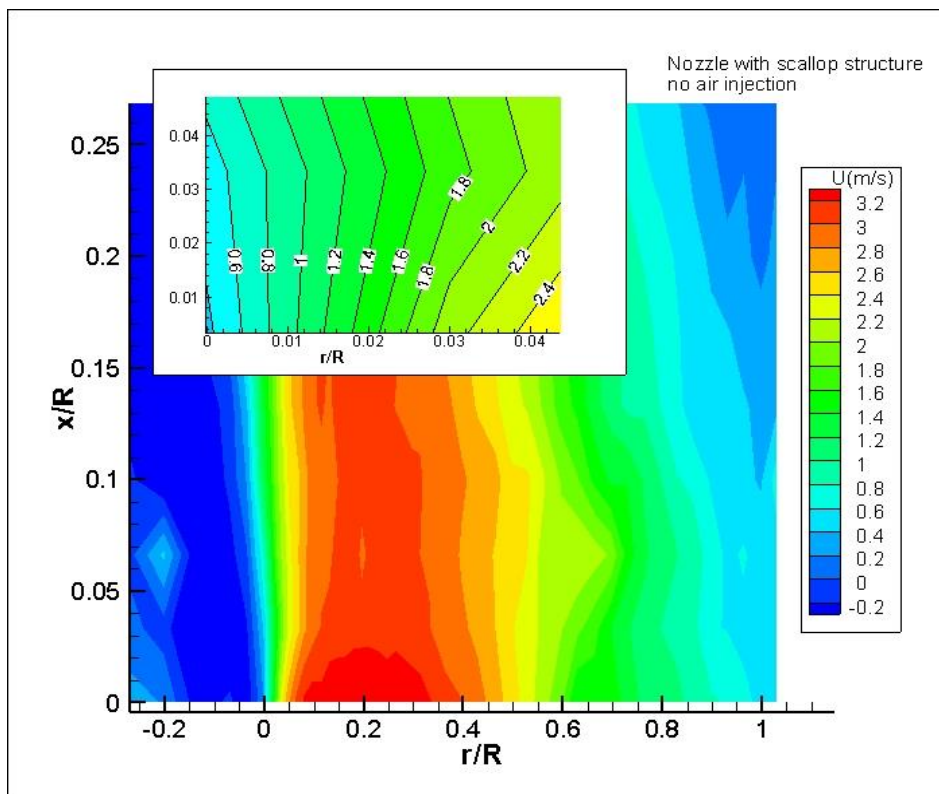
Figure 7-8 Axial velocity distribution in nozzle with scallop riblets
without central air injection.

Figure 7-9 shows axial velocity distributions for a nozzle with scallop riblet structures without central air injection. Results show that using riblet nozzle modifies the flow near the wall and shrinks the wall region more and the flow is accelerated. The acceleration in axial velocity helps in keep the swirling structure of the flow further the downstream. This acceleration pushes the CRZ in the downstream direction which reduces the possibility of the CIVB. Although the results are taken at 0.3mm downstream from nozzle exit due to the LDA specifications, the results show an increase in axial velocity on the wall which is similar to when using riblet in diffusion flows which refer to a reduction in wall shear stress. Further modification in velocity distribution was obtained when using central air injection as shown in figure 7-10. The air injection in the centre pushes the CRZ further downstream while the scallop riblet helps to reduce the wall effect on the axial velocity and reduce the wall shear stress limiting the contacts of the high-velocity flow with riblet tips only.
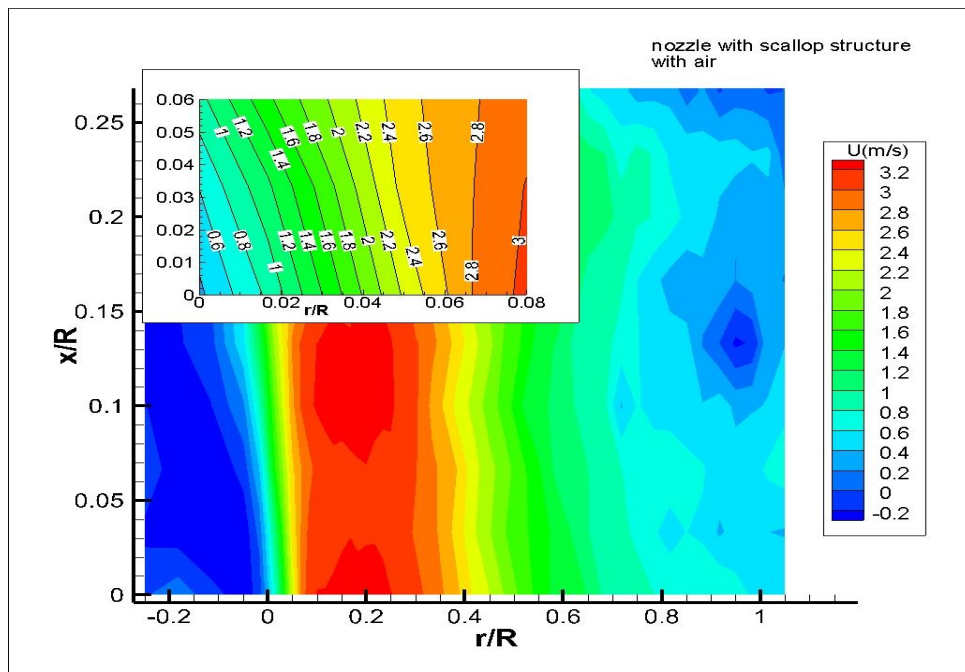
Figure 7-10 axial velocity distribution in nozzle with scallop riblets and central air injection.

Figure 7.11 shows the axial velocity distribution in the nozzle with 150 μm stainless steel wire with no air injection. The results show that the velocity distribution near the wall was improved and the high-velocity region comes close to the wall compared to the smooth nozzle and scallop nozzle without central air injection.
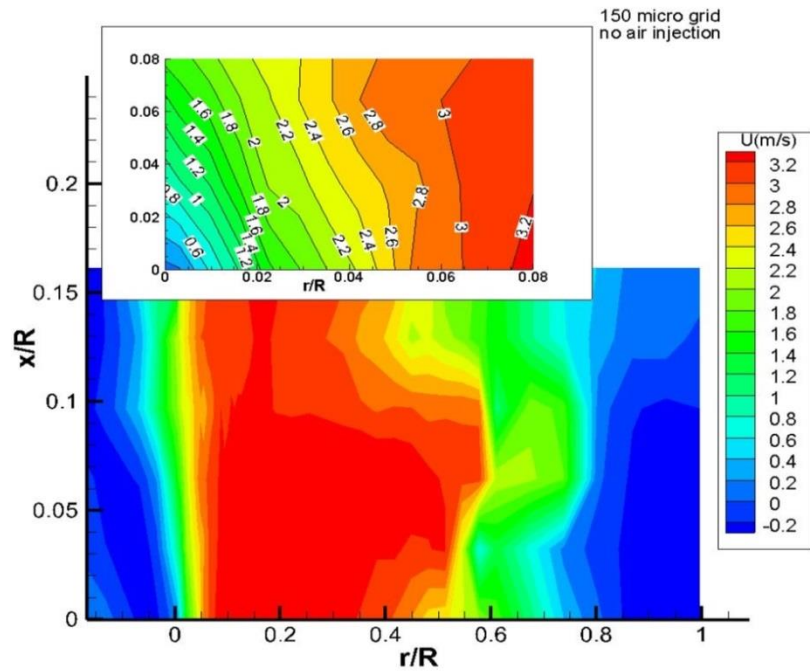
Figure 7-11 the axial velocity distribution in nozzle with 150 μm
stainless steel wire with no air injection.

Figure 7-12 shows the axial velocity distribution in the nozzle with 150 μm stainless steel wire with air injection. The results show a significant push of the CRZ in the centre of the nozzle while the velocity distribution near the wall keeps high velocity profile.
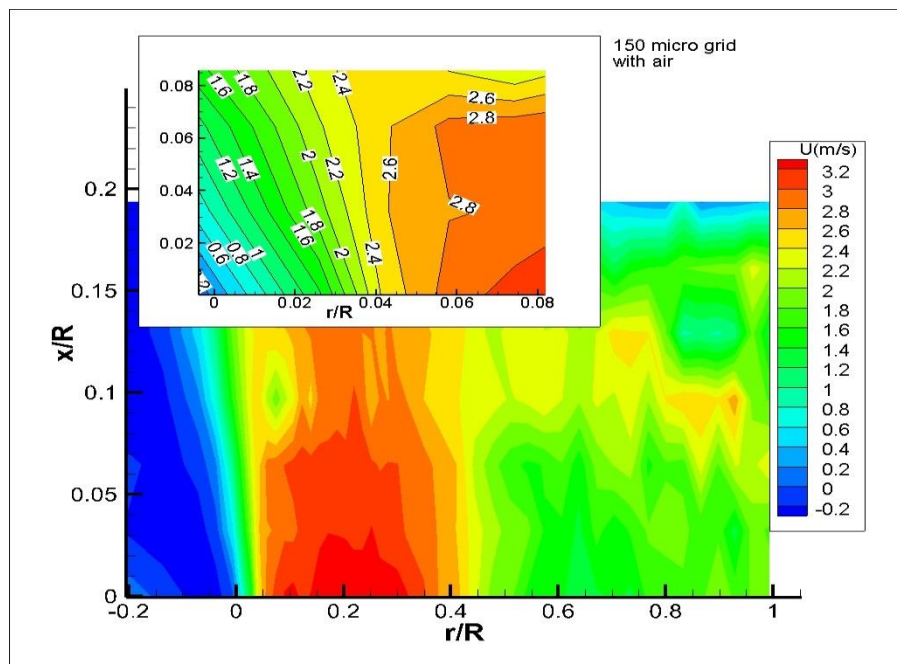
Figure 7-12 Axial velocity distribution in nozzle with 150um stainless
steel wire with air injection.

162
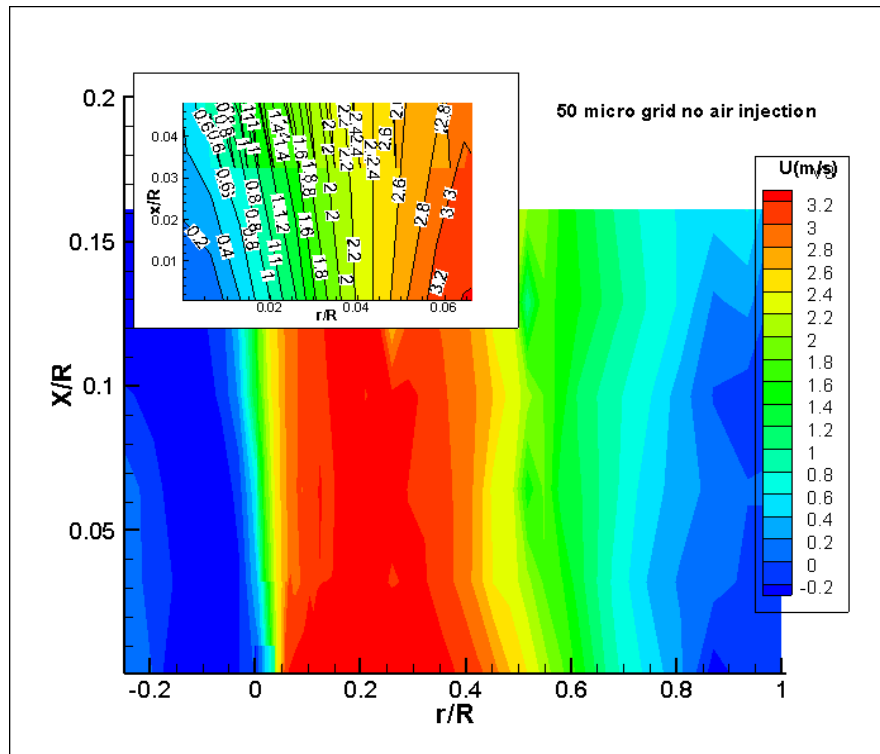
Figure 7-13 the axial velocity distribution in nozzle with 50um stainless steel wire with no air injection.
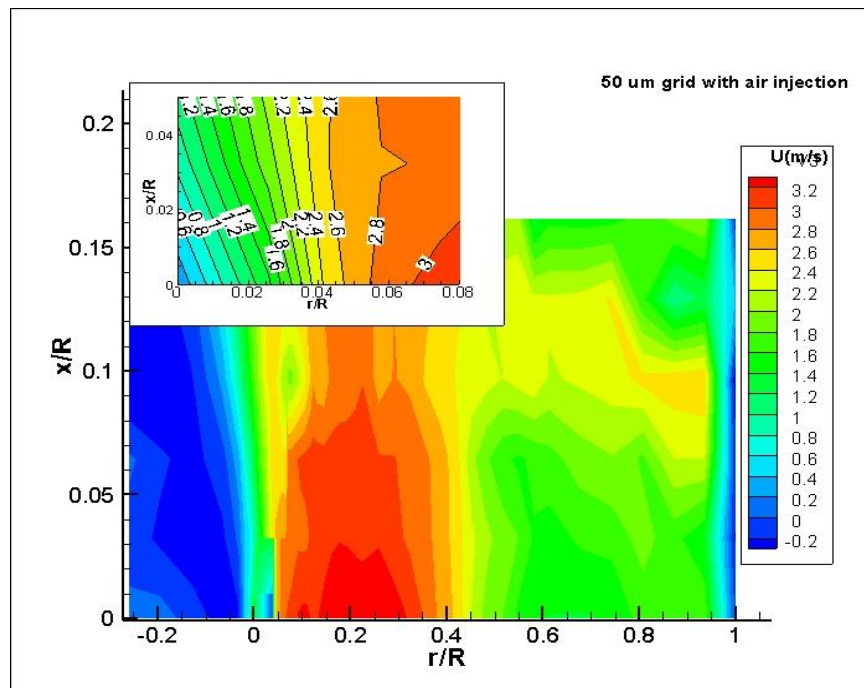
Figure 7-14 The axial distribution in nozzle with 50um stainless steel wire and air injection

163

Figure 7-15 showed that the velocity gradient in the downstream direction for the nozzle with the 150 μm mesh is less than the velocity gradient for the 50 μm mesh, which means that the wall effect on the near wall layer of fluid is less than the effect in case of the 50 μm. Also the outer fluid interaction with the swirl flow is less when using a 150 μm geometry, with a lower velocity decay downstream. This result is important because it explains the improvement in boundary layer flashback when using these mesh wires. According to the Lewis von Elbe formula for the laminar flame speed the sharp velocity gradient increases flashback, where the flame attacks the low velocity region near the wall to penetrate towards the premixing channels.
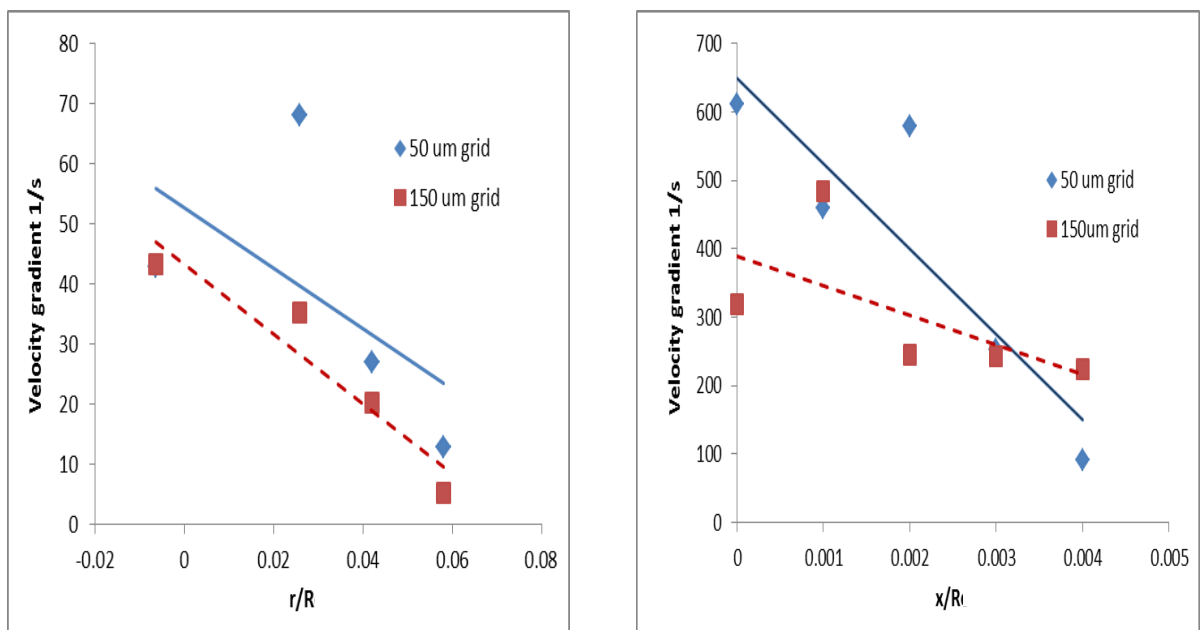
Figure 7-15 Velocity gradient in the radial direction (r/R) (left), and in downstream direction (x/R)(right).

7.4 Combustion Tests

Although using the appropriate diameter of central fuel injector or central air injection can considerably tackle upstream flame propagation through the central core, especially CIVB, some drawbacks can arise, i.e. the system could be more likely subjected to wall boundary layer flashback (BLF), especially at higher tangential flow rates. Large diameter fuel injectors enforce the outer shear layer to propagate radially outwards and to stabilise at the nozzle lip, Figure 7-16a. In most practical applications this contact between flame and nozzle lip has some consequences represented by life degradation of

A) Central fuel injection   B) Central air injection

Figure 7-16 Effect of using central fuel injector and central air injection on the outer boundary layer propagation.

nozzle material due to continuous high temperatures in addition to the possibility of increasing pollutants level. At high equivalence ratios, the outer boundary layer between the shear layer and the nozzle wall starts an upstream propagation via low-velocity sublayer leading to flame flashback. High momentum axial air injection also performs the same function of the central fuel injector, i.e. the high resistance against central upstream flow breakdown propagation imposes radial propagation of the flow. Hence the outer shear layer locates on the burner rim or inside the nozzle, Figure 7-16b. Despite using central air injection can maintain a stable flame slightly longer than that of using central fuel injectors, boundary layer flashback can onset when increasing equivalence ratios.

Thus this chapter describes the appropriate techniques to reduce the possibility of boundary layer flashback when central fuel injectors or central air injection are used as flame stabilisation techniques.

Flame flashback via wall boundary layer depends on many parameters such as the flow field characteristics, equivalence ratio, pressure, temperature, wall temperature, confinement type, the state of the boundary layer and the geometry of interior liners in the burner nozzle Eichler and Sattelmayer (2011a); Ebi and Clemens (2016). The geometry of the nozzle wall plays an important role in upstream flame propagation during boundary layer flashback, i.e. The interaction between nozzle wall and flame can affect directly the amount of heat flux which consequently changes the wall quenching distance Gruber et al. (2012).

Furthermore, the interaction between nozzle wall surface and the parallel flow generates a viscous drag which produces an adverse pressure gradient, consequently promoting velocity gradient. The degree of wall roughness is of particular importance in this context as it promotes the amount of heat transfer, hence decreasing or increasing the shear wall stress. Consequently, the velocity distribution mode and the difference in Reynold stresses, especially in the sublayer. The contribution of the effect of the surface type on the mean velocity profile and hence the wall turbulent boundary layer usually is described by a roughness function which represents the difference in normalised velocity distribution between smooth and rough surfaces Antonia and Krogstad (2001). The direction of flame movement on the wall is also important when considering its effect on flame flashback mechanism and its quenching position. From one hand, when flame front is parallel to the wall, the quenching mechanism called Head-on quenching (HOQ); on the other, when the flame is perpendicular to the wall the mechanism is called side-wall quenching (SWQ) Dabireau et al. (2003).

However, in swirling flows the flow directions are very complex compared to other flow types, as the existence of coherent structures and their interaction with each other make the analyses and prediction of wall boundary layer characteristics a seriously challenging task. These flows are extremely affected by the variation of flow streamlines and the adverse pressure gradient downstream all directions (axial,

azimuthal and radial). Therefore the flame direction on the wall during boundary layer flashback (BLF) cannot be simply studied for a certain direction, and the predicted movement will depend on the inside linear geometry of the nozzle.

Although most swirling flows are turbulent, the flame-wall interaction is considered laminar flow due to the considerable reduction of flow velocity in the adjacent region to the wall that results from viscous friction. Thus, most hypotheses about boundary layer flashback are based on laminar flame speed. However, this correlation can be adopted for turbulent flows as well. Microsurfaces of different geometries can positively increase the boundary layer flashback resistance. Those surfaces have high potentials in reducing drag effect in the wall adjacent region. However, their ability in dealing with drag forces depends mainly on their configuration and the nature of the drag force itself.

Two different geometrical grid configurations were used as shown in figure 5-26, those grids can change the flow field characteristics and hence boundary layer adjacent to nozzle wall as previously seen. Stability limits for different grids were determined under different configurations with without central fuel injector, and with and without central air injection at various inlet tangential flow rates. Central air injection was kept at 50 LPM which accounts for 10% of the total mass flow rate to avoid swirl strength degradation. The burner inlet tangential velocity has been used to illustrates the flame flashback trends, as this allows a fair comparison between cases without considering the change of Re at the burner mouth and enables comparison with different size burners. Experiments were repeated five times until a deviation not greater than 5% in tangential velocity was achieved.

During LDA measurements the main concern with using different grid sizes was the possibility of seeding can block the grids during the test, thus after each test a new piece of grid material is used. The velocity profile and turbulence intensity measurements were carried out at 0.3 mm downstream the burner mouth.

To achieve a complete understanding of the effect of wall microstructures surfaces on flame stability it is vital to ensure that BL flame flashback mechanism is kept. Thus two

techniques have been used to enforce flame propagation via wall boundary layer, i.e. diffusive fuel injector and axial air injection.

For a diffusive fuel injector, the outside diameter was 23 mm. This diameter is enough to ensure BLF as proved before Hatem et al. (2015). While air injection is proved to be more efficient in preventing upstream flame propagation through the central core, hence high resistance against CIVB, consequently the flashback mechanism is mainly BLF. Figure 7-17 shows the difference in flame flashback trends when using a diffusive fuel injector as a flame stabiliser or bluff body and that when the 50 μm grid was used as linear for the nozzle wall.
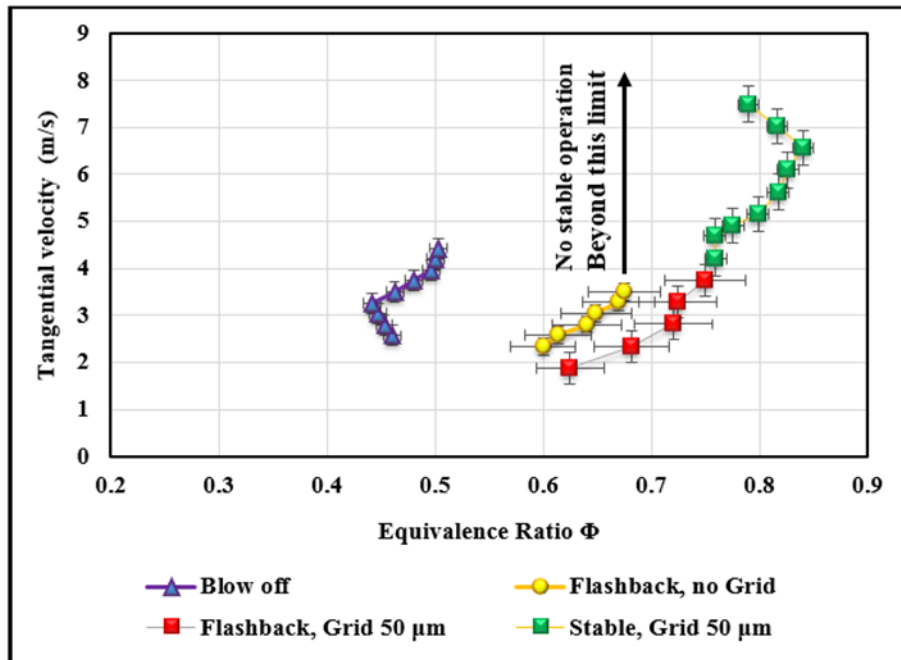
Figure 7-17 The effect of using the 50 μm Grid microsurfaces on the stability of operation.

As can be seen from figure 7-17, when no grid is used, the stability operation region is located at $\Phi \sim 0.45-0.65$, and the maximum tangential velocity that can be achieved is almost 4 m/s. This could be attributed to the limitation of the nozzle surface resistance to boundary layer flashback at high tangential velocities. Higher values of tangential velocity led to the outward radial propagation of the CRZ which in turn pushes the high momentum flow region closer to the wall. Due to the lack of damping mechanism against BLF, flashback can occur earlier.

By contrast when the micro mesh is imposed (50 μm grid) the change in drag force, and hence downstream velocity gradient will positively support the BLF resistance. For this reason, a flame flashback occurs at slightly higher equivalence ratios. Moreover, at higher flow rates the potential flame flashback resistance provided by the micro mesh consolidates the flame stability, and no flashback is observed.

The change in drag force adjacent to nozzle leads to a decrease in the turbulence fluctuation compared with that when no grid is being used as shown in figure 7-18. Consequently, this reduction in turbulence decreases the local turbulent flame speed, hence promoting good flashback resistance.
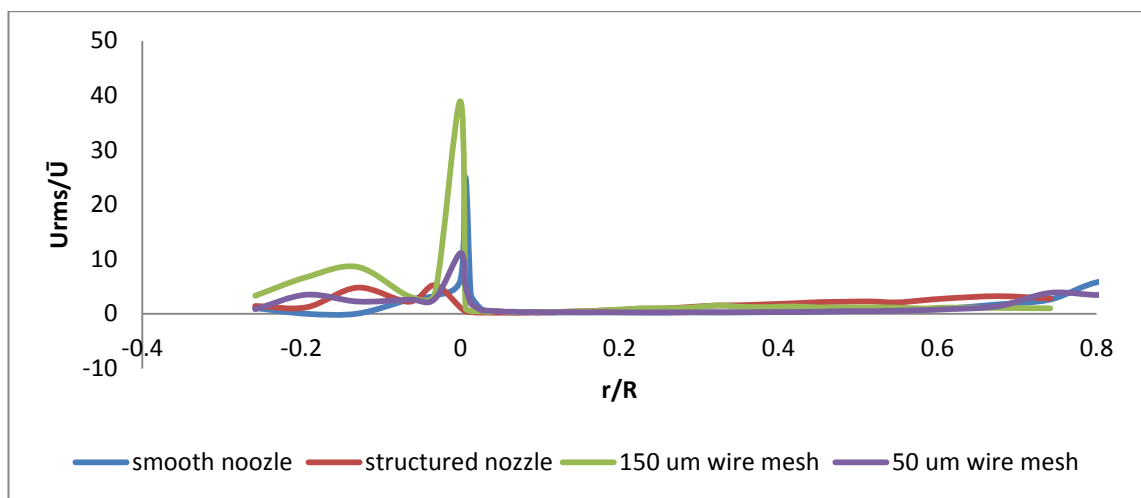
Figure 7-18 The effect of using 50 μm Grid microsurfaces on turbulence intensity.

The effect mentioned above of the micromesh on turbulence intensity values revealed the considerable variation in flow field velocity and hence the axial velocity gradient. The effect of using another micromesh configuration (150 μm) on flame flashback trends is almost the same for that of 50 μm regarding equivalence ratios. However, this configuration led to flame flashback late up to 5 m/s of tangential velocity range, figure 7-18. This difference in flashback trends suggested that wider micromesh configuration has less effect on velocity gradient and other flow field characteristics close to the nozzle wall.
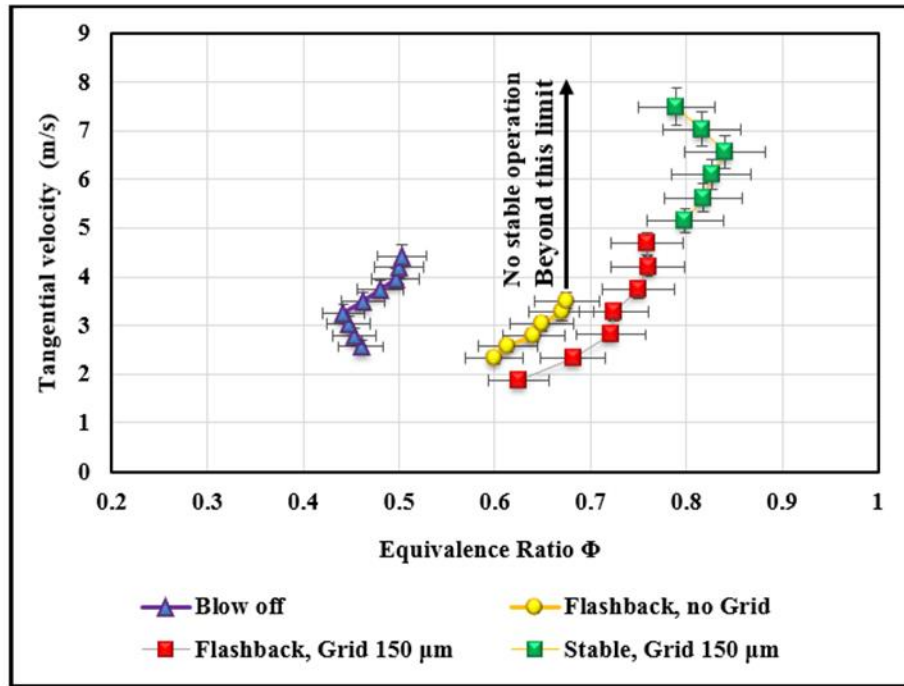
Figure 7-20 The effect of using 150 μm grid microsurfaces on flame flashback trends.

Diffusive air injection has proved its potentials for flame flashback resistance Hatem et al. (2017). However, this resistance is mainly against CIVB, as it has been visually observed that the high momentum axial jet at the central axis enforces the flame to propagate via the nozzle wall boundary. Thus, the use of air injection has proved to be
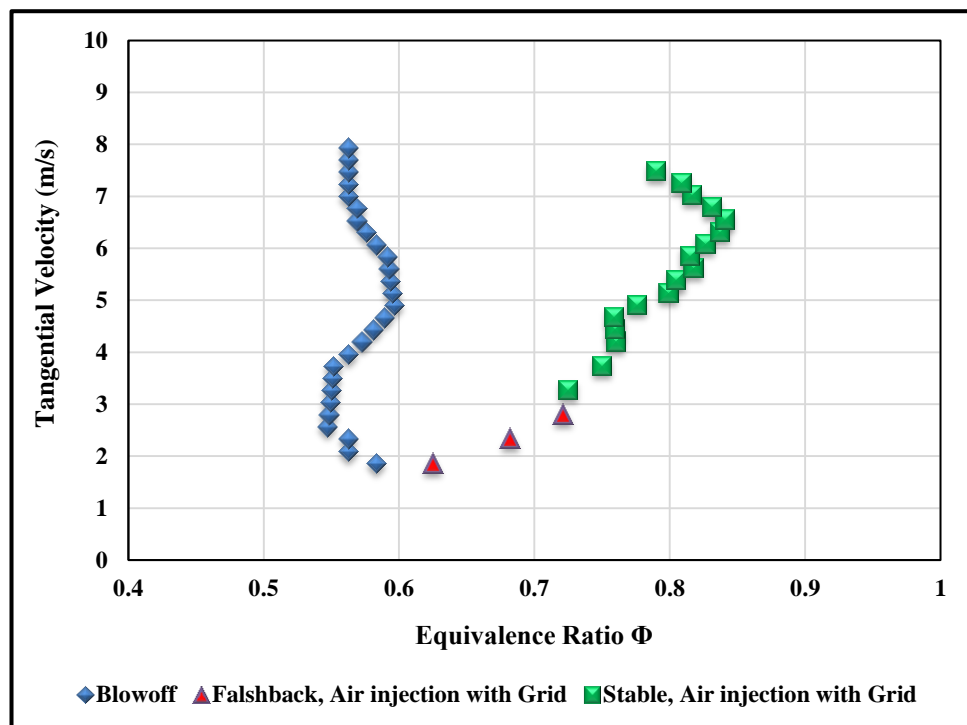
Figure 7-19 Effect of using air injection with 150um micromesh grid for flame stabilisation purposes.

a potential technique to resist BLF mechanism in combination with microsurfaces. Figure 7-21 shows a comparison between two configurations.

From figure 7-21 it can be observed that at a tangential velocity of 1.8 m/s blow off and flashback curves are very close to each other leading to a narrow stability region. Upon increasing equivalence ratio and tangential velocity, the stability map became wider. However, there is still some limits over which the flame is not stable, and flame flashback is observed. The last conditions where flashback is observed were tangential velocity = 6 m/s, Φ=0.83. Beyond these values, no flashback is observed.

When the grid is used for additional stability support, significant improvement in flashback resistance is achieved. The flame flashback is observed for inlet tangential velocity ranging from 2 to 2.8 m/s; beyond this limit, no flame flashback occurs, and operation is stable for higher equivalence ratios and high tangential flow rates.

This finding is interesting for switching to higher power operations at constant equivalence ratio or switching to another fuel blend which might have stability operation regions overlapping with the original fuel stability margin. Moreover, the high BLF resistance at high flow rates is very important in protecting the nozzle inside walls due to harsh environment conditions represented by high temperatures when the flame comes in touch with the nozzle walls.
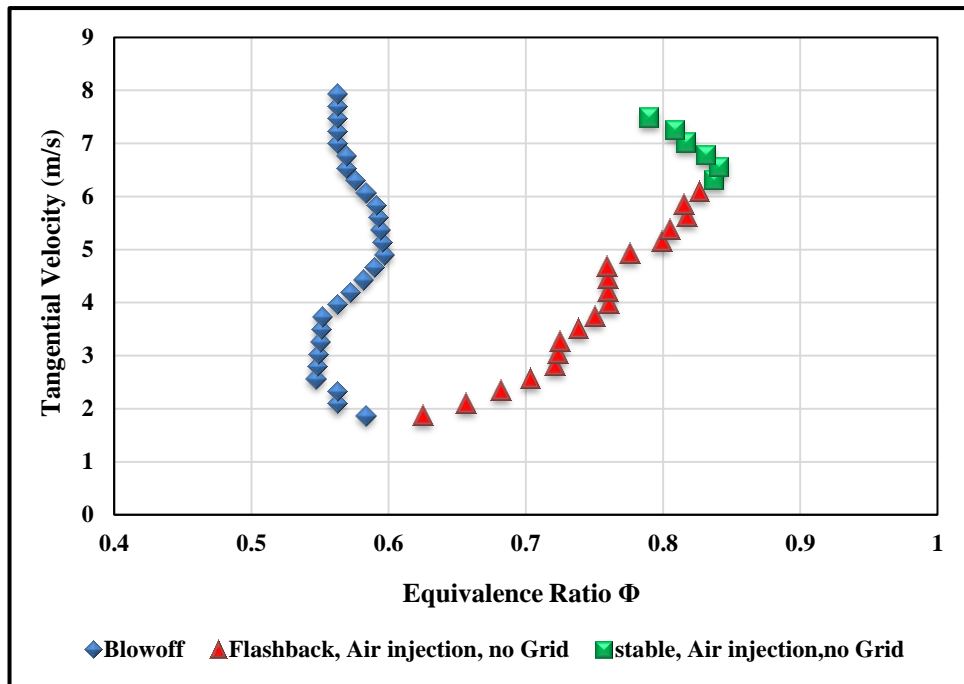
Figure 7-21 Effect of using air injection for flame stabilisation purposes

Based on the previous results, it appears that the two flame flashback resistance mechanisms, i.e., air injection and microsurfaces are working together to achieve high flame flashback resistance for BLF and CIVB.

Figure 7-22a represents stable operation where the flame is anchored downstream of the nozzle. The equivalence ratio is increased by increasing the tangential gas flow rate at constant tangential and diffusive airflow rates; the flame is still stable for a period at constant equivalence ratio, then it starts to move forward and backwards, mainly via burner central axis which refers to the CIVB conditions, figure 7-22b.

However, the axial air injection pushes the flame downstream to its initial stable position. Further increase of the equivalence ratio initiates more violence flame propagation as can be seen from figure 7-22c. Nevertheless, the high momentum diffusive air injection is still coherent enough to prevent upstream propagation via central core.

This process of outer shear layer propagation is observed from one side of the flame, figure 7-22d, and the rest of the outer shear layer propagates towards the nozzle inside

the boundary layer, figure 7-22e. Finally, the entire annular shear layer became totally in contact with the nozzle surface or the grid.
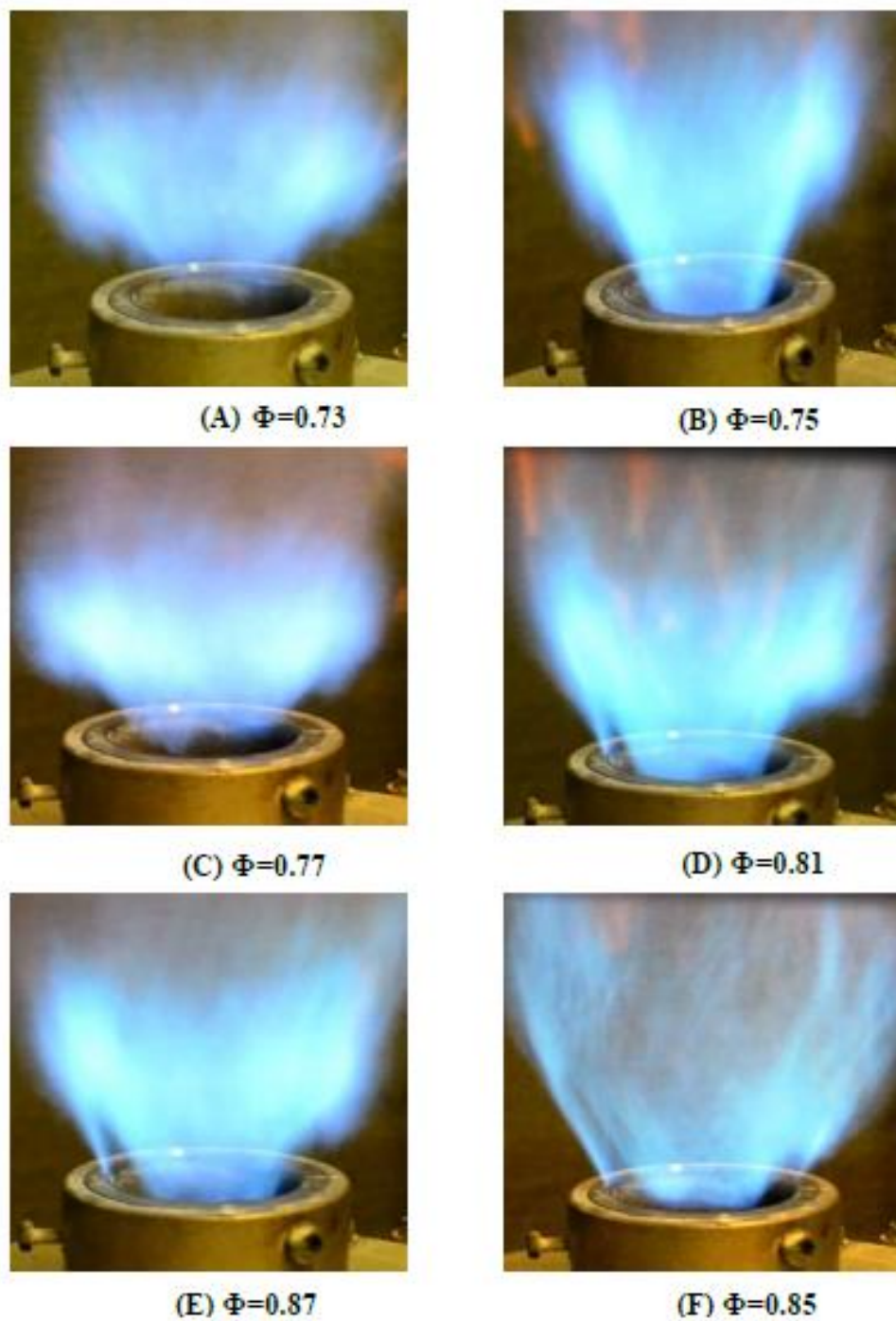
Figure 7-22 Flashback resistance scenario for CIVB and BLFB simultaneously.

7.5 Summary of experimental work

The main outcomes of this chapter can be summarised as follows:

1. Construct microstructure on surfaces, which are exposed to fluid flow, because a modification of the velocity profile near the wall and reduce the effect of the wall on the flow field, which reduces the drag and wall shear stress.

2. Increasing resistance against boundary layer flame flashback needs enhancement of the surface characteristics of the nozzle interior wall in such way that those geometrical modifications lead to increase the velocity gradient close to the nozzle wall to be higher than critical velocity gradient, hence avoid being overcome by turbulent flame speed in this region.

3. Two woven steel micromesh configurations 50 μm and 150 μm have used to investigate their effect on velocity gradient and hence flame flashback trends; those surface modifications have been analysed and investigated numerically by other work.

4. Results showed that micromesh configurations have very good potentials in terms of increasing flame flashback resistance; this observed visually and through increasing operation stability margins compared with nozzle base case (nozzle wall without micromesh).

5. Both air injection and micromesh configurations increase the stability limits considerably, stability margins increased both in equivalence ratio and inlet tangential velocity, and was observed for both micromesh 50 and 150 μm. However, 150 μm reveals slightly better performance. This outcome is vital for combustor systems that require increase in power while keeping constant equivalence ratio. Moreover, such technique provides the possibility of switching from one fuel to another.

6. From an industrial point of view using such techniques is considered as a commercial solution to protect swirl combustors from CIVB and BLF at the same time.

CHAPTER 8

CONCLUSIONS AND RECOMMENDATIONS FOR FUTURE WORK

8.1 Introduction

Propagation of the flame from the combustion chamber into the mixing zone is a phenomenon known as a flashback is one of the inherent problems of lean premixed combustion and essentially determines the reliability of low NOx burners. Flashback can appear as one of the following four phenomena: flashback due to turbulent flame propagation in the core flow, flashback due to the conditions in the boundary layer, flashback induced by combustion instabilities and flashback caused by combustion induced vortex breakdown. The presence of hydrogen in syngas significantly increases the potential for flashback. This problem is considered a serious obstacle in the way of development of gas turbine combustors to switch to a different fuel, whereas using low pollutant blends becomes an urgent desire for low emission requirements. However, it is obvious from the results of in flashback mechansims that to improve swirling system against one mechanism worsen the system to another. A central bluff body, central fuel injection or air injection are common techniques used to improve the swirl burner to reduce CIVB but accepting the worsen to boundary layer flashback. Improvement of the system against boundary layer flashback be could obtained using wall cooling or air injection through tiny slots parallel to the burner walls to dilute the fuel mixture near the wall. However, such techniques increase NOx emissions. Flashback mechanisms are sensitive to the flow structure, especially the boundary layer flashback since it is related to the velocity gradient at the wall according to Lewis Von Elbe formula.

Therefore, passive techniques to control and modify the velocity gradient near the wall numerically and experimentally have been studied in this study. A technique inspired from nature known as sharkskin effects were used, where regular roughness generated by small protrusions from surface called riblets similar to ones that stir up the shark skin and help the sharks to swim fast due to a reduction in drag force.

The wide range of possible geometries that could be investigated in this study and the difficulty of manufacturing microstructured surfaces with high accuracy leads to the use of numerical simulations to choose the optimum geometries.

The numerical part of the study used an in-house LES code (Hydro3D) to simulate the flow over different riblets and compare the results with published experimental studies. Different geometries were numerically tested, i.e., blade, triangle, scallop, diamond, lotus, and sharkskin. However, the main conclusions from numerical studies are:

❖ The code has good accuracy in detecting the flow structure near complex geometries since the results of the drag reduction over blade riblet are compared to experimental results for the same geometry. The comparison shows high accuracy in the range of the studies parameters.

❖ The most significant effect of riblets on the flow is represented by uniforming the flow near the wall and reducing the drag. The mechanism in which these effects are obtained is still not completely revealed. Due to the viscosity of the fluid and the presence of the channel walls, the velocity inside the channel slowdown, moving further along the channel. The slow motion of the flow inside the channel settles the fluid inside the channel and made a fluidic bed, which prevents the high speed from reaching the wall and leads to reduction of drag.

❖ The riblet geometry plays the significant role in drag reduction. The height (h), the space (s) between riblets and riblet thickness (t) has a different impact on the riblet performance. Height to space (h/s) ratio is a more common parameter used to describe the geometrical shape of the riblet, also dimensionless parameters i.e. s^+, h^+ and t^+ are often used in studying the riblets parameters. For each shape, at a range of h/s or s^+ the riblet reaches the best performance. Where the riblet works as a pin to hold the small fluid vortices and prevent them from reaching the wall surface, also the riblets restrict the normal and lateral fluid motion, which significantly reduce the fluctuation in the flow.

❖ The increase in the height of the riblets usually leads to increase the interaction between the riblets pin and the high momentum flow in the buffer zone, which increase the skin friction and increase the drag. Short riblets could lay totally in the viscous sublayer, which eliminates the riblet action on the outer region flow.

❖ The increase in riblet space (s) at a constant velocity also means an increase in s^+ which will allow the vortices to enter the valleys between riblets and increase the wetted area that is in contact with high momentum flow. More wetted area means more skin friction and more drag. The same results are obtained when the velocity was increased at constant riblet space since the vortex diameter is less at high velocity which helps to the vortex to enter between riblets and increase the skin friction. The optimum vortex diameter in this study was found in the range of 25-35 in wall units.

❖ The decrease in riblet space (s) at a constant velocity, also means a decrease in s^+ that will push the vortices to the buffer zone, but at the same time, it will blockage the flow near the wall causing on the increase in pressure drag. The same results are obtained when velocity was decreased at constant riblet space due to the cover the riblets create with viscous sublayer. The optimum s^+ for the different tested shapes was in the range of the 13-25 in wall units.

❖ Although the channelled flow near the wall will increase the velocity in the streamwise direction which increases the turbulent intensity in the streamwise direction, the restriction of the lateral and normal velocities cause a reduction in the total turbulent kinetic energy and turbulent intensity.

❖ The blade riblets with an h/s ratio around 0.5 give an optimum drag reduction around 10.3% compared to the smooth surface. The scallop riblets show a good drag reduction around 6.7 %; close drag reduction was obtained by diamond and lotus riblets around 6.5%, triangle riblets show less drag reduction near 2.9%. More complicated geometries such sharkskin gives no significant drag reduction.

❖ Although the riblet thickness is a significant parameter to a rigid structure, the thickness of the base riblet causes more pressure drag. The numerical resuts show that the triangle riblets have high-pressure gradient around 22.4 Pa/m which exceed 30 times the pressure gradient for a smooth surface; the scallop riblets show a pressure gradient around 14.7 Pa/m and the diamond and lotus around 13.5 Pa/m. The blade riblet show negative pressure gradient around 30 Pa/m. The negative pressure gradient means fluid acceleration in the streamwise direction while the positive pressure gradient means slow velocities which cause pressure drag.

The numerical simulation results support the hypothesis of the study and show that the Hydro3D code is a good numerical tool to study flow over different riblet shapes. In practical application, the manufacturing riblets on metallic surfaces are more complicated and limited, so the scallop riblet was chosen to be constructed since we used Wire Electrical Discharge Machining (WEDM) as the manufacturing method.. From the experimental results these points are concluded:

❖ The velocity profile in the streamwise direction shows that using riblets help in increase the velocity gradient near the wall and accelerate the velocity to reach the mainstream velocity in short distance from the wall compared to the smooth surface. The lotus riblets show the best velocity profile. However, the error bars in representing the results show that the riblets have nearly the same results. The velocity gradient for each riblet has two regions; the sharp velocity gradient at $y^+ < 6$, and low-velocity gradient at $y^+ > 6$, while for the smooth surface the sharp velocity gradient occurs at $y^+=12$ and the low-velocity gradient occurs at $y^+<12$. This result is important for boundary layer flashback, where the boundary layer flashback attacks the sharp velocity gradient region near the wall as the velocity of the flow is in value less than the turbulent flame speed. However, bringing the sharp velocity gradient closer to the wall as in cases of using riblets will force the leading flame tip closer to the wall, which quenches the flame due to the increase the heat transfer rate with wall.

❖ Although the limitation to reach the riblet surface with LDA beam, the LDA results support the hotwire results of velocity over the riblets.

❖ The manufactured riblet surfaces show an antifouling behave, where the seeding particles are washed away from the surface and have no chance to settle on the surface as in the smooth surface case.

Since the lotus, diamond and scallop riblets show no significant difference in performance, the scallop riblet geometry was chosen to be applied to a burner nozzle. Also, three different stainless steel woven wire mesh were used as a liner. The wire diameters were 50μm and 150 μm.. The main conclusions from these results are:

❖ Although swirl flows have more complicated structures than the diffusion flow, the swirl flow near the wall is similar to other flow patterns. So, using scallop structures reduces the radial distance where the viscous wall effect on the flow and the high-velocity region ($u/U > 0.5$) is shifted closer to the wall. These shifting results in a modification of the flow structure in the thin shear layer downstream the nozzle exit, which helps to avoid CIVB if combined with central air injection.

❖ Applied microstructures inside burner nozzles using WEDM have its potential difficulties. On the one hand, the access to the work piece is limited due to the mechanism of wire feeding. On the other hand, the more complicated geometries show no big difference.

❖ A slight improvement in velocity gradient in the radial direction is found when using woven mesh compared to the scallop geometry. However, in the combustion tests, using different meshes give different levels of improvement against boundary layer flashback.

❖ The velocity gradient for the different wire mesh shows that the wire mesh has a similar effect on the flow as the riblets. Because the wire mesh trappes some fluid (air) in the texture (holes), which work as fluid bubbles that provide a

fluidic bed for the coming flow, reduce the contact of the high momentum flow with the wall. An increase in the wire diameter causes the flow to get in contact with more area and increase the turbulence.

❖ Using micromeshes prove their potential for BLF resistance. The structure changes the behaviour of the boundary sublayer in such a way that the fresh mixture velocity is still high even near the wall which in turn increases the velocity gradient greater than a critical value that can overcome turbulent flame speed.

❖ The geometry and size of the micromesh are important. Fine micromeshes with wire diameter 150 μm gave better results than coarse ones with a wire diameter of 50 μm. The effect of using a micromesh can be observed visually. The effect leads to an increase of the operation stability map in both cases, with and without air injection. The optimum conditions were when using the two techniques together, i.e. the diffusive air injection and micromesh surfaces.

❖ For industrial requirements the use of air injection and micromeshes for flame stabilisation requirements seems to be useful from the commercial point of view, the availability of air and possibility of commercial production of such microsurfaces consolidates that. However, there is still considerable research required for prediction of the manufacturing cost of some micromeshs with more detail of flow control.

8.2 Future Work

The numerical and experimental works revealed some questions that could not be answered due to the lack of time, but they could be investigated in future works to give a clear picture of the effect of the roughness on boundary layer flashback. The most important issues are:

❖ In term of fluid flow, the numerical and experimental tests are done using riblets aligned with the streamwise flow direction. How much the results will be affected by changing the angle between the flow and the riblets?. The Hydro3D

code is flexible and can solve the flow over different complex geometries, but the crucial parameter will be the time cost since the normal run for tested riblets was around seven days using Cardiff university super computer (ARCCA).

❖ For the same issue above, the experimental rig is designed to investigate the effect of the flow angle with the manufactured surfaces, but it needs more measurement tools to overcome the difficulties of approaching too close to the structured surfaces. BLIF or Schlerin measuring systems can be used to capture the flow structure.

❖ In term of manufacturing, RAM manufacturing could be used to apply more complex geometries on surfaces that are difficult to access, such as at the entrance of nozzle.

❖ Investigate the effect of the microstructure on the flashback instability. Since the microstructure changes the swirl flow structure near the wall, the system pressure oscillations associated with oscillations in the combustion heat release rate will change too.

❖ Carry more combustion tests using all structures available, i.e. microstructures and micromesh on different nozzles and different fuel blends.

APPENDIX A .

In this appendix, the numerical results for different geometry that not included in Chapter 6 are mentioned here.

A-1 Blade riblet (low Re)

A blade riblet was tested at low Re=1000, the blade has h/s ratio around 0.7. The blade geometry was 200 μm height and 280μm in space as shown in figure A-1.
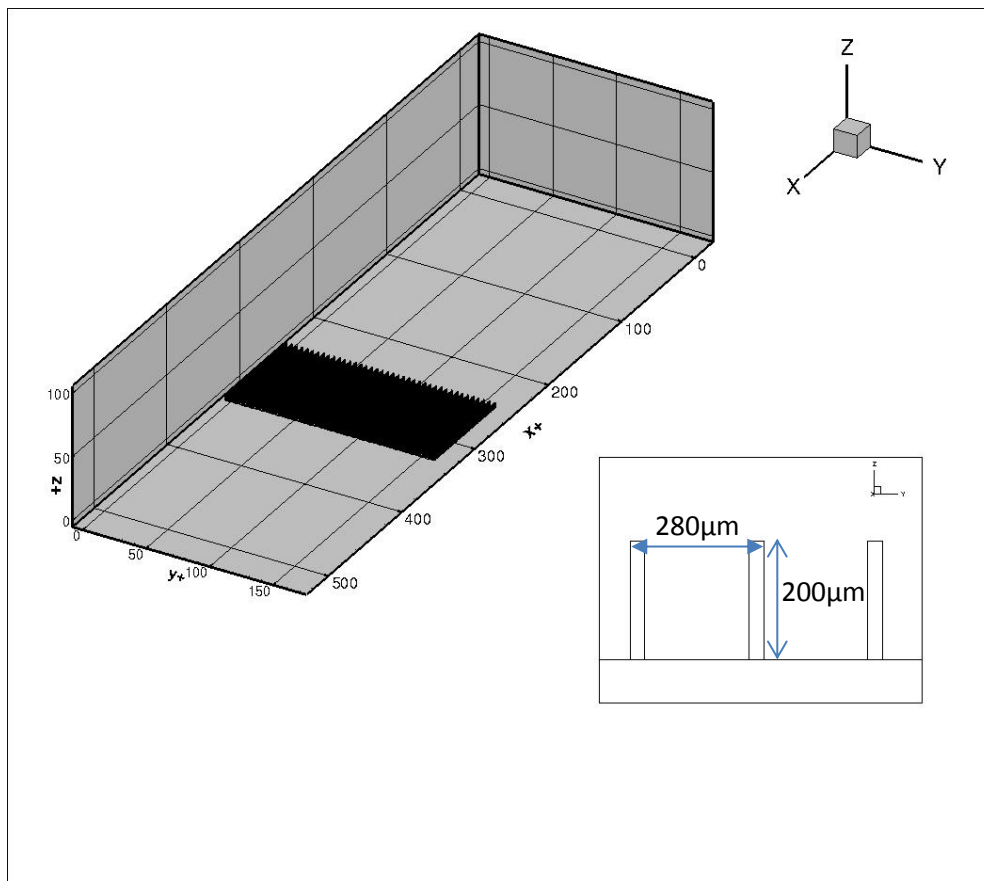
Figure A-1 blade riblet geometry and riblet patch lay out in channel.

The results showed that the riblet was covered totally with viscous layer and the riblet has no effect on the flow. The streamwise velocity distribution is shown in figure A-2.
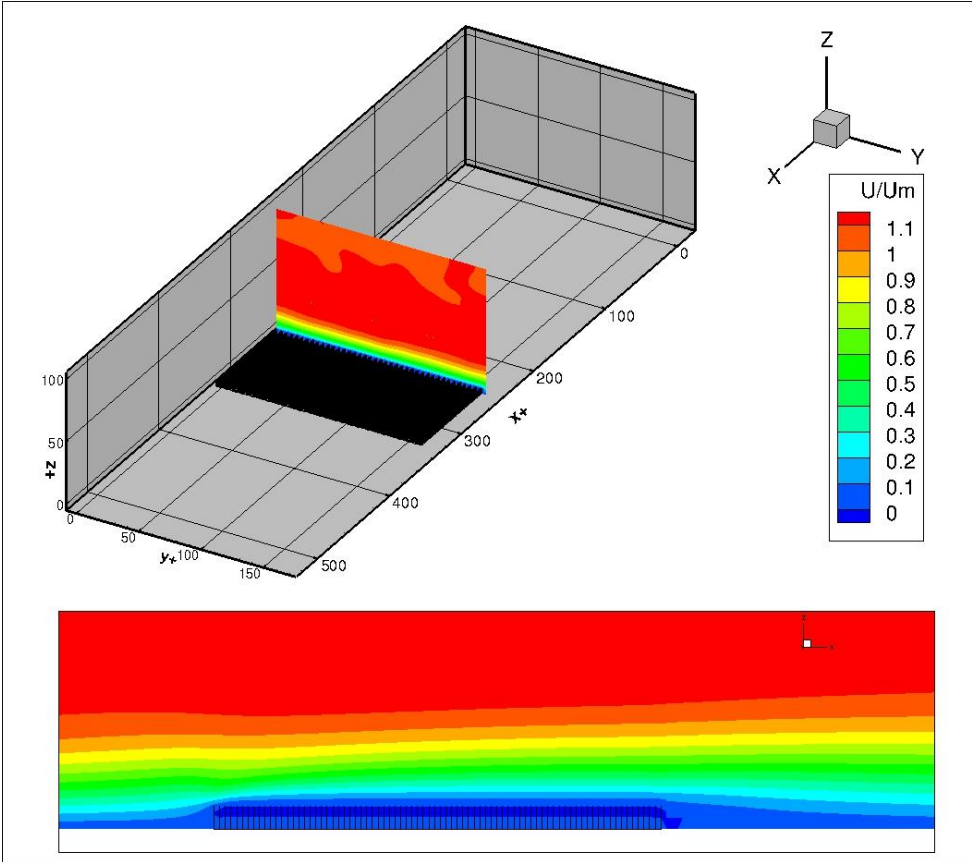
Figure A-2 streamwise velocity distribution with boundary layer profile at
y^+=78.

The normal and lateral velocity distributions are shown in figures A-3 and A-4 respectively.
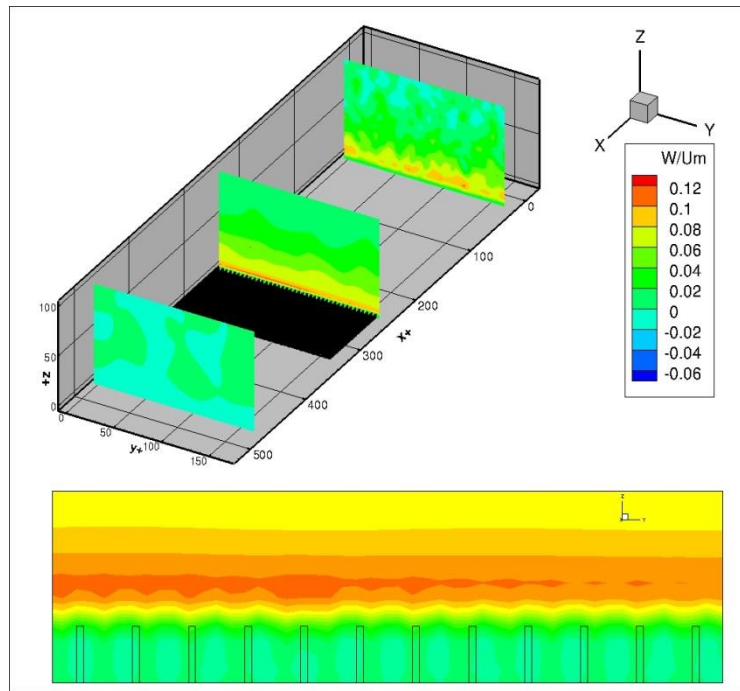
Figure A-4 Normal velocity distribution at channel inlet and outlet and at the riblets start (up). Normal velocity distribution at x+=185
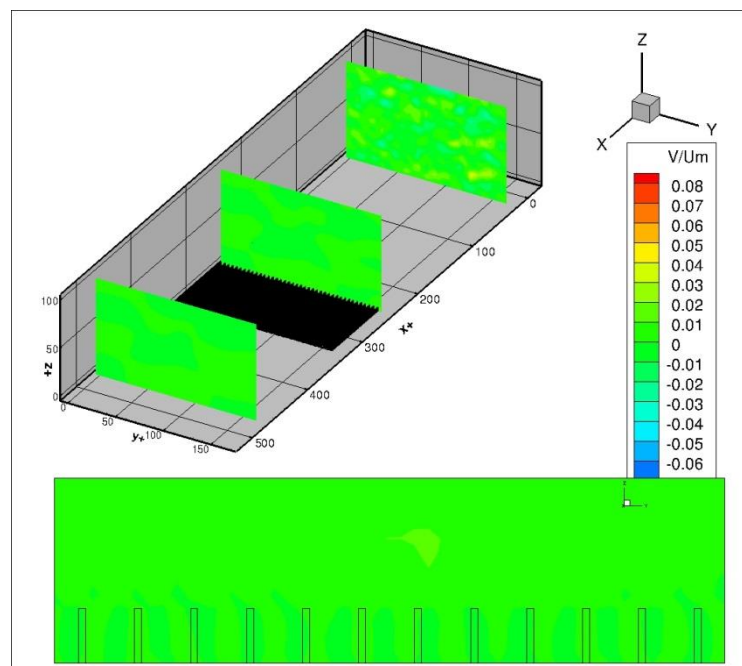
Figure A-3 Lateral velocity distribution at channel inlet and outlet and at the riblets start (up). Lateral velocity distribution at x+=185

A-2 Triangular riblet

The triangular riblet was numerically tested to verify the Hydro3D code. The riblet utilizes from 250μm height and 250μm space, Re =13500.
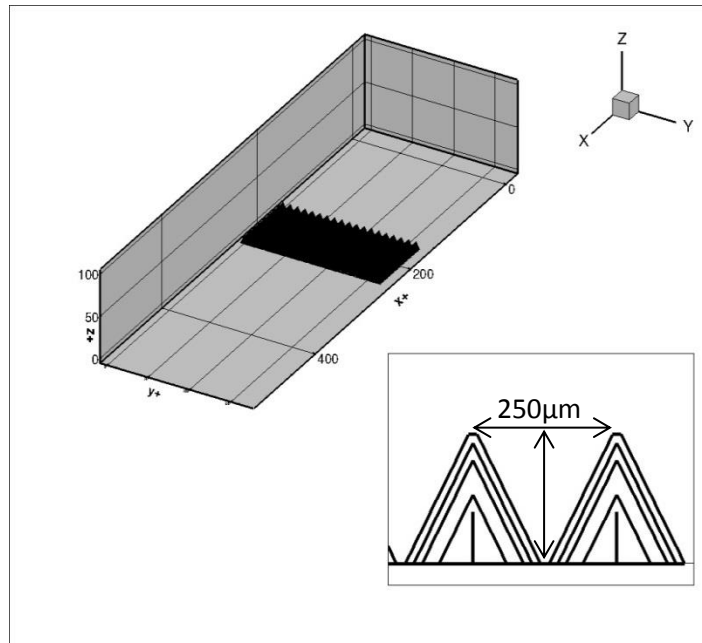
Figure A-5 triangular riblet geometry and riblet patch lay out in channel.

The streamwise velocity distribution over the triangular riblets is shown in figure A-6. The results showed the effect of the riblet on the flow. An increase in streamwise velocity just over the riblets due to a reduction in the wall effect.
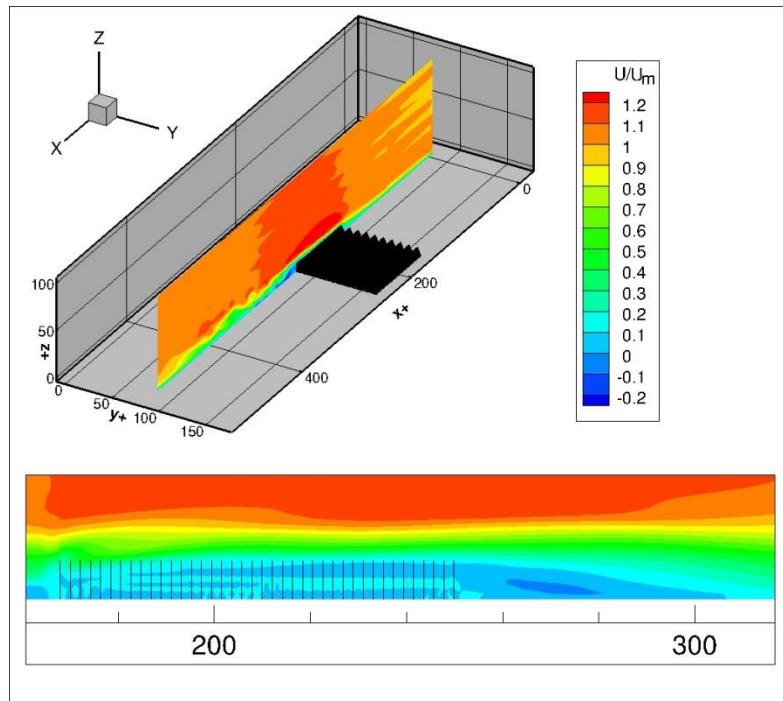
Figure A-6 streamwise velocity distribution with boundary
layer profile at $y^+=78$.

The streamwise velocity close the triangular riblet is shown in figure A-7.
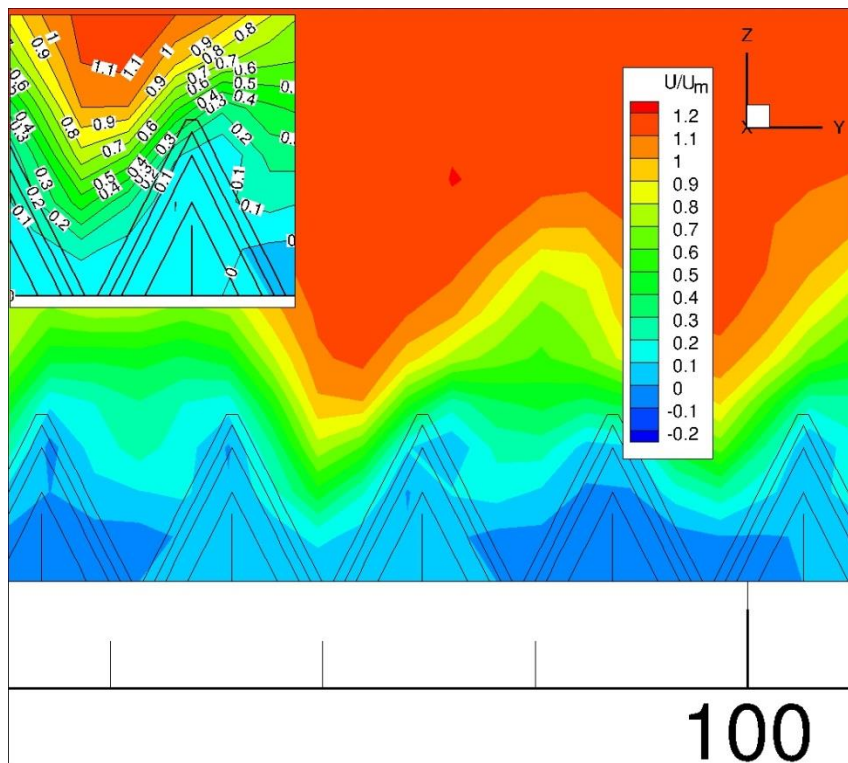
Figure A-7 The streamwise velocity close the triangular riblet at $x^+=185$

The velocity distribution in lateral direction is shown in figure A-8.
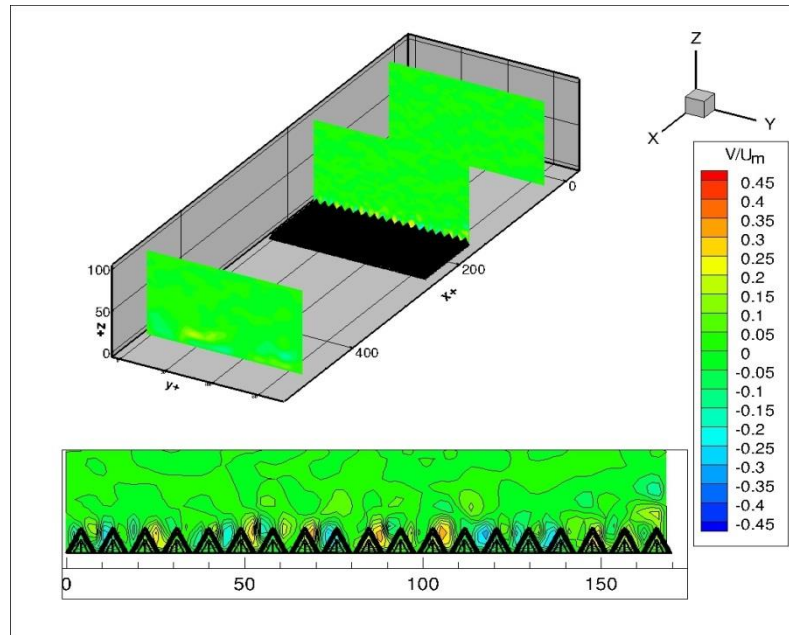
Figure A-8 Lateral velocity distribution at channel inlet and outlet and at the
riblets start (up). Lateral velocity distribution at $x^+=185$

The velocity in normal direction is shown in figure A-9. The results showed that the normal velocity is located over the riblets far from the wall which reduce the wall shear stress.
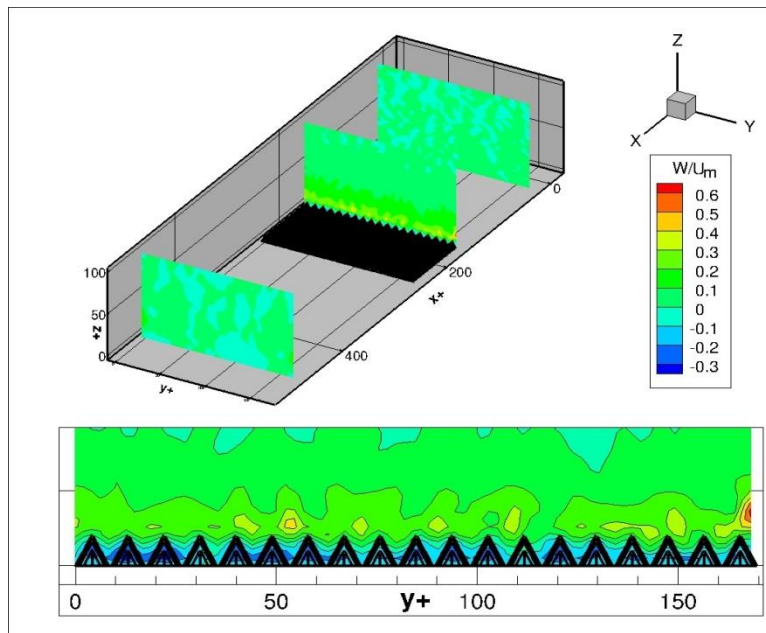
Figure A-9 Normal velocity distribution at channel inlet and outlet and at
the riblets start (up). Normal velocity distribution at $x^+=185$

The TKE at riblet tips is shown figure A-10, and the TKE at riblet base is shown in figure A-11.
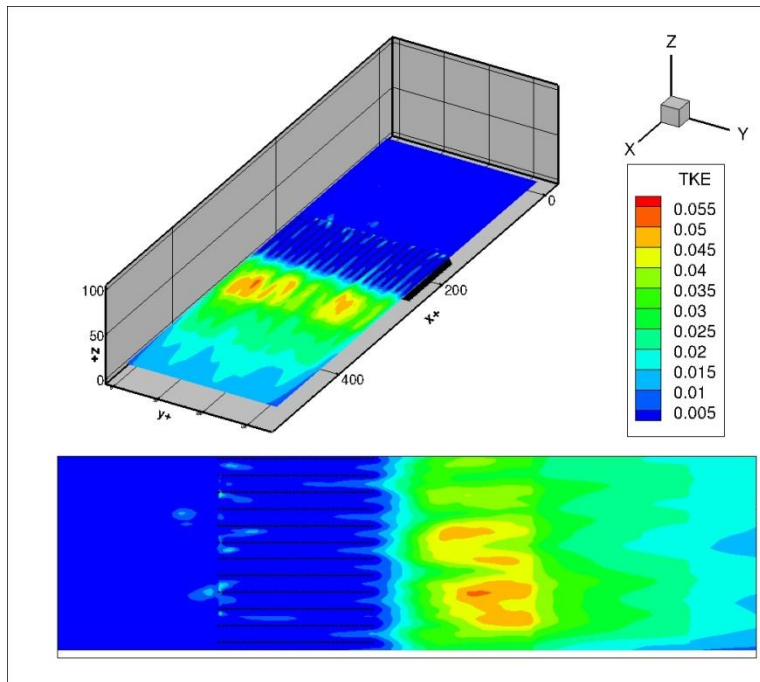
Figure A-10 TKE at riblet tips z^+=5.5
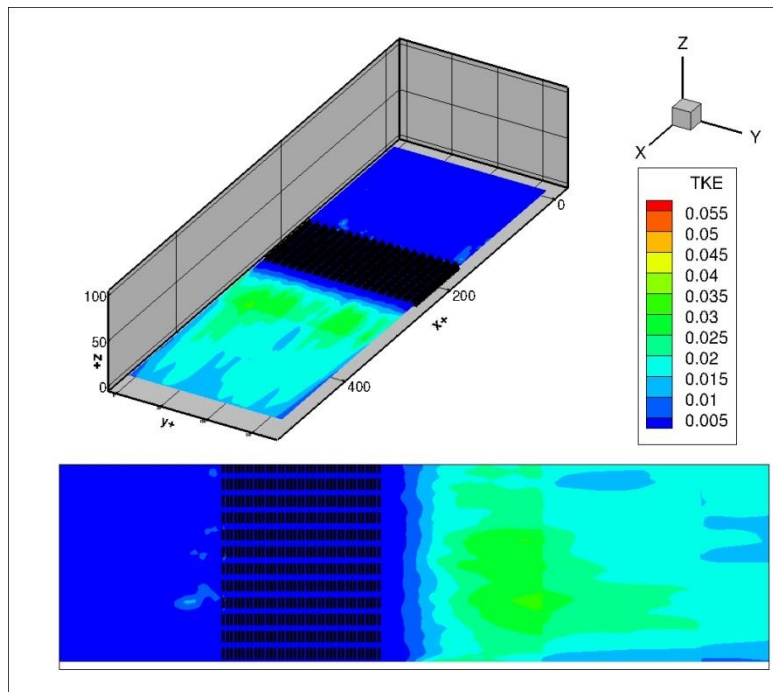
Figure A-11 TKE at riblet base z^+=2

A-3 Diamond riblet

The diamond riblet geometry design was extended from scallop riblet design to study the effect of the length of riblet along flow side. However, the actual dimensions of diamond riblets were depending on the manufacturing limitation. The numerical design was slightly different than the manufactured one. The numerical design utilities from 260µm space between riblets, 130µm height and 280µm width as shown in figure A-19, the Re=13500.
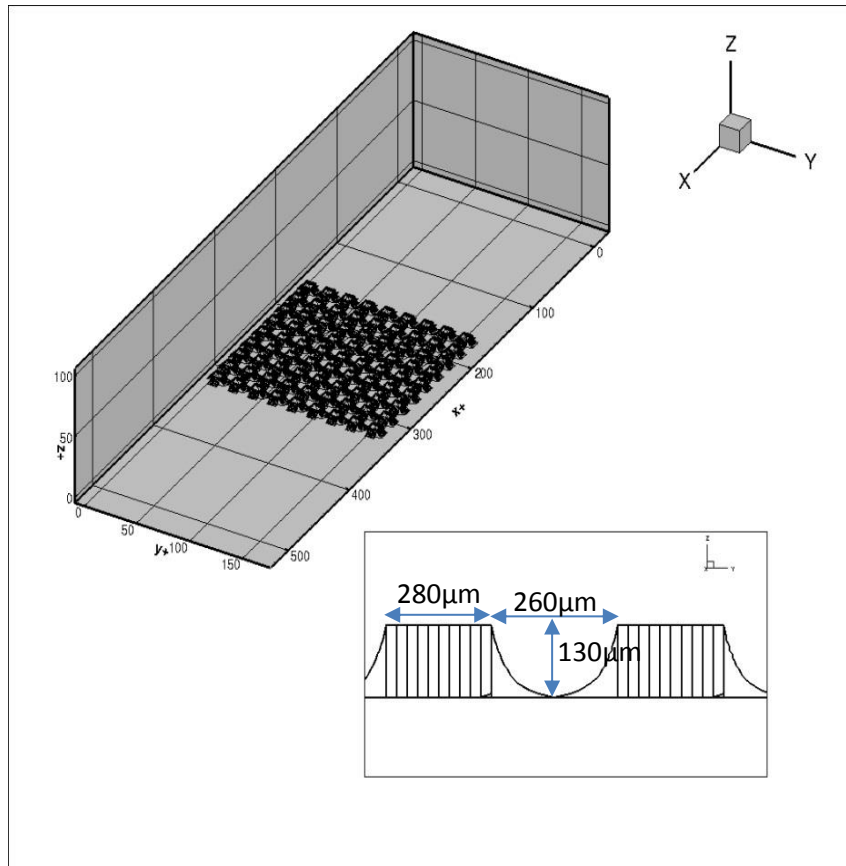
Figure A-12 geometry of diamond riblets and patch location in channel.

The streamwise velocity distribution over the diamond riblets is shown in figures A-20 and figure A-21. The results showed the effect of the riblet on the flow. More fluctuations in streamwise velocity behind each riblet were noticed due to the change in dimension.

The velocity distribution in lateral direction is shown in figures A-14 and A-15.
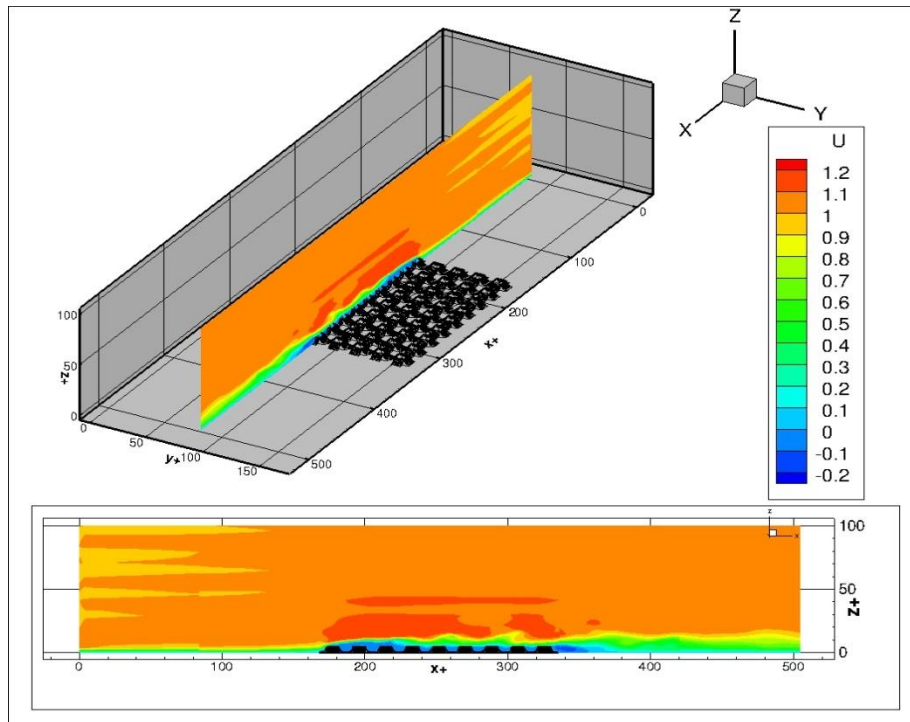
Figure A-14 stream wise velocity distribution with boundary layer profile at y+=78.
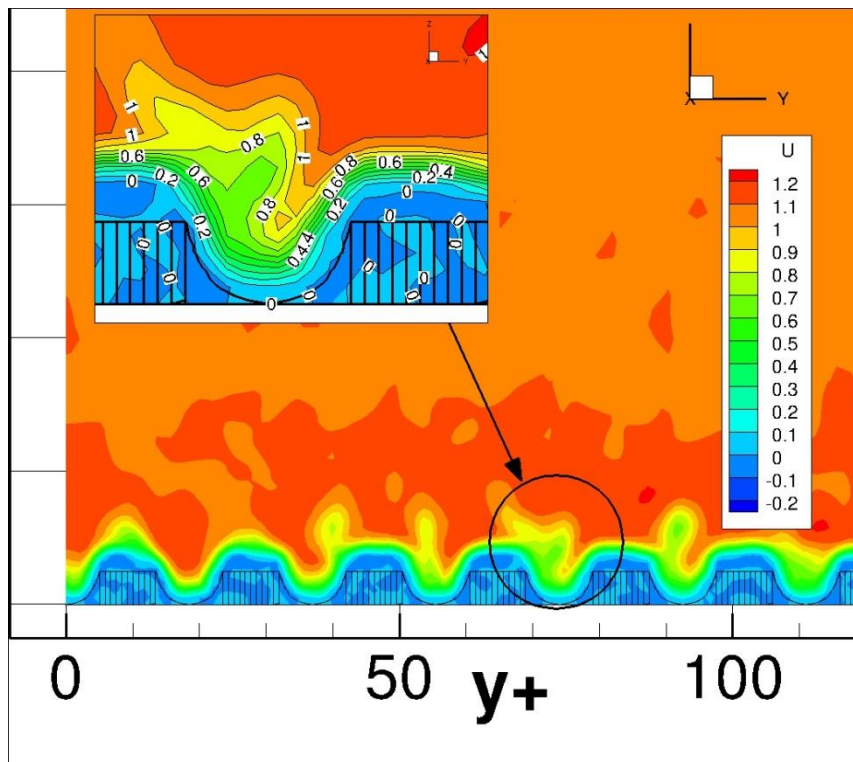
Figure A-15 The streamwise velocity close the Diamond riblet at $x^+=185$
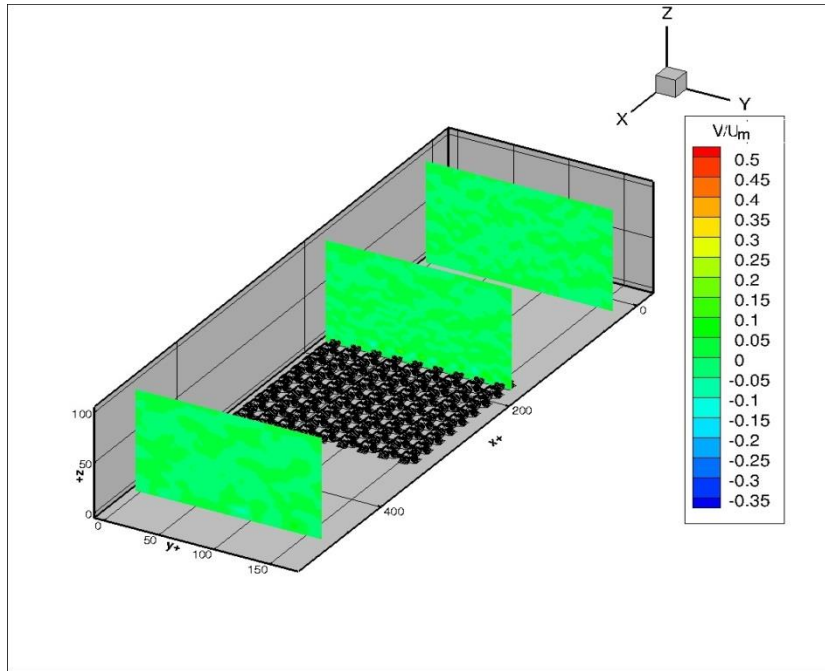
Figure A-16 Lateral velocity distribution at channel inlet and outlet and at the riblets start.

The velocity in normal direction is shown in figure A-16 and A-17. The results showed
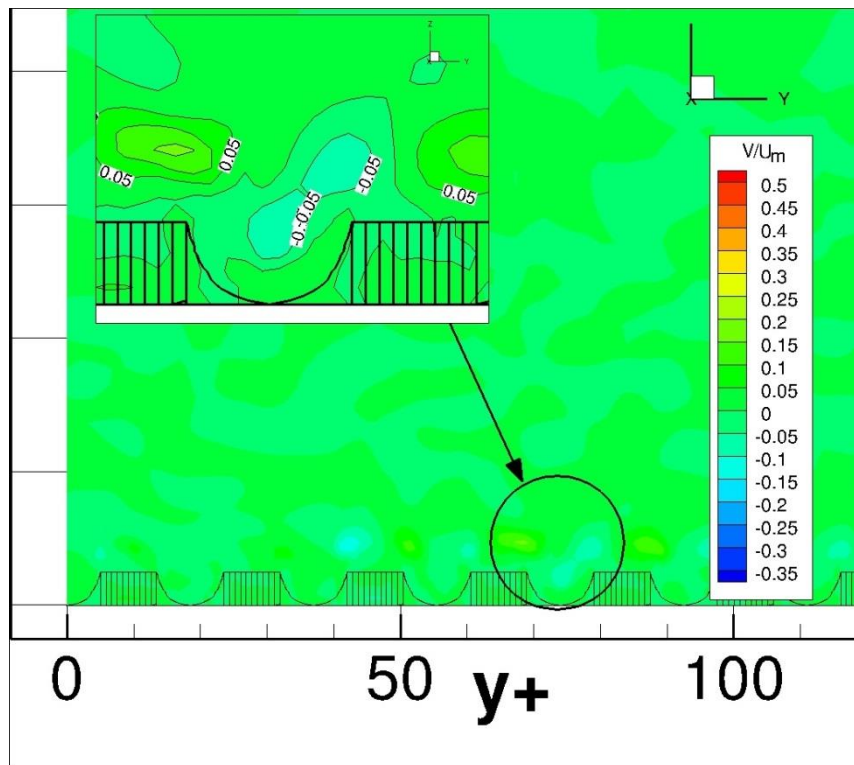
Figure A-17 Lateral velocity distribution at x+=185

increase in the normal velocity component compared to the blade or scallop riblets.
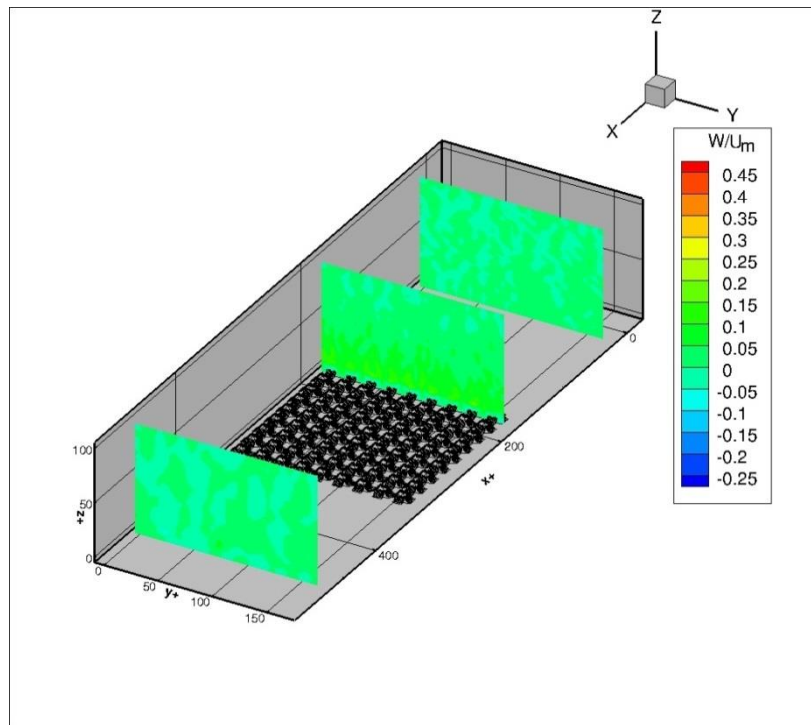
Figure A-18 Normal velocity distribution at channel inlet and outlet and at the riblets start
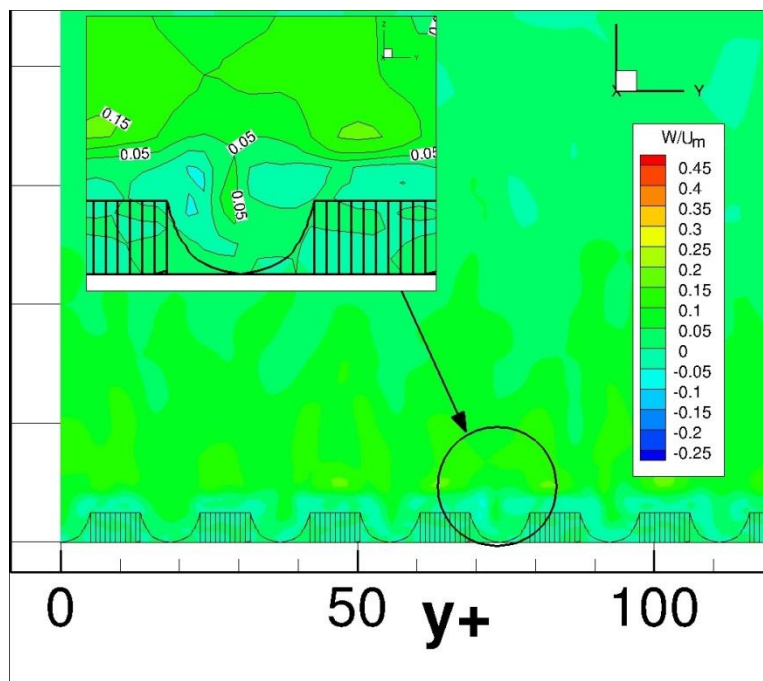
Figure A-19 Normal velocity distribution over diamond riblets at x+=185

The TKE at riblet tips is shown figure A-20.
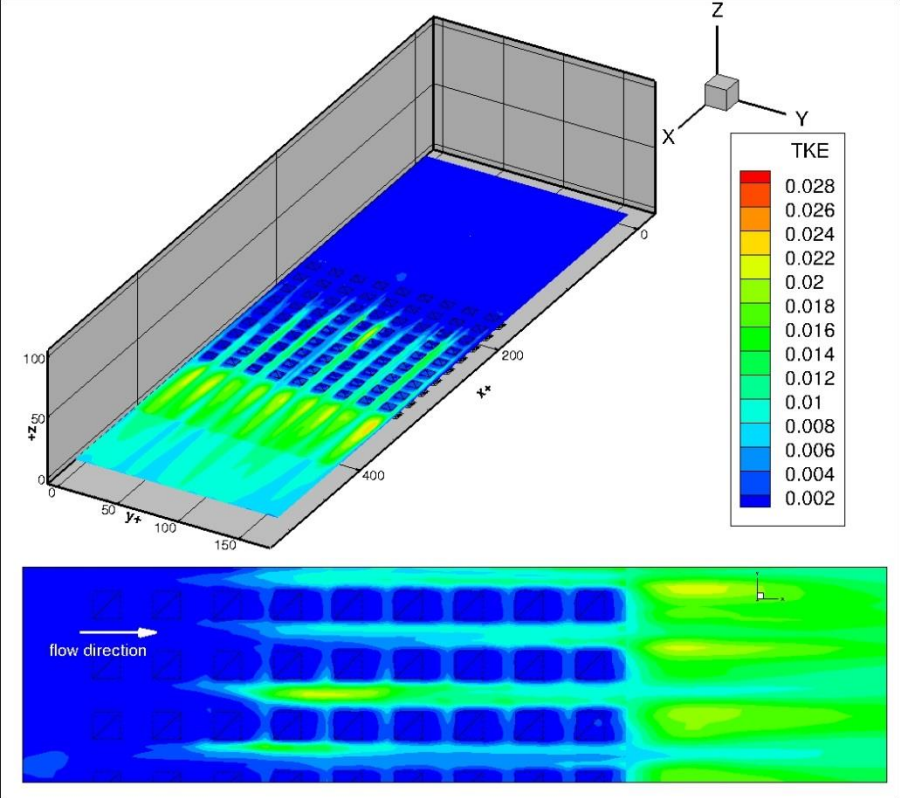
Figure A-20 TKE at diamond riblet tips z$^+$=5.5

A-4 Numerical extracted data

Table A-1 shows a spread sheet of a vertical plan at x⁺=185 (6 pages of 64), the data in this sheet were used to calculate the pressure drop as described in chapter six. For each slide the same amount of data were extracted and processed.

Table A-1 Sprees sheet for the slice at $x+=185$ for scallop riblet Re = 13500.

| x	y	z	Um	Vm	Wm	p	PM	ppm	vis	dUdX	dVdX	dWdX	dUdY	dVdY	dWdY	dUdZ	dVdZ	dWdZ	TKE	Shear Stress	U/Um	V/Um	W/Um	X+	Y+	Z+
1	-1.73472E-18	-1.73472E-18	0	0	0	-4846.10498	-2541.8313	1874279.88	2.8571E-05	0	0	0	0	0	0	13.4390116	0	-4.29021406	0.00035321	0.00070642	0	0	0	167.920105	-2.91295E-16	-2.91295E-16
1	0.00625	-1.73472E-18	0	2.1682E-23	0	-4846.10645	-2541.8313	1874280	2.8571E-05	0	0	0	1.3876E-20	-1.3877E-16	0	13.171258	3.08548832	-4.07625866	0.00047359	0.00073677	0	0	0	167.920105	1.04949999	-2.91295E-16
1	0.0125	1.7346E-22	-9.7568E-23	0	0	-4846.11133	-2541.83618	1874280.12	2.8571E-05	2.7753E-16	2.0816E-16	0	0	-1.3876E-16	0	12.2140074	7.21127748	-3.97563696	0.00047727	0.0007796	1.7346E-22	-1.7346E-18	0	167.920105	2.09899998	-2.91295E-16
1	0.018750001	-1.73472E-18	-1.7345E-18	1.7345E-18	0	-4846.11523	-2541.84326	1874279.75	2.8571E-05	2.1682E-22	2.7754E-16	0	-1.3878E-16	1.3876E-16	0	9.53435898	10.7119532	-3.13254881	0.00051629	0.00085512	0	-1.7345E-18	0	167.920105	3.1485002	-2.91295E-16
1	0.025	-1.73472E-18	-4.3364E-19	8.6727E-19	0	-4846.11328	-2541.84424	1874279.25	2.8571E-05	2.8621E-16	-6.9382E-17	0	0	1.3877E-16	0	5.11567068	11.065197	1.64666939	0.00034226	0.00058185	-1.7345E-18	-4.3364E-23	0	167.920105	4.19799995	-2.91295E-16
1	0.03125	-1.73472E-18	0	-1.0841E-23	0	-4846.10889	-2541.84131	1874278.25	2.8571E-05	0	6.9382E-17	0	1.3877E-16	0	0	4.2651577	6.42434025	6.52968931	0.00014655	0.00021477	0	4.3364E-23	0	167.920105	5.24749994	-2.91295E-16
1	0.037500002	-1.73472E-18	8.6727E-23	-4.3364E-23	0	-4846.104	-2541.8374	1874277	2.8571E-05	1.3876E-16	-6.9375E-17	0	-2.7753E-16	-1.1275E-16	0	8.88169861	4.15374088	3.63900852	0.0001128	0.0001657	8.6728E-23	-4.3364E-23	0	167.920105	6.29700041	-2.91295E-16
1	0.043749999	-1.73472E-18	3.4691E-18	-1.0841E-18	0	-4846.10303	-2541.83374	1874275.75	2.8571E-05	5.4641E-16	2.6019E-16	0	-6.9389E-17	6.9382E-21	0	14.2542315	7.85944128	-1.13193929	0.00011602	0.00017947	-3.4691E-18	-1.4093E-18	0	167.920105	7.34649992	-2.91295E-16
1	0.050000001	-1.73472E-18	8.6727E-19	1.7346E-18	0	-4846.11084	-2541.8335	1874274.75	2.8571E-05	1.3877E-16	6.9382E-17	0	2.4284E-16	1.1274E-16	0	13.2674341	12.8292522	1.58786547	0.00011665	0.00017398	-8.6727E-19	4.3364E-23	0	167.920105	8.39599991	-2.91295E-16
1	0.056249999	-1.73472E-18	-2.4401E-19	8.6728E-23	0	-4846.12451	-2541.83599	1874273.88	2.8571E-05	6.9382E-17	-6.9385E-17	0	6.9382E-17	-3.4694E-17	0	7.19387388	11.5838881	5.03756523	5.7947E-05	8.1961E-05	-4.3364E-19	-4.3364E-23	0	167.920105	9.44549942	-2.91295E-16
1	0.0625	-1.73472E-18	0	1.3009E-18	0	-4846.13525	-2541.83789	1874273.62	2.8571E-05	-1.3009E-21	6.9385E-17	0	3.4691E-17	-1.3226E-16	0	5.8824234	7.99495363	1.69321513	4.34E-05	6.2083E-05	0	-4.3364E-19	0	167.920105	10.4949999	-2.91295E-16
1	0.068750002	-1.73472E-18	0	1.3416E-18	0	-4846.13965	-2541.8374	1874273.38	2.8571E-05	0	2.6453E-16	0	-1.3876E-16	1.7345E-16	0	9.15172195	9.70403767	-1.22970223	3.9291E-05	5.9683E-05	0	-1.6532E-18	0	167.920105	11.5445004	-2.91295E-16
1	0.075000003	-1.73472E-18	0	1.7345E-18	0	-4846.13818	-2541.83813	1874272.75	2.8571E-05	2.7754E-16	-2.7754E-16	0	3.4691E-17	2.7102E-16	0	10.0499725	14.0940142	3.71619534	3.84E-05	5.5549E-05	-1.7345E-18	1.7345E-18	0	167.920105	12.5940008	-2.91295E-16
1	0.081249997	-1.73472E-18	4.3364E-23	4.3364E-23	0	-4846.13379	-2541.8418	1874272.12	2.8571E-05	-6.9385E-17	-2.5152E-16	0	1.3876E-16	-1.3877E-16	0	5.79638386	11.0521164	8.92800617	2.9333E-05	4.1487E-05	4.3364E-19	1.7346E-18	0	167.920105	13.6434994	-2.91295E-16
1	0.087499999	-1.73472E-18	-1.7345E-18	2.1682E-23	0	-4846.12842	-2541.84326	1874270.75	2.8571E-05	0	-3.4691E-17	0	-3.1222E-16	-1.3877E-16	0	5.13010311	2.34362578	6.09953165	6.7151E-05	9.7018E-05	0	-2.1682E-23	0	167.920105	14.6929998	-2.91295E-16
1	0.09375	-1.73472E-18	0	0	0	-4846.12451	-2541.84204	1874269.12	2.8571E-05	5.5508E-16	0	0	-1.3875E-16	1.7345E-21	0	13.9035387	2.72196102	2.78544378	0.00014602	0.00025136	-3.4691E-18	0	0	167.920105	15.7425003	-2.91295E-16
1	0.100000001	-1.73472E-18	-8.6728E-23	1.7345E-18	0	-4846.12598	-2541.84326	1874272.25	2.8571E-05	5.5506E-16	0	0	2.7753E-16	0	0	15.3332214	6.25401211	6.4759655	0.00016241	0.00024811	-1.7344E-18	0	0	167.920105	16.7919998	-2.91295E-16
1	0.106250003	-1.73472E-18	0	-4.3366E-19	0	-4846.12842	-2541.84619	1874278	2.8571E-05	1.3876E-16	0	0	1.3876E-16	0	0	2.92278576	5.41335917	9.91757298	0.00019589	0.00027733	8.6728E-23	0	0	167.920105	17.8415012	-2.91295E-16
1	0.112499997	-1.73472E-18	8.6728E-23	1.7345E-18	0	-4846.12256	-2541.84082	1874277	2.8571E-05	1.3876E-16	5.6373E-21	0	-6.9382E-21	-2.4284E-20	0	19.3682709	-2.30798817	6.92368603	0.00056303	0.00108792	8.6728E-23	0	0	167.920105	18.8909988	-2.91295E-16
1	0.118749999	-1.73472E-18	3.4691E-18	-1.0841E-22	0	-4846.13086	-2541.8457	1874278.88	2.8571E-05	-6.9382E-21	-4.8567E-16	0	6.5046E-22	0	0	19.3360023	5.62327719	4.24480724	0.00083864	0.00142603	0	-3.0355E-22	0	167.920105	19.9405003	-2.91295E-16
1	0.125	-1.73472E-18	1.4906E-22	0	0	-4846.1499	-2541.8623	1874282.75	2.8571E-05	1.5177E-16	0	0	0	2.7753E-20	0	-5.05536795	1.07308137	6.2704916	0.00029345	0.00050215	9.4858E-23	0	0	167.920105	20.9899998	-2.91295E-16
2	0.131249994	-1.73472E-18	0	1.0841E-19	0	-4846.15527	-2541.86792	1874281.5	2.8571E-05	-1.7345E-21	6.9382E-17	0	-7.5887E-21	6.9382E-21	0	-0.94108045	-7.75597191	8.24911213	0.00012339	0.00021063	0	4.3364E-23	0	167.920105	22.0394993	-2.91295E-16
3	0.137500003	-1.73472E-18	-1.7345E-18	0	0	-4846.15137	-2541.8623	1874279.25	2.8571E-05	3.4691E-21	1.3876E-16	0	1.3876E-20	1.3876E-16	0	9.01039505	-10.299654	7.85356569	0.00017359	0.00024679	0	8.6728E-23	0	167.920105	23.0890007	-2.91295E-16
1	0.143749997	-1.73472E-18	0	1.7345E-18	0	-4846.14209	-2541.85376	1874278.62	2.8571E-05	2.7753E-16	-2.7754E-16	0	1.3876E-20	-6.9389E-17	0	12.1671677	-9.5069561	7.19634628	0.00017044	0.00024131	1.7346E-22	1.7345E-18	0	167.920105	24.1385002	-2.91295E-16
1	0.150000006	-1.73472E-18	-8.6728E-23	-8.6727E-19	0	-4846.13379	-2541.8501	1874282.25	2.8571E-05	2.7753E-16	1.3876E-16	0	-1.3443E-20	-1.3876E-16	0	8.247262	-9.26683998	6.62531757	0.00026123	0.00044598	1.7346E-22	-8.6727E-19	0	167.920105	25.1880016	-2.91295E-16
1	0.15625	-1.73472E-18	1.7345E-18	-8.6729E-19	0	-4846.12891	-2541.84961	1874284.62	2.8571E-05	8.6727E-18	1.7345E-17	0	-6.9396E-17	0	0	6.2216897	-8.92034721	4.95190334	9.5619E-05	0.00013693	5.4205E-24	1.0841E-23	0	167.920105	26.2374992	-2.91295E-16
1	0.162499994	-1.73472E-18	-4.3364E-19	0	0	-4846.12598	-2541.8501	1874283.5	2.8571E-05	1.3877E-16	1.3877E-16	0	1.7345E-17	2.6017E-17	0	4.36944818	-9.01965714	1.13337564	0.00013935	0.00019916	-8.6727E-19	-8.6727E-19	0	167.920105	27.2869987	-2.91295E-16
1	0.168750003	-1.73472E-18	1.4906E-19	4.3366E-19	0	-4846.12402	-2541.8501	1874282.25	2.8571E-05	-3.4693E-17	-5.2039E-17	0	6.9382E-17	1.7342E-17	0	3.24166322	-3.85615134	-2.28089261	0.00013426	0.00019036	2.1682E-19	3.2523E-19	0	167.920105	28.3365002	-2.91295E-16
1	0.174999997	-1.73472E-18	1.6261E-23	-1.0841E-23	0	-4846.12451	-2541.84888	1874282	2.8571E-05	4.3364E-18	3.4697E-17	0	0	4.3365E-17	0	3.6238029	2.04888749	-2.59151077	0.00017774	0.00026334	2.7102E-24	-6.505E-19	0	167.920105	29.3859997	-2.91295E-16
1	0.181250006	-1.73472E-18	-4.3364E-19	5.4203E-19	0	-4846.12646	-2541.84741	1874281.62	2.8571E-05	-3.4693E-17	-1.2251E-16	0	-2.1682E-22	-1.7342E-17	0	6.57634258	4.16919756	-2.06428123	0.00015444	0.0002187	2.1682E-19	8.6729E-19	0	167.920105	30.4355011	-2.91295E-16
1	0.1875	-1.73472E-18	1.3551E-18	8.6725E-19	0	-4846.12744	-2541.84717	1874280.25	2.8571E-05	0	1.3877E-16	0	-5.2037E-17	-6.9386E-17	0	9.17506504	8.24685383	-2.08547306	0.00028309	0.00040677	0	-8.6727E-19	0	167.920105	31.4850006	-2.91295E-16
1	0.193749994	-1.73472E-18	-8.6728E-23	0	0	-4846.12842	-2541.84888	1874279.12	2.8571E-05	6.9385E-17	-6.9382E-17	0	1.7346E-17	0	0	7.53716516	11.7741032	-1.37244618	0.00041529	0.00064653	-4.3364E-19	-4.3364E-23	0	167.920105	32.5345001	-2.91295E-16
1	0.200000003	-1.73472E-18	-2.1682E-23	1.7345E-18	0	-4846.13086	-2541.85107	1874280	2.8571E-05	-1.7347E-17	1.3877E-16	0	3.4691E-17	-4.336E-17	0	4.39794779	12.9804506	1.41333163	0.00033452	0.00051733	2.1683E-19	-8.6727E-19	0	167.920105	33.5839996	-2.91295E-16
1	0.206249997	-1.73472E-18	0	-4.3364E-19	0	-4846.13428	-2541.85254	1874282.25	2.8571E-05	0	8.6732E-17	0	5.2036E-17	-3.4691E-17	0	3.76160884	12.6230946	5.26816654	0.00014184	0.00020062	0	-5.4205E-19	0	167.920105	34.6334991	-2.91295E-16
1	0.212500006	-1.73472E-18	-1.7346E-22	5.4205E-19	0	-4846.13721	-2541.85352	1874284.75	2.8571E-05	-1.3877E-16	2.0816E-16	0	1.3876E-20	1.6478E-16	0	5.69757032	12.4895229	6.78308201	0.00012061	0.00020437	8.6727E-19	-1.3009E-18	0	167.920105	35.6830025	-2.91295E-16
1	0.21875	-1.73472E-18	-8.6728E-23	6.5046E-19	0	-4846.13916	-2541.85376	1874286.88	2.8571E-05	2.7752E-16	-2.4285E-16	0	6.9381E-17	3.4692E-17	0	7.54221201	11.0158749	5.42750788	0.00010085	0.00014905	1.7346E-22	1.5177E-18	0	167.920105	36.7324982	-2.91295E-16
1	0.224999994	-1.73472E-18	1.7345E-18	-2.1682E-19	0	-4846.14062	-2541.85181	1874289	2.8571E-05	-3.079E-16	1.5612E-16	0	-1.3876E-20	1.7347E-17	0	9.79232597	10.6035662	3.27231288	8.3205E-05	0.00011825	1.7345E-18	-8.6726E-19	0	167.920105	37.7819977	-2.91295E-16
1	0.231250003	-1.73472E-18	1.7345E-18	1.2467E-18	0	-4846.14014	-2541.84937	1874290.25	2.8571E-05	0	-2.5586E-16	0	-6.938E-17	6.9381E-17	0	11.2050409	11.2523174	2.45623469	7.3267E-05	0.00010372	0	1.7346E-18	0	167.920105	38.831501	-2.91295E-16
1	0.237499997	-1.73472E-18	0	-8.6727E-19	0	-4846.13477	-2541.84912	1874289.38	2.8571E-05	-1.3877E-16	0	0	0	-6.9383E-17	0	9.64993191	13.0702858	3.70968747	9.8946E-05	0.00014547	8.6727E-19	0	0	167.920105	39.8810005	-2.91295E-16
1	0.243750006	-1.73472E-18	0	1.3009E-18	0	-4846.12451	-2541.85059	1874287	2.8571E-05	0	-1.3877E-16	0	6.9382E-17	-1.0407E-16	0	7.51926613	12.0680532	4.21339226	0.00011182	0.00016137	0	8.6727E-19	0	167.920105	40.9305	-2.91295E-16

1	0.25	-1.73472E-18	1.7345E-18	4.3364E-19	0	-4846.11182	-2541.84985	1874284.25	2.8571E-05	-2.7754E-16	2.255E-16	0	-1.3876E-16	-6.7214E-17	0	9.49771023	8.74183369	4.06052637	9.5685E-05	0.00013867	1.7345E-18	-1.3009E-18	0	167.920105	41.9799995	-2.91295E-16
1	0.256249994	-1.73472E-18	1.7347E-18	1.3009E-18	0	-4846.10205	-2541.84888	1874280.75	2.8571E-05	2.7754E-16	-4.3366E-18	0	1.3876E-20	3.4687E-17	0	12.0251322	9.10687065	4.84135151	6.7619E-05	0.00010604	-1.7345E-18	2.7102E-20	0	167.920105	43.0294991	-2.91295E-16
1	0.262499988	-1.73472E-18	1.7345E-18	-8.6729E-19	0	-4846.10156	-2541.85107	1874277.25	2.8571E-05	-1.3876E-20	6.9389E-17	0	1.3877E-16	-2.163E-18	0	13.4087172	10.8121653	4.13626337	6.1512E-05	0.00010119	1.7347E-18	-8.6732E-19	0	167.920105	44.0789986	-2.91295E-16
1	0.268750012	-1.73472E-18	-1.7346E-18	-1.7346E-18	0	-4846.10693	-2541.85474	1874274.88	2.8571E-05	6.9382E-17	1.0407E-16	0	-2.7754E-16	3.4691E-16	0	15.8082905	10.8913555	2.89035654	3.7852E-05	5.448E-05	4.3364E-23	6.5046E-23	0	167.920105	45.1285019	-2.91295E-16
1	0.275000006	-1.73472E-18	1.7345E-18	-1.7346E-18	0	-4846.1167	-2541.85938	1874274.12	2.8571E-05	2.7754E-16	-6.8517E-16	0	-6.9382E-21	-5.2037E-21	0	11.6265535	10.1269627	5.45838118	6.0546E-05	9.8465E-05	-1.7345E-18	3.469E-18	0	167.920105	46.1780014	-2.91295E-16
1	0.28125	-1.73472E-18	-8.6719E-19	-6.5046E-23	0	-4846.12549	-2541.86426	1874274.12	2.8571E-05	-6.9385E-17	-8.6727E-22	0	-8.6728E-22	-2.5584E-16	0	4.03900862	7.84668541	8.32214355	4.342E-05	6.5593E-05	-4.3364E-23	0	0	167.920105	47.2275009	-2.91295E-16
1	0.287499994	-1.73472E-18	1.6261E-23	1.6261E-19	0	-4846.12842	-2541.86621	1874274.38	2.8571E-05	2.602E-16	-4.3366E-17	0	3.4691E-21	-2.6018E-21	0	4.73334408	2.03452635	6.69758081	7.1357E-05	0.00010506	-1.7346E-18	2.7102E-19	0	167.920105	48.2770004	-2.91295E-16
1	0.293749988	-1.73472E-18	0	1.0841E-23	0	-4846.12549	-2541.86499	1874274.88	2.8571E-05	0	-5.2036E-17	0	6.9383E-17	4.77E-17	0	9.20556927	3.61752009	4.59136724	5.3483E-05	8.6802E-05	0	-3.2523E-23	0	167.920105	49.3264961	-2.91295E-16
1	0.300000012	-1.73472E-18	0	8.6723E-19	0	-4846.12305	-2541.8623	1874275.62	2.8571E-05	1.3877E-16	-1.3877E-16	0	0	1.0408E-16	0	8.69866276	5.66197824	5.50705004	7.7193E-05	0.00011361	-8.6727E-19	8.6727E-19	0	167.920105	50.3760033	-2.91295E-16
1	0.306250006	-1.73472E-18	-8.6736E-19	-3.2523E-23	0	-4846.12402	-2541.85986	1874276.5	2.8571E-05	0	-1.8647E-16	0	6.9382E-17	-1.3876E-16	0	5.93046331	5.55190039	5.62485933	4.8824E-05	9.0075E-05	0	1.3009E-18	0	167.920105	51.4255028	-2.91295E-16
1	0.3125	-1.73472E-18	8.6725E-19	-5.9625E-23	0	-4846.12842	-2541.85742	1874277.25	2.8571E-05	0	1.6912E-16	0	-3.4691E-17	-1.0407E-16	0	6.78517437	4.83103418	1.67125785	5.7549E-05	9.333E-05	0	-8.6726E-19	0	167.920105	52.4749985	-2.91295E-16
1	0.318749994	-1.73472E-18	0	0	0	-4846.1333	-2541.85352	1874277.62	2.8571E-05	6.9384E-17	-6.9382E-21	0	6.9382E-21	-1.7347E-17	0	9.89088345	7.64302874	-1.95719421	6.3676E-05	9.1985E-05	-4.3364E-19	0	0	167.920105	53.524498	-2.91295E-16
1	0.324999988	-1.73472E-18	-8.6728E-23	-1.0841E-18	0	-4846.14014	-2541.84985	1874277.88	2.8571E-05	1.3876E-16	1.7346E-16	0	-2.6018E-21	-7.8055E-17	0	10.0676727	12.5682554	-0.74092567	0.00012431	0.00017581	8.6728E-23	-1.0841E-18	0	167.920105	54.5739975	-2.91295E-16
1	0.331250012	-1.73472E-18	2.1683E-19	1.3009E-18	0	-4846.15039	-2541.84766	1874277.88	2.8571E-05	1.7349E-17	1.5612E-16	0	-6.9382E-21	8.6727E-17	0	8.17678642	14.0649958	2.40875363	0.00017892	0.00026137	-4.3367E-19	-9.7568E-19	0	167.920105	55.6235008	-2.91295E-16
1	0.337500006	-1.73472E-18	0	3.2523E-23	0	-4846.15918	-2541.84424	1874277.5	2.8571E-05	0	0	0	3.4694E-17	7.8055E-17	0	6.71586847	12.5206761	4.15568066	0.00020349	0.00028831	0	0	0	167.920105	56.6730003	-2.91295E-16
1	0.34375	-1.73472E-18	-1.7345E-18	-8.6728E-23	0	-4846.15918	-2541.83618	1874277.25	2.8571E-05	6.9382E-21	0	0	-1.3878E-16	3.4691E-21	0	6.31539631	8.42479229	6.21785831	0.00025224	0.00039422	0	0	0	167.920105	57.7224998	-2.91295E-16
1	0.349999994	-1.73472E-18	-3.4692E-18	8.6728E-23	0	-4846.15381	-2541.8252	1874277.88	2.8571E-05	2.0815E-20	6.9382E-17	0	6.9386E-17	0	0	9.74931526	5.59762096	7.44989634	0.00062171	0.00101877	-1.7347E-18	4.3364E-23	0	167.920105	58.7719994	-2.91295E-16
1	0.356249988	-1.73472E-18	-1.5718E-18	-8.6727E-19	0	-4846.14893	-2541.81592	1874278.25	2.8571E-05	-6.9389E-17	-2.6018E-21	0	1.3878E-16	-3.4691E-21	0	10.0074177	3.79587245	6.66646147	0.0010974	0.00158733	8.6732E-19	0	0	167.920105	59.8214989	-2.91295E-16
1	0.362500012	-1.73472E-18	8.6728E-23	-8.6728E-23	0	-4846.13965	-2541.80298	1874276.75	2.8571E-05	0	0	0	-6.9399E-17	0	0	14.644186	-1.08804512	4.37055206	0.00548523	0.01067291	0	0	0	167.920105	60.8710022	-2.91295E-16
1	0.368750006	-1.73472E-18	1.7345E-18	0	0	-4846.12842	-2541.7998	1874277.88	2.8571E-05	-2.7752E-16	0	0	-1.3877E-16	3.4691E-21	0	20.8741703	-0.00602739	2.72841811	0.00682086	0.01172033	-1.7346E-22	0	0	167.920105	61.9205017	-2.91295E-16
1	0.375	-1.73472E-18	2.1673E-19	8.6728E-23	0	-4846.12451	-2541.81372	1874280.62	2.8571E-05	1.648E-16	6.9382E-17	0	1.3876E-20	0	0	8.80324554	2.05505896	5.13899946	0.00114864	0.0017359	-1.7346E-18	4.3364E-23	0	167.920105	62.9700012	-2.91295E-16
1	0.381249994	-1.73472E-18	0	-4.3364E-23	0	-4846.1167	-2541.82056	1874280.12	2.8571E-05	-1.7345E-21	0	0	1.3877E-16	-3.4691E-21	0	0.98717129	-5.30350208	7.59967422	0.00092893	0.00164776	0	0	0	167.920105	64.0195007	-2.91295E-16
1	0.387499988	-1.73472E-18	3.2523E-23	-1.7346E-18	0	-4846.09912	-2541.81299	1874277.75	2.8571E-05	0	0	0	-1.3876E-20	-6.9382E-17	0	11.5736332	-10.037818	6.94983673	0.00848652	0.01646249	0	0	0	167.920105	65.0690002	-2.91295E-16
1	0.393750012	-1.73472E-18	-2.0191E-18	-3.4691E-22	0	-4846.08398	-2541.8186	1874272.75	2.8571E-05	-2.7753E-16	1.3877E-16	0	1.7345E-21	0	0	16.3809147	-7.53191853	5.9091692	0.01136038	0.02033064	-1.7346E-22	-8.6727E-19	0	167.920105	66.1184998	-2.91295E-16
1	0.400000006	-1.73472E-18	6.5046E-23	8.6728E-23	0	-4846.0791	-2541.83545	1874269.12	2.8571E-05	3.4692E-17	0	0	-1.3875E-16	6.9379E-17	0	9.34841824	-5.88848782	4.24450731	0.00339754	0.00610568	2.1682E-23	0	0	167.920105	67.1679993	-2.91295E-16
1	0.40625	-1.73472E-18	4.3364E-19	4.3364E-19	0	-4846.07617	-2541.83984	1874269.75	2.8571E-05	2.7754E-16	-6.9382E-17	0	-6.9384E-17	6.0711E-17	0	4.70044374	-0.64060223	1.94186175	0.00071505	0.0011452	-1.7345E-18	-4.3364E-23	0	167.920105	68.2174988	-2.91295E-16
1	0.412499994	-1.73472E-18	0	-4.3364E-23	0	-4846.0752	-2541.83765	1874272.25	2.8571E-05	1.3877E-16	-8.6733E-17	0	1.3876E-16	6.9389E-17	0	4.28949404	3.78352356	0.02232536	0.00060175	0.00088948	-8.6727E-19	7.5889E-19	0	167.920105	69.2669983	-2.91295E-16
1	0.418749988	-1.73472E-18	-1.7345E-18	0	0	-4846.07568	-2541.83325	1874275.62	2.8571E-05	-2.6019E-17	-6.9389E-17	0	3.4691E-17	1.4744E-16	0	4.00703096	9.42098904	-1.10672331	0.00055383	0.00080989	-1.6261E-23	8.6732E-19	0	167.920105	70.3164978	-2.91295E-16
1	0.425000012	-1.73472E-18	-8.6726E-19	8.6729E-19	0	-4846.07812	-2541.83105	1874277.75	2.8571E-05	7.3722E-17	-3.9897E-16	0	1.3009E-21	-5.204E-17	0	3.73304439	15.026268	-0.24668156	0.00055937	0.00082598	-4.3363E-19	2.6018E-18	0	167.920105	71.3660049	-2.91295E-16
1	0.431250006	-1.73472E-18	8.6723E-19	-1.7345E-18	0	-4846.08154	-2541.83081	1874278.62	2.8571E-05	0	-3.4691E-17	0	3.4684E-17	-3.6426E-16	0	3.78431177	16.3450394	1.97537899	0.00033361	0.00052635	0	2.1682E-19	0	167.920105	72.4155045	-2.91295E-16
1	0.4375	-1.73472E-18	0	-8.6727E-19	0	-4846.08447	-2541.83057	1874279.5	2.8571E-05	-1.3876E-16	3.1223E-16	0	-3.4691E-21	5.2035E-17	0	4.64623785	17.4277992	4.20252848	0.00023163	0.00038401	-8.6728E-23	-1.9514E-18	0	167.920105	73.4649963	-2.91295E-16
1	0.443749994	-1.73472E-18	0	-1.0841E-18	0	-4846.08643	-2541.83008	1874280.12	2.8571E-05	-6.9383E-17	-1.6479E-16	0	0	5.2037E-17	0	6.47189808	15.4367914	5.55946779	0.00016545	0.00025632	-4.3364E-23	8.6726E-19	0	167.920105	74.5144958	-2.91295E-16
1	0.449999988	-1.73472E-18	-1.7345E-18	1.0841E-18	0	-4846.08838	-2541.82886	1874279.88	2.8571E-05	-1.3876E-16	2.0816E-16	0	-6.9378E-17	1.3009E-21	0	7.69340372	13.0329437	6.49612045	0.0001692	0.00024814	-8.6728E-23	-1.3009E-18	0	167.920105	75.5639954	-2.91295E-16
1	0.456250012	-1.73472E-18	-1.7346E-18	0	0	-4846.09033	-2541.82739	1874279.25	2.8571E-05	1.5612E-16	-1.3877E-16	0	6.9382E-21	1.0409E-16	0	6.59499073	9.90949726	7.49846268	0.00014453	0.00020921	-8.6726E-19	8.6727E-19	0	167.920105	76.6135025	-2.91295E-16
1	0.462500006	-1.73472E-18	-4.3346E-19	0	0	-4846.08984	-2541.82544	1874277.62	2.8571E-05	0	2.7753E-16	0	6.9381E-17	-6.9382E-17	0	0.21949841	1.5473243	5.59967422	0.00055651	0.00082373	0	1.7346E-22	0	167.920105	77.663002	-2.91295E-16
1	0.46875	-1.73472E-18	-6.5046E-23	0	0	-4846.07812	-2541.8208	1874274.12	2.8571E-05	-1.3876E-20	0	0	-1.3876E-16	-1.0407E-20	0	19.447382	-3.6344316	3.09885812	0.00122369	0.00188102	0	0	0	167.920105	78.7125015	-2.91295E-16
1	0.474999994	-1.73472E-18	-2.1682E-18	4.3364E-23	0	-4846.07422	-2541.82129	1874272.5	2.8571E-05	2.7754E-16	6.9382E-17	0	0	0	0	19.1076393	2.6408565	3.76059198	0.00071117	0.00133297	-1.7345E-18	4.3364E-23	0	167.920105	79.762001	-2.91295E-16
1	0.481249988	-1.73472E-18	1.7344E-18	0	0	-4846.08301	-2541.82788	1874273.75	2.8571E-05	0	3.4691E-21	0	-1.3878E-16	-6.9385E-17	0	-0.58777702	-8.40186787	3.52179956	0.00022656	0.00035069	0	0	0	167.920105	80.8115005	-2.91295E-16
1	0.487500012	-1.73472E-18	-1.7345E-18	0	0	-4846.08398	-2541.83032	1874274.62	2.8571E-05	2.7755E-16	1.3876E-16	0	-1.3876E-20	-1.3876E-16	0	10.2987719	-15.8987322	-0.97378588	0.00029597	0.00041974	-3.4693E-18	-8.6727E-19	0	167.920105	81.8610001	-2.91295E-16
1	0.493750006	-1.73472E-18	-1.7346E-22	-3.4692E-18	0	-4846.08203	-2541.82812	1874274.75	2.8571E-05	-2.7753E-16	2.7754E-16	0	2.7753E-16	6.9382E-17	0	19.7930641	-16.5113792	-4.05218554	0.00084207	0.00143791	-1.7346E-22	-1.7345E-18	0	167.920105	82.9104996	-2.91295E-16
1	0.5	-1.73472E-18	-1.7346E-22	-3.4691E-18	0	-4846.0752	-2541.82275	1874274.75	2.8571E-05	-2.7753E-16	0	0	0	2.7753E-16	0	28.8041649	-14.1673937	-0.46993631	0.00096355	0.00178763	-1.7346E-22	0	0	167.920105	83.9599991	-2.91295E-16
1	-1.73472E-18	0.00625	0.06780066	0	-0.025	-4846.10254	-2541.83032	1874280	3.6467E-05	-12.7793741	0	3.224	-0.26775357	3.08548832	0.214	6.69631243	0	1.81599748	0.00169503	0.00317454	0.08399382	0	-0.03	167.920105	-2.91295E-16	1.04949999
1	0.00625	0.00625	0.09198654	0.01144902	-0.028	-4846.10352	-2541.82959	1874280.12	3.7126E-05	-13.9831715	-1.33713675	0.427	-0.6125021	3.60563874	0.157	6.63946056	2.66837144	1.91542816	0.00225071	0.00370746	0.08232036	0.0192843	-0.03	167.920105	1.04949999	1.04949999
1	0.0125	0.00625	0.09661336	0.04751371	-0.027	-4846.10938	-2541.83447	1874280	3.7134E-05	-12.7082777	-2.12830019	-0.728	-1.81844926	3.81323218	0.471	4.67027235	5.20876265	1.83233011	0.00281961	0.00489736	0.07633755	0.04507048	-0.02	167.920105	2.09899998	1.04949999
1	0.018750001	0.00625	0.06300251	0.06918415	-	-4846.11523	-2541.84375	1874279.62	3.5625E-05	-7.03537273	-5.49991179	1.416	-3.54916835	1.92695975	2.811	0.41969299	6.31762695	2.26864696	0.00300968	0.00522697	0.05958975	0.06694971	-0.02	167.920105	3.1485002	1.04949999

1					0.015																					
1	0.025	0.00625	0.03137366	0.0669017	0.019	-4846.11572	-2541.84741	1874279	3.4381E-05	-2.25053239	-7.72480392	-0.852	-2.63460088	-2.14380646	4.831	-2.86698651	6.41627169	5.2594223	0.00164532	0.00272529	0.03197294	0.06915748	0.01	167.920105	4.19799995	1.04949999
1	0.03125	0.00625	0.0218559	0.04061131	0.045	-4846.11377	-2541.84619	1874278.25	3.3503E-05	-3.87932944	-6.22590971	-3.912	1.88301373	-3.45572758	0.996	-2.61031723	4.34941959	7.77448225	0.00031969	0.00039819	0.02665724	0.04015213	0.041	167.920105	5.24749994	1.04949999
1	0.037500002	0.00625	0.04978629	0.02615321	0.023	-4846.11035	-2541.84326	1874277.25	3.2088E-05	-10.4164476	-5.39267445	-0.264	4.99453735	0.71755064	-3.831	-1.31228101	2.23647237	4.12250853	0.0001852	0.00022482	0.05551061	0.02596088	0.023	167.920105	6.29700041	1.04949999
1	0.043749999	0.00625	0.08687229	0.04538926	-0.007	-4846.1084	-2541.8396	1874276.25	3.2193E-05	-14.9264736	-7.33381081	4.148	2.19286823	4.33775616	-1.026	0.21288714	4.03516483	0.07346372	0.00018547	0.00024743	0.08908895	0.04912151	-0.01	167.920105	7.34649992	1.04949999
1	0.050000001	0.00625	0.08302377	0.07543702	0.008	-4846.11377	-2541.83838	1874275	3.3278E-05	-13.1496572	-8.70414829	2.299	-3.53017902	1.86222363	3.084	2.17021728	6.90415573	2.83893871	0.00017101	0.00022051	0.08292147	0.08018283	0.01	167.920105	8.39599991	1.04949999
1	0.056249999	0.00625	0.04324492	0.07330158	0.029	-4846.12549	-2541.83984	1874273.88	3.302E-05	-7.66837597	-8.52468109	-0.781	-3.6925056	-2.41714954	0.052	2.39894581	6.44982576	5.84742975	8.6258E-05	0.000105	0.04496171	0.0723993	0.031	167.920105	9.44549942	1.04949999
1	0.0625	0.00625	0.03187492	0.04936083	0.011	-4846.13525	-2541.84155	1874273.5	3.311E-05	-5.41739321	-6.04581404	1.751	0.97892374	-0.93992531	-3.134	1.79662108	5.01924181	2.62850332	7.73E-05	9.5529E-05	0.03676515	0.04996846	0.011	167.920105	10.4949999	1.04949999
1	0.068750002	0.00625	0.05862013	0.05838159	-0.003	-4846.1377	-2541.84204	1874273	3.4025E-05	-8.46854877	-8.18416786	4.242	2.08377409	3.04952908	1.011	1.25807357	7.18235922	-0.26191032	7.1213E-05	9.0345E-05	0.05719826	0.06065023	-0.01	167.920105	11.5445004	1.04949999
1	0.075000003	0.00625	0.06773769	0.08493112	0.027	-4846.13525	-2541.84399	1874272.5	3.3259E-05	-11.4069023	-10.91506	-0.694	-1.67766964	0.6740399	5.078	1.66294408	9.72247505	4.26948023	6.5409E-05	8.0799E-05	0.06281233	0.08808758	0.023	167.920105	12.5940008	1.04949999
1	0.081249997	0.00625	0.03951092	0.06530289	0.056	-4846.13379	-2541.84766	1874272.25	3.2502E-05	-6.92950106	-7.07625628	-4.722	-2.45993567	-5.87519598	1.191	0.8838566	8.17702389	9.12862968	5.8644E-05	7.3149E-05	0.0362274	0.06907573	0.056	167.920105	13.6434994	1.04949999
1	0.087499999	0.00625	0.03196839	0.01590823	0.038	-4846.13086	-2541.84985	1874271.75	3.315E-05	-6.27117157	-2.42925358	-2.982	4.05357695	-4.16507721	-3.071	-1.65225756	4.20757437	6.12350035	0.00012051	0.00014517	0.03206315	0.01464766	0.038	167.920105	14.6929998	1.04949999
1	0.09375	0.00625	0.0737731	0.01553137	0.019	-4846.12891	-2541.84961	1874272.12	3.2596E-05	-14.2548409	-1.91307485	2.009	5.10155821	1.95519269	0.188	-0.26721135	3.66048002	2.88610983	0.00024877	0.0003842	0.08689712	0.01701226	0.017	167.920105	15.7425003	1.04949999
1	0.100000001	0.00625	0.07946291	0.03470294	0.039	-4846.13086	-2541.85083	1874275.75	3.3134E-05	-16.2870693	-3.37028146	-1.375	-5.49037552	1.34569907	3.566	2.99192238	2.98125029	6.70444727	0.00026033	0.00040087	0.09583264	0.03908758	0.04	167.920105	16.7919998	1.04949999
1	0.106250003	0.00625	0.01791798	0.01908988	0.055	-4846.13281	-2541.85278	1874280.62	3.6796E-05	-7.49131918	-1.57313287	-5.478	2.01752496	-4.28100157	0.223	0.67303175	2.41167855	10.279829	0.00029369	0.00038237	0.01826741	0.0338335	0.062	167.920105	17.8415012	1.04949999
1	0.112499997	0.00625	0.10714949	-0.01921272	0.034	-4846.13281	-2541.85059	1874282.25	3.7123E-05	-15.5705738	-4.16626215	-2.282	8.20661163	0.10495902	-2.836	4.94782209	0.62549824	7.04604292	0.00059837	0.00106045	0.12105169	-0.01442493	0.043	167.920105	18.8909988	1.04949999
1	0.118749999	0.00625	0.11909093	0.02832724	0.019	-4846.1416	-2541.85669	1874284.25	4.9076E-05	-16.6561871	3.8679533	-1.407	-12.2118168	1.69053459	-0.327	3.88412833	0.37900299	2.93373704	0.00080692	0.00137559	0.12085002	0.03514548	0.027	167.920105	19.9405003	1.04949999
1	0.125	0.00625	-0.01291225	0.00982473	0.034	-4846.15479	-2541.86914	1874284.5	4.9208E-05	2.85628462	5.09285545	-1.842	-10.138545	-6.68962717	2.002	-5.84738159	-2.25817704	4.88108492	0.00031	0.00051303	-0.03159605	0.00670676	0.039	167.920105	20.9899998	1.04949999
1	0.131249994	0.00625	-0.0096825	-0.04012083	0.049	-4846.15771	-2541.8728	1874281.75	3.3942E-05	2.47780895	3.4702363	-3.425	7.03288031	-5.68636656	0.791	-6.19976759	-5.50665712	7.79719257	0.00018006	0.0002556	-0.00588175	-0.04847483	0.052	167.920105	22.0394993	1.04949999
1	0.137500003	0.00625	0.05002239	-0.07002761	0.045	-4846.15479	-2541.86841	1874279.5	3.2377E-05	-8.35248089	4.15888405	-4.268	6.55412245	-0.87549198	-0.526	-3.45005703	-6.17570543	7.15661621	0.00026821	0.00038756	0.05631498	-0.06437284	0.049	167.920105	23.0890007	1.04949999
1	0.143749997	0.00625	0.07651	-0.05390529	0.038	-4846.14746	-2541.86182	1874278.75	3.3487E-05	-11.8710051	5.42279959	-3.326	-0.38156685	0.51640719	-0.614	-2.32774949	-6.75281811	5.68490553	0.00024152	0.00033725	0.0760448	-0.05941848	0.045	167.920105	24.1385002	1.04949999
1	0.150000006	0.00625	0.05778004	-0.0442317	0.036	-4846.13867	-2541.85669	1874282	3.408E-05	-9.760252	5.9550848	-2.302	-2.9727385	0.2933045	-1.122	-3.09458232	-6.9471302	5.12841892	0.00036544	0.00051355	0.05154539	-0.05791775	0.041	167.920105	25.1880016	1.04949999
1	0.15625	0.00625	0.04360534	-0.03917027	0.027	-4846.13184	-2541.85376	1874284.12	3.4091E-05	-7.24958992	7.17363977	-1.986	-1.9389087	0.12359113	-2.746	-2.93796349	-6.04583168	4.02564049	0.00021119	0.00028574	0.03888556	-0.05575217	0.031	167.920105	26.2374992	1.04949999
1	0.162499994	0.00625	0.02737485	-0.0391861	0.009	-4846.12793	-2541.85278	1874283.12	3.3122E-05	-4.64990056	7.95550013	0.031	-1.49001276	2.53209734	-3.616	-1.55580378	-5.53717184	0.68750554	0.00021498	0.00026891	0.02730905	-0.05637286	0.007	167.920105	27.2869987	1.04949999
1	0.168750003	0.00625	0.01953308	-0.01715729	-0.007	-4846.125	-2541.85181	1874282.25	3.123E-05	-4.14340448	3.14889455	2.492	-0.37282264	5.53427124	-1.862	0.50321204	-3.67873454	-1.94393063	0.0002597	0.00030403	0.0202604	-0.02410095	-0.01	167.920105	28.3365002	1.04949999
1	0.174999997	0.00625	0.02979231	0.01020294	-0.012	-4846.125	-2541.84961	1874282.75	3.1425E-05	-4.44133902	-1.43798864	2.416	1.66733932	4.01267338	0.108	2.27904272	-0.90331227	-1.2141695	0.00041886	0.00051013	0.02264877	0.01280555	-0.02	167.920105	29.3859997	1.04949999
1	0.181250006	0.00625	0.0477686	0.02827244	-0.012	-4846.12598	-2541.84766	1874282.75	3.2991E-05	-6.86561823	-3.77288938	1.313	2.77563071	3.09898281	0.253	4.44777155	2.23497677	0.45385113	0.00061767	0.00086763	0.04110214	0.02605748	-0.01	167.920105	30.4355011	1.04949999
1	0.1875	0.00625	0.05216397	0.05491088	-0.005	-4846.12695	-2541.84839	1874281.62	3.4711E-05	-9.89041233	-4.86988401	1.146	0.48041189	3.80245662	0.345	4.33935738	5.86534786	1.35321784	0.00083135	0.00117765	0.05734416	0.05154284	-0.01	167.920105	31.4850006	1.04949999
1	0.193749994	0.00625	0.04534608	0.06965222	0.006	-4846.12891	-2541.85156	1874280.25	3.4195E-05	-7.84712553	-6.74867058	0.751	-2.38855839	2.36679721	1.749	0.66701746	7.00417471	2.02744365	0.00074985	0.00100205	0.04710729	0.07358815	-0.01	167.920105	32.5345001	1.04949999
1	0.200000003	0.00625	0.03682386	0.07769658	0.019	-4846.1333	-2541.85498	1874280.25	3.3538E-05	-4.32873726	-9.41717529	-0.710	-1.88777792	0.42449543	3.320	-3.78916979	6.93131113	3.44111705	0.00047203	0.00058463	0.02748718	0.08112781	0.009	167.920105	33.5839996	1.04949999
1	0.206249997	0.00625	0.03282608	0.08018149	0.034	-4846.1377	-2541.8584	1874281.38	3.6698E-05	-4.53331804	-9.98740196	-1.866	0.64981103	-0.24546368	2.684	-5.42197895	6.36571836	5.23675823	0.00017585	0.00021489	0.02351006	0.07889434	0.033	167.920105	34.6334991	1.04949999
1	0.212500006	0.00625	0.03779336	0.07976522	0.041	-4846.14209	-2541.86133	1874283.38	3.663E-05	-6.11675024	-10.9290218	-2.958	1.89030099	-0.80361003	0.079	-3.20487309	6.80744648	5.69131279	0.00014095	0.00019796	0.03560982	0.07805952	0.042	167.920105	35.6830025	1.04949999
1	0.21875	0.00625	0.04822334	0.0650991	0.034	-4846.14404	-2541.86133	1874285.38	3.4197E-05	-7.74602318	-11.1815338	-2.516	2.04737949	-0.9429791	-1.755	-0.63737989	5.26891804	5.16099119	0.00013121	0.0001651	0.04713882	0.06884921	0.034	167.920105	36.7324982	1.04949999
1	0.224999994	0.00625	0.06701445	0.06251283	0.019	-4846.14307	-2541.85815	1874287.5	3.491E-05	-10.3880072	-11.1186447	-0.159	1.83141387	0.11822172	-1.486	1.59003916	4.78754711	4.16625738	0.00016774	0.00022198	0.06120203	0.06627229	0.02	167.920105	37.7819977	1.04949999
1	0.231250003	0.00625	0.07416453	0.0698127	0.011	-4846.14111	-2541.85498	1874288.88	3.4385E-05	-12.6602697	-11.3941298	0.450	-0.07119675	1.23335946	0.218	3.88812661	6.69411707	3.34205842	0.00023355	0.00035208	0.0700315	0.07032698	0.015	167.920105	38.831501	1.04949999
1	0.237499997	0.00625	0.05966242	0.08013582	0.018	-4846.13525	-2541.85474	1874287.75	3.3641E-05	-11.6735725	-11.1046104	-0.268	-1.84288657	0.40786755	0.878	3.94304967	8.28432465	4.16546726	0.00028195	0.00039671	0.06031208	0.08168929	0.023	167.920105	39.8810005	1.04949999
1	0.243750006	0.00625	0.04966758	0.07082679	0.024	-4846.12695	-2541.85596	1874285.5	3.4884E-05	-7.34802485	-11.0680008	-1.342	-0.07611111	-2.16422534	0.175	1.56135225	8.0754261	5.22404909	0.00026443	0.00033777	0.04699541	0.07542533	0.026	167.920105	40.9305	1.04949999
1	0.25	0.00625	0.06557762	0.05826132	0.027	-4846.1167	-2541.85571	1874282.88	3.5867E-05	-8.97680855	-9.22146034	-1.116	2.25293517	-1.48059261	0.314	1.20846295	7.08750963	5.47864103	0.00021991	0.00028227	0.05936069	0.05463646	0.025	167.920105	41.9799995	1.04949999
1	0.256249994	0.00625	0.07607941	0.06234934	0.035	-4846.11035	-2541.85571	1874279.38	3.4785E-05	-14.4626493	-8.61663437	-1.119	1.95550525	1.03516626	0.037	2.62611556	7.16115427	5.4977541	0.00015867	0.00020631	0.07515708	0.05691794	0.03	167.920105	43.0294991	1.04949999
1	0.262499988	0.00625	0.07527219	0.06871663	0.028	-4846.11133	-2541.85889	1874276.5	3.4426E-05	-15.786623	-8.70253563	-0.987	1.89157617	0.8922416	-0.975	2.43385768	7.53323412	4.7248764	0.00013735	0.00017176	0.08380448	0.06757603	0.026	167.920105	44.0789986	1.04949999
1	0.268750012	0.00625	0.08402871	0.06705149	0.021	-4846.1167	-2541.86279	1874275	3.4775E-05	-15.1680107	-7.22719908	0.727	-0.89108014	-0.34260035	0.661	1.61221766	7.59768009	4.59339523	0.00010033	0.00011697	0.09880181	0.06807098	0.018	167.920105	45.1285019	1.04949999
1	0.275000006	0.00625	0.0665144	0.06560179	0.039	-4846.125	-2541.86719	1874274.62	3.3812E-05	-12.0136852	-4.57561064	-1.237	-5.88464642	-1.52233672	2.715	1.01131606	7.27617455	6.91976881	0.0001176	0.00014032	0.07266596	0.06329352	0.034	167.920105	46.1780014	1.04949999

1	0.28125	0.00625	0.02823786	0.04815564	0.055	-4846.1333	-2541.87134	1874274.5	3.296E-05	-5.58922005	-4.38137388	-3.143	-3.4466083	-4.04622221	0.619	-0.75567854	4.76458788	8.68209839	9.7121E-05	0.00011304	0.0252438	0.04904179	0.052	167.920105	47.2275009	1.04949999
1	0.287499994	0.00625	0.02411706	0.00866978	0.042	-4846.13574	-2541.87231	1874274.88	3.1508E-05	-4.86386108	-3.31283617	-2.073	2.58328271	-2.11458492	-1.865	-4.44998121	0.25055492	6.15303612	0.0001496	0.0001748	0.0295834	0.01271579	0.042	167.920105	48.2770004	1.04949999
1	0.293749988	0.00625	0.04371392	0.01885873	0.030	-4846.13428	-2541.87109	1874275.25	3.079E-05	-9.23477364	-3.92278242	-0.315	1.98265636	1.81372344	-0.595	-4.85862017	0.21109925	3.83856177	0.00015989	0.00021067	0.05753481	0.0226095	0.029	167.920105	49.3264961	1.04949999
1	0.300000012	0.00625	0.04570444	0.0313888	0.037	-4846.13232	-2541.86841	1874275.75	3.1207E-05	-9.07159328	-6.0716424	-1.350	-1.63755035	0.96718884	0.516	-2.06428695	0.02669638	4.62939692	0.00013716	0.00016114	0.05436664	0.03538736	0.034	167.920105	50.3760033	1.04949999
1	0.306250006	0.00625	0.03638943	0.02901117	0.037	-4846.13184	-2541.86475	1874276.25	3.2222E-05	-6.59526539	-5.41067314	-2.062	-0.95674497	-0.41547245	-1.918	-0.78515166	0.29252341	4.82895613	6.8236E-05	9.0503E-05	0.0370654	0.03469938	0.035	167.920105	51.4255028	1.04949999
1	0.3125	0.00625	0.04554133	0.02330712	0.009	-4846.1333	-2541.86108	1874277.12	3.3254E-05	-6.26042175	-8.38383579	0.848	1.98021173	1.04556513	-3.791	0.88128299	-0.01851507	2.16629577	9.058E-05	0.00011079	0.04240734	0.03019396	0.01	167.920105	52.4749985	1.04949999
1	0.318749994	0.00625	0.06446605	0.04587104	-0.013	-4846.13477	-2541.85596	1874277.75	3.4077E-05	-9.59501743	-9.04047871	1.927	1.64125085	3.8686142	-1.206	3.86479497	3.79831934	0.32059953	0.00012098	0.00015296	0.06181802	0.04776893	-0.01	167.920105	53.524498	1.04949999
1	0.324999988	0.00625	0.06179319	0.07935051	-0.001	-4846.13916	-2541.85156	1874278.25	3.5609E-05	-12.4536772	-11.4957199	-0.752	-0.85704726	3.21097922	2.183	4.55055904	7.46659517	2.85983062	0.00034323	0.00046703	0.06292295	0.0785516	-0	167.920105	54.5739975	1.04949999
1	0.331250012	0.00625	0.04617234	0.08609632	0.020	-4846.14844	-2541.85059	1874278.25	3.5705E-05	-9.53943634	-11.003006	-2.798	-1.67589998	-0.02380506	2.448	2.54269361	9.03613853	5.51565075	0.00045939	0.00062643	0.05110491	0.08790623	0.015	167.920105	55.6235008	1.04949999
1	0.337500006	0.00625	0.04279791	0.07507501	0.028	-4846.15723	-2541.84912	1874278.12	3.508E-05	-5.0702281	-9.86629295	-2.172	-0.93609571	-2.8201046	1.904	0.10375415	9.62599087	6.07479239	0.00043878	0.00051386	0.04197418	0.07825403	0.026	167.920105	56.6730003	1.04949999
1	0.34375	0.00625	0.04540399	0.05048615	0.038	-4846.15918	-2541.84351	1874277.75	3.518E-05	-7.21809292	-7.60743046	-2.076	1.51672494	-3.46151519	1.647	-0.80433506	7.84748125	7.22902203	0.00044265	0.0005164	0.03947123	0.05265496	0.039	167.920105	57.7224998	1.04949999
1	0.349999994	0.00625	0.07458666	0.03935187	0.048	-4846.15527	-2541.83472	1874277.88	3.4372E-05	-11.5054531	-6.70180941	-3.253	1.84601212	-2.31446218	0.224	0.94353271	4.80204201	7.73540449	0.00066743	0.00090433	0.06093322	0.03498513	0.047	167.920105	58.7719994	1.04949999
1	0.356249988	0.00625	0.06833297	0.02848938	0.045	-4846.15088	-2541.82568	1874277.5	3.416E-05	-10.4077168	-2.59607291	-2.991	2.4474318	-3.34282827	-1.54	1.7988379	3.21931982	7.38080692	0.00117726	0.00148309	0.06254636	0.0237242	0.042	167.920105	59.8214989	1.04949999
1	0.362500012	0.00625	0.12303024	-0.00468838	0.027	-4846.14209	-2541.81494	1874276.5	3.5267E-05	-14.5769367	-0.68097711	-1.443	5.43336916	-1.90094733	-1.969	4.25301552	1.29867983	5.90700674	0.00418381	0.00779968	0.09152616	-0.00680028	0.027	167.920105	60.8710022	1.04949999
1	0.368750006	0.00625	0.15209746	0.01816209	0.016	-4846.13232	-2541.81226	1874277.88	3.5535E-05	-21.5580845	4.29290009	-1.054	-2.92047286	1.57155359	0.384	5.12248039	-1.87341237	4.32168198	0.0053548	0.00901543	0.13046357	-3.7671E-05	0.017	167.920105	61.9205017	1.04949999
1	0.375	0.00625	0.04432171	0.0202099	0.037	-4846.12842	-2541.82324	1874279.38	3.4916E-05	-10.3702936	6.21465015	-2.323	-9.9435091	-2.64874005	2.435	-0.9321928	-2.45731401	6.13960266	0.00145697	0.00204818	0.05502028	0.01284412	0.032	167.920105	62.9700012	1.04949999
1	0.381249994	0.00625	-0.00474061	-0.0290674	0.054	-4846.12158	-2541.82935	1874278.12	3.4101E-05	-0.9991169	5.82011652	-3.182	1.38519502	-6.04644442	0.905	-3.12985635	-6.11455917	8.11382961	0.00108759	0.00179045	0.00616982	-0.03314689	0.047	167.920105	64.0195007	1.04949999
1	0.387499988	0.00625	0.10582966	-0.06057456	0.052	-4846.10645	-2541.82568	1874275.12	3.4291E-05	-11.1598997	7.15984726	-3.230	7.69686031	-1.11420667	-0.845	1.04529393	-7.6729846	7.30125999	0.00593358	0.01122593	0.07233521	-0.06273636	0.043	167.920105	65.0690002	1.04949999
1	0.393750012	0.00625	0.10445803	-0.02054228	0.041	-4846.09326	-2541.82983	1874271.25	3.5239E-05	-18.2570362	10.1701078	-2.051	-1.11260569	2.07466221	-1.353	1.52886724	-8.09397507	6.00681114	0.00819528	0.01448217	0.10238072	-0.04707449	0.037	167.920105	66.1184998	1.04949999
1	0.400000006	0.00625	-0.02092555	-0.04265971	0.028	-4846.08691	-2541.83984	1874269.75	3.7763E-05	-11.8289089	7.85703325	0.928	-5.84024096	3.44566154	-1.984	-2.57842898	-7.26309109	3.71079326	0.0033787	0.00563675	0.05842762	-0.03680305	0.027	167.920105	67.1679993	1.04949999
1	0.40625	0.00625	-0.02501062	-0.03725624	0.016	-4846.08252	-2541.8418	1874270.75	3.4777E-05	-5.03659105	2.56024337	2.571	-2.52946448	4.83601046	-2.111	-3.4218843	-2.97880697	1.39221287	0.0010387	0.0014381	0.02937777	-0.00400376	0.012	167.920105	68.2174988	1.04949999
1	0.412499994	0.00625	0.00062518	-0.02055066	0.003	-4846.08008	-2541.83911	1874272.88	2.9785E-05	-4.58534765	-3.33655024	2.38	-0.34670651	5.03080082	-1.524	-0.55338615	0.53318262	0.07607179	0.00090644	0.00120016	0.02680934	0.02364702	1E-04	167.920105	69.2669983	1.04949999
1	0.418749988	0.00625	0.02352062	0.01422071	-0.002	-4846.08008	-2541.83472	1874275.38	2.9606E-05	-4.75279284	-9.716959	2.164	-0.27822456	5.62136412	-0.135	0.86789709	3.8000102	-0.81495923	0.00083216	0.00113322	0.02504395	0.05888119	-0.01	167.920105	70.3164978	1.04949999
1	0.425000012	0.00625	0.02461591	0.05315103	0.004	-4846.08105	-2541.83228	1874277.12	2.9983E-05	-4.54059267	-13.8527431	1.549	-0.11135964	3.46202016	1.541	0.23639058	8.29748726	-0.00442113	0.00086464	0.0011865	0.02333153	0.09391417	-0	167.920105	71.3660049	1.04949999
1	0.431250006	0.00625	0.02446017	0.07634886	0.016	-4846.08496	-2541.83228	1874278.5	3.0172E-05	-4.81811571	-14.5738878	0.201	0.45659712	1.2007668	2.224	-0.49224255	10.7720528	1.35932636	0.00056093	0.00073506	0.02365195	0.10215651	0.012	167.920105	72.4155045	1.04949999
1	0.4375	0.00625	0.0271169	0.0930313	0.026	-4846.08936	-2541.83374	1874279.75	2.9986E-05	-5.19496107	-15.8511801	-2.259	1.34379447	-0.45412481	1.792	-1.1522876	12.8481874	2.93742061	0.00038491	0.00051561	0.02903899	0.10892374	0.026	167.920105	73.4649963	1.04949999
1	0.443749994	0.00625	0.02879225	0.08568273	0.032	-4846.09229	-2541.83472	1874280	3.326E-05	-6.53632212	-13.4326429	-2.292	1.52358437	-2.1974299	1.146	-2.59384489	10.3928061	4.85743523	0.00023595	0.00030747	0.04044936	0.09647994	0.035	167.920105	74.5144958	1.04949999
1	0.449999988	0.00625	0.03917215	0.07198612	0.038	-4846.09473	-2541.83472	1874279.62	3.6871E-05	-8.92609119	-12.1330242	-1.55	0.06154627	-2.76364303	0.969	-4.07444525	9.66064739	6.4318943	0.00024759	0.00032482	0.04808377	0.08145589	0.041	167.920105	75.5639954	1.04949999
1	0.456250012	0.00625	0.04789627	0.04787347	0.044	-4846.09766	-2541.83447	1874278.88	3.5565E-05	-6.13504744	-9.15100479	-1.066	-3.7369473	-5.74280119	-0.448	-3.87671399	7.4873395	7.32028627	0.00029021	0.00039017	0.04121869	0.06193436	0.047	167.920105	76.6135025	1.04949999
1	0.462500006	0.00625	0.03278617	0.01430206	0.035	-4846.09814	-2541.8335	1874277.62	3.8459E-05	-3.73197985	-5.55957747	-0.109	6.42620182	-6.77197075	-2.2	-3.40193439	3.33332705	5.79258823	0.0007232	0.00110032	0.00137187	0.00967078	0.035	167.920105	77.663002	1.04949999
1	0.46875	0.00625	0.10602996	-0.00800727	0.020	-4846.08936	-2541.82886	1874275	3.8435E-05	-16.6967907	-6.21240807	0.843	9.4440794	0.54676652	-0.92	4.63493395	-0.45292476	3.88878131	0.00154706	0.00246009	0.12154613	-0.0227152	0.019	167.920105	78.7125015	1.04949999
1	0.474999994	0.00625	0.08892853	0.01471873	0.021	-4846.0835	-2541.82739	1874273.62	3.5077E-05	-13.8487673	0.44047391	1.619	-10.0175896	-2.3837204	0.211	4.31227207	-2.59841299	5.7546339	0.00092817	0.00167455	0.11942274	0.01650535	0.024	167.920105	79.762001	1.04949999
1	0.481249988	0.00625	0.00108462	-0.04872331	0.02	-4846.08447	-2541.83057	1874274.38	3.7343E-05	-3.43821383	1.00572193	-6.183	-4.40442753	-9.26978111	-2.367	0.40336949	-8.27296925	7.61555195	0.00025419	0.00031876	-0.00367361	-0.05251167	0.022	167.920105	80.8115005	1.04949999
1	0.487500012	0.00625	0.04535885	-0.09888278	0.004	-4846.08398	-2541.83252	1874275.25	3.8573E-05	-7.66792488	9.52334023	-4.833	10.1904068	-4.05474997	-3.787	8.35438156	-11.9083605	4.77355099	0.00043917	0.00058769	0.06436732	-0.09936707	-0.01	167.920105	81.8610001	1.04949999
1	0.493750006	0.00625	0.10454345	-0.10456097	-0.004	-4846.0835	-2541.83203	1874275.88	3.8404E-05	-10.851882	10.9443579	3.026	9.25270557	0.86567015	0.251	13.1898546	-9.93018341	1.86248589	0.00097871	0.00158818	0.12370666	-0.10319612	-0.03	167.920105	82.9104996	1.04949999
1	0.5	0.00625	0.16635762	-0.08356787	0.018	-4846.08057	-2541.82983	1874276.25	3.8031E-05	-25.4524555	7.81890869	-1.811	9.0111084	2.34398794	3.582	12.8241844	-8.10730648	3.40846395	0.0011149	0.00183196	0.18002604	-0.08854621	-0	167.920105	83.9599991	1.04949999
1	-1.73472E-18	0.0125	0.05186277	0	0.018	-4846.10938	-2541.84106	1874278.88	4.5747E-05	-16.5149975	0	7.129	-0.11370423	5.33674288	0.198	-8.7523365	0	4.33924961	0.00169842	0.00312472	0.08370391	0	0.023	167.920105	-2.91295E-16	2.09899998
1	0.00625	0.0125	0.08050261	0.02677002	0.019	-4846.11182	-2541.84229	1874278.88	4.4875E-05	-15.5615673	-2.03184032	5.77	-2.02604055	5.20876265	0.016	-9.46305656	2.29643178	3.74548459	0.00215363	0.00357612	0.08299326	0.03335464	0.024	167.920105	1.04949999	2.09899998
1	0.0125	0.0125	0.0790011	0.06516404	0.028	-4846.12061	-2541.84961	1874279	4.2623E-05	-9.93014717	-6.55606365	6.257	-6.21976709	3.64925575	0.353	-13.6297035	2.36660933	0.98723358	0.0028001	0.00478594	0.0583784	0.06510953	0.023	167.920105	2.09899998	2.09899998
1	0.018750001	0.0125	0.01123434	0.06970372	0.041	-4846.12891	-2541.85938	1874279	4.1645E-05	-2.66078091	-7.46526241	7.040	-7.53725863	1.2075094	3.427	-17.5810986	-1.32134938	-1.55978346	0.00310987	0.00513812	0.00524616	0.07897034	0.028	167.920105	3.1485002	2.09899998
1	0.025	0.0125	-0.03480605	0.06892367	0.073	-4846.13184	-2541.86328	1874279	4.2068E-05	3.85917521	-7.72801399	0.699	-3.03001046	-1.96820796	5.505	-15.6073561	-2.2571888	-2.24881649	0.00168564	0.00262644	-0.03583733	0.0802034	0.066	167.920105	4.19799995	2.09899998
1	0.03125	0.0125	-0.02711174	0.0510065	0.099	-4846.13135	-2541.86328	1874278.75	4.0688E-05	7.93755102	-5.94456863	-6.331	1.55470526	-4.17979908	-1.137	-12.745389	-0.80554414	-2.28364825	0.00038274	0.00045698	-0.03262896	0.05436774	0.097	167.920105	5.24749994	2.09899998
1	0.037500002	0.0125	-0.0073155	0.02392388	0.053	-4846.12842	-2541.86035	1874277.88	3.6821E-05	4.16298532	-7.23429823	0.303	2.82320452	-0.31425443	-7.701	-13.5254717	-0.46968168	-2.18687439	0.000298	0.00034844	-0.01640351	0.0279559	0.052	167.920105	6.29700041	2.09899998
1	0.043749999	0.0125	0.00975654	0.04504912	0.005	-4846.12451	-2541.8562	1874277.25	3.933E-05	-3.11937141	-8.6553812	10.13	3.48249865	4.66768408	-1.284	-16.0526218	-0.6673066	-1.82210422	0.0002625	0.00032293	0.00266109	0.05043956	9E-04	167.920105	7.34649992	2.09899998

1	0.050000001	0.0125	0.02795378	0.08268619	0.034	-4846.12598	-2541.85522	1874276.12	5.9902E-05	-5.35745955	-10.6619349	6.691	2.18605924	2.41466045	5.774	-13.6693726	-1.71968317	-0.99278867	0.00019722	0.00023312	0.02712771	0.08630195	0.035	167.920105	8.39599991	2.09899998
1	0.056249999	0.0125	0.02552067	0.08160396	0.066	-4846.13281	-2541.85522	1874274.75	5.6055E-05	-3.06886697	-10.3909931	-0.665	-0.37359616	-1.88491404	-0.21	-7.45195246	-1.27661192	-0.48399839	0.00011515	0.00013411	0.02998682	0.08062281	0.073	167.920105	9.44549942	2.09899998
1	0.0625	0.0125	0.00885426	0.05980363	0.030	-4846.1377	-2541.85449	1874274.12	4.3717E-05	-2.92016506	-8.94302845	3.863	-1.14087224	0.73253387	-6.109	-7.08307886	-0.22350952	-0.76182532	0.0001606	0.00019058	0.02245776	0.06274053	0.033	167.920105	10.4949999	2.09899998
1	0.068750002	0.0125	0.00743304	0.0885649	0.001	-4846.13818	-2541.85571	1874273.25	5.036E-05	-2.954144	-10.3529997	10.29	-0.13367698	4.70323277	1.641	-10.7196684	1.28779542	-1.99496865	0.00013071	0.00016587	0.01572592	0.0897795	-0	167.920105	11.5445004	2.09899998
1	0.075000003	0.0125	0.02174671	0.12007789	0.058	-4846.13818	-2541.86011	1874272.88	4.6731E-05	-1.90445995	-13.0818291	-0.101	-0.37421709	0.99466515	9.390	-11.409955	0.43261835	-1.85726523	0.00010933	0.00012861	0.0207868	0.12153095	0.053	167.920105	12.5940008	2.09899998
1	0.081249997	0.0125	0.01267073	0.09988224	0.113	-4846.14014	-2541.8645	1874273.38	4.0865E-05	0.7576012	-9.45242119	-10.23	-3.31520295	-5.51490355	1.854	-9.5737524	1.27347255	0.15110548	0.00010128	0.00011835	0.01104821	0.1022128	0.114	167.920105	13.6434994	2.09899998
1	0.087499999	0.0125	-0.02382806	0.05182938	0.075	-4846.14062	-2541.86743	1874274.88	3.6562E-05	0.9670043	-6.60117292	-3.554	-1.15106761	-4.51654339	-6.243	-10.8776827	4.58832741	-0.16302206	0.00018193	0.00022503	-0.02065322	0.05259468	0.077	167.920105	14.6929998	2.09899998
1	0.09375	0.0125	-0.01439058	0.04371434	0.041	-4846.14453	-2541.87109	1874279	3.3699E-05	-1.12005246	-6.28447962	7.234	4.64417934	-1.22632384	0.580	-17.6530514	4.27868509	-1.69966507	0.00030321	0.00039689	-0.00334014	0.045756	0.036	167.920105	15.7425003	2.09899998
1	0.100000001	0.0125	0.02576358	0.03752256	0.084	-4846.14844	-2541.8728	1874283.75	3.5154E-05	-3.52918839	-1.87965834	-1.618	0.94024289	-1.24880111	7.393	-15.8438501	-1.32735717	-0.71317071	0.00028586	0.00036508	0.03739903	0.03726563	0.084	167.920105	16.7919998	2.09899998
1	0.106250003	0.0125	0.00547464	0.01486641	0.116	-4846.1499	-2541.87256	1874287.75	4.1415E-05	-4.14825439	-4.33939171	-8.660	1.95590055	-2.35575271	0.341	-8.256814	-1.14298248	0.54956144	0.00033449	0.00039329	0.0084129	0.03014598	0.128	167.920105	17.8415012	2.09899998
1	0.112499997	0.0125	0.05356054	-0.00878623	0.07	-4846.15674	-2541.87524	1874292.88	5.2084E-05	-4.74041986	-3.60670733	2.612	3.21109772	-2.03267622	-7.346	-19.2141933	2.66738915	0.21282008	0.00054268	0.0006723	0.06184778	0.00781873	0.088	167.920105	18.8909988	2.09899998
1	0.118749999	0.0125	0.05732178	0.00216851	0.024	-4846.16455	-2541.8811	1874294.75	6.2901E-05	-0.21337991	5.90577507	3.649	-10.7952013	-2.88367438	-2.165	-19.1164188	-3.62608171	-1.48381102	0.00059137	0.00091935	0.0485516	0.00473754	0.037	167.920105	19.9405003	2.09899998
1	0.125	0.0125	-0.04897118	-0.00805108	0.055	-4846.16699	-2541.88599	1874288.88	5.4929E-05	12.1836195	5.76168966	-3.440	-10.0838995	-5.88566208	4.863	-7.02795744	-3.24591136	-3.51853895	0.00054797	0.00070613	-0.07309227	-0.02822721	0.061	167.920105	20.9899998	2.09899998
1	0.131249994	0.0125	-0.07151433	-0.05481922	0.094	-4846.16553	-2541.88721	1874283.12	4.1028E-05	10.3852482	5.80935621	-6.424	2.39732361	-3.91752768	2.275	-11.6684237	-1.35852957	-3.46715593	0.00025177	0.00032359	-0.07749709	-0.06883322	0.097	167.920105	22.0394993	2.09899998
1	0.137500003	0.0125	-0.0282537	-0.07320268	0.086	-4846.16309	-2541.88525	1874280.25	4.0068E-05	5.28322172	8.06689548	-3.841	3.87201715	-1.24616075	-2.112	-17.0541096	-0.83926624	-3.90567708	0.00033893	0.00045095	-0.04312572	-0.07719631	0.089	167.920105	23.0890007	2.09899998
1	0.143749997	0.0125	-0.00588906	-0.08140353	0.070	-4846.15771	-2541.88086	1874278.75	4.3097E-05	8.05521107	10.540967	-2.321	0.35547483	-0.77142441	-2.028	-15.7251053	-1.63726199	-6.16953468	0.00033324	0.000418	-0.02909687	-0.08441023	0.071	167.920105	24.1385002	2.09899998
1	0.150000006	0.0125	-0.02574917	-0.08636259	0.065	-4846.14795	-2541.87354	1874279.75	4.3114E-05	6.39149475	8.88136578	-4.468	-0.61021394	0.70698607	-1.659	-12.526845	-1.70096672	-6.59613419	0.00040476	0.00047671	-0.03868228	-0.08683912	0.064	167.920105	25.1880016	2.09899998
1	0.15625	0.0125	-0.03642745	-0.07226293	0.051	-4846.13916	-2541.86572	1874281.25	4.0804E-05	3.13651419	9.48060989	-3.156	1.53877997	1.4099592	-4.441	-10.6788187	-1.34488904	-5.39249039	0.00033327	0.00041544	-0.03672455	-0.0755729	0.05	167.920105	26.2374992	2.09899998
1	0.162499994	0.0125	-0.022435	-0.0619925	0.016	-4846.13281	-2541.8606	1874281.62	3.7512E-05	2.53242493	10.2973852	2.303	3.44117475	2.3670969	-5.97	-6.81348562	-0.75552511	-3.80157566	0.00037993	0.00043934	-0.01944755	-0.06921465	0.009	167.920105	27.2869987	2.09899998
1	0.168750003	0.0125	0.00606068	-0.03796387	-0.011	-4846.12842	-2541.85718	1874281.75	3.3497E-05	-0.57757413	6.09953308	5.85	3.83484554	4.63385868	-1.902	-3.19323421	-2.56385851	-2.1580174	0.00054135	0.00062721	0.00629015	-0.04598418	-0.02	167.920105	28.3365002	2.09899998
1	0.174999997	0.0125	0.02884437	0.00035686	-0.01	-4846.12744	-2541.85327	1874282.5	3.4556E-05	-6.14747953	0.90802348	5.247	3.94455862	5.91370964	2.397	-2.25112081	-3.6271565	-0.67988914	0.00088805	0.00106902	0.02848803	-0.0112914	-0.02	167.920105	29.3859997	2.09899998
1	0.181250006	0.0125	0.04810052	0.04022851	0.002	-4846.12842	-2541.85205	1874283.12	3.9458E-05	-10.2525206	-2.84861159	4.102	2.06031418	6.76865864	2.567	-3.78504109	-0.01046266	0.32075277	0.00107261	0.00146601	0.05559715	0.02793721	0.006	167.920105	30.4355011	2.09899998
1	0.1875	0.0125	0.03867503	0.08136342	0.016	-4846.13232	-2541.85645	1874282.12	4.1706E-05	-8.9403801	-5.75040245	3.301	-3.78075767	4.76920223	1.573	-7.87322283	1.93811727	0.35405585	0.00101439	0.00140215	0.05424197	0.07331685	0.017	167.920105	31.4850006	2.09899998
1	0.193749994	0.0125	-0.00107832	0.08568047	0.031	-4846.13721	-2541.86279	1874280.88	4.0257E-05	-2.09886146	-9.54139233	2.836	-8.12852573	1.06596339	2.087	-10.0246916	0.10717376	-0.68811184	0.00067964	0.0008734	0.00833772	0.08755218	0.025	167.920105	32.5345001	2.09899998
1	0.200000003	0.0125	-0.04783981	0.08453727	0.046	-4846.14258	-2541.86841	1874280.12	3.9715E-05	3.13373971	-12.0089978	-0.069	-6.0889945	-0.63845563	3.209	-10.0894613	0.30732113	-2.69205689	0.00040551	0.00048465	-0.04736462	0.08664139	0.043	167.920105	33.5839996	2.09899998
1	0.206249997	0.0125	-0.06603064	0.08014812	0.062	-4846.14844	-2541.87427	1874279.38	4.5781E-05	7.06191015	-11.7601347	-4.474	0.58429647	-0.12386531	2.252	-10.0517118	-1.12727547	-6.02841139	0.00018833	0.00021771	-0.06777474	0.07957149	0.065	167.920105	34.6334991	2.09899998
1	0.212500006	0.0125	-0.04356605	0.08286896	0.071	-4846.15234	-2541.87891	1874280	4.6521E-05	8.29607868	-10.3430748	-5.000	4.78459787	-1.09680033	-0.076	-10.8025074	-2.76081872	-5.61178017	0.00016604	0.00019506	-0.04006092	0.08509307	0.071	167.920105	35.6830025	2.09899998
1	0.21875	0.0125	-0.01367973	0.06114088	0.069	-4846.15332	-2541.87988	1874281.12	4.0955E-05	3.63629627	-12.7980833	-1.425	4.7958169	-2.0199008	-1.525	-14.3395634	-1.71927202	-2.22221923	0.00024379	0.00028295	-0.00796725	0.06586147	0.065	167.920105	36.7324982	2.09899998
1	0.224999994	0.0125	0.01416412	0.05240699	0.053	-4846.1499	-2541.87744	1874282.25	4.5513E-05	-3.93303323	-10.5268402	2.624	4.52550554	1.42519855	-1.819	-14.8041773	-3.1809516	-0.04729152	0.00031334	0.00038772	0.01988674	0.05984434	0.052	167.920105	37.7819977	2.09899998
1	0.231250003	0.0125	0.03956332	0.08059736	0.036	-4846.14404	-2541.87524	1874282	4.7919E-05	-8.53604031	-11.3426113	2.312	2.35211015	3.49677706	-8E-04	-10.6507034	-1.2560221	1.60657525	0.00036015	0.00052302	0.04860158	0.08367646	0.042	167.920105	38.831501	2.09899998
1	0.237499997	0.0125	0.03967182	0.0955606	0.044	-4846.13818	-2541.87451	1874280.25	4.1676E-05	-7.0672431	-13.7672892	0.053	-2.32677388	1.38130867	1.882	-8.06316566	-0.8935231	0.90176362	0.00040073	0.0005112	0.04928812	0.10355406	0.052	167.920105	39.8810005	2.09899998
1	0.243750006	0.0125	0.0119327	0.08632821	0.060	-4846.13574	-2541.87427	1874280.25	4.6925E-05	-2.77030301	-13.7399168	0.488	-2.734586	-1.19681501	1.313	-10.8836737	0.67549223	-0.75377387	0.00038	0.00044493	0.0195169	0.10094282	0.065	167.920105	40.9305	2.09899998
1	0.25	0.0125	0.01151539	0.08847275	0.071	-4846.13428	-2541.875	1874279.38	5.3514E-05	-2.49051046	-11.8924503	1.307	1.0647645	-0.91427213	0.273	-15.4623766	2.81060147	-1.05695319	0.00033754	0.00039015	0.01510579	0.08859387	0.068	167.920105	41.9799995	2.09899998
1	0.256249994	0.0125	0.03290607	0.09898314	0.079	-4846.13525	-2541.87817	1874276.75	4.5904E-05	-4.23257828	-10.9936094	-1.326	1.22539604	0.44572479	-0.754	-14.0954466	1.58704042	-1.08325946	0.00029748	0.00034613	0.03282645	0.08951443	0.069	167.920105	43.0294991	2.09899998
1	0.262499988	0.0125	0.0267441	0.09828021	0.066	-4846.13965	-2541.88281	1874275.12	4.1953E-05	-4.55650377	-13.1632719	0.564	-1.01389647	0.43652526	-0.904	-12.4709578	0.57756782	-1.37927032	0.00027175	0.00031876	0.03042322	0.09416543	0.059	167.920105	44.0789986	2.09899998
1	0.268750012	0.0125	0.00938859	0.09433829	0.058	-4846.146	-2541.88721	1874275.75	4.8198E-05	-5.5596447	-10.8878927	4.612	-1.42253971	-0.25705963	2.194	-18.3028965	2.46572566	-0.73917085	0.00026586	0.00034131	0.02015272	0.09497101	0.057	167.920105	45.1285019	2.09899998
1	0.275000006	0.0125	0.0048892	0.08670039	0.087	-4846.15137	-2541.89014	1874276.38	4.6014E-05	-1.7517792	-7.96683884	-1.331	-2.36789846	-2.83309531	4.088	-19.2363625	1.77574992	-0.8303718	0.00025227	0.00030828	0.01264145	0.09095218	0.086	167.920105	46.1780014	2.09899998
1	0.28125	0.0125	-0.01047753	0.05693995	0.110	-4846.15479	-2541.89062	1874276.25	3.8906E-05	5.7245307	-4.44765806	-6.693	-5.46130228	-7.02562618	-0.767	-12.5125866	-1.24150193	-1.15011811	0.00021292	0.00028043	-0.00944598	0.05955735	0.109	167.920105	47.2275009	2.09899998
1	0.287499994	0.0125	-0.05637071	0.0017811	0.075	-4846.15625	-2541.8894	1874276.38	3.642E-05	5.82059097	-1.73749447	-3.026	-4.1029458	-4.55349302	-4.844	-12.8186007	-3.36032581	-1.93280375	0.00035696	0.00043657	-0.05562476	0.00313194	0.077	167.920105	48.2770004	2.09899998
1	0.293749988	0.0125	-0.06307552	-0.0022271	0.045	-4846.15576	-2541.88672	1874276.5	3.6252E-05	2.90525603	-0.91513836	1.496	2.38569045	-0.22385821	-1.524	-13.719821	-5.9382329	-3.20699286	0.00040009	0.00052913	-0.06073276	0.00263874	0.048	167.920105	49.3264961	2.09899998
1	0.300000012	0.0125	-0.02464672	-0.00436174	0.058	-4846.15234	-2541.88232	1874276.5	3.8135E-05	5.41485786	0.37190077	-2.488	4.07346249	0.08142406	0.990	-8.25435543	-7.68367386	-4.45945549	0.0002752	0.00034788	-0.02580359	0.0003337	0.058	167.920105	50.3760033	2.09899998
1	0.306250006	0.0125	-0.00362653	0.00021058	0.065	-4846.14844	-2541.8772	1874276.25	3.8491E-05	4.73041058	-1.20139337	-1.264	2.94557285	-0.04521149	-2.463	-7.81437445	-5.52315283	-3.74896932	0.00018997	0.00022452	-0.0098144	0.00365654	0.06	167.920105	51.4255028	2.09899998
1	0.3125	0.0125	0.01729077	-0.00067211	0.029	-4846.14453	-2541.87231	1874276.75	5.5409E-05	-2.08614206	-3.489748	5.703	4.64995146	3.50579929	-4.508	-10.5457935	-5.33793306	-2.10410285	0.00016249	0.00019209	0.01101604	-0.00023144	0.027	167.920105	52.4749985	2.09899998
1	0.318749994	0.0125	0.04939814	0.04821906	0.001	-4846.14111	-2541.86743	1874277.38	6.821E-05	-8.24458981	-7.43547869	6.324	3.6692791	7.48511744	0.693	-9.06444931	-1.88937151	-0.9785136	0.00015475	0.00019663	0.04830994	0.04747899	0.004	167.920105	53.524498	2.09899998
1	0.324999988	0.0125	0.05336762	0.09658577	0.035	-4846.14209	-2541.86523	1874277.75	5.2559E-05	-10.0472307	-12.3624554	0.186	-1.32209921	5.23781204	5.195	-7.89308834	-0.11891516	0.09448873	0.00039824	0.00052186	0.05688198	0.09333244	0.036	167.920105	54.5739975	2.09899998
1	0.331250012	0.0125	0.02176356	0.11379914	0.070	-4846.14697	-2541.86548	1874277.75	4.3222E-05	-7.2558341	-14.3641109	-3.893	-4.44679785	2.15939355	3.215	-9.48778629	-0.60741383	-0.24045299	0.00052851	0.00070135	0.03178367	0.11295173	0.069	167.920105	55.6235008	2.09899998

1	0.337500006	0.0125	-0.01250764	0.11497923	0.073	-4846.15234	-2541.86597	1874277.75	4.8543E-05	-1.20087934	-14.6605415	-2.185	-3.34703207	-1.18865848	1.734	-11.2972546	1.43840408	-0.9198395	0.00064394	0.00079541	0.00129693	0.1203249	0.076	167.920105	56.6730003	2.09899998
1	0.34375	0.0125	-0.02666105	0.08792169	0.079	-4846.15479	-2541.86475	1874277.75	4.5277E-05	2.88845062	-11.073081	-3.897	0.83977932	-4.82395411	1.660	-12.0955572	2.85870361	-0.41861343	0.00092372	0.00115299	-0.01005419	0.09809352	0.09	167.920105	57.7224998	2.09899998
1	0.349999994	0.0125	0.00829152	0.06262444	0.095	-4846.15332	-2541.86035	1874277.25	3.8745E-05	2.3980732	-10.5797405	-6.555	2.6031754	-4.6281662	0.151	-13.9751043	2.55916762	-1.05271816	0.00102141	0.00133256	0.01179416	0.06002552	0.097	167.920105	58.7719994	2.09899998
1	0.356249988	0.0125	0.03217494	0.03875183	0.103	-4846.15137	-2541.85498	1874276.25	4.1995E-05	-1.90834177	-4.89398861	-3.161	3.30947828	-3.50335717	-1.828	-14.7172375	1.64378691	-0.72230756	0.00141883	0.00169461	0.02248547	0.0402415	0.092	167.920105	59.8214989	2.09899998
1	0.362500012	0.0125	0.07530604	0.01632641	0.077	-4846.15039	-2541.85181	1874276.25	6.1384E-05	-7.55075502	-0.71679658	2.847	3.32363796	-5.09272528	-3.059	-16.8114376	2.68815589	2.21283269	0.00203062	0.0030644	0.05316269	0.0162335	0.074	167.920105	60.8710022	2.09899998
1	0.368750006	0.0125	0.0776973	-0.01032246	0.049	-4846.14746	-2541.85083	1874276.75	6.1173E-05	-7.17347288	4.77705336	3.933	-5.18521357	-3.75599766	0.232	-18.0776596	-2.44044352	-0.80721784	0.0025173	0.00374035	0.064031	-0.02341766	0.054	167.920105	61.9205017	2.09899998
1	0.375	0.0125	-0.01483091	-0.02696692	0.080	-4846.14404	-2541.85278	1874275.88	4.273E-05	1.5780313	13.1442966	-0.208	-8.25234509	-4.24115086	3.792	-14.157917	-6.93702078	-1.94425523	0.00136241	0.00170176	-0.01165241	-0.03071643	0.077	167.920105	62.9700012	2.09899998
1	0.381249994	0.0125	-0.0532821	-0.06776346	0.109	-4846.13965	-2541.854	1874274.25	4.2397E-05	3.51589799	11.9334497	-4.337	1.97748852	-5.21567583	1.161	-12.5339422	-4.88078928	0.75480264	0.0010089	0.00145296	-0.0391232	-0.07643199	0.101	167.920105	64.0195007	2.09899998
1	0.387499988	0.0125	0.00175403	-0.086781	0.096	-4846.13135	-2541.85327	1874272.62	4.6407E-05	-1.68875611	15.4182472	-4.617	4.65871668	-1.97941363	-2.107	-15.7954617	-3.00886893	0.07043171	0.00211408	0.00357704	0.01306617	-0.09591232	0.091	167.920105	65.0690002	2.09899998
1	0.393750012	0.0125	-0.00939906	-0.08081991	0.068	-4846.12207	-2541.85278	1874272	4.8768E-05	-0.94470078	15.656414	-1.136	-3.62371755	0.40989325	-3.59	-16.9250278	-4.58345461	-2.92403412	0.00304741	0.00479116	0.01911084	-0.1011747	0.075	167.920105	66.1184998	2.09899998
1	0.400000006	0.0125	-0.07577121	-0.11083104	0.032	-4846.11133	-2541.85059	1874272.75	4.8562E-05	1.74745619	14.1275396	2.236	-4.95075607	5.11517334	-4.615	-15.6185255	-4.88253069	-5.56387377	0.00243541	0.00322481	-0.03223036	-0.09078864	0.046	167.920105	67.1679993	2.09899998
1	0.40625	0.0125	-0.05863594	-0.07770876	0.006	-4846.10156	-2541.84644	1874273.88	4.0675E-05	2.77634859	6.5492878	3.894	2.02504492	7.79628086	-3.635	-13.1632719	-4.22982645	-5.02558565	0.00181211	0.00220838	-0.04277355	-0.03723508	0.017	167.920105	68.2174988	2.09899998
1	0.412499994	0.0125	-0.02159652	-0.03699496	-0.014	-4846.09619	-2541.84204	1874275.5	3.3626E-05	2.08869815	-0.13539296	6.764	4.28978586	6.77882385	-2.207	-7.18460989	-3.0611155	-2.94607568	0.00160665	0.00189728	-0.00691733	0.00666478	1E-03	167.920105	69.2669983	2.09899998
1	0.418749988	0.0125	-0.00841861	0.01218275	-0.02	-4846.09277	-2541.83789	1874276.38	3.3217E-05	-1.42450047	-9.55273151	5.534	0.78977561	7.76429319	-0.08	-3.50942421	-3.31970763	-1.23877406	0.00104176	0.00125004	0.01084871	0.04750013	-0.01	167.920105	70.3164978	2.09899998
1	0.425000012	0.0125	-0.0124383	0.06505135	-0.005	-4846.09131	-2541.83496	1874277.25	3.3288E-05	-4.11241436	-16.7164116	1.886	-1.3601377	6.97203302	2.174	-3.73232317	-1.35763872	-1.22515965	0.00104315	0.00134338	0.00295488	0.10371859	-0	167.920105	71.3660049	2.09899998
1	0.431250006	0.0125	-0.00778621	0.11276612	0.018	-4846.09473	-2541.83618	1874278.75	3.8442E-05	-1.41546345	-18.4080315	0.857	-1.3886795	4.550704	2.941	-5.20306587	1.37041271	-2.7559979	0.00081852	0.00095192	-0.00615303	0.13465066	0.017	167.920105	72.4155045	2.09899998
1	0.4375	0.0125	-0.00902672	0.15097715	0.039	-4846.10254	-2541.84229	1874279.88	4.0186E-05	5.23387814	-22.3062706	-1.765	-2.10160446	-0.37924695	3.498	-7.73509693	3.06883907	-3.81529498	0.00058617	0.0006829	-0.0144036	0.16060233	0.037	167.920105	73.4649963	2.09899998
1	0.443749994	0.0125	-0.03047054	0.12891674	0.056	-4846.10938	-2541.84814	1874280	4.028E-05	5.70654726	-21.2236996	-3.144	-2.92216063	-3.18754196	3.494	-10.3595209	3.11337805	-3.91769314	0.00036034	0.00042106	-0.03242306	0.12991008	0.061	167.920105	74.5144958	2.09899998
1	0.449999988	0.0125	-0.04538951	0.11721411	0.076	-4846.11475	-2541.85205	1874279	4.4523E-05	2.56665754	-18.2280922	-2.724	-1.28286707	-2.90546274	2.462	-11.9737806	4.76362658	-3.86665916	0.00033436	0.00038645	-0.05093057	0.1207581	0.08	167.920105	75.5639954	2.09899998
1	0.456250012	0.0125	-0.03387127	0.08748627	0.087	-4846.12012	-2541.85571	1874277.62	4.446E-05	7.16941118	-15.4732399	-4.130	0.67251009	-6.32731199	-0.639	-13.3935337	4.6548667	-3.61059451	0.00035195	0.00041559	-0.04845892	0.09359174	0.092	167.920105	76.6135025	2.09899998
1	0.462500006	0.0125	-0.01628033	0.04738047	0.0	-4846.12354	-2541.85742	1874277.12	4.873E-05	6.88554049	-11.0036888	-1.402	8.51165676	-7.94027138	-3.432	-11.7916622	2.29592371	-1.56219125	0.00065124	0.00086944	-0.04252418	0.04166659	0.072	167.920105	77.663002	2.09899998
1	0.46875	0.0125	0.05051968	0.00034892	0.056	-4846.12109	-2541.85474	1874276.62	7.3546E-05	-3.50298357	-8.94412994	7.466	7.71421432	-5.93174553	-0.038	-19.0863514	0.61744607	1.70751321	0.00123509	0.00186954	0.05793667	-0.00566156	0.049	167.920105	78.7125015	2.09899998
1	0.474999994	0.0125	0.03203028	-0.01631007	0.069	-4846.11377	-2541.85083	1874275.5	6.607E-05	-2.72366309	1.81101227	7.007	-4.23156881	-7.82005262	3.726	-16.5101924	-5.26718569	1.98440039	0.00081203	0.00128019	0.0539034	-0.03248016	0.072	167.920105	79.762001	2.09899998
1	0.481249988	0.0125	-0.00472226	-0.09119097	0.084	-4846.1084	-2541.8501	1874275.38	4.1406E-05	-3.0308013	8.52041245	-6.244	4.04210424	-9.30993462	-0.981	-5.65983915	-2.48106265	2.34843588	0.00024504	0.00028968	0.00504212	-0.10341212	0.095	167.920105	80.8115005	2.09899998
1	0.487500012	0.0125	0.06829629	-0.14140013	0.054	-4846.1084	-2541.85205	1874275.88	6.5629E-05	-12.702363	11.9038372	0.714	12.7864676	-1.65721142	-5.753	-10.6600227	-1.86994386	3.56033969	0.00039107	0.00053361	0.10442978	-0.14885451	0.06	167.920105	81.8610001	2.09899998
1	0.493750006	0.0125	0.1186684	-0.12766989	0.030	-4846.11084	-2541.854	1874276.12	0.00011119	-16.0431824	15.2739582	18.26	4.46980667	3.80105686	-1.365	-14.4147577	1.35036504	3.99141693	0.0005892	0.00094928	0.16487318	-0.1241273	0.023	167.920105	82.9104996	2.09899998
1	0.5	0.0125	0.12658468	-0.09725029	0.052	-4846.1084	-2541.85376	1874276.75	0.00013458	-19.5562115	12.8313828	8.751	-0.731341	3.64575648	3.092	-16.5436802	2.19647884	1.76829445	0.0006083	0.00099734	0.16030231	-0.10134134	0.043	167.920105	83.9599991	2.09899998

APPENDIX B .

Experimental mesurments

It worthy to mention here that the tables of experimental tests are too big, so the listed table below are just a sample of data extracted from experimental works. The rest of the data are put in DVD with this thesis.

B-1 Isothermal LDA Measurements

The table B-1 below is the LDA data for the case of isothermal swirl flow, 500 LPM, with grid mesh 150µm (5 pages of 54). The columns that are highlighted represent (x the parallel direction of burner exit), (y the downstream direction) and (LDA1-mean is the axial velocity). The measurement points were taken to be in plane exactly in the middle of the nozzle exit and extend to downstream direction. The starting point was chosen to be 9mm off the internal edge of the nozzle. Two different matrix of point were taken to generate the plot of velocity distribution downstream the nozzle., so the first mesh is finned gradually to capture the flow in the region over the nozzle wall and at 9mm the step change became only 0.5mm to capture the effect of the wire mesh on the flow just off the wall. At 5mm downstream the steps were increase to reduce the time of the experimental.

Figure B-1 LDA result of isothermal swirl flow. flow rate 500LPM, wire mesh 150um and central air injection.

Version	DXEX v5										
Project	D:\Mohammed\500anwg15045.lda										
Date/Time	14:25:59										
Position	1	0.00 mm	0.00 mm	0.00 mm							
Region	New Region										
X [mm]	Y [mm]	Z [mm]	Date_Time	CountStohr and (2011)	Data RateStohr and (2011) [#/s]	ValidationStohr and (2011) [%]	LDA1-Mean [m/s]	LDA1-RMS [m/s]	LDA1-MeanConf [m/s]	LDA1-RMSConf [m/s]	LDA1-AnodeCur [µA]
0	0	0	14:25:59	100	9.667592391	#N/A	-0.0247801	0.355374008	0.070004206	0.049500449	#N/A
2	0	0	14:26:17	61	4.154092463	#N/A	0.1336839	0.158691517	0.040154494	0.028393515	#N/A
4	0	0	14:26:35	89	6.166425944	#N/A	-0.1128758	0.542127787	0.113270392	0.080094262	#N/A
6	0	0	14:26:53	1299	86.6432967	#N/A	-0.3150094	0.69663632	0.037898746	0.02679846	#N/A
7	0	0	14:27:10	7109	474.1912799	#N/A	-0.1210141	0.632278753	0.014699107	0.010393838	#N/A
8	0	0	14:27:28	20000	4682.746076	#N/A	0.8385613	0.96155837	0.013326852	0.009423508	#N/A
9	0	0	14:27:34	20000	9686.00603	#N/A	2.23464	0.982107489	0.013611656	0.009624894	6.400000095
9.5	0	0	14:27:38	20000	4990.858345	#N/A	2.804519	0.929270174	0.01287935	0.009107075	166.4000092
10	0	0	14:27:45	12370	824.6919543	#N/A	3.1303461	0.696961927	0.012282813	0.00868526	70.40000153
10.5	0	0	14:28:02	13681	912.1426867	#N/A	3.2144726	0.702233912	0.011767788	0.008321082	76.80000305
11	0	0	14:28:19	20000	2536.871911	#N/A	3.2121722	0.708450026	0.009818862	0.006942984	28.80000114

11.5	0	0	14:28:29	20000	2589.253716	#N/A	3.2523921	0.671677419	0.009309207	0.006582603	70.40000153
12	0	0	14:28:39	20000	2392.185782	#N/A	3.2835205	0.633427034	0.00877907	0.00620774	64
12.5	0	0	14:28:50	20000	2029.080588	#N/A	3.2840862	0.650869817	0.009020821	0.006378684	73.59999847
13	0	0	14:29:02	20000	1551.549885	#N/A	3.2824225	0.646988018	0.008967021	0.006340641	#N/A
13.5	0	0	14:29:17	19558	1304.036996	#N/A	3.2866351	0.63148167	0.008850457	0.006258218	#N/A
14	0	0	14:29:35	20000	2165.154823	#N/A	3.3060288	0.624667602	0.008657668	0.006121896	128
14.5	0	0	14:29:47	19234	1282.648948	#N/A	3.2828627	0.680532847	0.009617931	0.006800904	16
15	0	0	14:30:04	15768	1051.632304	#N/A	3.211656	0.685328289	0.010697448	0.007564238	32
15.5	0	0	14:30:22	20000	3865.803388	#N/A	3.1326196	0.720668067	0.0099882	0.007062724	25.60000038
16	0	0	14:30:29	20000	4431.187696	#N/A	3.1438358	0.727237839	0.010079254	0.007127109	76.80000305
16.5	0	0	14:30:36	20000	1939.284007	#N/A	3.0708259	0.763601662	0.010583244	0.007483483	281.6000061
17	0	0	14:30:48	20000	1687.2801	#N/A	2.9990583	0.792349066	0.010981672	0.007765215	#N/A
17.5	0	0	14:31:03	13564	904.9891907	#N/A	2.969522	0.827839711	0.013932352	0.009851661	9.600000381
18	0	0	14:31:20	15720	1048.163264	#N/A	2.846725	0.870433855	0.013607533	0.009621979	41.60000229
19	0	0	14:31:38	16615	1108.004587	#N/A	2.6661794	0.952385965	0.014482114	0.010240401	6.400000095
20	0	0	14:31:55	10236	682.5355898	#N/A	2.3751929	1.0423194	0.020193564	0.014279006	#N/A
21	0	0	14:32:13	16974	1131.729796	#N/A	2.2007808	1.099067214	0.016534879	0.011691925	48
22	0	0	14:32:30	9195	613.070556	#N/A	1.9785834	1.166040346	0.023835123	0.016853977	16
23	0	0	14:32:48	15982	1066.115502	#N/A	1.741686	1.198849235	0.018587401	0.013143277	#N/A
24	0	0	14:33:04	20000	2163.941601	#N/A	1.5331975	1.236942568	0.017143578	0.01212234	#N/A
25	0	0	14:33:16	20000	2818.615042	#N/A	1.3382557	1.261325144	0.017481512	0.012361295	#N/A
26	0	0	14:33:25	13301	886.7660735	#N/A	1.3927531	1.367338282	0.0232384	0.01643203	#N/A

27	0	0	14:33:43	20000	2042.01244	#N/A	1.1768967	1.487563753	0.020617097	0.014578489	#N/A
28	0	0	14:33:54	20000	2425.796502	#N/A	0.9673368	1.46793968	0.020345115	0.014386169	#N/A
29	0	0	14:34:05	20000	1372.803295	#N/A	0.9616023	1.519105715	0.021054257	0.014887608	35.20000076
30	0	0	14:34:22	20000	2488.567455	#N/A	0.8637019	1.511810322	0.020953146	0.014816112	#N/A
31	0	0	14:34:33	20000	2644.975106	#N/A	0.8024239	1.540400137	0.02134939	0.015096299	#N/A
32	0	0	14:34:43	20000	1702.767889	#N/A	0.7552782	1.616495222	0.022404041	0.015842049	#N/A
33	0	0	14:34:57	20000	1800.302151	#N/A	0.7192404	1.594781573	0.022103098	0.01562925	#N/A
34	0	0	14:35:10	20000	1580.629398	#N/A	0.7349086	1.662067204	0.023035652	0.016288666	28.80000114
35	0	0	14:35:25	20000	1800.826824	#N/A	0.8145393	1.696644416	0.02351488	0.016627531	#N/A
36	0	0	14:35:38	20000	1439.661727	#N/A	0.6748579	1.659457326	0.02299948	0.016263088	#N/A
37	0	0	14:35:55	20000	1972.702594	#N/A	0.5784466	1.636587571	0.022682514	0.016038959	9.600000381
38	0	0	14:36:07	20000	3819.126806	#N/A	0.5067541	1.638607519	0.022710509	0.016058755	#N/A
39	0	0	14:36:15	20000	2384.734524	#N/A	0.5974009	1.6659377	0.023089296	0.016326598	28.80000114
39	-1	0	14:36:25	20000	3711.323849	#N/A	0.3829881	1.572477949	0.021793977	0.015410669	#N/A
38	-1	0	14:36:33	20000	1556.262293	#N/A	0.4002141	1.63543877	0.022666592	0.016027701	#N/A
37	-1	0	14:36:48	20000	2069.024877	#N/A	0.5501285	1.563808911	0.021673828	0.01532571	#N/A
36	-1	0	14:37:00	20000	4680.639119	#N/A	0.4716777	1.655158153	0.022939895	0.016220955	#N/A
35	-1	0	14:37:06	20000	2693.727107	#N/A	0.3698389	1.557973666	0.021592953	0.015268524	#N/A
34	-1	0	14:37:17	20000	1974.803238	#N/A	0.5702869	1.639074149	0.022716977	0.016063328	#N/A
33	-1	0	14:37:29	20000	1984.425677	#N/A	0.6018675	1.605596573	0.02225299	0.01573524	#N/A
32	-1	0	14:37:42	15607	1040.60087	#N/A	0.5156272	1.616585296	0.025363483	0.017934691	#N/A
31	-1	0	14:37:58	12726	848.8960148	#N/A	0.6307884	1.530733974	0.026596647	0.01880667	6.400000095

30	-1	0	14:38:16	20000	1758.177014	#N/A	0.7699234	1.535773063	0.021285261	0.015050952	#N/A	
29	-1	0	14:38:30	20000	1861.461072	#N/A	0.8304882	1.519274271	0.021056594	0.01488926	#N/A	
28	-1	0	14:38:42	20000	2641.345661	#N/A	0.8189134	1.405929922	0.019485682	0.013778458	#N/A	
27	-1	0	14:38:52	20000	2072.387443	#N/A	1.0181105	1.41013817	0.019544007	0.0138197	#N/A	
26	-1	0	14:39:04	20000	1716.726723	#N/A	1.1844599	1.416734981	0.019635436	0.01388435	#N/A	
25	-1	0	14:39:18	20000	3880.126402	#N/A	1.3675719	1.378661644	0.019107753	0.013511222	#N/A	
24	-1	0	14:39:26	20000	2309.086001	#N/A	1.4764766	1.280334105	0.017744969	0.012547588	#N/A	
23	-1	0	14:39:36	20000	2529.9208	#N/A	1.6715805	1.285413231	0.017815364	0.012597365	#N/A	
22	-1	0	14:39:46	20000	3654.98957	#N/A	1.7987257	1.192530695	0.016528045	0.011687093	#N/A	
21	-1	0	14:39:54	20000	3920.64727	#N/A	2.0249461	1.203702282	0.01668288	0.011796577	#N/A	
20	-1	0	14:40:01	20000	3709.013326	#N/A	2.229353	1.154139885	0.015995963	0.011310854	#N/A	
19	-1	0	14:40:09	20000	3874.922543	#N/A	2.5236949	1.110387468	0.01538957	0.010882069	#N/A	
18	-1	0	14:40:17	20000	4456.977121	#N/A	2.7583502	1.034753912	0.014341316	0.010140842	#N/A	
17.5	-1	0	14:40:23	20000	7216.450088	#N/A	2.8658011	1.036701046	0.014368303	0.010159924	22.39999962	
17	-1	0	14:40:29	20000	5479.451735	#N/A	2.860838	1.005628582	0.01393765	0.009855406	#N/A	
16.5	-1	0	14:40:34	20000	4150.478693	#N/A	2.9647987	0.981403011	0.013601892	0.00961799	#N/A	
16	-1	0	14:40:42	20000	5566.077504	#N/A	3.0560663	0.895960955	0.012417696	0.008780637	#N/A	
15.5	-1	0	14:40:47	20000	3064.674137	#N/A	3.1696066	0.884429166	0.012257869	0.008667623	54.40000153	
15	-1	0	14:40:56	20000	6409.758531	#N/A	3.0824249	0.936267856	0.012976335	0.009175654	#N/A	
14.5	-1	0	14:41:01	20000	8357.515898	#N/A	3.134678	0.966555433	0.01339611	0.00947248	#N/A	
14	-1	0	14:41:06	20000	3678.593497	#N/A	3.1762169	0.909324613	0.012602911	0.008911604	#N/A	
13.5	-1	0	14:41:14	20000	2524.094263	#N/A	3.1770722	1.005498176	0.013935842	0.009854128	#N/A	

13	-1	0	14:41:24	20000	12930.21408	#N/A	3.1619837	1.053714124	0.014604098	0.010326657	#N/A
12.5	-1	0	14:41:27	20000	21372.3341	#N/A	3.1918087	1.12780757	0.015631006	0.011052791	16
12	-1	0	14:41:31	20000	16085.73844	#N/A	3.1630065	1.18447296	0.016416368	0.011608125	19.20000076
11.5	-1	0	14:41:34	20000	10470.2277	#N/A	3.108778	1.139971897	0.015799599	0.011172004	73.59999847
11	-1	0	14:41:39	20000	9111.32907	#N/A	3.0953869	1.159240648	0.016066657	0.011360842	35.20000076
10.5	-1	0	14:41:42	20000	8303.079127	#N/A	3.0429107	1.136969763	0.015757991	0.011142582	22.39999962
10	-1	0	14:41:48	20000	7337.173447	#N/A	3.0652439	1.133550842	0.015710606	0.011109076	54.40000153
9.5	-1	0	14:41:52	20000	10264.60453	#N/A	2.7942178	1.304420536	0.018078798	0.012783641	19.20000076
9	-1	0	14:41:57	20000	14208.11901	#N/A	2.4701813	1.255334695	0.017398486	0.012302588	9.600000381
8	-1	0	14:42:00	20000	11106.0882	#N/A	1.1570048	1.378843828	0.019110278	0.013513007	22.39999962
7	-1	0	14:42:04	20000	2923.631563	#N/A	0.0631294	1.08196772	0.014995682	0.010603549	108.8000031
6	-1	0	14:42:13	20000	2559.590265	#N/A	-0.337173	1.814358473	0.025146354	0.017781158	204.8000031
4	-1	0	14:42:25	6983	470.2657062	#N/A	-0.4422313	1.430784756	0.03356143	0.023731515	#N/A
2	-1	0	14:42:42	467	31.95693578	#N/A	-0.316105	1.539686814	0.139796244	0.098850872	#N/A
0	-1	0	14:43:02	45	3.14756285	#N/A	-0.2563611	1.66255369	0.491253223	0.347368485	#N/A
0	-2	0	14:43:19	83	5.678275966	#N/A	-0.03519	1.145628065	0.247966373	0.175338704	#N/A
2	-2	0	14:43:37	590	41.05551565	#N/A	-0.3499754	1.169526201	0.094451396	0.066787222	#N/A
4	-2	0	14:43:54	3807	258.7664612	#N/A	-0.4095442	1.274466304	0.040490211	0.028630903	#N/A
6	-2	0	14:44:12	11430	762.385614	#N/A	-0.1247565	1.19888598	0.021980109	0.015542284	#N/A
7	-2	0	14:44:29	20000	4832.605753	#N/A	0.4111183	1.184767438	0.016420449	0.011611011	48
8	-2	0	14:44:35	20000	9879.040501	#N/A	1.6416264	1.397821379	0.0193733	0.013698992	3.200000048
9	-2	0	14:44:39	20000	5718.222117	#N/A	2.5500514	1.258405993	0.017441053	0.012332687	214.4000092

9.5	-2	0	14:44:45	20000	7601.344777	#N/A	2.7792514	1.290562533	0.017886731	0.012647829	230.4000092
10	-2	0	14:44:49	20000	5271.47269	#N/A	2.9318322	1.179649857	0.016349522	0.011560858	28.80000114
10.5	-2	0	14:44:56	20000	2143.15694	#N/A	3.0621386	1.040124351	0.014415748	0.010193473	28.80000114
11	-2	0	14:45:07	20000	4166.837785	#N/A	3.0847038	1.132874884	0.015701237	0.011102451	#N/A
11.5	-2	0	14:45:14	20000	5321.259929	#N/A	3.1305887	1.153591585	0.015988363	0.01130548	#N/A
12	-2	0	14:45:20	20000	4468.557655	#N/A	3.1235759	1.054246407	0.014611475	0.010331873	#N/A
12.5	-2	0	14:45:27	20000	3904.005197	#N/A	3.1653065	1.062498895	0.014725852	0.010412749	#N/A
13	-2	0	14:45:34	20000	3160.886599	#N/A	3.1703946	1.034884392	0.014343125	0.010142121	48
13.5	-2	0	14:45:43	20000	2999.369221	#N/A	3.1879737	0.98947216	0.013713727	0.00969707	64
14	-2	0	14:45:52	20000	2645.64748	#N/A	3.1464632	0.977742633	0.01355116	0.009582117	128
14.5	-2	0	14:46:02	20000	1971.829943	#N/A	3.1291594	0.989756635	0.01371767	0.009699858	41.60000229
15	-2	0	14:46:14	20000	4137.146198	#N/A	3.1060269	1.013873435	0.01405192	0.009936208	#N/A
15.5	-2	0	14:46:21	20000	4489.081691	#N/A	3.0473122	1.026238051	0.014223289	0.010057384	70.40000153
16	-2	0	14:46:28	20000	6617.936068	#N/A	3.0532836	1.025687855	0.014215664	0.010051992	6.400000095
16.5	-2	0	14:46:33	20000	5583.255118	#N/A	3.0117849	1.05385754	0.014606085	0.010328062	#N/A
17	-2	0	14:46:39	20000	5057.796452	#N/A	2.9275334	1.065096089	0.014761848	0.010438203	#N/A
17.5	-2	0	14:46:45	20000	3251.097501	#N/A	2.8695094	1.027363684	0.01423889	0.010068416	#N/A
18	-2	0	14:46:54	20000	3773.836761	#N/A	2.7713265	1.056521909	0.014643013	0.010354174	#N/A
19	-2	0	14:47:02	20000	2089.11191	#N/A	2.6112996	1.05468627	0.014617571	0.010336184	#N/A
20	-2	0	14:47:13	20000	1825.761832	#N/A	2.3021237	1.141746024	0.015824188	0.011189391	12.80000019
21	-2	0	14:47:27	20000	2674.799197	#N/A	2.062799	1.197086026	0.016591181	0.011731736	6.400000095
22	-2	0	14:47:36	20000	2808.256724	#N/A	1.8795869	1.285418522	0.017815437	0.012597416	#N/A

23	-2	0	14:47:46	20000	3918.247674	#N/A	1.6539331	1.318931356	0.018279913	0.01292585	12.80000019
24	-2	0	14:47:53	20000	2110.487332	#N/A	1.422775	1.334547227	0.018496343	0.01307889	#N/A
25	-2	0	14:48:06	20000	2770.33604	#N/A	1.1572004	1.34969531	0.01870629	0.013227345	19.20000076
26	-2	0	14:48:14	20000	2456.637917	#N/A	1.0643063	1.391752082	0.019289182	0.013639511	32
27	-2	0	14:48:25	19601	1307.316036	#N/A	1.0000647	1.437447036	0.020124258	0.01423	19.20000076
28	-2	0	14:48:41	20000	2414.617826	#N/A	0.8662665	1.476297979	0.020460958	0.014468082	#N/A
29	-2	0	14:48:53	20000	1950.47674	#N/A	0.8072639	1.486377745	0.02060066	0.014566866	#N/A
30	-2	0	14:49:05	17949	1196.814129	#N/A	0.6933853	1.523820686	0.022293687	0.015764017	#N/A
31	-2	0	14:49:22	10578	705.4937061	#N/A	0.6938093	1.572001498	0.029959032	0.021184235	#N/A
32	-2	0	14:49:39	18006	1200.757397	#N/A	0.7228286	1.542048808	0.022524628	0.015927317	#N/A
33	-2	0	14:49:56	20000	1778.219885	#N/A	0.66474	1.551201696	0.021499096	0.015202157	#N/A
34	-2	0	14:50:09	20000	1668.561559	#N/A	0.618411	1.58322041	0.021942864	0.015515948	#N/A
35	-2	0	14:50:24	20000	3738.5284	#N/A	0.5156431	1.504518142	0.020852079	0.014744646	#N/A
36	-2	0	14:50:31	20000	1855.700419	#N/A	0.4927132	1.519974079	0.021066293	0.014896118	#N/A
37	-2	0	14:50:45	20000	1780.828236	#N/A	0.5211557	1.587412349	0.022000963	0.01555703	#N/A
38	-2	0	14:50:58	20000	2118.110256	#N/A	0.6435282	1.626934444	0.022548725	0.015944356	#N/A
39	-2	0	14:51:10	20000	2173.442522	#N/A	0.6993687	1.629364629	0.022582406	0.015968173	#N/A

B-2 Combustion test

The combustion experiments were carried out in combustion lab. in Cardiff University. Only the nozzle with smooth surface and nozzle with wire mesh were tested under flashback condition for different flow rates and with and without air injection. The tables B-2 and B-3 are show results for a nozzle with a 150um wire mesh samples of the results for the geometries. The red cells represent the flow rates where flashback was obtained. The 50um and 250um results were put on DVD with this thesis.

Table B-1 Flashback result for nozzle with 150um wire mesh and no central air injection.

Tang Area 0.005353

Airflow (l/min)	Gas Flow Pre (l/min)	Air Flow Dif (l/min)	Estatus	Air used g/s	Gas used g/s	FAR act	Equivl. Rat	Air density kg/m^3	Gas density kg/m^3	Total density (Tangentials) kg/m^3	Tangential velocity m/s	Mix.Mass flow rate (kg/s)
400	28	0	Blow	8.14	0.311267	0.038239	0.656184	1.221	0.667	1.1848	1.870339	0.008451
450	30	0	Blow	9.1575	0.3335	0.036418	0.624938	1.221	0.667	1.1864	2.103309	0.009491
500	33	0	Blow	10.175	0.36685	0.036054	0.618688	1.221	0.667	1.1867	2.336829	0.010542
550	35	0	Blow	11.1925	0.389083	0.034763	0.596531	1.221	0.667	1.1879	2.569807	0.011582
600	38	0	Blow	12.21	0.422433	0.034597	0.593691	1.221	0.667	1.1880	2.803327	0.012632
650	41	0	Blow	13.2275	0.455783	0.034457	0.591287	1.221	0.667	1.1881	3.036848	0.013683
700	44	0	Blow	14.245	0.489133	0.034337	0.589227	1.221	0.667	1.1882	3.270369	0.014734
750	47	0	Blow	15.2625	0.522483	0.034233	0.587441	1.221	0.667	1.1883	3.503889	0.015785
800	50	0	Blow	16.28	0.555833	0.034142	0.585879	1.221	0.667	1.1884	3.73741	0.016836

850	54	0	Blow	17.2975	0.6003	0.034704	0.595529	1.221	0.667	1.1879	3.97147	0.017898
900	58	0	Blow	18.315	0.644767	0.035204	0.604106	1.221	0.667	1.1875	4.205532	0.01896
950	62	0	Blow	19.3325	0.689233	0.035652	0.611781	1.221	0.667	1.1871	4.439594	0.020022
1000	66	0	Blow	20.35	0.7337	0.036054	0.618688	1.221	0.667	1.1867	4.673658	0.021084
1050	70	0	Blow	21.3675	0.778167	0.036418	0.624938	1.221	0.667	1.1864	4.907722	0.022146
1100	73	0	Blow	22.385	0.811517	0.036253	0.622097	1.221	0.667	1.1865	5.141241	0.023197
1150	76	0	Blow	23.4025	0.844867	0.036102	0.619503	1.221	0.667	1.1867	5.374761	0.024247
1200	79	0	Blow	24.42	0.878217	0.035963	0.617126	1.221	0.667	1.1868	5.60828	0.025298
1250	82	0	Blow	25.4375	0.911567	0.035836	0.614939	1.221	0.667	1.1869	5.8418	0.026349
1300	84	0	Blow	26.455	0.9338	0.035298	0.605709	1.221	0.667	1.1874	6.074777	0.027389
1350	86	0	Blow	27.4725	0.956033	0.0348	0.597163	1.221	0.667	1.1878	6.307756	0.028429
1400	88	0	Blow	28.49	0.978267	0.034337	0.589227	1.221	0.667	1.1882	6.540737	0.029468
1450	91	0	Blow	29.5075	1.011617	0.034283	0.588303	1.221	0.667	1.1883	6.774258	0.030519
1500	93	0	Blow	30.525	1.03385	0.033869	0.581192	1.221	0.667	1.1887	7.00724	0.031559
1550	96	0	Blow	31.5425	1.0672	0.033834	0.580587	1.221	0.667	1.1887	7.240761	0.03261
1600	99	0	Blow	32.56	1.10055	0.033801	0.58002	1.221	0.667	1.1887	7.474282	0.033661
1650	102	0	Blow	33.5775	1.1339	0.03377	0.579488	1.221	0.667	1.1887	7.707803	0.034711
1700	105	0	Blow	34.595	1.16725	0.03374	0.578986	1.221	0.667	1.1888	7.941324	0.035762
400	29	0	Blue	8.14	0.322383	0.039605	0.67962	1.221	0.667	1.1836	1.870891	0.008462
450	33	0	Blue	9.1575	0.36685	0.04006	0.687431	1.221	0.667	1.1831	2.104961	0.009524
500	37	0	Blue	10.175	0.411317	0.040424	0.693681	1.221	0.667	1.1828	2.339031	0.010586
550	40	0	Blue	11.1925	0.444667	0.039729	0.68175	1.221	0.667	1.1834	2.572545	0.011637
600	45	0	Blue	12.21	0.50025	0.040971	0.703055	1.221	0.667	1.1823	2.807171	0.01271
650	49	0	Blue	13.2275	0.544717	0.041181	0.70666	1.221	0.667	1.1822	3.041242	0.013772
700	54	0	Blue	14.245	0.6003	0.042141	0.723142	1.221	0.667	1.1813	3.275873	0.014845
750	57	0	Blue	15.2625	0.63365	0.041517	0.712429	1.221	0.667	1.1819	3.509383	0.015896
800	61	0	Blue	16.28	0.678117	0.041653	0.714772	1.221	0.667	1.1818	3.743454	0.016958
850	65	0	Blue	17.2975	0.722583	0.041774	0.71684	1.221	0.667	1.1816	3.977525	0.01802

900	69	0	Blue	18.315	0.76705	0.041881	0.718678	1.221	0.667	1.1816	4.211596	0.019082
950	73	0	Blue	19.3325	0.811517	0.041977	0.720323	1.221	0.667	1.1815	4.445667	0.020144
1000	79	0	Blue	20.35	0.878217	0.043156	0.740551	1.221	0.667	1.1804	4.680864	0.021228
1050	84	0	Blue	21.3675	0.9338	0.043702	0.749925	1.221	0.667	1.1800	4.915501	0.022301
1100	90	0	Blue	22.385	1.0005	0.044695	0.766969	1.221	0.667	1.1791	5.150706	0.023386
1150	96	0	Blue	23.4025	1.0672	0.045602	0.782531	1.221	0.667	1.1783	5.385917	0.02447
1200	100	0	Blue	24.42	1.111667	0.045523	0.781172	1.221	0.667	1.1784	5.619988	0.025532
1250	107	0	Blue	25.4375	1.189483	0.046761	0.80242	1.221	0.667	1.1773	5.855777	0.026627
1300	112	0	Blue	26.455	1.245067	0.047064	0.807612	1.221	0.667	1.1771	6.090422	0.0277
1350	120	0	Blue	27.4725	1.334	0.048558	0.83325	1.221	0.667	1.1758	6.3268	0.028807
1400	125	0	Blue	28.49	1.389583	0.048774	0.83697	1.221	0.667	1.1756	6.561448	0.02988
1450	128	0	Blue	29.5075	1.422933	0.048223	0.827504	1.221	0.667	1.1761	6.794937	0.03093
1500	130	0	Blue	30.525	1.445167	0.047344	0.812419	1.221	0.667	1.1768	7.027852	0.03197
1550	133	0	Blue	31.5425	1.478517	0.046874	0.804355	1.221	0.667	1.1772	7.261347	0.033021
1600	135	0	Blue	32.56	1.50075	0.046092	0.790937	1.221	0.667	1.1779	7.494271	0.034061
400	28	0	F	8.14	0.311267	0.038239	0.656184	1.221	0.667	1.1848	1.870339	0.008451
500	33	0	F	10.175	0.36685	0.036054	0.618688	1.221	0.667	1.1867	2.336829	0.010542
600	43	0	F	12.21	0.478017	0.03915	0.671808	1.221	0.667	1.1840	2.80606	0.012688
700	50	0	F	14.245	0.555833	0.03902	0.669576	1.221	0.667	1.1841	3.273644	0.014801
800	61	0	F	16.28	0.678117	0.041653	0.714772	1.221	0.667	1.1818	3.743454	0.016958
900	110	0	Blue	19.3325	0.855983	0.044277	0.759793	1.221	0.667	1.1773	4.216136	From this flow rate onward no flashback
1000	85	0	Blue	21.3675	0.944917	0.044222	0.758853	1.221	0.667	1.1776	4.684277	observed even at high tangential gas
1050	91	0	Blue	22.385	1.011617	0.045192	0.775491	1.221	0.667	1.1768	4.919497	flow rates (110 LPM and higher
1100	98	0	Blue	23.4025	1.089433	0.046552	0.798833	1.221	0.667	1.1757	5.155299	
1200	109	0	Blue	25.4375	1.211717	0.047635	0.817418	1.221	0.667	1.1749	5.625177	
1300	119	0	Blue	27.4725	1.322883	0.048153	0.826306	1.221	0.667	1.1745	6.094476	
1400	130	0	Blue	29.5075	1.445167	0.048976	0.840433	1.221	0.667	1.1739	6.56436	
1500	135	0	Blue	31.5425	1.50075	0.047579	0.816451	1.221	0.667	1.1753	7.030744	

| 1600 | 139 | 0 | Blue | 33.5775 | 1.545217 | 0.046019 | 0.789694 | 1.221 | 0.667 | 1.1767 | 7.496568 |

Table B-2 flashback results for nozzle with 150 um grid and central air injection.

| | | | | | | | | Tang Area | 0.005353 | | | |

Airflow (l/min)	Gas Flow Pre	Air Flow Dif	Estatus	Air used	Gas used	FAR	Equivl. Rat	Air density	Gas density	Total density (Tangentials)	Tangential velocity m/s	Mix.Mass flow rate (kg/s)
	(l/min)	(l/min)		g/s	g/s	act		kg/m^3	kg/m^3	kg/m^3		
400	28	50	Blow	9.1575	0.311267	0.03399	0.583275	1.221	0.667	1.1848	2.09552	0.009469
450	30	50	Blow	10.175	0.3335	0.032776	0.562444	1.221	0.667	1.1864	2.328798	0.010509
500	33	50	Blow	11.1925	0.36685	0.032776	0.562444	1.221	0.667	1.1867	2.56238	0.011559
550	35	50	Blow	12.21	0.389083	0.031866	0.54682	1.221	0.667	1.1879	2.795577	0.012599
600	38	50	Blow	13.2275	0.422433	0.031936	0.548022	1.221	0.667	1.1880	3.029126	0.01365
650	41	50	Blow	14.245	0.455783	0.031996	0.549052	1.221	0.667	1.1881	3.26267	0.014701
700	44	50	Blow	15.2625	0.489133	0.032048	0.549945	1.221	0.667	1.1882	3.496211	0.015752
750	47	50	Blow	16.28	0.522483	0.032094	0.550726	1.221	0.667	1.1883	3.72975	0.016802
800	50	50	Blow	17.2975	0.555833	0.032134	0.551415	1.221	0.667	1.1884	3.963286	0.017853
850	54	50	Blow	18.315	0.6003	0.032776	0.562444	1.221	0.667	1.1879	4.197251	0.018915
900	58	50	Blow	19.3325	0.644767	0.033351	0.572311	1.221	0.667	1.1875	4.431227	0.019977
950	62	50	Blow	20.35	0.689233	0.033869	0.581192	1.221	0.667	1.1871	4.665213	0.021039
1000	66	50	Blow	21.3675	0.7337	0.034337	0.589227	1.221	0.667	1.1867	4.899208	0.022101
1050	70	50	Blow	22.385	0.778167	0.034763	0.596531	1.221	0.667	1.1864	5.133211	0.023163
1100	73	50	Blow	23.4025	0.811517	0.034676	0.595049	1.221	0.667	1.1865	5.366758	0.024214
1150	76	50	Blow	24.42	0.844867	0.034597	0.593691	1.221	0.667	1.1867	5.600303	0.025265
1200	79	50	Blow	25.4375	0.878217	0.034524	0.592441	1.221	0.667	1.1868	5.833847	0.026316

1250	82	50	Blow	26.455	0.911567	0.034457	0.591287	1.221	0.667	1.1869	6.067388	0.027367
1300	84	50	Blow	27.4725	0.9338	0.03399	0.583275	1.221	0.667	1.1874	6.300457	0.028406
1350	86	50	Blow	28.49	0.956033	0.033557	0.575835	1.221	0.667	1.1878	6.53352	0.029446
1400	88	50	Blow	29.5075	0.978267	0.033153	0.568909	1.221	0.667	1.1882	6.76658	0.030486
1450	91	50	Blow	30.525	1.011617	0.033141	0.568693	1.221	0.667	1.1883	7.00011	0.031537
1500	93	50	Blow	31.5425	1.03385	0.032776	0.562444	1.221	0.667	1.1887	7.233163	0.032576
1550	96	50	Blow	32.56	1.0672	0.032776	0.562444	1.221	0.667	1.1887	7.46669	0.033627
1600	99	50	Blow	33.5775	1.10055	0.032776	0.562444	1.221	0.667	1.1887	7.700217	0.034678
1650	102	50	Blow	34.595	1.1339	0.032776	0.562444	1.221	0.667	1.1887	7.933743	0.035729
1700	105	50	Blow	35.6125	1.16725	0.032776	0.562444	1.221	0.667	1.1888	8.167269	0.03678
400	29	50	Blue	9.1575	0.322383	0.035204	0.604106	1.221	0.667	1.1836	2.095843	0.00948
450	33	50	Blue	10.175	0.36685	0.036054	0.618688	1.221	0.667	1.1831	2.329837	0.010542
500	37	50	Blue	11.1925	0.411317	0.036749	0.630619	1.221	0.667	1.1828	2.563846	0.011604
550	40	50	Blue	12.21	0.444667	0.036418	0.624938	1.221	0.667	1.1834	2.797476	0.012655
600	45	50	Blue	13.2275	0.50025	0.037819	0.648974	1.221	0.667	1.1823	3.031895	0.013728
650	49	50	Blue	14.245	0.544717	0.038239	0.656184	1.221	0.667	1.1822	3.265931	0.01479
700	54	50	Blue	15.2625	0.6003	0.039332	0.674933	1.221	0.667	1.1813	3.500402	0.015863
750	57	50	Blue	16.28	0.63365	0.038922	0.667902	1.221	0.667	1.1819	3.734016	0.016914
800	61	50	Blue	17.2975	0.678117	0.039203	0.672727	1.221	0.667	1.1818	3.968064	0.017976
850	65	50	Blue	18.315	0.722583	0.039453	0.677016	1.221	0.667	1.1816	4.202115	0.019038
900	69	50	Blue	19.3325	0.76705	0.039677	0.680853	1.221	0.667	1.1816	4.436168	0.0201
950	73	50	Blue	20.35	0.811517	0.039878	0.684307	1.221	0.667	1.1815	4.670224	0.021162
1000	79	50	Blue	21.3675	0.878217	0.041101	0.705287	1.221	0.667	1.1804	4.905225	0.022246
1050	84	50	Blue	22.385	0.9338	0.041715	0.715838	1.221	0.667	1.1800	5.139771	0.023319
1100	90	50	Blue	23.4025	1.0005	0.042752	0.733622	1.221	0.667	1.1791	5.374813	0.024403
1150	96	50	Blue	24.42	1.0672	0.043702	0.749925	1.221	0.667	1.1783	5.609875	0.025487
1200	100	50	Blue	25.4375	1.111667	0.043702	0.749925	1.221	0.667	1.1784	5.843959	0.026549
1250	107	50	Blue	26.455	1.189483	0.044963	0.771558	1.221	0.667	1.1773	6.079544	0.027644

1300	112	50	Blue	27.4725	1.245067	0.04532	0.7777	1.221	0.667	1.1771	6.31414	0.028718
1350	120	50	Blue	28.49	1.334	0.046823	0.803491	1.221	0.667	1.1758	6.550274	0.029824
1400	125	50	Blue	29.5075	1.389583	0.047093	0.808109	1.221	0.667	1.1756	6.784887	0.030897
1450	128	50	Blue	30.525	1.422933	0.046615	0.79992	1.221	0.667	1.1761	7.018466	0.031948
1500	130	50	Blue	31.5425	1.445167	0.045816	0.786212	1.221	0.667	1.1768	7.251525	0.032988
1550	133	50	Blue	32.56	1.478517	0.045409	0.779219	1.221	0.667	1.1772	7.485096	0.034039
1600	135	50	Blue	33.5775	1.50075	0.044695	0.766969	1.221	0.667	1.1779	7.718148	0.035078
400	33	50	F	9.1575	0.36685	0.04006	0.687431	1.221	0.667	1.1788	2.097185	0.009524
500	42	50	F	11.1925	0.4669	0.041715	0.715838	1.221	0.667	1.1781	2.565763	0.011659
600	56	50	F	13.2275	0.622533	0.047064	0.807612	1.221	0.667	1.1737	3.036546	0.01385
700	110	50	Blue,no f	15.2625	0.644767	0.042245	0.724928	1.221	0.667	1.1786	3.278136	from this flow rate no flashback observed
800	68	50	Blue	17.2975	0.755933	0.043702	0.749925	1.221	0.667	1.1776	3.747422	
900	77	50	Blue	19.3325	0.855983	0.044277	0.759793	1.221	0.667	1.1773	4.216136	
950	81	50	Blue	20.35	0.90045	0.044248	0.759299	1.221	0.667	1.1775	4.450207	
1000	85	50	Blue	21.3675	0.944917	0.044222	0.758853	1.221	0.667	1.1776	4.684277	
1050	91	50	Blue	22.385	1.011617	0.045192	0.775491	1.221	0.667	1.1768	4.919497	
1100	98	50	Blue	23.4025	1.089433	0.046552	0.798833	1.221	0.667	1.1757	5.155299	
1150	103	50	Blue	24.42	1.145017	0.046888	0.804607	1.221	0.667	1.1755	5.389947	
1200	109	50	Blue	25.4375	1.211717	0.047635	0.817418	1.221	0.667	1.1749	5.625177	
1250	113	50	Blue	26.455	1.256183	0.047484	0.814822	1.221	0.667	1.1751	5.859244	
1300	119	50	Blue	27.4725	1.322883	0.048153	0.826306	1.221	0.667	1.1745	6.094476	
1350	125	50	Blue	28.49	1.389583	0.048774	0.83697	1.221	0.667	1.1741	6.329709	
1400	130	50	Blue	29.5075	1.445167	0.048976	0.840433	1.221	0.667	1.1739	6.56436	
1450	133	50	Blue	30.525	1.478517	0.048436	0.831167	1.221	0.667	1.1745	6.797841	
1500	135	50	Blue	31.5425	1.50075	0.047579	0.816451	1.221	0.667	1.1753	7.030744	
1550	138	50	Blue	32.56	1.5341	0.047116	0.808513	1.221	0.667	1.1757	7.264232	
1600	139	50	Blue	33.5775	1.545217	0.046019	0.789694	1.221	0.667	1.1767	7.496568	

References

Agustin Valera-Medina et al. 2008. Large Coherent Structures Visualization in a Swirl Burner. *14th Int Symp on Applications of Laser Techniques to Fluid Mechanics Lisbon, Portugal, 07-10 July, 2008*.

Antonia, R. A. and Krogstad, P. Å. 2001. Turbulence structure in boundary layers over different types of surface roughness. *Fluid Dynamics Research* 28(2), pp. 139-157.

ASME. 2015. *Engineering History* [Online]. Available at: https://www.asme.org/about-asme/who-we-are/engineering-history/landmarks/135-neuchatel-gas-turbine [Accessed.

Bacher, E. V. and Smith, C. R. 1986. Turbulent Boundary-Layer Modification by Surface Riblets. *Aiaa Journal* 24(8), pp. 1382-1385.

Baskharone, E. A. 2006. *Principles of Turbomachinery in Air-Breathing Engines*. Cambridge University Press.

Baumgartner, G. et al. 2016. Experimental Investigation of the Transition Mechanism from Stable Flame to Flashback in a Generic Premixed Combustion System with High-Speed Micro-Particle Image Velocimetry and Micro-PLIF Combined with Chemiluminescence Imaging. *Journal of Engineering for Gas Turbines and Power* 138(2), p. 021501.

Bechert, D. W. and Bartenwerfer, M. 1989. The Viscous-Flow on Surfaces with Longitudinal Ribs. *Journal of Fluid Mechanics* 206, pp. 105-129.

Bechert, D. W. et al. eds. 1986. *DRAG REDUCTION MECHANISMS DERIVED FROM SHARK SKIN*. ICAS Proceedings 1986: 15th Congress of the International Council of the Aeronautical Sciences. London, Engl.

Bechert, D. W. et al. 2000. Experiments with three-dimensional riblets as an idealized model of shark skin. *Experiments in Fluids* 28(5), pp. 403-412.

Bechert, D. W. et al. 1997. Experiments on drag-reducing surfaces and their optimization with an adjustable geometry. *Journal of Fluid Mechanics* 338, pp. 59-87.

Benhalilou, M. and Kasagi, N. 1999. Numerical prediction of heat and momentum transfer over micro-grooved surface with a nonlinear k–ε model. *International Journal of Heat and Mass Transfer* 42(14), pp. 2525-2541.

Benim, A. C. and Syed, K. J. 2015a. Chapter 1 - Introduction. In: Syed, A.C.B.J. ed. *Flashback Mechanisms in Lean Premixed Gas Turbine Combustion*. Boston: Academic Press, pp. 1-3.

Benim, A. C. and Syed, K. J. 2015b. Chapter 8 - Flashback Due to Flame Propagation in Boundary Layers. In: Syed, A.C.B.J. ed. *Flashback Mechanisms in Lean Premixed Gas Turbine Combustion*. Boston: Academic Press, pp. 59-71.

Benjamin W. Niebel , A. B. D., Richard A. Wysk. 1989. *Modern Manufacturing process Engineering*. 1st ed.

Berlad, A. and Potter, A. 1957. Relation of boundary velocity gradient for flash-back to burning velocity and quenching distance. *Combustion and Flame* 1(1), pp. 127-128.

References

Bissacco, G. et al. 2011. Feasibility of wear compensation in micro EDM milling based on discharge counting and discharge population characterization. *CIRP Annals - Manufacturing Technology* 60(1), pp. 231-234.

Bixler, G. D. and Bhushan, B. 2012. Biofouling: lessons from nature. *Philos Trans A Math Phys Eng Sci* 370(1967), pp. 2381-2417.

Bixler, G. D. and Bhushan, B. 2013a. Fluid Drag Reduction with Shark-Skin Riblet Inspired Microstructured Surfaces. *Advanced Functional Materials* 23(36), pp. 4507-4528.

Bixler, G. D. and Bhushan, B. 2013b. Shark skin inspired low-drag microstructured surfaces in closed channel flow. *J Colloid Interface Sci* 393, pp. 384-396.

Bixler, G. D. and Bhushan, B. 2014. Rice- and butterfly-wing effect inspired self-cleaning and low drag micro/nanopatterned surfaces in water, oil, and air flow. *Nanoscale* 6(1), pp. 76-96.

Bollinger, L. E. 1952. Studies on Burner Flames of Hydrogen- Oxygen Mixtures at High Pressure *Wright Air Development Center* (WADC Tech. Rep.), pp. 52-59.

Bollinger, L. E. and Edse, R. 1956. Effect of Burner-Tip Temperature on Flash Back of Turbulent Hydrogen-Oxygen Flames. *Industrial & Engineering Chemistry* 48(4), pp. 802-807.

Bomminayuni, S. and Stoesser, T. 2011. Turbulence statistics in an open-channel flow over a rough bed. *Journal of Hydraulic Engineering* 137(11), pp. 1347-1358.

Bradshaw, P. 1971. Calculation of three-dimensional turbulent boundary layers. *Journal of Fluid Mechanics* 46(3), pp. 417-445.

BROGLIO, R. 2014. Plant Efficiency Still Rules, No Matter Which Way the Political/Economic Winds Blow. *Power Engineering* 118(12).

Cambridge, U. o. 2017. *Hot-Wire Anemometers* [Online]. Available at: http://www-g.eng.cam.ac.uk/whittle/current-research/hph/hot-wire/hot-wire.html [Accessed.

Cevheri, M. et al. 2016. A local mesh refinement approach for large-eddy simulations of turbulent flows. *International Journal for Numerical Methods in Fluids*.

Chen, H. et al. 2014. Flow over bio-inspired 3D herringbone wall riblets. *Experiments in Fluids* 55(3).

Choi, K. S. 1989. Near-Wall Structure of a Turbulent Boundary-Layer with Riblets. *Journal of Fluid Mechanics* 208, pp. 417-458.

Chu, D. C. and Karniadakis, G. E. M. 1993. A Direct Numerical-Simulation of Laminar and Turbulent-Flow over Riblet-Mounted Surfaces. *Journal of Fluid Mechanics* 250, pp. 1-42.

COSPP. 2010. *Gas Turbines breaking the 60% efficiency barrier* [Online]. Available at: http://www.cospp.com/articles/print/volume-11/issue-3/features/gas-turbines-breaking.html [Accessed: 3].

References

Coyle, E. D. and Simmons, R. A. 2014. *Understanding the Global Energy Crisis*. West Lafayette, IN: Purdue University Press, p. 318.

Dabireau, F. et al. 2003. Interaction of flames of H2 + O2 with inert walls. *Combustion and Flame* 135(1–2), pp. 123-133.

Dam, B. et al. 2011. Flashback propensity of syngas fuels. *Fuel* 90(2), pp. 618-625.

Davu, D. et al. eds. 2005. *Investigation on flashback propensity of syngas premixed flames*. 41st AIAA/ASME/SAE/ASEE Joint Propulsion Conference and Exhibit. Tucson, AZ.

Dean, B. and Bhushan, B. 2012. The effect of riblets in rectangular duct flow. *Applied Surface Science* 258(8), pp. 3936-3947.

DeGroot, C. T. et al. 2016. Drag Reduction Due to Streamwise Grooves in Turbulent Channel Flow. *Journal of Fluids Engineering* 138(12), pp. 121201-121201-121210.

Denkena, B. et al. 2010. Ductile and brittle material removal mechanisms in natural nacre - A model for novel implant materials. *Journal of Materials Processing Technology* 210(14), pp. 1827-1837.

DISA. 1995. Type 55M10 Instruction Manual. In: Department, D.I. ed. p. 20.

Djenidi, L. and Antonia, R. A. 1996. Laser Doppler anemometer measurements of turbulent boundary layer over a riblet surface. *Aiaa Journal* 34(5), pp. 1007-1012.

Duan, Z. et al. eds. 2015. *Parametric analysis of flashback propensity with various fuel compositions and burner materials*. ASME Turbo Expo 2015: Turbine Technical Conference and Exposition, GT 2015. American Society of Mechanical Engineers (ASME).

Dugger, G. L. 1955. Flame Stability of Preheated Propane-Air Mixtures. *Industrial & Engineering Chemistry* 47(1), pp. 109-114.

Durst, F. et al. 1981. *Principles and practice of laser-Doppler anemometry*. Academic Press.

Dynamics, D. 2013. Experimental Techniques: Laser Doppler Anemometry (LDA). In: Dynamics, D. ed.

Dynamics, D. 2016. MiniCTA_MultichannelCTA_Anemometer_System.

Ebi, D. and Clemens, N. T. 2016. Experimental investigation of upstream flame propagation during boundary layer flashback of swirl flames. *Combustion and Flame* 168, pp. 39-52.

EIA. 2016a. *Annual review outlook 2016*.

EIA. 2016b. Short-Term Energy Outlook (STEO). p. 50.

Eichler, C. et al. 2012. Experimental Investigation of Turbulent Boundary Layer Flashback Limits for Premixed Hydrogen-Air Flames Confined in Ducts. *Journal of Engineering for Gas Turbines and Power* 134(1), p. 011502.

Eichler, C. and Sattelmayer, T. 2011a. Experiments on Flame Flashback in a Quasi-2D Turbulent Wall Boundary Layer for Premixed Methane-Hydrogen-Air Mixtures. *Journal of Engineering for Gas Turbines and Power* 133(1), p. 011503.

Eichler, C. and Sattelmayer, T. 2011b. Experiments on Flame Flashback in a Quasi-2D Turbulent Wall Boundary Layer for Premixed Methane-Hydrogen-Air Mixtures. *Journal of Engineering for Gas Turbines and Power-Transactions of the Asme* 133(1), p. 011503.

El-Samni, O. A. et al. 2005. Turbulent flow over thin rectangular riblets. *Journal of Mechanical Science and Technology* 19(9), pp. 1801-1810.

Energy Information Administraions. 2013. *Today in Energy*.

Fares Amer Hatem, A. V.-M., Nick Syred, Philp J Bowen. 2017. Experimental investigation of the Effect of Air Diffusive injection on premixing swirl flames.

Fine, B. 1958. The Flashback of Laminar and Turbulent Burner Flames at Reduced Pressure. *Combustion and Flame* 2(3), pp. 253-266.

Fine, B. 1959. Effect of Initial Temperature on Flash Back of Laminar and Turbulent Burner Flames. *Industrial & Engineering Chemistry* 51(4), pp. 564-566.

Fox, J. S. and Bhargava, A. eds. 1984. *FLAME SPEED AND FLASHBACK GRADIENT FOR SIMULATED BIOMASS GASIFICATION PRODUCTS*. Proceedings of the Intersociety Energy Conversion Engineering Conference.

Fraga, B. and Stoesser, T. 2016. Influence of bubble size, diffuser width, and flow rate on the integral behavior of bubble plumes. *Journal of Geophysical Research: Oceans* 121(6), pp. 3887-3904.

Fraga, B. et al. 2016. A LES-based Eulerian-Lagrangian approach to predict the dynamics of bubble plumes. *Ocean Modelling* 97, pp. 27-36.

France, D. H. 1977. Flashback of Laminar Monoport Burner Flames. *Journal of the Institute of Fuel* 50(404), pp. 147-152.

Friedmann, E. 2010. The Optimal Shape of Riblets in the Viscous Sublayer. *Journal of Mathematical Fluid Mechanics* 12(2), pp. 243-265.

Gazzani, M. et al. 2014. Using Hydrogen as Gas Turbine Fuel: Premixed Versus Diffusive Flame Combustors. *Journal of Engineering for Gas Turbines and Power* 136(5), pp. 051504-051504.

Giampaolo, T. 2006. *Gas Turbine Handbook : Principles and Practices*. Lilburn, GA: Fairmount Press.

Global Carbon Budget. 2014. *Global Carbon Budget 2014* [Online]. Available at: http://www.globalcarbonproject.org/carbonbudget/14/files/GCP_budget_2014_lowres_v1.02.pdf [Accessed.

Goldstein, D. et al. 1995. Direct Numerical-Simulation of Turbulent-Flow over a Modeled Riblet Covered Surface. *Journal of Fluid Mechanics* 302, pp. 333-376.

References

Gruber, A. et al. 2012. Direct numerical simulation of premixed flame boundary layer flashback in turbulent channel flow. *Journal of Fluid Mechanics* 709, pp. 516-542.

Gruber, A. et al. 2015. Modeling of mean flame shape during premixed flame flashback in turbulent boundary layers. *Proceedings of the Combustion Institute* 35(2), pp. 1485-1492.

Gruber, A. et al. 2010. Turbulent flame-wall interaction: a direct numerical simulation study. *Journal of Fluid Mechanics* 658, pp. 5-32.

Haecheon, C. et al. 1993. Direct numerical simulation of turbulent flow over riblets. *Journal of Fluid Mechanics* 255, pp. 503-539.

Hatem, F. A. et al. 2017. Experimental investigation of the Effect of Air Diffusive injection on premixing swirl flames.*55th AIAA Aerospace Sciences Meeting*. American Institute of Aeronautics and Astronautics.

Hatem, F. A. et al. 2015. Experimental Investigation of the Effects of Fuel Diffusive Injectors on Premixed Swirling Flames.*53rd AIAA Aerospace Sciences Meeting*. American Institute of Aeronautics and Astronautics.

Hoferichter, V. et al. 2017. Prediction of Confined Flame Flashback Limits Using Boundary Layer Separation Theory. *Journal of Engineering for Gas Turbines and Power* 139(2).

Huang, S. and Li, Q. S. 2010. A new dynamic one-equation subgrid-scale model for large eddy simulations. *International Journal for Numerical Methods in Engineering* 81(7), pp. 835-865.

J T Black , R. A. K. 2013. *DeGarmo's Materials and Processes in Manufacturing*. 11th ed.

J. B. Klemp, A. A. 1972. High Reynolds number steady separated flow past a wedge of negative angle. *The Journal of Fluid Mechanics* 56(3), pp. 577-590.

Jameson, E. C. 2001. *Electrical Discharge Machining*. United State of America Society of Manufacturing Engineers, p. 329.

Jin, Y. and Herwig, H. 2014. Turbulent flow and heat transfer in channels with shark skin surfaces: Entropy generation and its physical significance. *International Journal of Heat and Mass Transfer* 70, pp. 10-22.

Jung, Y. C. and Bhushan, B. 2010. Biomimetic structures for fluid drag reduction in laminar and turbulent flows. *Journal of Physics Condensed Matter* 22(3).

K. S. Choi, K. K. P., T. V. Troung 1996. *Emerging techniques in drag reduction*. London p. 339.

Kara, S. et al. 2015. Free-surface versus rigid-lid LES computations for bridge-abutment flow. *Journal of Hydraulic Engineering* 141(9).

Kara, S. et al. eds. 2014. *Water surface response to flow through bridge openings*. 7th International Conference on Fluvial Hydraulics, RIVER FLOW 2014. Lausanne. CRC Press/Balkema.
Kara, S. et al. 2012. Turbulence statistics in compound channels with deep and shallow overbank flows. *Journal of Hydraulic Research* 50(5), pp. 482-493.

References

Kates, R. W. et al. 2003. Global change and local places: lessons learned. *Global change and local places: estimating, understanding, and reducing greenhouse gases*, p. 239.

Khitrin, L. N. et al. 1965. Peculiarities of laminar- and turbulent-flame flashbacks. *Symposium (International) on Combustion* 10(1), pp. 1285-1291.

Kim, D. et al. 2014. The effect of baffle spacing on hydrodynamics and solute transport in serpentine contact tanks. *Journal of Hydraulic Research* 52(1), p. 154.

Kitoh, O. 1987. Swirling flow through a bend. *Journal of Fluid Mechanics* 175, pp. 429-446.

Kitoh, O. 1991. Experimental study of turbulent swirling flow in a straight pipe. *Journal of Fluid Mechanics* 225, pp. 445-479.

Kline, S. J. et al. 1967. The structure of turbulent boundary layers. *Journal of Fluid Mechanics* 30(4), pp. 741-773.

Koeltzsch, K. et al. 2002. Flow over convergent and divergent wall riblets. *Experiments in Fluids* 33(2), pp. 346-350.

Kröner, M. et al. 2003. Flashback Limits for Combustion Induced Vortex Breakdown in a Swirl Burner. *Journal of Engineering for Gas Turbines and Power* 125(3), p. 693.

Kurdyumov, V. et al. 2007. Experimental and numerical study of premixed flame flashback. *Proceedings of the Combustion Institute* 31(1), pp. 1275-1282.

Kwon, B. H. et al. 2014. Experimental study on the reduction of skin frictional drag in pipe flow by using convex air bubbles. *Experiments in Fluids* 55(4).

Lachmann G. V. 1961. *Boundary Layer and Flow Control* Pergamon, Oxford, UK. .

Lautrup, B. 2003. *Boundary layer* [Online]. Copenhagen, Denmark The Niels Bohr Institute. Available at: http://www.cns.gatech.edu/PHYS-4421/lautrup/7.6/ [Accessed.

Lee, S. J. and Lee, S. H. 2001. Flow field analysis of a turbulent boundary layer over a riblet surface. *Experiments in Fluids* 30(2), pp. 153-166.

Lee, S. T. and T'Ien, J. S. 1982. A numerical analysis of flame flashback in a premixed laminar system. *Combustion and Flame* 48, pp. 273-285.

Lefebvre, A. H. and Ballal, D. R. 2010. Gas turbine combustion alternative fuels and emissions.

Lewis, B. and Von Elbe, G. 1934. On the Theory of Flame Propagation. *Journal of Chemical Physics* 2(8), p. 537.

Lewis, B. and von Elbe, G. 1943. Stability and structure of burner flames. *Journal of Chemical Physics* 11(2), pp. 75-97.
LG Motion. 2016. Linear Dovetail Slide Assemblies.

Liang, J. F. and Liao, Y. S. 2014. Methods to measure wire deflection in wire EDM machining. *International Journal of Automation Technology* 8(3), pp. 461-467.

Lietz, C. et al. eds. 2014. *Large Eddy Simulation of premixed flame flashback in a turbulent channel*. 52nd AIAA Aerospace Sciences Meeting - AIAA Science and Technology Forum and Exposition, SciTech 2014.

Lieuwen, T. et al. 2008a. Fuel Flexibility Influences on Premixed Combustor Blowout, Flashback, Autoignition, and Stability. *Journal of Engineering for Gas Turbines and Power* 130(1), pp. 011506-011506-011510.

Lieuwen, T. et al. 2008b. Burner development and operability issues associated with steady flowing syngas fired combustors. *Combustion Science and Technology* 180(6), pp. 1169-1192.

Lin, Y.-C. et al. 2013. Turbulent Flame Speed as an Indicator for Flashback Propensity of Hydrogen-Rich Fuel Gases. *Journal of Engineering for Gas Turbines and Power* 135(11), p. 111503.

Luo, Y. et al. 2016. Experimental Investigations on Manufacturing Different-Shaped Bio-Inspired Drag-Reducing Morphologies and Hydrodynamic Testing. *Experimental Techniques* 40(3), pp. 1129-1136.

Mallens, R. M. M. and De Goey, L. P. H. 1998. Flash-back of Laminar Premixed Methane/Air Flames on Slit and Tube Burners. *Combustion Science and Technology* 136(1-6), pp. 41-54.

Marentic F. J., M. T. L. 1986. Drag reduction article In: Application, E.P. ed. *the 3M Company* USA.

Martin, S. and Bhushan, B. 2014. Fluid flow analysis of a shark-inspired microstructure. *Journal of Fluid Mechanics* 756, pp. 5-29.

Martin, S. and Bhushan, B. 2016a. Fluid flow analysis of continuous and segmented riblet structures. *RSC Advances* 6(13), pp. 10962-10978.

Martin, S. and Bhushan, B. 2016b. Modeling and optimization of shark-inspired riblet geometries for low drag applications. *Journal of Colloid and Interface Science* 474, pp. 206-215.

Mehta, R. D. and Bradshaw, P. 1979. Design rules for small low speed wind tunnels. *The Aeronautical Journal (1968)* 83(827), pp. 443-453.

Melling, A. 1997. Tracer particles and seeding for particle image velocimetry. *Measurement Science and Technology* Volume 8(Issue 12), pp. pp. 1406-1416.

Mitutoyo. 2012. VISION MEASURING MACHINES. In: Ltd, M.U. ed. uk p. 32.

Nicoud, F. and Ducros, F. 1999a. Subgrid-scale stress modelling based on the square of the velocity gradient tensor. *Flow, Turbulence and Combustion* 62(3), pp. 183-200.

Nicoud, F. and Ducros, F. 1999b. Subgrid-scale stress modelling based on the square of the velocity gradient tensor. *Flow Turbulence and Combustion* 62(3), pp. 183-200.
Norton Rose Fulbright. 2013. *Shale gas handbook*. Second ed., p. 152.

Nugroho, B. et al. 2013. Large-scale spanwise periodicity in a turbulent boundary layer induced by highly ordered and directional surface roughness. *International Journal of Heat and Fluid Flow* 41, pp. 90-102.

Oner, C. and Altun, S. 2009. Biodiesel production from inedible animal tallow and an experimental investigation of its use as alternative fuel in a direct injection diesel engine. *Applied Energy* 86(10), pp. 2114-2120.

Pallav, K. et al. 2014. Comparative assessment of the laser induced plasma micromachining and the micro-EDM processes. *Journal of Manufacturing Science and Engineering, Transactions of the ASME* 136(1).

Papanicolaou, A. N. et al. 2012. Effects of a fully submerged boulder within a boulder array on the mean and turbulent flow fields: Implications to bedload transport. *Acta Geophysica* 60(6), pp. 1502-1546.

Park, S. R. and Wallace, J. M. 1994. Flow Alteration and Drag Reduction by Riblets in a Turbulent Boundary-Layer. *Aiaa Journal* 32(1), pp. 31-38.

Plee, S. L. and Mellor, A. M. 1978. Review of Flashback Reported in Prevaporizing-Premixing Combustors. *Combustion and Flame* 32(2), pp. 193-203.

Radmanesh, M. et al. 2017. The effects of rectangular riblets on rectangular micro air vehicles for drag reduction. *Proceedings of the Institution of Mechanical Engineers, Part G: Journal of Aerospace Engineering* 231(2), pp. 364-373.

Razak, A. M. Y. 2007. 6 - Gas turbine combustion. In: Razak, A.M.Y. ed. *Industrial Gas Turbines*. Woodhead Publishing, pp. 137-173.

Richards, G. A. et al. 2001. Issues for low-emission, fuel-flexible power systems. *Progress in Energy and Combustion Science* 27(2), pp. 141-169.

Samira Sayad Saravi, K. C., Tze Pei Chong, Alexandros Vathylakis;. 2014. Design of Serrate-Semi-Circular Riblets with Application to Skin Friction Reduction on Engineering Surfaces. *International Journal of Flow Control* 6(3).

Sattelmayer, T. et al. 2016. Interaction of Flame Flashback Mechanisms in Premixed Hydrogen-Air Swirl Flames. *Journal of Engineering for Gas Turbines and Power* 138(1).

Sayad, P. et al. 2015. Visualization of different flashback mechanisms for H2/CH4 mixtures in a variable-swirl burner. *Journal of Engineering for Gas Turbines and Power* 137(3), p. 031507.

Schafer, O. et al. 2003. Flashback in lean prevaporized premixed combustion: Nonswirling turbulent pipe flow study. *Journal of Engineering for Gas Turbines and Power-Transactions of the Asme* 125(3), pp. 670-676.

Schlichting, H. 2000. *Boundary-layer theory*. 8th rev. and enl. ed. ed. Berlin
New York: Springer.
Schobert, H. and Schobert, H. 2013. *Fuels and the global carbon cycle Chemistry of Fossil Fuels and Biofuels*. Cambridge University Press.

Seebregts, A. J. 2010. *Gas-Fired Power*. EIA.

Serope Kalpakjian, S. R. S. 2008. *Manufacturing Processes for Engineering Materials*. 5th ed.

References

Shaffer, B. et al. 2013. Study of fuel composition effects on flashback using a confined jet flame burner. *Journal of Engineering for Gas Turbines and Power* 135(1).

Song, X.-w. et al. 2017. Skin friction reduction characteristics of variable ovoid non-smooth surfaces. *Journal of Zhejiang University-SCIENCE A* 18(1), pp. 59-66.

Sreenivasa Rao M, V. N. 2013. Review on Wire-Cut EDM Process. *International Journal of Advanced Trends in Computer Science and Engineering* 2(6), pp. 12-16.

Sreenivasan, K. R. and Raghu, S. 2000. The control of combustion instability: A perspective. *Current Science* 79(6), pp. 867-883.

Steenbergen, W. and Voskamp, J. 1998. The rate of decay of swirl in turbulent pipe flow. *Flow Measurement and Instrumentation* 9(2), pp. 67-78.

Stoesser, T. et al. 2010. Calculation of primary and secondary flow and boundary shear stresses in a meandering channel. *Advances in Water Resources* 33(2), pp. 158-170.

Stohr, M. and , I. B., C. Carter2 andW. Meier1. 2011. Dynamics of vortex-flame interaction in a turbulent swirl flam. *Proceedings of the European Combustion Meeting 2011*.

Sultanian, B. 2015. *Fluid mechanics: an intermediate approach*. Boca Raton: CRC Press.

Sunggyu Lee , J. G. S., and Sudarshan K . Loyalka. 2014. *Handbook of Alternative Fuel Technologies*. Second ed.

Surleraux, A. et al. 2016. Iterative surface warping to shape craters in micro-EDM simulation. *Engineering with Computers* 32(3), pp. 517-531.

Suzuki, Y. and Kasagi, N. 1994. Turbulent Drag Reduction-Mechanism above a Riblet Surface. *Aiaa Journal* 32(9), pp. 1781-1790.

Swaminathan, N. and Bray, K. N. C. 2011. *Turbulent Premixed Flames*. Cambridge University Press.

Syred, N. et al. 2012. The effect of hydrogen containing fuel blends upon flashback in swirl burners. *Applied Energy* 89(1), pp. 106-110.

Syred, N. et al. 2014. Effect of inlet and outlet configurations on blow-off and flashback with premixed combustion for methane and a high hydrogen content fuel in a generic swirl burner. *Applied Energy* 116, pp. 288-296.

Taamallah, S. et al. 2016. Turbulent flame stabilization modes in premixed swirl combustion: Physical mechanism and Karlovitz number-based criterion. *Combustion and Flame* 166, pp. 19-33.
Taamallah, S. et al. 2015. Fuel flexibility, stability and emissions in premixed hydrogen-rich gas turbine combustion: Technology, fundamentals, and numerical simulations. *Applied Energy* 154, pp. 1020-1047.

The American Petroleum Institute. 2011. Crude Oil Category.

References

Thome, M. and Hirt, G. 2007. Economical and ecological benefits of process-integrated surface structuring. *Key Engineering Materials*. pp. 939-946.

Tuncer Cebeci, P. B. 1977. *Momentum transfer in boundary layers* HEMISPHERE.

UK Government. 2013. [Online]. Available at: https://www.gov.uk/government/uploads/system/uploads/attachment_data/file/407432/20150203_2013_Final_Emissions_statistics [Accessed.

UNFCCC. 2015. *Kyoto protocol* [Online]. Available at: http://www.kyotoprotocol.com/ [Accessed.

Valera-Medina, A. et al. 2011a. Studies of Swirl Burner Characteristics, Flame Lengths and Relative Pressure Amplitudes. *Journal of Fluids Engineering-Transactions of the Asme* 133(10).

Valera-Medina, A. et al. 2011b. Central recirculation zone analysis in an unconfined tangential swirl burner with varying degrees of premixing. *Experiments in Fluids* 50(6), pp. 1611-1623.

Volker Poloczek, H. H. 2008. Modren gas Turbine with High fuel flexibility. *Power-Gen Asia 2008*

von Elbe, G. and Mentser, M. 1945. Further Studies of the Structure and Stability of Burner Flames. *The Journal of Chemical Physics* 13(2), p. 89.

Vukoslavcevic, P. et al. 1992. Viscous Drag Reduction Using Streamwise-Aligned Riblets. *Aiaa Journal* 30(4), pp. 1119-1122.

Walsh, M. J. and Anders Jr, J. B. 1989. Riblet/LEBU research at NASA Langley. *Applied Scientific Research* 46(3), pp. 255-262.

Walsh, M. J. et al. 1984. Combined riblet and lebu drag reduction system.

Wierzba, I. and Kar, K. 1992. Flame flashback within turbulent streams of lean homogeneous fuel mixtures and air. *Journal of Energy Resources Technology, Transactions of the ASME* 114(2), pp. 142-145.

Wikipedia contributors. 2015 Fossil fuel

WMO/GAW. 2014. GREENHOUSE GAS BULLETIN. 10th p. 4.

Wohl, K. 1953. Quenching, flash-back, blow-off-theory and experiment. *Symposium (International) on Combustion* 4(1), pp. 68-89.

Yu, Z. Y. et al. 1998. Micro-EDM for three-dimensional cavities - Development of uniform wear method. *Cirp Annals 1998 - Manufacturing Technology, Vol 47, No 1* 47(1), pp. 169-172.

Zhang, D. Y. et al. 2011. Numerical Simulation and Experimental Study of Drag-Reducing Surface of a Real Shark Skin. *Journal of Hydrodynamics* 23(2), pp. 204-211.